FINAL SCIENTIFIC REPORT

Contract AF 04(695)-822

Department of Meteorology
The University of Wisconsin

November, 1967

Distribution List for

FINAL Scientific Report

Contract AF (04(695)-822)

	Copies
Contracting Agency	10
V. Suomi, U.W.	2
R. Parent, U.W.	2
E. Wahl, U.W.	1
T. Vonder Haar, U.W.	2
E. Smith, U.W.	1
D. Nelson, Aerospace	1
D. Nelson	1
R. Hankins	1
R. Smith	1
J. Bohlson	1
SSEC Library	1
D. Johnson (NESC)	1
W. Nordberg (GSFC)	1
W. Bandeen (GSFC)	1
N. Bradshaw	1
(F. House)	1
(Meteorology file)	1
	30

FINAL SCIENTIFIC REPORT

Contract AF 04 (695)-822

The University of Wisconsin
Department of Meteorology

November , 1967

PRINCIPAL INVESTIGATORS: V. E. Suomi
R. J. Parent

SCIENTIFIC ADVISOR : E. W. Wahl

PROJECT SUPERVISOR : T. H. Vonder Haar

CONTRIBUTIONS BY

J. Bohlson
R. Hankins
D. Nelson
R. Smith
T. Vonder Haar

PREFACE

This report summarizes the major portion of research in atmospheric physics performed as required by the contract work agreement. Additional work has been documented and presented at earlier dates.

The first three papers in Section A discuss methods for extracting meteorological information from remote satellite measurements and a technique for reducing the data. The last paper presents a comparison of observed limb-darkening measurements with theoretical calculations. Section B contains the first comprehensive summary of the earth's global radiation budget using all available data from satellites flown prior to 1966. This work was supported in part by this contract.

A large group of workers have contributed to the papers in this report and their efforts are gratefully acknowledged.

CONTENTS

SECTION A

A TECHNIQUE FOR DETERMINING CLOUD TOP HEIGHTS UTILIZING SATELLITE DATA

by

JOHN STEWART BOHLSON

ABSTRACT

A technique for determining cloud top heights utilizing satellite measurements of infrared radiation in the broad band region is presented. The technique is based on adjusting a calculated upward radiation flux to equal an observed upward flux by placing a gray cloud at various heights which acts to attenuate the outgoing radiation as well as reradiate at a lower temperature. Seven charts based on theoretical and climatological data were constructed to show cloud top heights as a function of cloud cover for a given satellite IR radiation measurement. Five examples are given of cloud tops derived from these charts compared to the tops calculated from the actual radiosonde ascents. The charts yield a good approximation when the time of the year and the synoptic situation are taken into consideration. It is concluded that this technique could be useful in the future as a "backup" system and as a calibration device for the more conventional "window" estimations of cloud top heights.

INTRODUCTION

Estimations of cloud top heights based on satellite data are normally derived from infrared flux in the 8 to 12 micron "window" region. The principal reason for using this wavelength interval is that the vapor absorption coefficient is small and the outgoing intensity in this region is not changed to a large degree by absorption and radiation within the atmosphere from the intensity emitted by the underlying surface. Various authors have shown that the cloud top temperature can be approximated by using temperatures derived from infrared measurements in the 8 to 12 micron wavelength interval when the sky is covered with relatively dense clouds and a black body intensity distribution for the outgoing intensity is assumed (see, for instance: Bandeen et al., 1961, Fritz and Winston, 1962, and Hanel and Stroud, 1961).

The purpose of this study is to present a technique for determining cloud top heights utilizing satellite data in the broad band 3 to 30 micron region, based upon climatological and theoretical atmospheres. At the moment this study is of more theoretical interest. However, one can assume that future satellites will carry instrumentation for simultaneous readings of window, broad band, and television data.

The importance of the transmission properties of clouds for infrared satellite measurements of the atmosphere can clearly be seen when one considers the strong influence of clouds on the thermal energy exchange between the earth, the atmosphere, and space. Cloud layers which are opaque to long wave radiation provide a high cold radiating source near their tops for the upward radiation above the clouds. One must also include in the thermal energy exchange budget the clouds which are not opaque. In this case, radiation above the clouds does not only come from the clouds themselves, but also from the earth and the atmosphere beneath.

Satellite observations of the upward flux and radiosonde ascents from the same area make it possible to calculate an upward flux that equals the observed flux. This is done by placing a "black or partially black" cloud at various heights, the clouds effect being that of attenuation and reradiation at lower temperatures. This then is the basis for the determination of the cloud top height. Specifically, a broad band computer solution of the radiative transfer approximation was used to calculate the upward flux (see discussion in appendix).

UPWARD IRRADIANCE AT SATELLITE LEVEL AND CLOUD COVER

Several forms of the transfer equation exist for calculating the upward flux of infrared radiation at satellite level assuming the amount of cloud cover and cloud emissivities are available. The transfer equation for upward flux at a reference level in the atmosphere as used here is given by:

$$
\begin{aligned}
(1)\quad F\uparrow = & \int_0^u \sigma \bar{T}^4(u)_w \left(\partial \epsilon_F(u)_w / \partial u\right) du \\
& + \int_0^u \sigma \bar{T}^4(u)_c \left(\partial \epsilon_F(u)_c / \partial u\right) du \\
& + \int_0^u \sigma \bar{T}^4(u)_o \left(\partial \epsilon_F(u)_o / \partial u\right) du \\
& + \left(1 - \int_0^u \left(\partial \epsilon_F(u)_w / \partial u\right) du - \int_0^u \left(\partial \epsilon_F(u)_c / \partial u\right) du \right. \\
& \left. - \int_0^u \left(\partial \epsilon_F(u)_o / \partial u\right) du\right) \sigma T_0^4
\end{aligned}
$$

where the symbols used are compiled in the following table (1).

The effective longwave emissivity includes both the cloud scatter effects and the actual cloud emissivity which is equivalent to one minus the slab transmissivity. Kuhn (1963) has shown that one can obtain the longwave emissivity in a simple manner. One assumes that he can measure the equivalent infrared flux which is defined as the average of the upward and downward radiant fluxes, at a plane in the atmosphere parallel to the earth's surface, in this case the cloud top or

TABLE 1

Symbol	Definition
F	Upward longwave radiative flux
u	Optical depth (cm.) of absorbing gas
σ	Stefan-Boltzman constant, 0.817×10^{-10} cal./cm^2 min. deg.^{4}
$\bar{T}$	Mean air temperature (°K) of the atmospheric layer
$(u)_c$	Optical depth of atmospheric carbon dioxide (atmospheric centimeters)
$(u)_w$	Optical depth of atmospheric water vapor (precipitable centimeters)
$(u)_o$	Optical depth of atmospheric ozone (atmospheric centimeters)
T_0	Earth's surface temperature (°K)
ϵ^*	Effective emissivity
F_{E2}	The equivalent radiation at the cloud top which has two contributing radiation currents F_2 and F_2
$F_2\downarrow$	Downward longwave radiative flux at level 2
$F_2\uparrow$	Upward longwave radiative flux at level 2
$F_1\uparrow$	Upward longwave radiative flux at level 1
$F_1\downarrow$	Downward longwave radiative flux at level 1
F_{c2}	Longwave radiative flux from the cloud, level 2
C	Percentage cloud cover
F_{up}	Upward longwave radiative flux from the earth's surface

base. If one then considers the thermal energy budget at the base and top of the cloud, one can show that the observed fluxes reduce algebraically to the effective emissivity of the cloud (Fig. 1).

Calculations of the upward flux of infrared radiation at satellite level may take cloud cover into account in two ways. First, as was done by Kuhn (1966), a table may be constructed to show the effective emissivity as a function of a given combination of cloud types and a percentage cloud cover. However, such a table must be based on a large amount of data, and at present only limited data is available. Secondly, one can take cloud cover into account by using the following approach. The actual satellite reading of the upward flux is a function of the upward irradiance from the ground and the equivalent radiation at the top of the cloud. It can be shown that the equivalent radiation at the top of the cloud is given by equation (2) (see Kuhn 1963A):

$$(2)\quad F_{E2} = F_2 + F_2 = (1 - e^*) F_1 + {}^*F_{c2} + F_2$$

and the actual satellite reading is given by equation (3):

$$(3)\quad \text{SATELLITE READING} = (1 - C) F_{up} + C \times F_2$$

The symbols used are defined in table (1), and the relationships are shown schematically in figure (1).

This second method, which was used in this study, allows one to use a constant effective emissivity, but it requires an accurate estimation of the percentage cloud cover. Yamamoto, Tanaka, and Kamitana

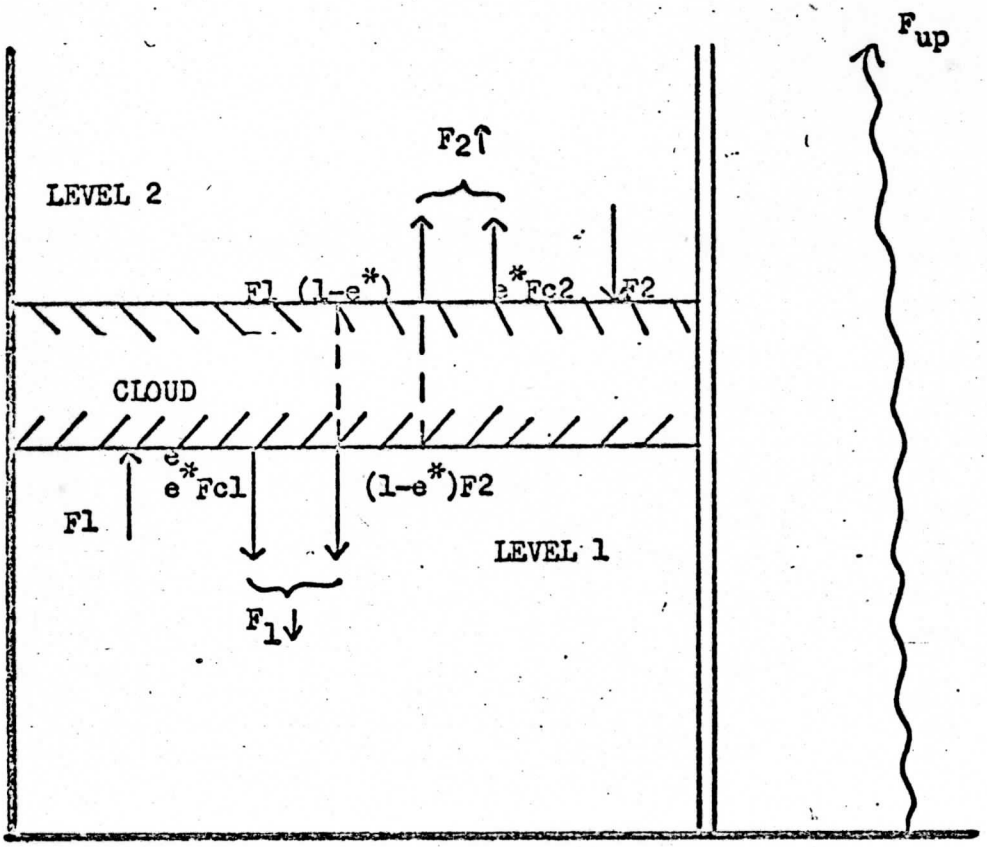

(Fig. 1) CLOUD LAYER AND GROUND FLUXES

(1966) have shown that the emissivity of clouds in the spectral interval from 8 to 12 microns exponentially approaches 1.0 as the number of droplets in a column approaches 10^7 per square centimeter. We assume that a similar relationship holds for the broad band region. This limits the study to those clouds in which the number of cloud droplets in a column of 1 sq. cm. through the vertical thickness of the cloud is 5×10^6 or greater. This limitation then results in a value for the effective emissivity within the range from 0.9 to 1.0. The effect of varying the effective emissivity for a given satellite reading is shown in figure (2). Using the values 0.9 and 1.0 would yield a change in cloud height of about 25 mb., which is within the accuracy of the calculated cloud height. A value of 0.96 for the effective emissivity was used for convenience. Clouds with droplet concentrations less than 5×10^6 per sq. cm. are here considered to be "thin" and thus having effective emissivities less than 0.9. Clouds with bases above 300 mb. are thin because there is not enough water vapor at this height to reasonably expect the limiting concentration. Thin clouds should have effective emissivities a good deal lower than 1.00 even for overcast conditions. For example, Kuhn (1966) estimates a value of 0.65 for an overcast of cirrus clouds. Therefore, calculations are considered of marginal value for cloud bases above 300 mb.

CLOUD HEIGHT AS A FUNCTION

OF EFFECTIVE EMISSIVITY

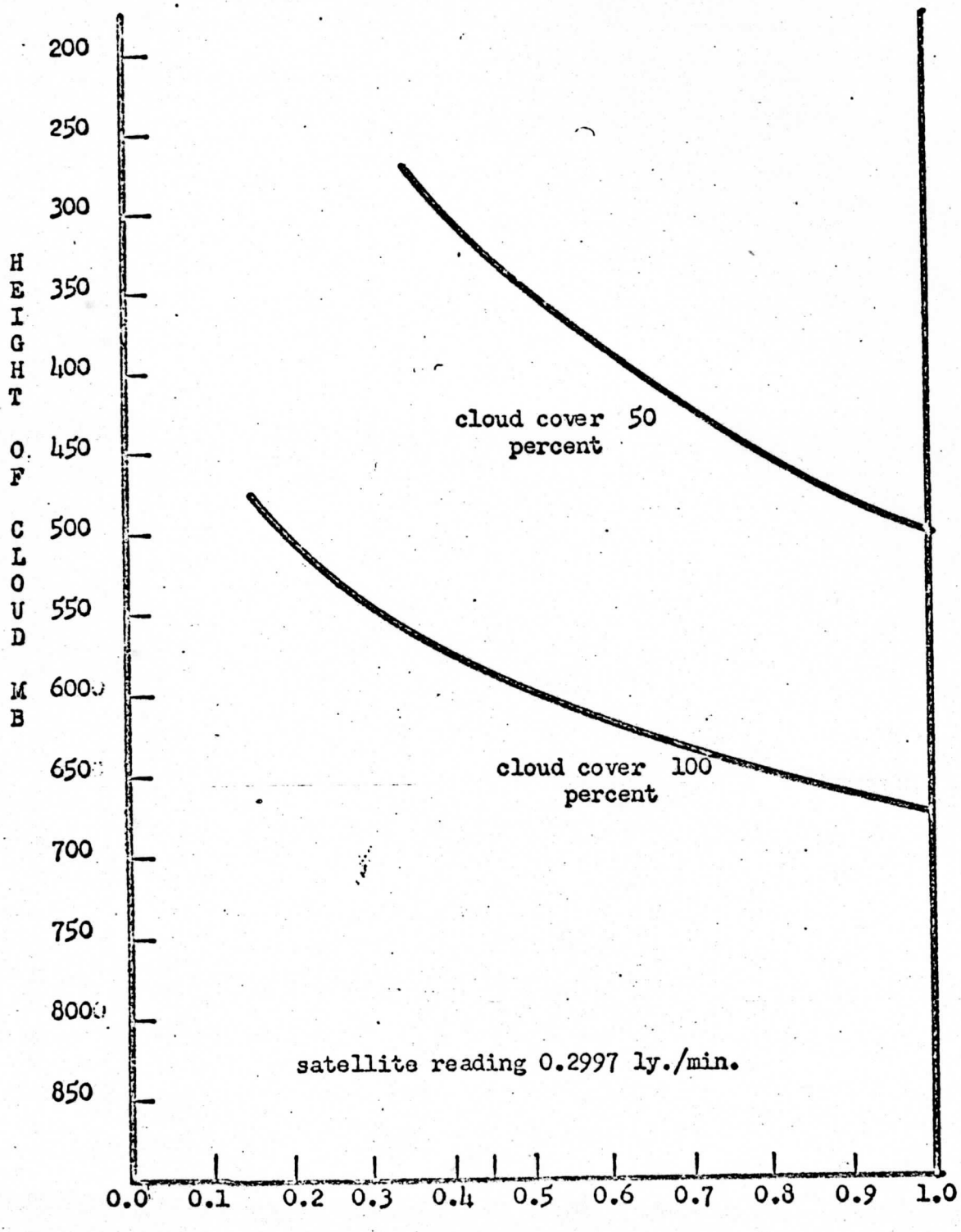

(Fig. 2)

CLOUD TOP HEIGHT CHARTS

Initial calculations to determine the effects of varying the percentage cloud cover and the effective emissivity were based on temperature and pressure data taken from the U. S. Standard Atmosphere (1962, and the moisture data (in this case, saturation mixing ratio was used for the entire ascent) was obtained from the Smithsonian Meteorological Tables (1958). For a more up-to-date approach, the graphs for Atmospheres A through G were based on climatological soundings of temperature and pressure from the "Air Force Interim Supplemental Atmospheres to 90 Kilometers" (1963), and the mixing ratio from moisture data by London (1957). The pressure, temperature, and moisture data above 200 mb. were taken from Mastenbrook (1965), for all eight soundings.

The climatological soundings used were:

Atmosphere	
A	15°N yearly mean sounding
B	30°N January
C	30°N July
D	45°N July
E	45°N January
F	60°N July
G	60° N January

(see appendix)

The cloud top height charts were constructed by utilizing the transfer equation for calculating the upward flux for the seven mean atmospheric ascents. First, the upward flux at satellite level was calculated for the "no cloud" condition, using the surface temperature as determined by the surface radiosonde measurement. Second, a 50 mb. thick partially black cloud was inserted along the sounding and the upward flux recalculated as the gray cloud was raised in 25 mb. increments from a cloud top at 925 mb. to a top at 150 mb. With this data, it was then possible to construct cloud top height charts for the seven climatological radiosonde ascents. Indeed, using this technique allows one to construct a similar chart for any sounding.

One can see from these calculations that the range of values for the satellite measurement of the upward irradiance is from 0.2000 ly./min. to 0.3800 ly./min. for overcast sky conditions.

It is apparent that any given cloud top can result in a number of pairs of satellite readings and cloud covers. For example, a cloud top at 500 mb. during January at 30°N could be the result of a satellite reading of 0.3500 ly./min. with a 12 percent cloud cover, a satellite reading of 0.3300 ly./min. and a 38 percent cloud cover, or a satellite reading of 0.3000 ly./min. with an 82 percent cloud cover (fig. 3).

An apparent problem arises when an inversion is present in the sounding used for the calculations. This may be explained by considering the inversion in the lower layers of the 60°N (January) atmosphere.

The cloud top height as determined in this study was based on the

ly./min. and a 38 percent cloud cover, or a satellite reading of 0.3000 ly./min. with an 82 percent cloud cover (fig. 3).

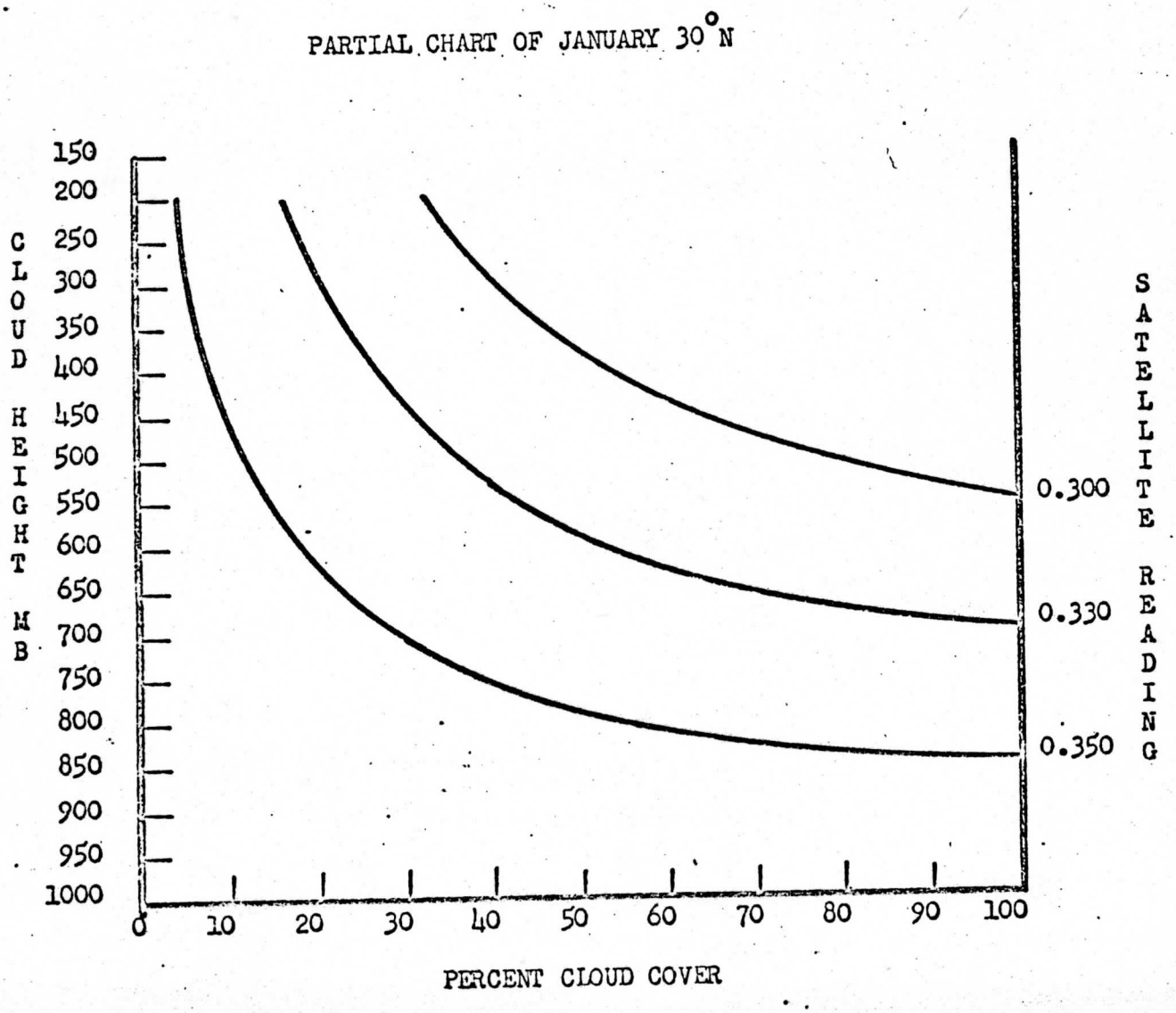

(Fig. 3)

attenuation and re-radiation at a lower temperature of the upward streaming flux when a cloud was placed at various heights in the troposphere. In this case, the highest temperature is in the layer between 950 mb. and 850 mb. rather than at the surface; therefore, the maximum upward flux at satellite level is not observed from the clear condition but rather from the particular instance when the cloud top is at the inversion boundaries. For example, a satellite reading of 0.2750 ly./min. would yield a cloud top either between 925 mb. and 900 mb. or between 875 mb. and 850 mb. for 100 percent cloud cover (table 2).

TABLE (2)

PRESSURE	TEMPERATURE	UPWARD FLUX AT 5.0 MB.
1000	-16.0	0.2719
975	-15.0	
950	-15.0	
925	-14.5	0.2747
900	-14.0	0.2756
875	-14.0	0.2756
850	-15.0	0.2737
825	-16.0	0.2716
800	-17.0	0.2696
775	-18.0	0.2675
750	-18.5	0.2664

The calculated values of the upward flux are given to 4 decimals as obtained on the computer program. The accuracy of satellite measurements obviously is considerably lower; values to two decimals are about all one can assume.

As previously mentioned, this problem is only an apparent one because once the presence of an inversion is known, one can place the cloud top at the top of the inversion. One may assume that cloud top heights derived from climatological ascents will be less erroneous in areas in which the variance of the daily ascents would be the least. Such an area would be the tropical oceanic regions where data coverage is sparse. The height of the trade wind inversion is quite well known; therefore, this technique should be useful in this area.

APPLICATION OF RESULTS

In order to test this method on a specific case, one must have satellite measurements of the broad band infrared radiation over an area where there are reliable radiosonde stations. March 4th, 1962 was selected because TIROS IV passed over San Antonio, Texas, Shreveport, La., Green Bay, Wis., Saint Cloud, Minn., and International Falls, Minn. at about 0900 G. M. T. The general synoptic features at this time were highs over Utah and the Texas panhandle and a low in northwest Iowa with a cold front extending from the low south through western Illinois, Missouri, Arkansas, and Louisiana. Figure (4) shows the upward flux in ly./min. as measured by TIROS IV, the satellite track, and the general synoptic situation on March 4th, 1962. The radiosonde ascents for all five stations were taken from the "Northern Hemisphere Data Tabulations" at 1200 G. M. T.

On March 4th, 1962 the satellite sensors over International Falls observed an outward flux of between 0.21 and 0.22 ly./min., at this time the sky cover was 100 percent. The calculated outward flux from equation (1), not considering clouds, is 0.2890 ly./min., employing the International Falls 1200 G. M. T. radiosonde ascent for this date. Recalculating the upward flux as described on page 12 produces a calculated flux of 0.2176 ly./min. when the cloud top is at 425 mb., and a calculated value of 0.2103 ly./min. when the cloud top is at 400 mb.

Therefore it may be concluded that the cloud tops over International Falls are between 21,000 and 23,000 ft. When comparing this result with the climatological cloud top height charts, one must realize that the air mass over a mid-continental station during early spring will usually be somewhat colder than the climatological ascent which was averaged around the entire latitude circle. And, it is evident that the radiosonde ascent for International Falls lies between the soundings for January 45°N and January 60°N. Therefore, the cloud top height, according to the climatological charts and by interpolation, is about 22,000 feet. This seems to be too high. However, the position of the storm center to the south-southwest of this station would very likely yield a high cirrus shield over Minnesota. The cirrus shield would further attenuate the upward flux, thus yielding a satellite reading that is too low, and a corresponding calculated cloud height somewhat higher than would be obtained from the low and middle clouds by themselves.

Using this same process for determining the cloud top height over Saint Cloud resulted in a calculated upward flux without clouds of 0.2876 ly./min. The cloud top height as calculated from the 1200 G.M.T. radiosonde ascent is between 19,000 and 21,000 ft. Interpolating between January 60°N and January 45°N places the cloud top at approximately 20,000 ft. The calculated value obtained, assuming clear skies, for the Green Bay ascent was 0.2909 ly./min., while the satellite sensors recorded a reading of about 0.24 ly./min. The corresponding

heights derived from the actual and climatological ascents are 19,000 and 19,000 to 20,000 ft. respectively. Again the actual sounding is somewhat colder than the climatological sounding, making interpolation necessary between the charts.

Moving southward, a satellite reading of between 0.27 and 0.28 ly./min. is noted for Shreveport. Figure (4) shows a frontal system approaching this station and an overcast sky. Calculations from the 1200 G. M. T. ascent provide an F_{up} value of 0.3589 ly./min., while a cloud top at 16,000 to 18,000 ft. would be necessary to attenuate the upward irradiance sufficiently to yield the observed readings. The radiosonde ascent for Shreveport is cooler than the climatological ascent for January 30°N but warmer than the ascent for January 45°N; therefore a height of 16,000 to 18,000 ft. can be deduced from the climatological charts.

Finally, San Antonio is in a high pressure area and has clear skies (fig. 4). The calculated upward flux for this station based on the 1200 G. M. TT. ascent is 0.3741 ly./min. for clear skies, while the calculated upward flux for the 30°N January climatological sounding with no clouds is 0.3935 ly./min. Two explanations for this small difference seem plausible. Either the high pressure cell at the surface with convergence aloft may induce cirrus which are not visible from the ground, or the difference in the distribution of water vapor between the actual sounding and the climatological sounding may be sufficient to account for the difference. One can see from the ascent for March 4th,

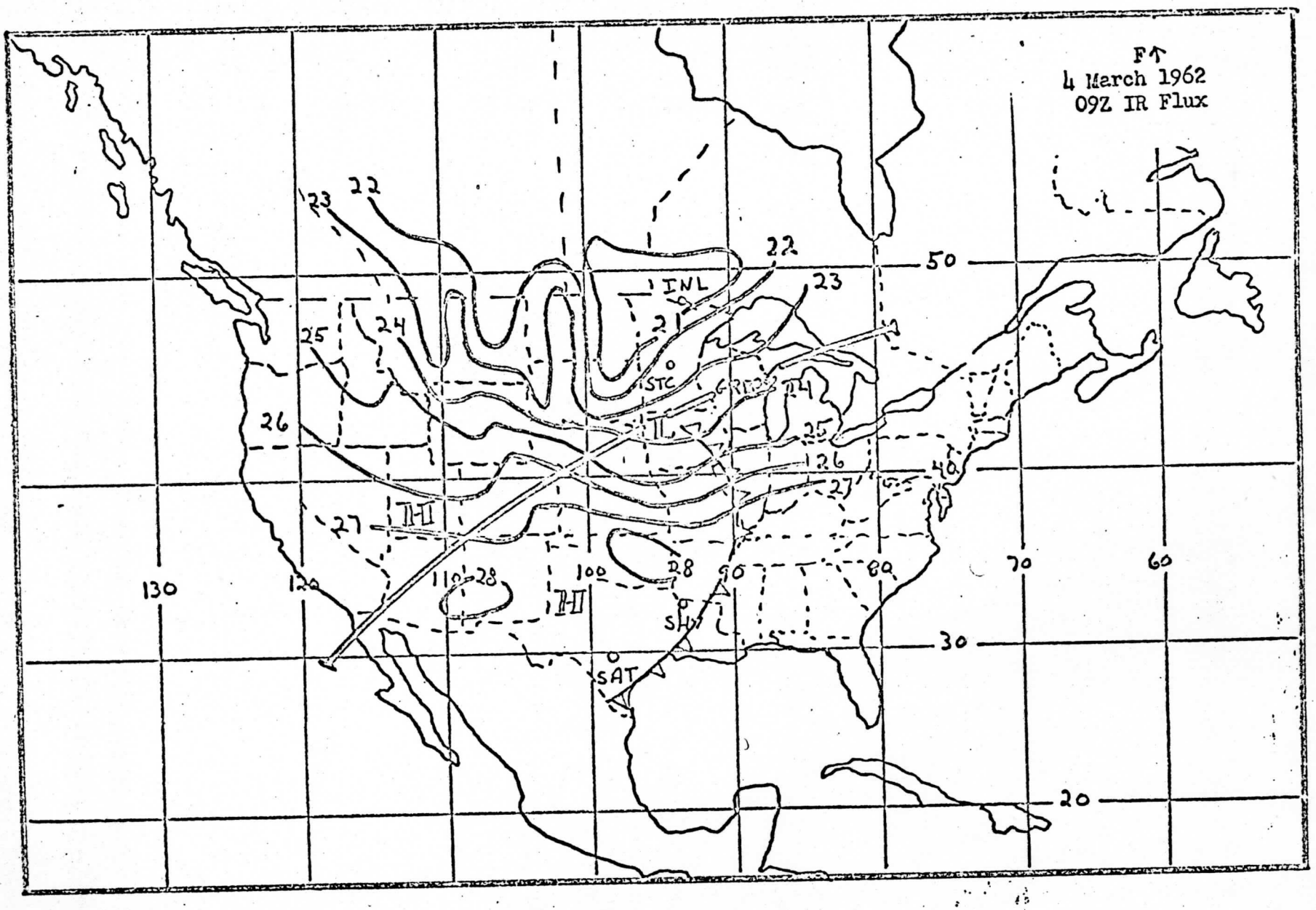
F↑
4 March 1962
09Z IR Flux
INL
STC
GRR
SHV
SAT
H
L
22
23
24
25
26
27
28
50
40
30
20
130
120
110
100
90
80
70
60

1962 for San Antonio that the layer between 1000 mb. and 900 mb. is very moist. The moisture then decreases rapidly to 700 mb, and again increases to 500 mb. At this level the mixing ratio is greater than the value for the climatological ascent. The moist layer at 500 mb. may act as a thin cloud with an effective emissivity much lower than 1.0 .

CONCLUSION

It is realistic to adjust a calculated upward flux to equal an observed upward flux by placing a "black" or "partially black" cloud at various heights which act to attenuate and re-radiate at a lower temperature.

Cloud top height charts may be constructed using a measured percentage of cloud cover and computer calculated upward irradiance values based on radiosonde ascents. These charts then provide a unique cloud height for any given combination of cloud cover and a given satellite measurement of the broad band infrared flux. There is one exception, however; if an inversion is present, a double solution will occur. A cloud top located directly above or below the inversion will yield the same calculated value of upward flux. The inversion is obvious from the sounding, and should not cause too much confusion.

This study suggests that it is possible to use such cloud top height charts when constructed from climatological data for various latitudes and times of the year in lieu of calculating a chart for each radiosonde ascent. The four examples presented in this study show good agreement between the cloud tops as derived from the actual sounding and those obtained from the climatological charts when interpolation between the charts was employed.

Although this study brought out interesting results about the

possibility of measuring cloud top heights using the broad band computer solution of the radiative transfer equation, it was not possible to verify any of the calculated cloud heights. Nevertheless, the heights obtained for the five stations in this particular case appeared to be reasonable considering the time of year and the synoptic situation.

The accuracy of this method will improve when better correction factors for the calculated upward flux can be derived. For example, work is now being done at the University of Wisconsin on a correction factor for aerosol absorption which is often quite important but was not taken into account in this study (Weinman, 1966). Simultaneous readings of broad band infrared radiation and television pictures covering the same area would obviously increase the accuracy of this technique.

If the accuracy of this technique can be established, then this method should be useful as a "backup" system and as a calibration device for the more conventional window estimations of cloud top heights.

ATMOSPHERE A

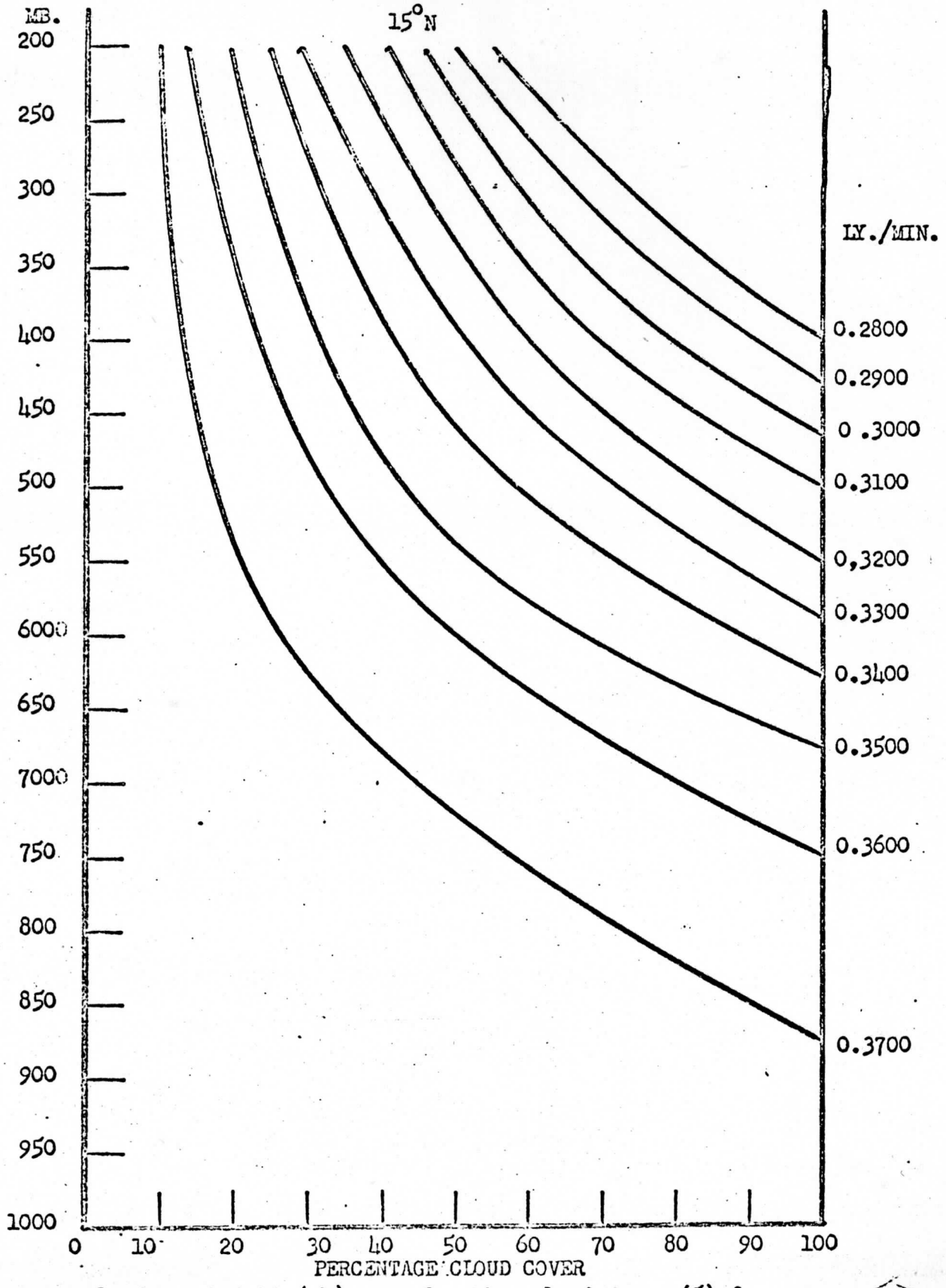

Cloud top height (mb) as a function cloud cover (%) for a given satellite IR radiation measurement. Valid for 15°N all seasons.

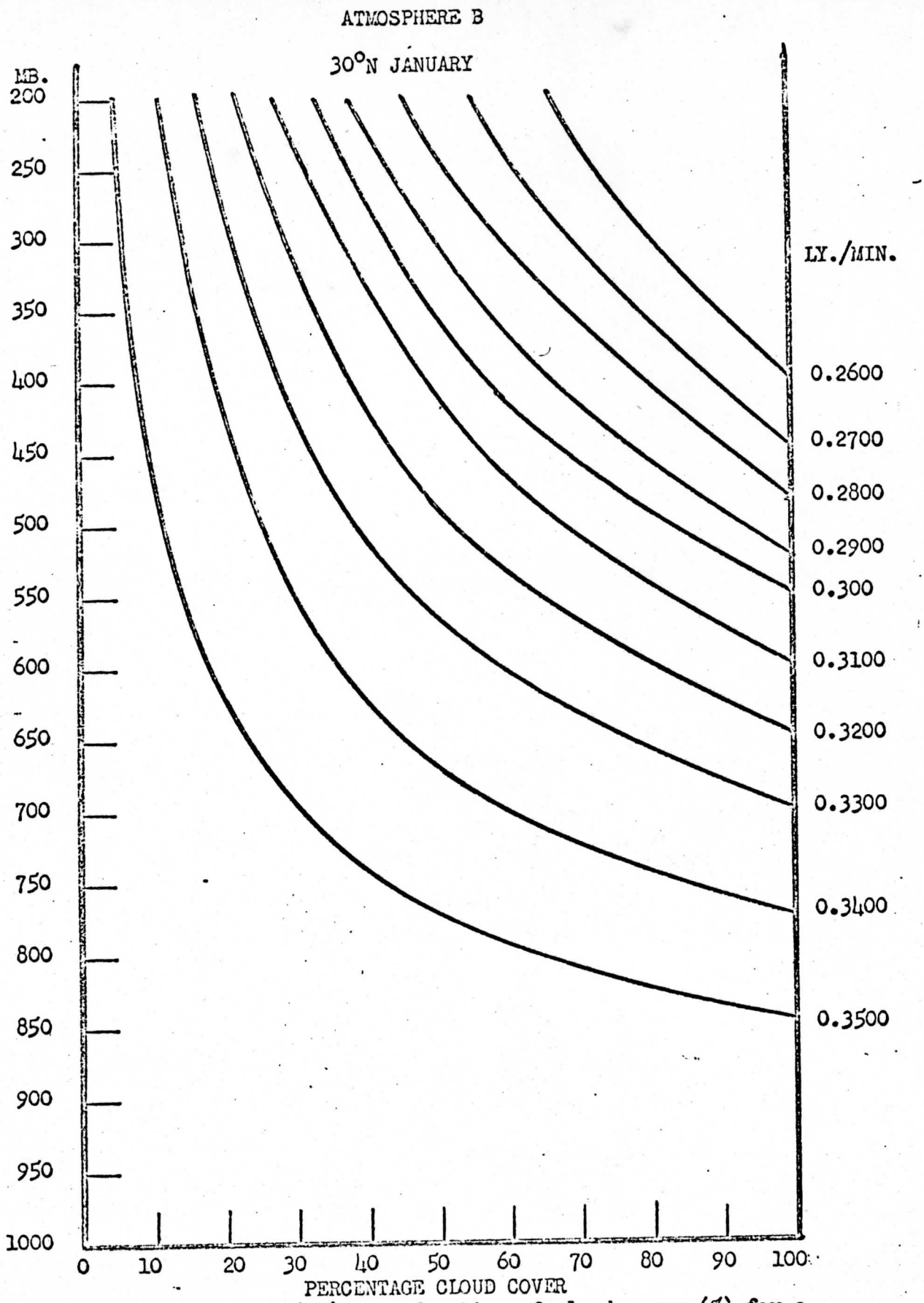

Cloud top height (mb) as a function of cloud cover (%) for a given satellite IR radiation measurement. Valid for 30°N winter

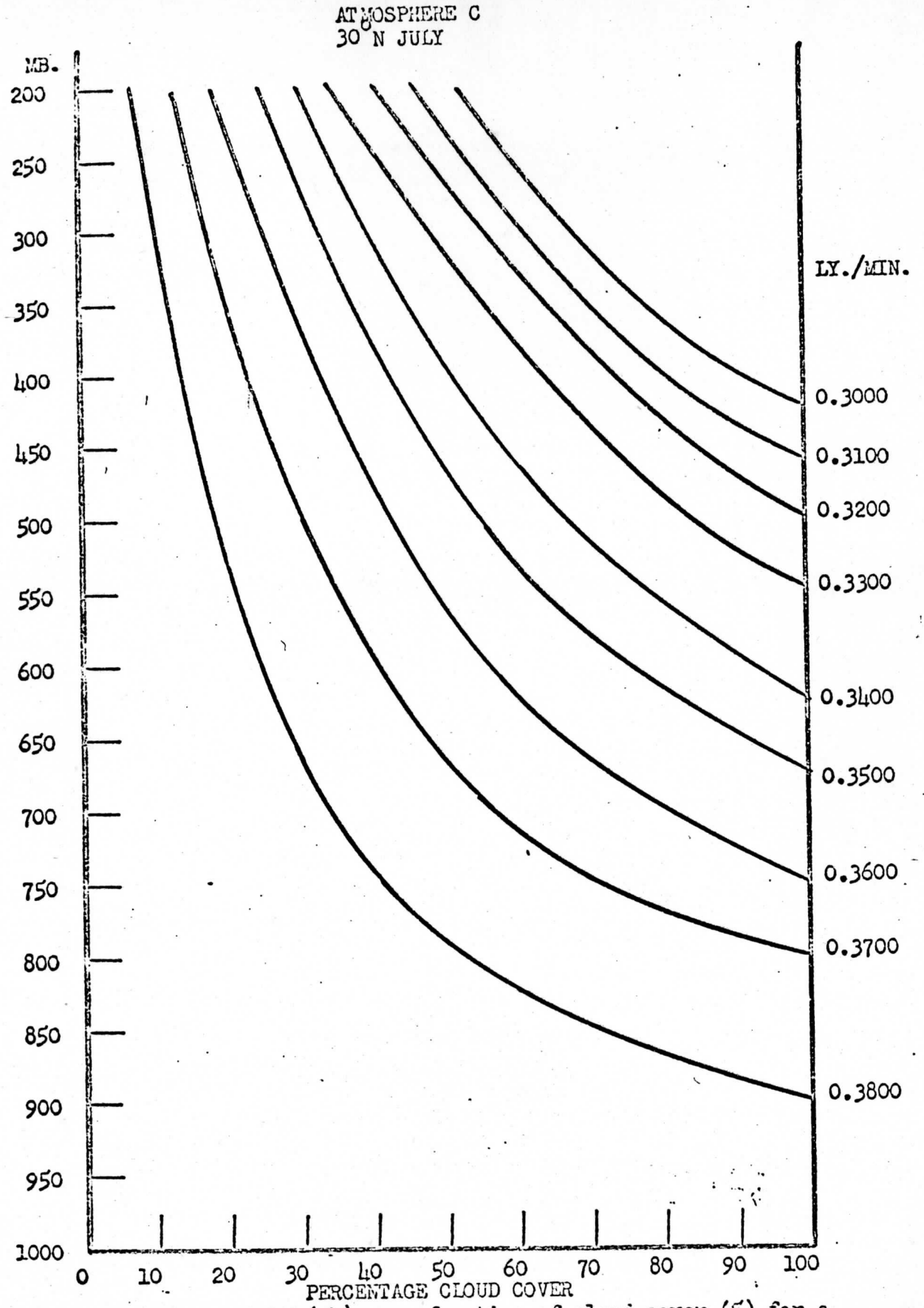

Cloud top height (mb) as a function of cloud cover (%) for a given satellite IR radiation measurement. Valid for 30°N Summer

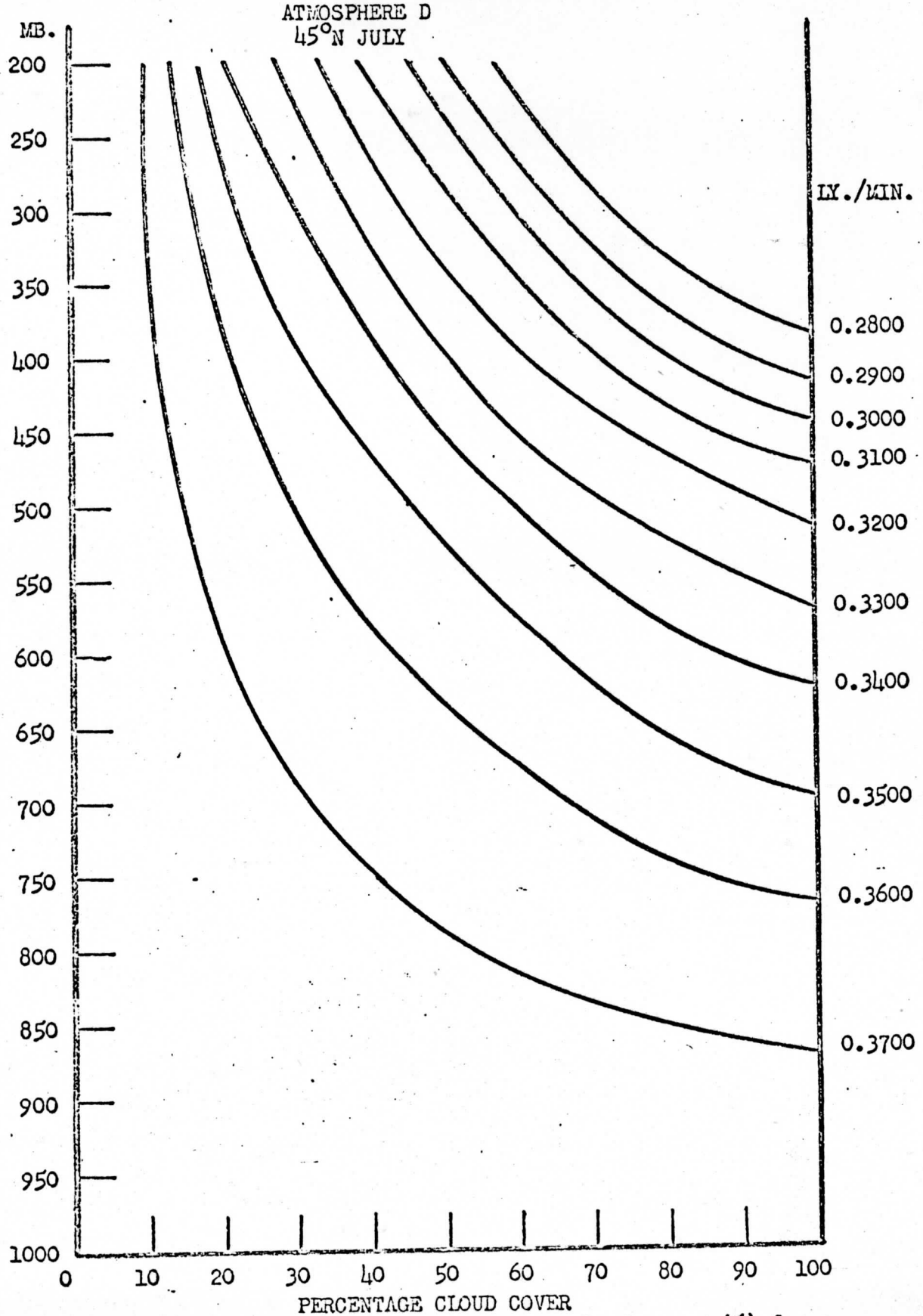

Cloud top height (mb) as a function of cloud cover (%) for a given satellite IR radiation measurement. Valid for 45°N Summer

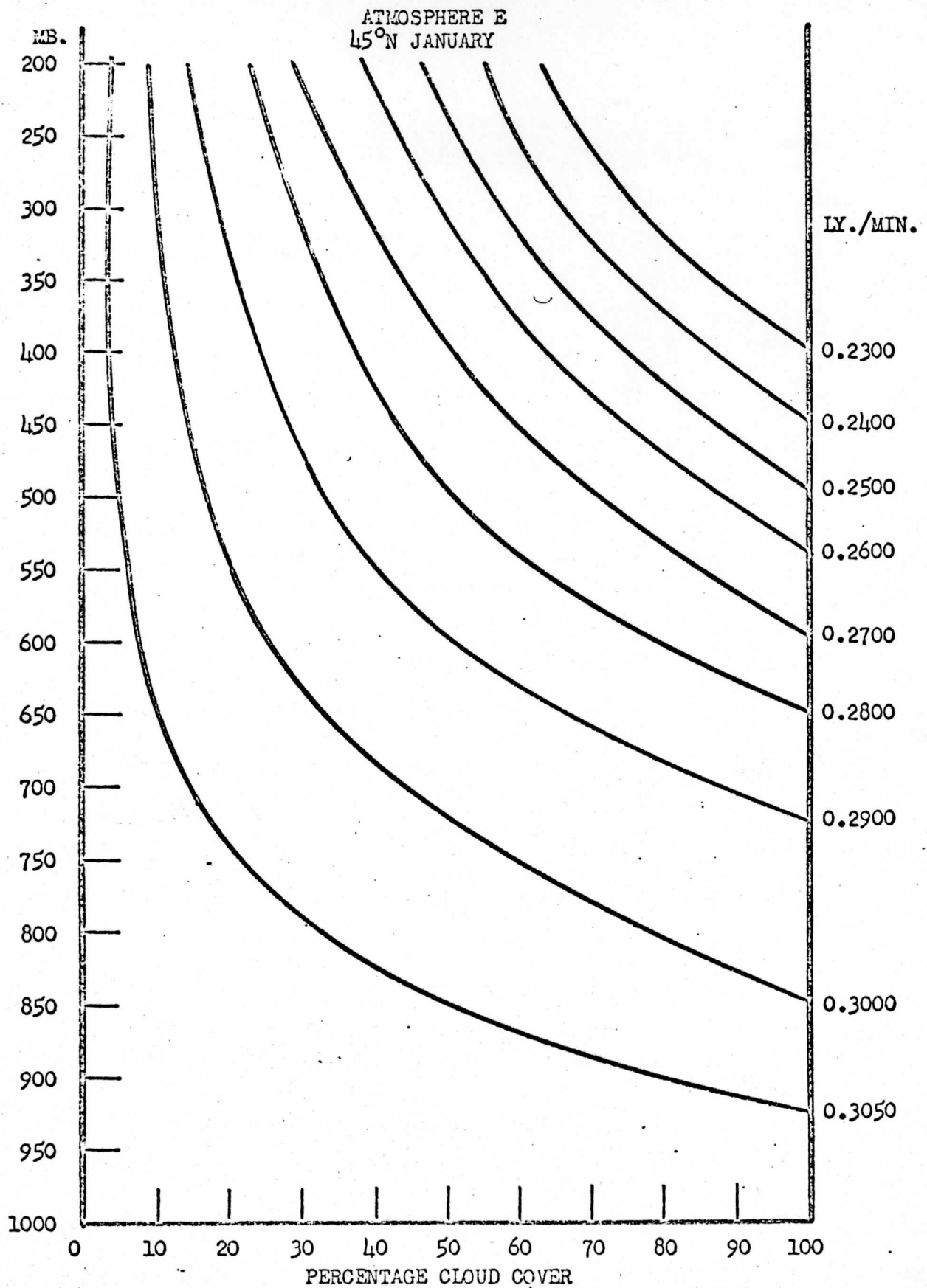

Cloud top height (mb) as a function of cloud cover (%) for a given satellite IR radiation measurement. Valid for 45°N Winter

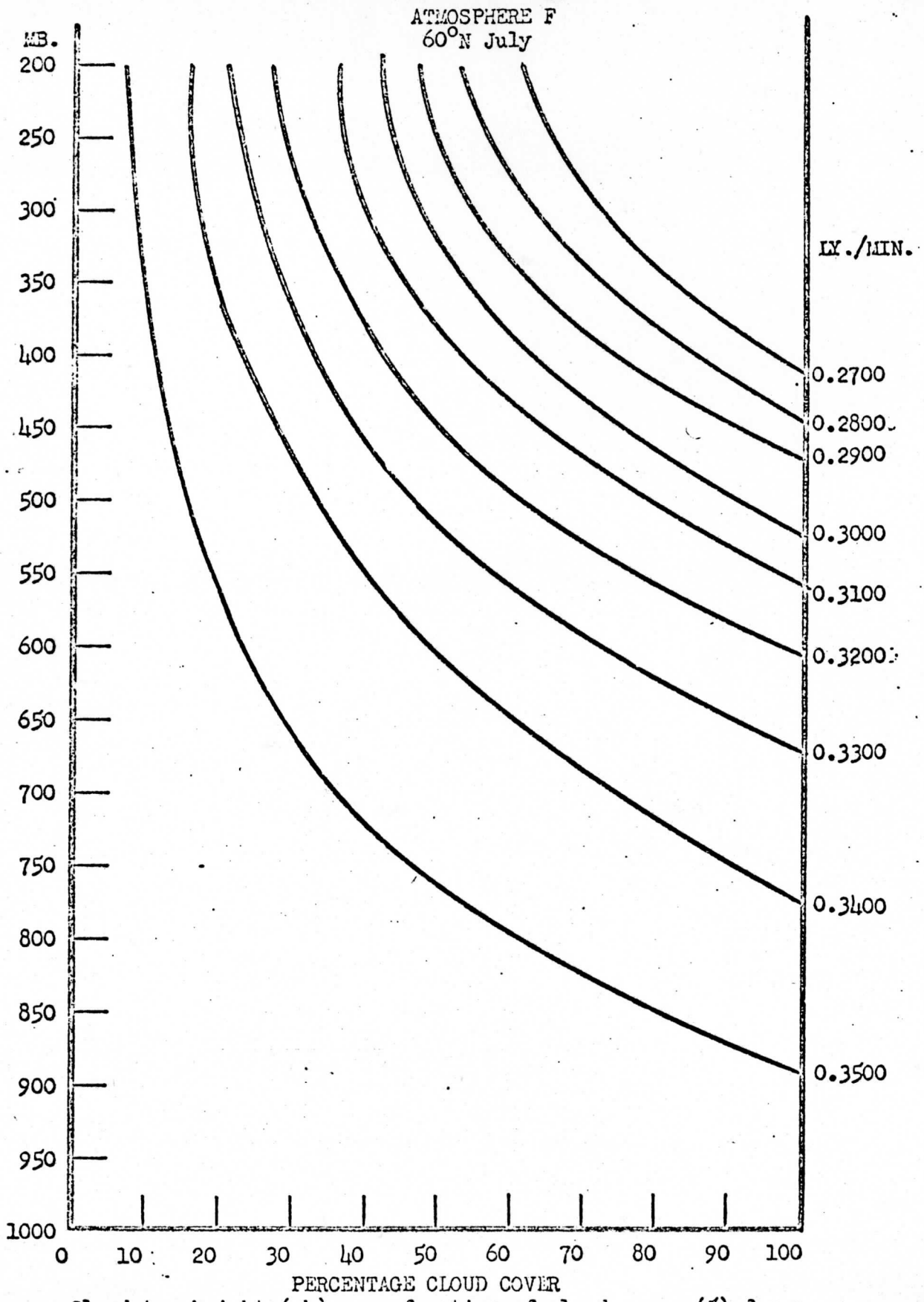

Cloud top height (mb) as a function of cloud cover (%) for a given satellite IR radiation measurement. Valid for 60°N Summer

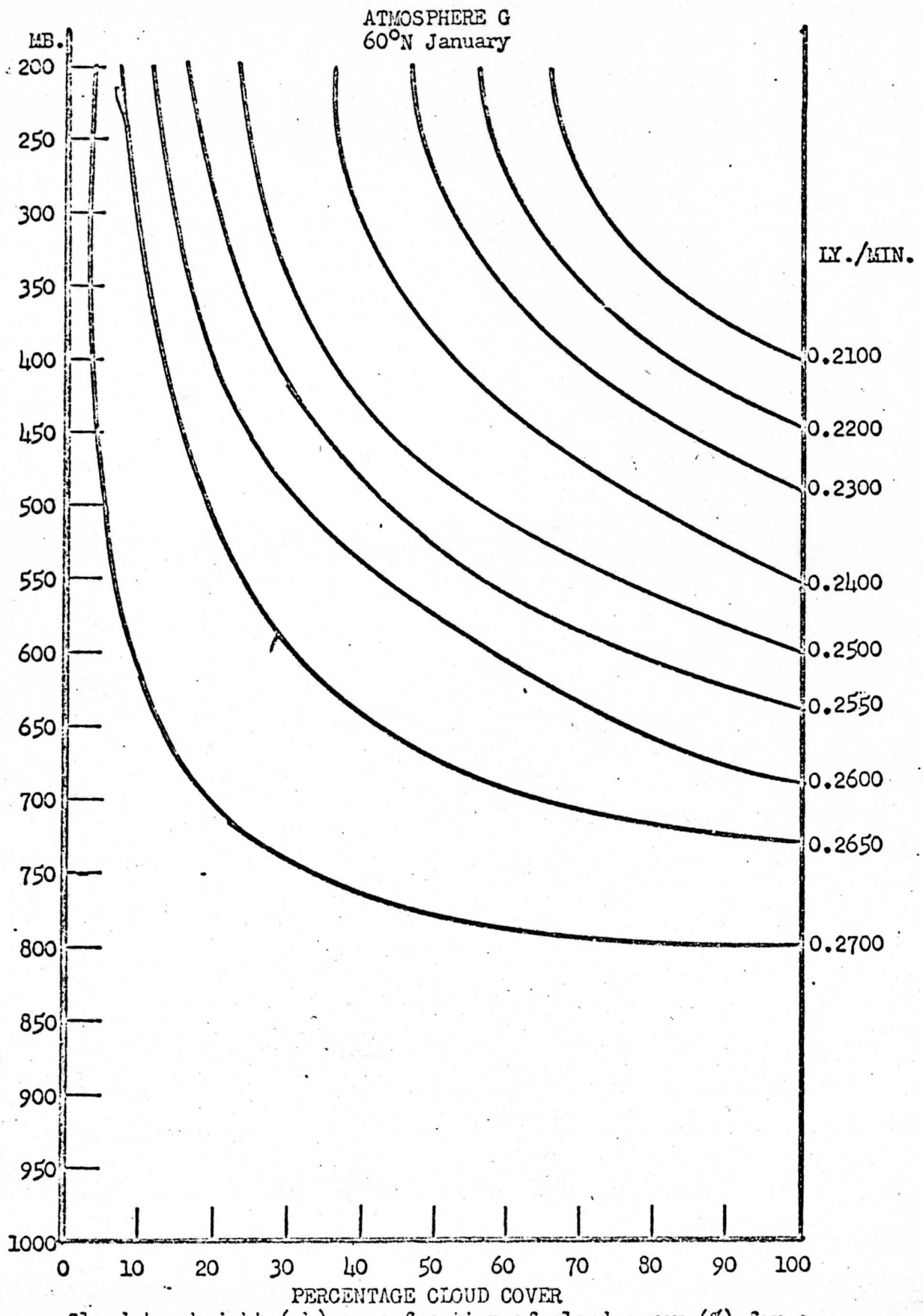

Cloud top height (mb) as a function of cloud cover (%) for a given satellite IR radiation measurement. Valid for 60°N Winter

APPENDIX

Summary of the upward fluxes at 5.0 mb. (assumed satellite level) in langleys per minute.

The upward flux values in the following tables are calculated values for the 5.0 mb. reference level as a 50 mb. thick gray cloud is lifted through the atmosphere from a cloud top at 925 mb. to a top at 150 mb. in 25 mb. increments. The pressure is given in millibars, the temperature in degrees Celsius, and the mixing ratio in grams per kilogram.

A brief summary of a comparison between the observed upward flux and the computed upward flux is presented following the data tables.

STANDARD ATMOSPHERE

PRESS	TEMP	MIX	SATELLITE READING AT 5.0 MB.
1000	14.3	10.14	.3394
975	12.7	9.75	
950	11.2	8.75	
925	10.1	8.40	.3327
900	8.5	7.75	.3301
875	7.2	7.22	.3278
850	5.6	6.60	.3251
825	3.9	6.20	.3220
800	2.3	5.55	.3191
775	0.7	5.32	.3161
750	- 0.9	4.76	.3131
725	- 2.9	4.25	.3093
700	- 4.5	3.85	.3061
675	- 6.4	3.81	.3023
650	- 8.4	3.25	.2982
625	-10.3	3.17	.2942
600	-12.3	2.54	.2900
575	-14.5	2.27	.2852
550	-16.5	2.01	.2808
525	-18.7	1.23	.2759
500	-21.2	1.44	.2702
475	-23.7	1.22	.2645
450	-26.3	0.971	.2585
425	-28.8	0.823	.2547
400	-31.3	0.656	.2458
375	-34.7	0.534	.2391

STANDARD ATMOSPHERE (CONTINUED)

PRESS	TEMP	MIX	SATELLITE READING AT 5.0 MB.
350	-37.8	0.414	.2319
325	-40.8	0.324	.2250
300	-44.5	0.244	.2165
275	-48.4	0.200	.2077
250	-52.3	0.158	.1989
225	-56.5	0.084	.1895
200	-56.5	0.010	.1895
175	-56.5	0.010	.1894
150	-56.5	0.009	.1894
125	-56.5	0.009	
100	-56.5	0.008	
75	-56.5	0.008	
50	-55.9	0.008	
25	-51.5	0.007	
20	-47.0	0.006	
15	-43.0	0.005	
10	-40.0	0.002	
5	-35.0	0.000	

ATMOSPHERE (A)

15° N

PRESS	TEMP	MIX	SATELLITE READING AT 5.0 MB.
1000	26.5	16.00	.3850
975	24.5	15.00	
950	23.0	14.00	
925	22.0	13.00	.3776
900	20.5	12.00	.3750
875	18.5	11.00	.3714
850	17.0	9.80	.3686
825	15.5	0.00	.3675
800	14.0	7.90	.3628
775	13.5	6.90	.3617
750	13.0	6.20	.3606
725	11.0	5.50	.3563
700	9.0	5.00	.3519
675	7.5	4.50	.3485
650	5.0	3.80	.3427
625	3.0	3.30	.3379
600	1.0	2.90	.3331
575	- 1.5	2.60	.3269
550	- 4.0	2.20	.3207
525	- 6.0	1.90	.3156
500	- 8.5	1.63	.3091
475	-11.5	1.40	.3012
450	-14.0	1.10	.2946
425	-17.0	0.80	.2866
400	-20.0	0.70	.2786

ATMOSPHERE (A) (CONTINUED)

PRESS	TEMP	MIX	SATELLITE READING AT 5.0 MB.
375	-23.0	0.50	.2706
350	-26.0	0.40	.2626
325	-29.0	0.30	.2534
300	-33.0	0.30	.2442
275	-37.0	0.20	.2339
250	-42.0	0.20	.2212
225	-47.5	0.10	.2076
200	-52.5	0.084	.1955
175	-57.5	0.010	.1835
150	-63.0	0.009	.1708
125	-73.0	0.009	
100	-80.0	0.008	
75	-74.0	0.008	
50	-65.0	0.008	
25	-52.0	0.007	
20	-50.0	0.006	
15	-45.0	0.005	
10	-38.0	0.002	
5	-27.0	0.000	

ATMOSPHERE (B)

30°N (JANUARY)

PRESS	TEMP	MIX	SATELLITE READING AT 5.0 MB.
1000	14.0	7.50	.3588
975	13.5	7.00	
950	12.5	6.20	
925	11.5	6.00	.3543
900	11.0	5.50	.3534
875	10.0	5.10	.3514
850	9.5	4.80	.3504
825	8.5	4.50	.3483
800	8.0	4.30	.3472
775	6.0	3.70	.3429
750	4.0	3.40	.3384
725	2.5	2.90	.3350
700	0.5	2.50	.3303
675	- 1.5	2.10	.3255
650	- 3.0	1.80	.3218
625	- 5.0	1.60	.3169
600	- 7.5	1.30	.3106
575	- 9.5	1.20	.3056
550	-12.0	1.00	.2992
525	-14.5	0.90	.2928
500	-17.0	0.80	.2863
475	-19.5	0.70	.2798
450	-22.5	0.50	.2721
425	-24.5	0.45	.2669
400	-27.0	0.40	.2604

ATMOSPHERE (B) (CONTINUED)

PRESS	TEMP	MIX	SATELLITE READING AT 5.0 MB.
375	-30.0	0.35	.2527
350	-33.0	0.30	.2449
325	-37.0	0.20	.2346
300	-41.0	0.15	.2243
275	-45.0	0.10	.2141
250	-49.0	0.009	.2038
225	-53.0	0.009	.1937
200	-57.0	0.009	.1804
175	-59.0	0.009	.1719
150	-61.0	0.008	.1735
125	-64.0	0.008	
100	-67.0	0.008	
75	-70.0	0.008	
50	-65.0	0.008	
25	-54.0	0.007	
20	-52.0	0.006	
15	-48.0	0.005	
10	-43.0	0.002	
5	-33.0	0.000	

ATMOSPHERE (C)

30°N (JULY)

PRESS	TEMP	MIX	SATELLITE READING AT 5.0 MB.
1000	28.0	13.50	.3935
975	26.0	12.50	
950	23.5	11.90	
925	21.5	10.90	.3824
900	20.5	9.10	.3797
875	18.5	8.50	.3796
850	17.5	8.00	.3740
825	16.5	7.30	.3721
800	15.0	6.50	.3700
775	13.0	5.80	.3669
750	11.0	5.20	.3618
725	9.5	4.50	.3585
700	7.5	4.00	.3542
675	5.5	3.60	.3497
650	3.5	3.30	.3452
625	1.5	2.80	.3405
600	0.0	2.60	.3370
575	- 1.5	2.30	.3333
550	- 3.0	2.00	.3296
525	- 5.0	1.80	.3246
500	- 6.5	1.60	.3207
475	- 9.0	1.25	.3142
450	-12.0	1.00	.3063
425	-15.5	0.82	.2983
400	-18.0	0.69	.2903

ATMOSPHERE (C) (CONTINUED)

PRESS	TEMP	MIX	SATELLITE READING AT 5.0 MB.
375	-21.0	0.50	.2822
350	-25.0	0.38	.2716
325	-29.0	0.33	.2612
300	-31.0	0.28	.2559
275	-33.0	0.20	.2506
250	-37.0	0.16	.2399
225	-42.0	0.084	.2269
200	-47.0	0.010	.2140
175	-52.0	0.009	.2011
150	-58.0	0.009	.1862
125	-64.0	0.008	
100	-70.0	0.008	
75	-65.0	0.008	
50	-59.0	0.007	
25	-50.0	0.007	
20	-47.0	0.006	
15	-45.0	0.005	
10	-37.0	0.002	
5	-26.0	0.000	

ATMOSPHERE (D)

45°N (JULY)

PRESS	TEMP	MIX	SATELLITE READING AT 5.0 MB.
1000	20.2	11.0	.3782
975	19.5	10.10	
950	18.5	9.50	
925	17.5	9.00	.3737
900	16.2	8.50	.3714
875	15.1	7.80	.3694
850	14.0	7.30	.3673
825	13.0	6.50	.3653
800	12.0	6.00	.3633
775	10.2	5.50	.3597
750	8.5	5.00	.3561
725	7.2	4.50	.3529
700	5.5	4.00	.3496
675	4.2	3.60	.3467
650	2.5	3.30	.3428
625	1.3	3.00	.3400
600	- 0.5	2.60	.3357
575	- 2.2	2.30	.3315
550	- 4.0	2.00	.3217
525	- 6.5	1.80	.3208
500	- 8.5	1.60	.3157
475	-10.7	1.40	.3099
450	-14.0	1.20	.3013
425	-17.5	0.90	.2921
400	-20.5	0.70	.2842
375	-24.0	0.55	.2750

ATMOSPHERE (D) (CONTINUED)

PRESS	TEMP	MIX	SATELLITE READING AT 5.0 MB.
350	-27.0	0.45	.2672
325	-29.0	0.40	.2608
300	-32.0	0.34	.2530
275	-36.0	0.28	.2439
250	-41.0	0.19	.2311
225	-47.0	0.11	.2161
200	-53.0	0.08	.2016
175	-58.0	0.009	.1897
150	-58.0	0.009	.1895
125	-58.0	0.008	
100	-58.0	0.008	
75	-56.0	0.008	
50	-53.0	0.008	
25	-46.0	0.007	
20	-46.0	0.006	
15	-42.0	0.005	
10	-36.0	0.002	
5	-23.0	0.000	

ATMOSPHERE (E)

45°N (JANUARY)

PRESS	TEMP	MIX	SATELLITE READING AT 5.0 MB.
1000	- 1.5	2.60	.3093
975	- 2.0	2.50	
950	- 3.0	2.43	
925	- 3.5	2.40	.3056
900	- 4.5	2.30	.3037
875	- 5.0	2.10	.3027
850	- 6.0	2.00	.3007
825	- 7.0	1.83	.2986
800	- 7.5	1.70	.2976
775	- 8.5	1.51	.2954
750	- 9.5	1.40	.2932
725	-10.5	1.25	.2909
700	-12.0	1.10	.2875
675	-13.5	1.00	.2840
650	-15.0	0.90	.2805
625	-17.5	0.82	.2746
600	-19.5	0.72	.2699
575	-20.5	0.64	.2574
550	-22.5	0.54	.2625
525	-24.5	0.45	.2577
500	-27.0	0.40	.2516
475	-29.0	0.34	.2468
450	-31.0	0.28	.2419
425	-33.5	0.23	.2359
400	-36.0	0.20	.2299

ATMOSPHERE (E) (CONTINUED)

PRESS	TEMP	MIX	SATELLITE READING AT 5.0 MB.
375	-38.0	0.16	.2239
350	-42.0	0.15	.2157
325	-44.0	0.13	.2111
300	-46.0	0.10	.2064
275	-48.5	0.10	.2006
250	-51.0	0.098	.1938
225	-54.0	0.095	.1882
200	-58.0	0.058	.1791
175	-58.0	0.010	.1792
150	-54.5	0.009	.1877
125	-55.0	0.009	
100	-57.0	0.007	
75	-58.0	0.007	
50	-58.0	0.006	
25	-58.0	0.005	
20	-58.0	0.004	
15	-58.0	0.002	
10	-60.0	0.002	
5	-60.0	0.000	

ATMOSPHERE (F)
60°N (JULY)

PRESS	TEMP	MIX	SATELLITE READING AT 5.0 MB.
1000	13.2	7.20	.3599
975	12.0	6.90	
950	10.0	6.40	
925	9.5	6.00	.3539
900	8.0	5.50	.3512
875	7.0	5.10	.3493
850	5.5	4.70	.3465
825	4.5	4.40	.3446
800	3.5	4.00	.3426
775	2.0	3.70	.3395
750	1.0	3.50	.3374
725	- 0.5	3.20	.3343
700	- 1.5	2.90	.3321
675	- 3.0	2.70	.3287
650	- 4.0	2.40	.3264
625	- 5.5	2.20	.3229
600	- 7.5	1.90	.3182
575	- 9.5	1.70	.3134
550	-12.5	1.40	.3061
525	-14.5	1.20	.3011
500	-17.0	1.00	.2948
475	-19.5	0.85	.2885
450	-22.5	0.70	.2890
425	-25.5	0.55	.2733
400	-28.5	0.41	.2657
375	-32.0	0.31	.2569

ATMOSPHERE (F) (CONTINUED)

PRESS	TEMP	MIX	SATELLITE READING AT 5.0 MB.
350	-35.5	0.24	.2483
325	-39.0	0.19	.2397
300	-42.5	0.15	.2313
275	-46.5	0.11	.2219
250	-48.0	0.11	.2183
225	-48.0	0.11	.2183
200	-48.0	0.084	.2185
175	-48.0	0.010	.2186
150	-48.0	0.009	.2186
125	-48.0	0.009	
100	-48.0	0.008	
75	-48.0	0.008	
50	-48.0	0.008	
25	-44.0	0.007	
20	-43.0	0.006	
15	-39.0	0.005	
10	-36.0	0.002	
5	-23.0	0.000	

ATMOSPHERE (G)

60°N (JANUARY)

PRESS	TEMP	MIX	SATELLITE READING At 5.0 MB.
1000	-16.0	1.00	.2719
975	-15.0	1.00	
950	-15.0	0.99	
925	-14.5	0.98	.2747
900	-14.0	0.96	.2756
875	-14.0	0.95	.2756
850	-15.0	0.90	.2737
825	-16.0	0.85	.2716
800	-17.0	0.81	.2696
775	-18.0	0.75	.2675
750	-18.5	0.72	.2664
725	-19.5	0.70	.2642
700	-21.0	0.69	.2609
675	-22.0	0.65	.2587
650	-23.0	0.60	.2565
625	-24.5	0.54	.2530
600	-25.5	0.49	.2507
575	-27.0	0.42	.2473
550	-29.0	0.38	.2415
525	-31.5	0.33	.2369
500	-33.5	0.29	.2323
475	-36.0	0.22	.2265
450	-38.0	0.19	.2220
425	-40.5	0.16	.2163
400	-43.0	0.12	.2107

ATMOSPHERE (G) (CONTINUED)

PRESS	TEMP	MIX	SATELLITE READING AT 5.0 MB.
375	-45.0	0.10	.2062
350	-48.0	0.098	.1997
325	-51.0	0.096	.1932
300	-56.0	0.094	.1829
275	-56.0	0.092	.1829
250	-56.0	0.088	.1828
225	-56.0	0.086	.1828
200	-56.0	0.084	.1829
175	-56.0	0.010	.1830
150	-56.0	0.009	.1830
125	-56.0	0.009	
100	-56.0	0.008	
75	-57.0	0.008	
50	-59.0	0.008	
25	-62.0	0.007	
20	-61.0	0.006	
15	-60.0	0.005	
10	-57.0	0.002	
5	-48.0	0.000	

THE COMPUTED UPWARD IRRADIANCE

The computed upward flux was determined from the transfer equation using flux emissivities over isothermal atmospheric layers as described by Elasser (1960), Funk (1961), and Kuhn (1962). The carbon dioxide flux emissivities were reduced by 12 percent in the 15 micron carbon dioxide band to eliminate overlap with the rotational water vapor band. The carbon dioxide emissivities as functions of atmospheric centimeters of carbon dioxide were taken from Yamoto and Sasamori (1958). Water vapor flux emissivities as functions of optical depth were taken from Kuhn (1962). The ozone emission was omitted because of its small contribution to upward infrared flux. Water vapor and carbon dioxide emissions were computed separately and summed, assuming no overlap in the spectrum. A complete discussion of the more up-to-date computer program used in similar computations is given by Kuhn and Suomi (1966).

Kuhn (1966B) examined the differences between the observed and the calculated infrared upward flux and listed six major reasons for a difference between the values of the calculated and observed flux:

1. "Radiometersonde instrumental errors.
2. Errors in observed (radiosonde) air temperature.
3. Incorrect 'surface' radiative equilibrium temperature for calculations.

4. Incorrect estimation of water vapor above hygrister cutoff.
5. Presence of dust in the upper troposphere and/or lower stratosphere not considered in radiation calculations.
6. Over pressure correction to the optical depth."

Ten ascents of typical sounding conditions in the troposphere and lower stratosphere were examined, and the standard deviation is calculated to be 0.003 ly./min.

When comparing the calculated upward flux with the measured (by radiometer) it was found that a slightly nonlinear pressure correction to the optical depth for calculated infrared flux improved the agreement to a considerable extent.

The residual flux between the computed and observed radiation from 200 through 50 mb. implies the presence of aerosol layers. Ozone at these elevations should not be expected to attenuate the infrared flux by more than 0.0035 ly./min. The more recent computer programs (see Kuhn and Suomi, 1966) include terms for the transmission and emission of ozone and aerosols.

BIBLIOGRAPHY

Bandeen, W. R., R. A. Hanel, J. Licht, R. A. Stampfl, and W. G. Stroud, 1961: Infrared and reflected solar radiation measurements from the TIROS II meteorological satellite. J. Geophys. Research, 65, 3169-3185.

Fritz, S., and J. S. Winston, 1962: Synoptic use of radiation measurements from satellite TIROS II. Monthly Weather Review, 90, 1-9.

Hanel, R. A., and W. G. Stroud, 1961: The TIROS II radiation experiment. Tellus, 13, 486-488.

Kuhn, P. M., 1963A: Measured effective long-wave emissivity of clouds. Monthly Weather Review, October, 1963.

Kuhn, P. M., 1963B: Soundings of observed and computed infrared flux. J. Geophys. Research, vol. 68, no. 5, March, 1963.

Kuhn, P. M., and V. E. Suomi, 1966: Broad band computer solution of the radiative transfer approximation. Unpublished paper.

List, R. J., Smithsonian Meteorological Tables, City of Washington (1958).

London, J., 1957: A study of the atmospheric heat balance. Final Report, Contract Number AF 19(122)-165. Research Division, Department of Meteorology and Oceanography, College of Engineering, New York University.

Mastenbrook, H. J., 1965: Personal communication with author via P. M. Kuhn.

Wark, D. Q., G. Yamamoto, and J. H. Lienesch, 1962: Methods of estimating infrared flux and surface temperature from meteorological satellites. Journal of the Atmospheric Sciences, vol. 19, no. 5, Sept., 1962.

Weinman, J., 1966: Personal communication with author.

Yamamoto, G., M. Tanaka, and K. Kamitani, 1966: Radiative transfer in water clouds in the 10 micron window region. Journal of the Atmospheric Sciences, vol. 23, no. 3, May, 1966.

U. S. Air Force, Air Force Interim Supplemental Atmospheres to 90 Kilometers, Air Force Surveys in Geophysics, No. 153 (1963).

U. S. Standard Atmosphere, U. S. Government Printing Office, Washington 25, D. C. (1962).

DETERMINATION OF CLOUD BOUNDARIES USING SATELLITE DIGITAL INFRARED DATA

by

RUSSELL ALBERT HANKINS

ABSTRACT

A computerized technique for determining cloud boundaries utilizing satellite digital infrared data is presented. Gradients of black-body temperature are computed for portions of the infrared scan. Significant cloud boundaries are computed when the temperature gradient reaches a certain limit. Results using one set of criteria for determining cloud boundaries are shown and discussed. After the cloud boundaries were determined the variance of the cloud top temperatures between the boundaries were computed and examined to ascertain whether cloud tops of like variance and temperature belonged to the same cloud genera.

I. INTRODUCTION

By using a satellite-borne scanning infrared radiometer sensitive to the 8 to 12 micron "window" region, a fairly good estimation of the cloud top heights can be obtained. In such determinations many assumptions must be made. Most authors assume that the cloud tops, especially the tops of thick clouds, radiate approximately as a black-body, and that layers of cloud are opaque to infrared radiation. Other assumptions are that the atmospheric absorption is negligible above the level of the cloud tops and that reflected solar radiation does not contribute significantly to the response received. After using the above assumptions, Glahn (1966) states, "then if the vertical temperature structure of the atmosphere is a monotonically decreasing function of height from the surface of the earth to the maximum possible cloud height and is known for a particular geographical location, the cloud height can be inferred directly from the measured return from that location." These assumptions, as most authors are well aware, are not wholly true.

All clouds do not radiate as black-bodies. An ideal thick cloud would absorb all incident radiation from below and re-radiate at the cloud temperature. Since most clouds are far from ideal, the radiation received by the satellite will be an integrated value of the radiation received from the cloud and the surface. For a very thin cirrus with no

lower clouds the total upward radiation is mainly determined by the surface temperature.

Atmospheric absorption above the radiating surface may be large, especially for low clouds and clear conditions. Comparisons made by Fritz and Winston (1962), Nordberg et al. (1962), and others, show that in practically all cases the effective temperature in the atmospheric "window" region is lower than the surface temperature. Nordberg et al. (1962) have shown that the equivalent black-body temperature indicated by TIROS III, Channel 2, can be as much as 20.0 C lower than the observed sea surface temperature. Rasool (1964) has shown that the difference between the indicated equivalent black-body temperature and the surface temperature can be as large as 11.5 C or as low as 3.5 C for a hot, humid and a cold, dry atmosphere respectively.

Another problem is that the temperature profile may not be known and may contain isothermal regions or inversions which can cause ambiguities in cloud height determinations. With a stable lapse rate, a small error in temperature would result in substantial errors in the estimated height.

Also the spatial resolution of the radiometer may not be high enough. It is desirable that the scan-spot size be at least as small as the horizontal dimensions of the cloud system to be detected, otherwise the clouds occuply only a fraction of the scan-spot, and the radiometer

measures the integrated energy radiated from both clouds and their background.

Other errors which might introduce systematic differences in cloud height estimates are instrumental calibration and timing errors. These will not be discussed in this paper.

The main purpose of this paper is to present a technique for determining cloud boundaries from satellite infrared data. Relative and not absolute radiation values will be employed, so the previously mentioned assumptions will be made despite their shortcomings.

When using infrared radiation data to study cloud characteristics, one first has to distinguish between areas of cloud and no cloud. Once the boundary between these two areas is defined and located there still may exist two or more completely different cloud types within one cloud area such as a large cumulo-nimbus surrounded by broken cumulus. When the clouds are layered, only the top layer can be considered unless the top layer or layers are scattered or broken. If the transition from one cloud type to another is fairly abrupt it can be very simple to determine the boundary, but if the transition is gradual, it may be very difficult if not impossible to calculate the boundary. Once the cloud boundaries have been established, cloud characteristics between the boundaries can be studied.

II. DATA

This thesis is intended to present a method for determining cloud boundaries using satellite infrared radiation data; therefore, an infrared radiation scan from any satellite-mounted scanning radiometer with a narrow field of view can be used. The technique does not apply to a radiometer that integrates over a wide field of view. The Nimbus high resolution infrared radiation HRIR) scans are better than TIROS as they are more representative of the actual radiation from individual cloud masses. An example of a piece of actual data is shown in Table 1. Data were selected to include a wide variety of cloud types and patterns for boundary determinations.

ACTUAL SAMPLE OF DIGITAL DATA

(Degrees K)

234.86	230.96	233.60	235.48	234.86	235.48
234.23	233.60	233.60	231.63	232.95	232.95
234.86	228.88	232.30	228.88	228.16	225.19
222.84	227.43	216.02	223.64	217.81	218.68
220.38	213.24	219.54	212.29	217.81	215.11
212.29	216.02	209.33	212.29	205.16	207.28
204.08	201.87	206.23	201.87	202.98	206.23
201.87	207.28	208.31	204.08	206.23	200.73
205.16	200.73	206.23	197.23	202.98	196.03
194.81	202.98	198.42	205.16	197.23	202.98
191.03	194.81	194.81	196.03	201.81	192.31
199.58	196.03	194.84	198.42	192.31	198.42
193.57	193.57	196.03	188.42	192.31	196.03
192.31	199.31	192.31	198.58	196.03	188.42
200.73	193.57	198.42	192.31	198.42	193.31
193.57	205.16	196.03	206.23	197.23	202.98
199.58	197.23	204.08	193.57	197.23	197.23
194.81	196.03	201.87	200.73	200.73	198.42
201.87	199.58	199.58	200.73	201.87	201.87
198.42	205.16	194.81	206.23	198.42	199.58
201.87	198.42	206.23	194.81	206.23	199.58
199.58	201.87	202.98	207.28	205.16	209.33
205.16	209.33	205.16	207.28	209.33	205.16
209.33	201.87	207.28	205.16	201.87	205.16
205.16	207.28	208.31	199.58	207.28	197.23
202.98	205.16	200.73	201.87	194.81	199.58

TABLE 1

III. TECHNIQUE FOR DETERMINING CLOUD BOUNDARIES

3.1 Procedure:

A plot of a digital high resolution infrared radiation scan can be considered as a series of connected lines of varying degrees of slope. A representative slope or gradient of black-body temperatures can be computed over a certain number of digital data points. A representative sample of plotted HRIR scans was selected to include a number of cloud types and combinations. The procedure which most accurately defines what was considered to be significant boundaries follows.

Take the mean of the first three digital data points of an HRIR scan. Exclude consideration of the following six points (4 through 11) and then determine the mean of the next three points (10, 11, and 12). Now subtract the first mean from the last mean. This difference will be representative of the slope or temperature gradient for the first twelve points and can be represented by the following equation:

$$S_1 = \frac{1}{N} \sum_{i=10}^{12} ti - \frac{1}{N} \sum_{i=1}^{3} Ti$$

where S = slope or gradient of first twelve data points.

i = data point numbers.

T = black-body temperature.

N = number of points averaged or data interval.

A negative result indicates increasing temperature values, and a

positive result, decreasing values. Repeat the same procedure beginning with the second three data points (4, 5, and 6) and obtain a representative slope for points 4 through 15 by:

$$S_2 = \frac{1}{N}\sum_{i=13}^{15} Ti - \frac{1}{N}\sum_{i=4}^{6} Ti$$

Continue this process of determining slopes along the remainder of the scan. Cloud boundaries are considered significant when three or more consecutive slopes of like signs with values of nine degrees centigrade or greater are calculated. The end points of the boundary or transition zone are located at point six of the first slope and point seven of the last slope of the three or more consecutive slopes. These criteria were selected as they best described the boundaries of the test cases studied.

3.2 Results:

The procedure previously described defines transitional regions between either cloud areas of different top temperatures or cloudy and clear areas, the sharper transitions obviously can be determined with best results. In figure 1, an example of one of the most distinctive records is presented. Boundary conditions were obtained for scan segments ab, cd, ef, and gh. Between these boundaries, reasonably homogeneous scan behavior indicates either cloudy or clear conditions. For example, the segment bc represents a cloudy area with significant horizontal extension (33 points in the scan) which should be studied

for possible determination of additional characteristics. However, segment fg is rather short and appears to indicate a small cloudy area which is too small in linear dimensions to yield much additional information due to the random scatter inherent in the measurements. Segment de, on the other hand, clearly indicates a distinct break in the cloudy conditions defined by the segments bc and fg; whether this break reaches all the way to the surface or may contain small, non-resolved clouds cannot be determined without additional study. Along the segment hi, the satellite sensor is looking down to the earth's surface in a clear area. If this temperature level represents the earth's surface, then the break in de is likely to contain either a residue of scattered clouds together with clear areas or a more or less solid covering of rather low clouds whose top temperatures are not much lower than those of the surface observed in segment hi.

Figure 2 depicts another typical scan which might be representative of an overcast cloud deck with areas of towering cumulus. These boundaries are not as sharply defined as those in figure 1 but, none the less, the computerized technique is capable of determining boundary conditions for ab, cd, ef, gh, ij, kl, and mn. The segment bc could be considered a break between the higher clouds on either side but is actually at temperatures of a lower cloud cover, as are segments hi and lm. The scan segments de and jk are at temperatures considerably colder than the lower cloudy areas and could be characteristic of towering cumulus type cloud tops. The temperatures along segment

no are substantially colder than the rest of the scan, which may indicate higher towering cumulus or even cumulonimbus tops. Segments bc and jk are very short and will not be examined further; however, the rest of the reasonably homogeneous scan segments will be studied for additional traits. The transition zone along segment mn is a good example of a very sharp and distinct boundary between two cloud masses while segments ab, cd, and ef are rather ill-defined. Obviously the former can be determined with best results. The latter portion of segment fg is a good example of a poorly defined or very gradual transition that was not determined by the computer analysis. The cloudy area in the vicinity of g is at temperatures similar to segments de and jk while the area around f is more characteristic of segments bc, hi, and lm, but because of the weak temperature gradient between f and g, the criteria were not met and the boundary was not defined.

The computerized procedure determines cloud boundaries along a scan with the area between the boundaries exhibiting reasonably homogeneous scan behavior. This holds true for most of the scans studied; however, figure 3 portrays an extreme example of non-homogeneity. There is quite a variation in temperatures along segment lm with a number of minor, sharp transitions but none great enough to meet the pre-set criteria for boundaries The scan segments bc, de, fg, and jk also have a certain amount of non-homogeneity as do all cloud areas; but, none the less, the computer analysis clearly determines the boundaries ab, cd, ef, gh, ij, and kl.

Figures 4, 5, 6, and 7 depict other rather typical scans and the boundaries placed on them by the computer analysis.

In order to verify these objective computer results, I attempted to place the most significant cloud boundaries onto plots of the various scans independent of the computer results, i. e., I attempted to visually decide where to start and end homogeneous "cloudy" or "clear" scan segments. In almost all of the cases so treated the boundaries thus estimated agree to within a few individual scan points with the results of the computer analysis. This is a good indication that the computer analysis can arrive at the same scan characteristics as will a meteorologist working from the same raw data.

The criteria which determines transition zones or temperature gradients can be adjusted to compute lesser boundaries depending upon the needs of the user. Figure 8 illustrates the computer analysis using the previously described criteria, i. e., using a temperature change of nine degrees over twelve scan points. Only one cloud area, ab, is computed. A certain amount of non-homogeneity exists, however, there are no major boundary areas present even though the warmer temperatures may represent the earth's surface and the colder temperatures, low clouds If the user desires further break-down of the scan segment ab, either the critical temperature gradient of nine degrees can be made smaller or the data interval along the scan made greater; or even a combination of both effects. For an example, compare the computer analysis of figure 9, using a minimum temperature gradient of eight

degrees over a data interval of fifteen scan points, to that of figure 8. The scan is now divided into four areas instead of one. The scan segments ab and ef are now classified as cloudy regions, while the segments cd and gh might well be clear areas. The boundary scan points are not very distinct, but by using slightly modified criteria, the computer is capable of distinguishing them.

On the other hand, if only the most pronounced boundaries are desired, then a larger temperature change or a smaller data interval may be used. Figures 10 and 11 show the same scan of high clouds with variable heights. The computer procedure described in section 3.1 calculates five cloudy regions bc, de, fg, hi, and jk with segments bc and hi being colder than de, fg, and jk, while figure 11 with a minimum temperature gradient of twelve degrees over a data interval of eleven points contains only two cloudy areas — bc and de. If only an estimation of the over-all cloud tops and very distinct boundaries are needed, the breakdown of figure 11 is adequate It is up to the user to decide what his needs are and then use the appropriate criteria.

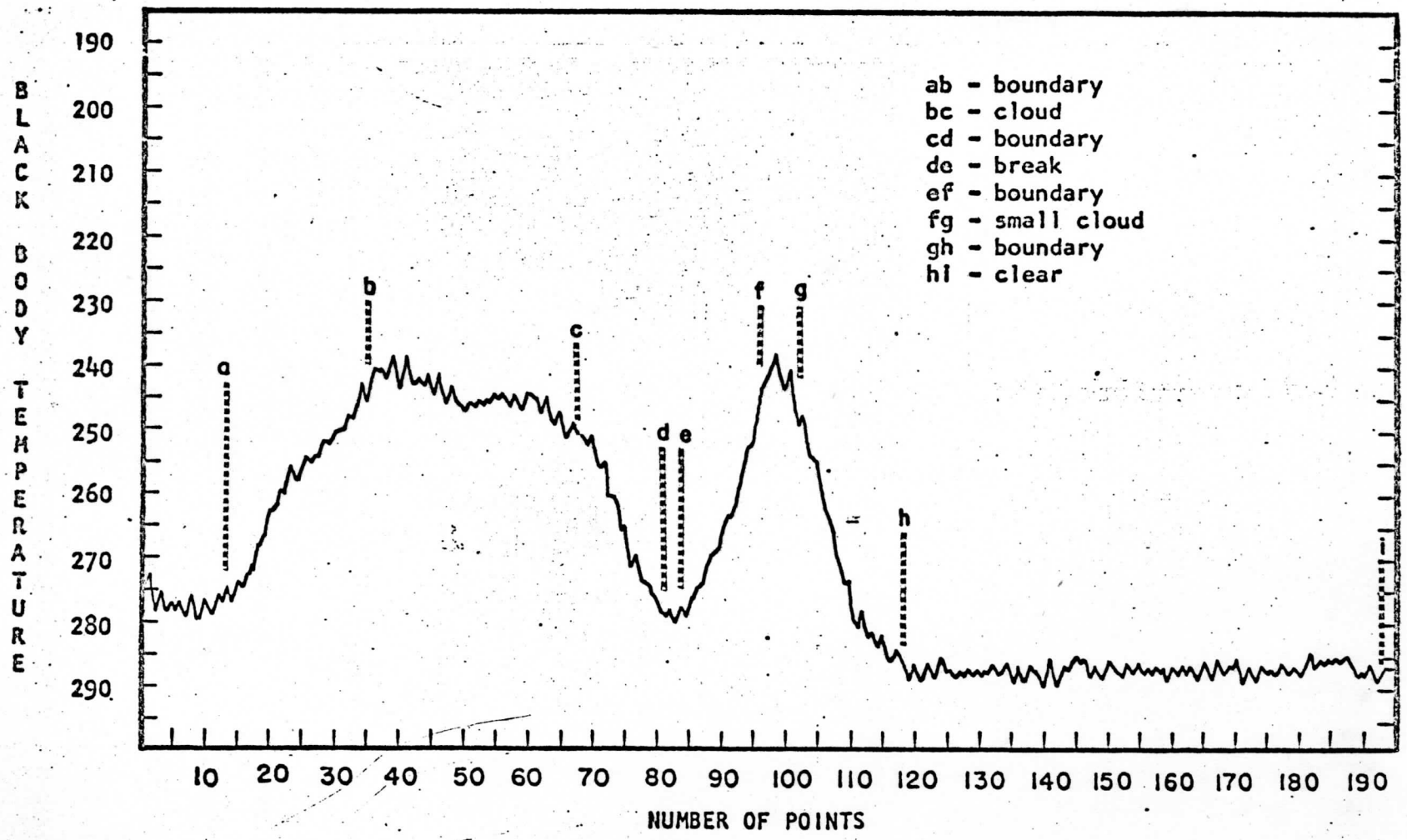
BLACK BODY TEMPERATURE
190
200
210
220
230
240
250
260
270
280
290
a
b
c
d
e
f
g
h
ab - boundary
bc - cloud
cd - boundary
de - break
ef - boundary
fg - small cloud
gh - boundary
hi - clear
10 20 30 40 50 60 70 80 90 100 110 120 130 140 150 160 170 180 190
NUMBER OF POINTS

Figure 1.

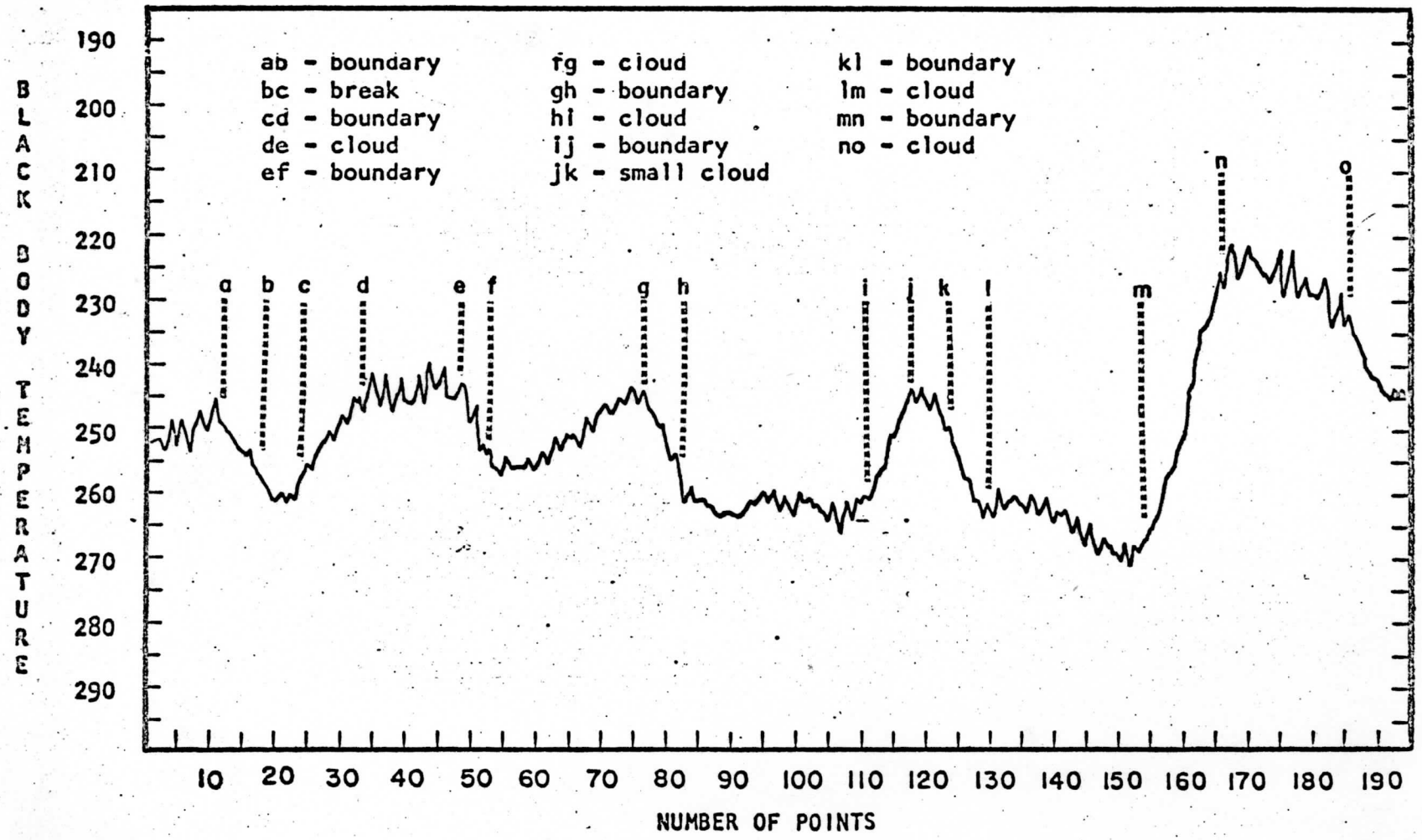
ab - boundary
bc - break
cd - boundary
de - cloud
ef - boundary
fg - cloud
gh - boundary
hi - cloud
ij - boundary
jk - small cloud
kl - boundary
lm - cloud
mn - boundary
no - cloud
a b c d e f g h i j k l m n o
BLACK BODY TEMPERATURE
190 200 210 220 230 240 250 260 270 280 290
10 20 30 40 50 60 70 80 90 100 110 120 130 140 150 160 170 180 190
NUMBER OF POINTS

Figure 2.

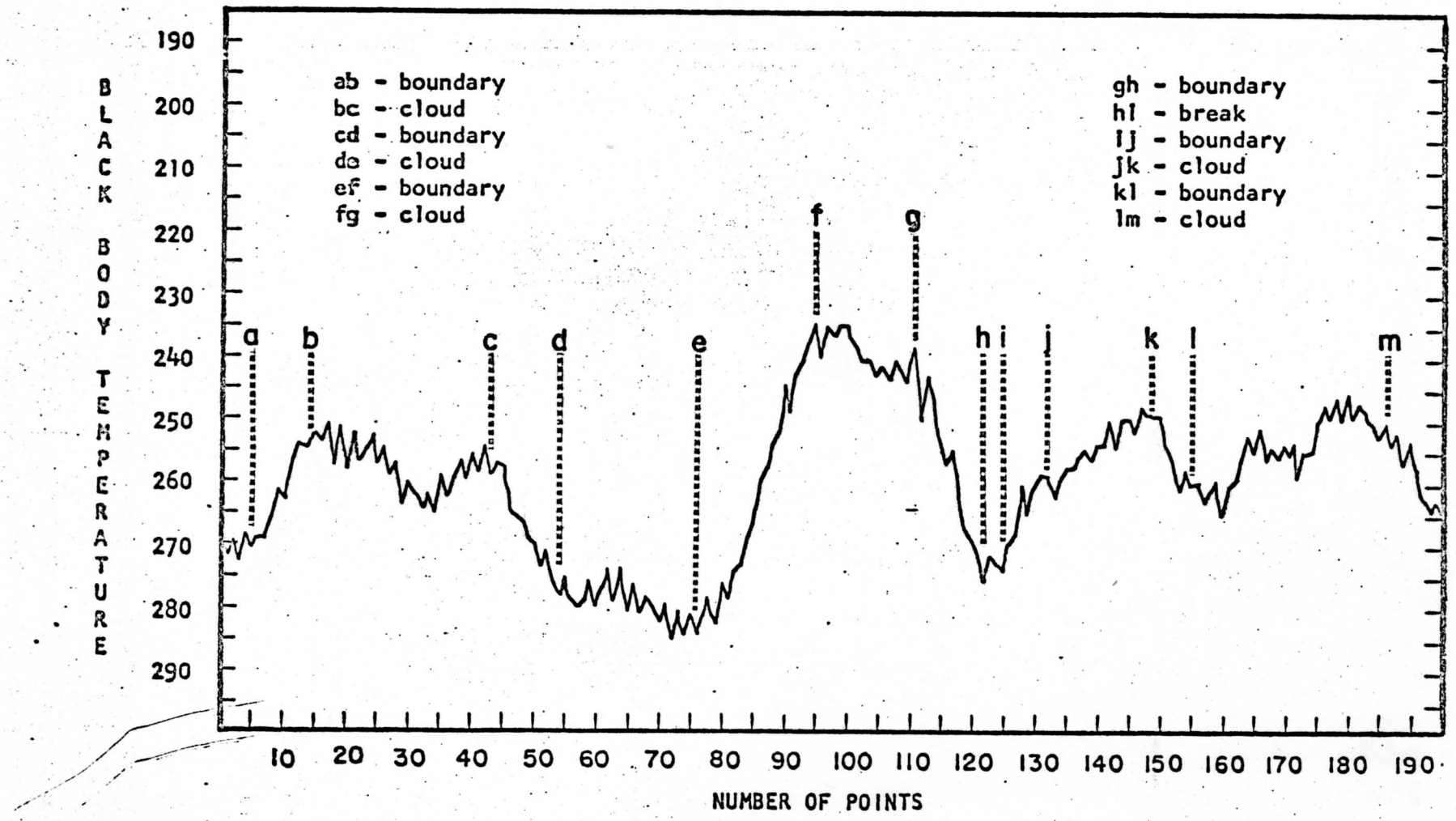
ab - boundary
bc - cloud
cd - boundary
de - cloud
ef - boundary
fg - cloud
gh - boundary
hi - break
ij - boundary
jk - cloud
kl - boundary
lm - cloud
a
b
c
d
e
f
g
h
i
j
k
l
m
BLACK BODY TEMPERATURE
190
200
210
220
230
240
250
260
270
280
290
10
20
30
40
50
60
70
80
90
100
110
120
130
140
150
160
170
180
190
NUMBER OF POINTS

Figure 3.

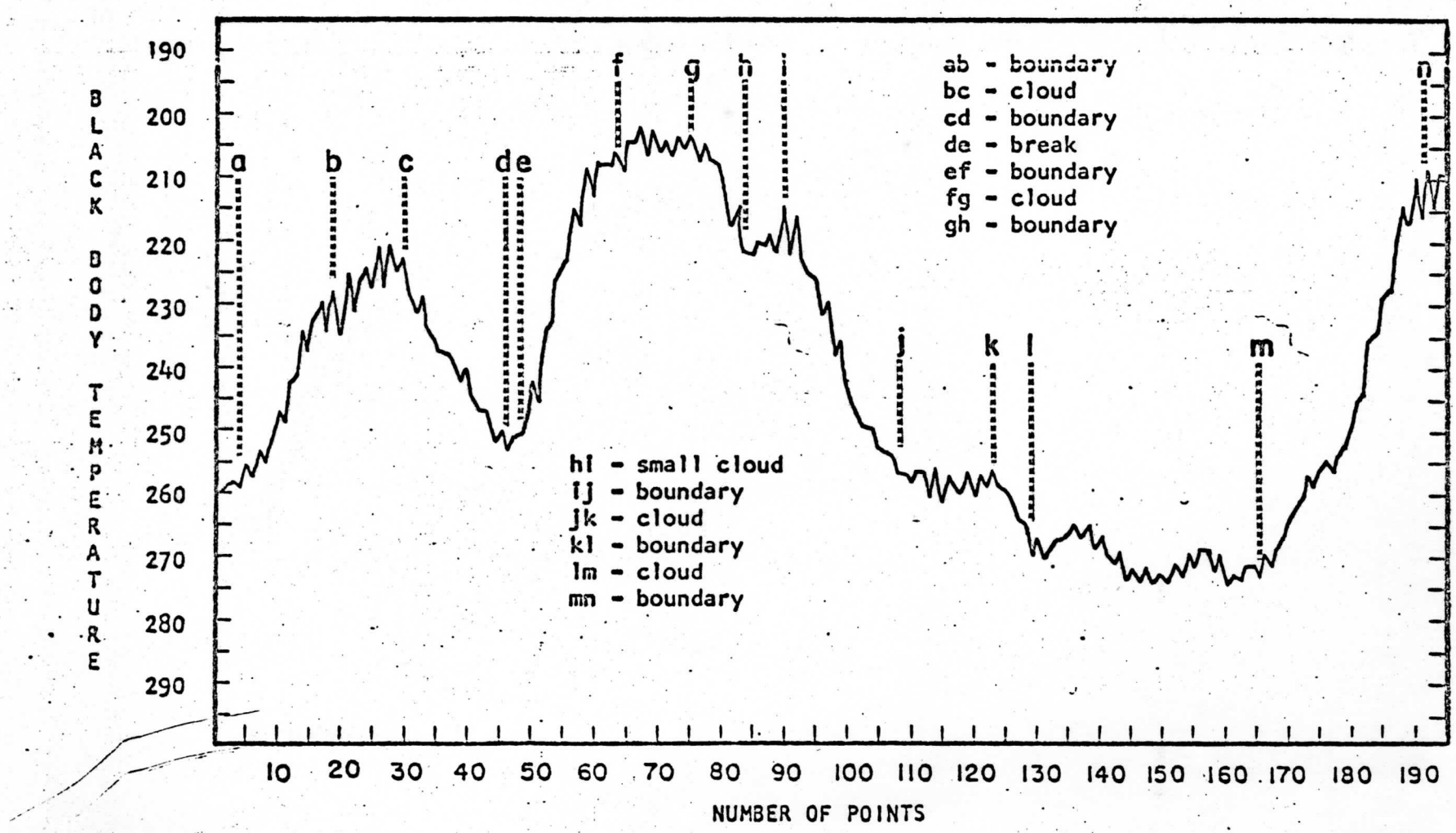
BLACK BODY TEMPERATURE
190
200
210
220
230
240
250
260
270
280
290
a
b
c
de
f
g
h
i
j
k
l
m
n
ab - boundary
bc - cloud
cd - boundary
de - break
ef - boundary
fg - cloud
gh - boundary
hi - small cloud
ij - boundary
jk - cloud
kl - boundary
lm - cloud
mn - boundary
10 20 30 40 50 60 70 80 90 100 110 120 130 140 150 160 170 180 190
NUMBER OF POINTS

Figure 4.

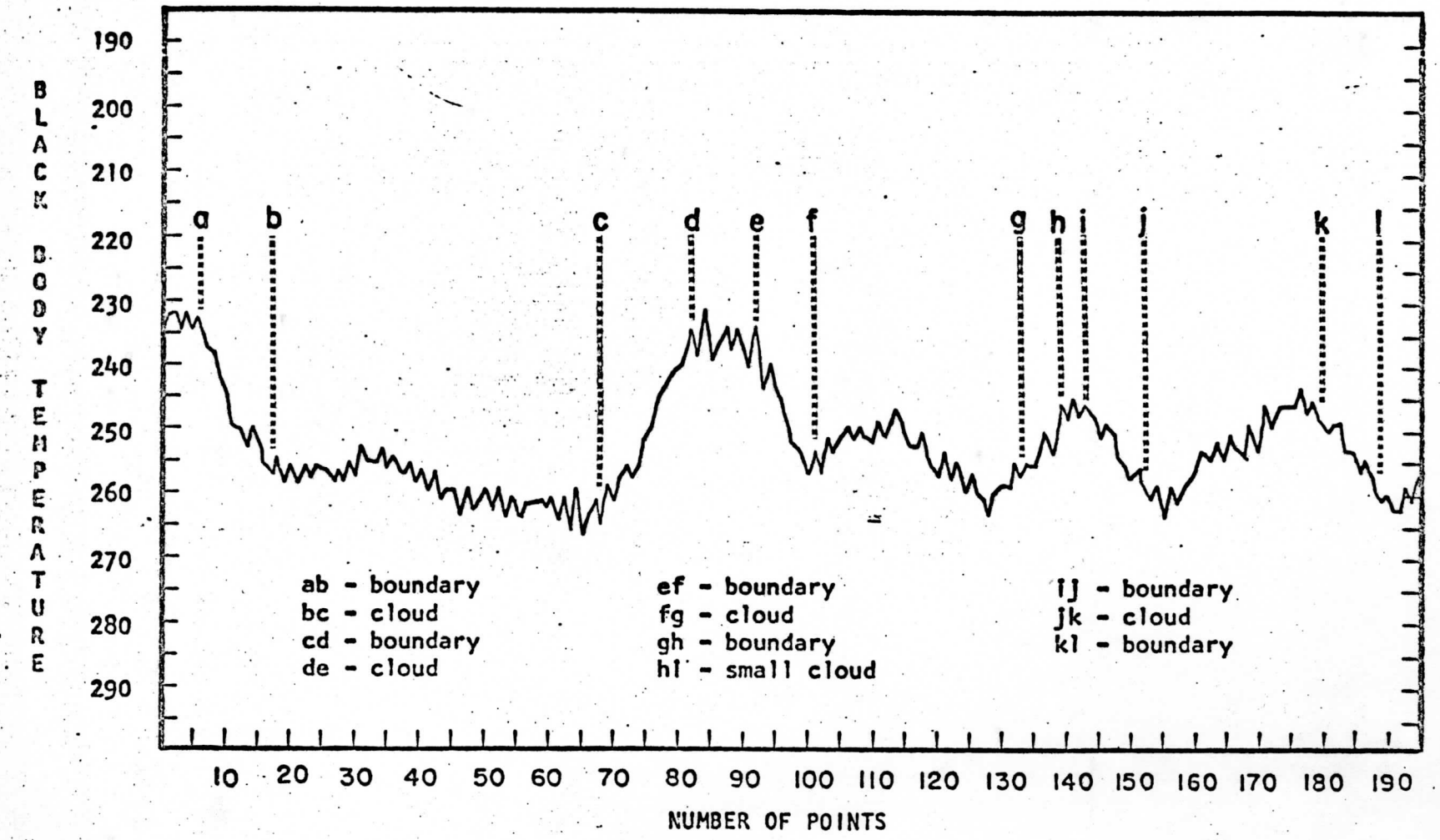
BLACK BODY TEMPERATURE
190
200
210
220
230
240
250
260
270
280
290
a
b
c
d
e
f
g
h
i
j
k
l
ab - boundary
bc - cloud
cd - boundary
de - cloud
ef - boundary
fg - cloud
gh - boundary
hi - small cloud
ij - boundary
jk - cloud
kl - boundary
10 20 30 40 50 60 70 80 90 100 110 120 130 140 150 160 170 180 190
NUMBER OF POINTS

Figure 5.

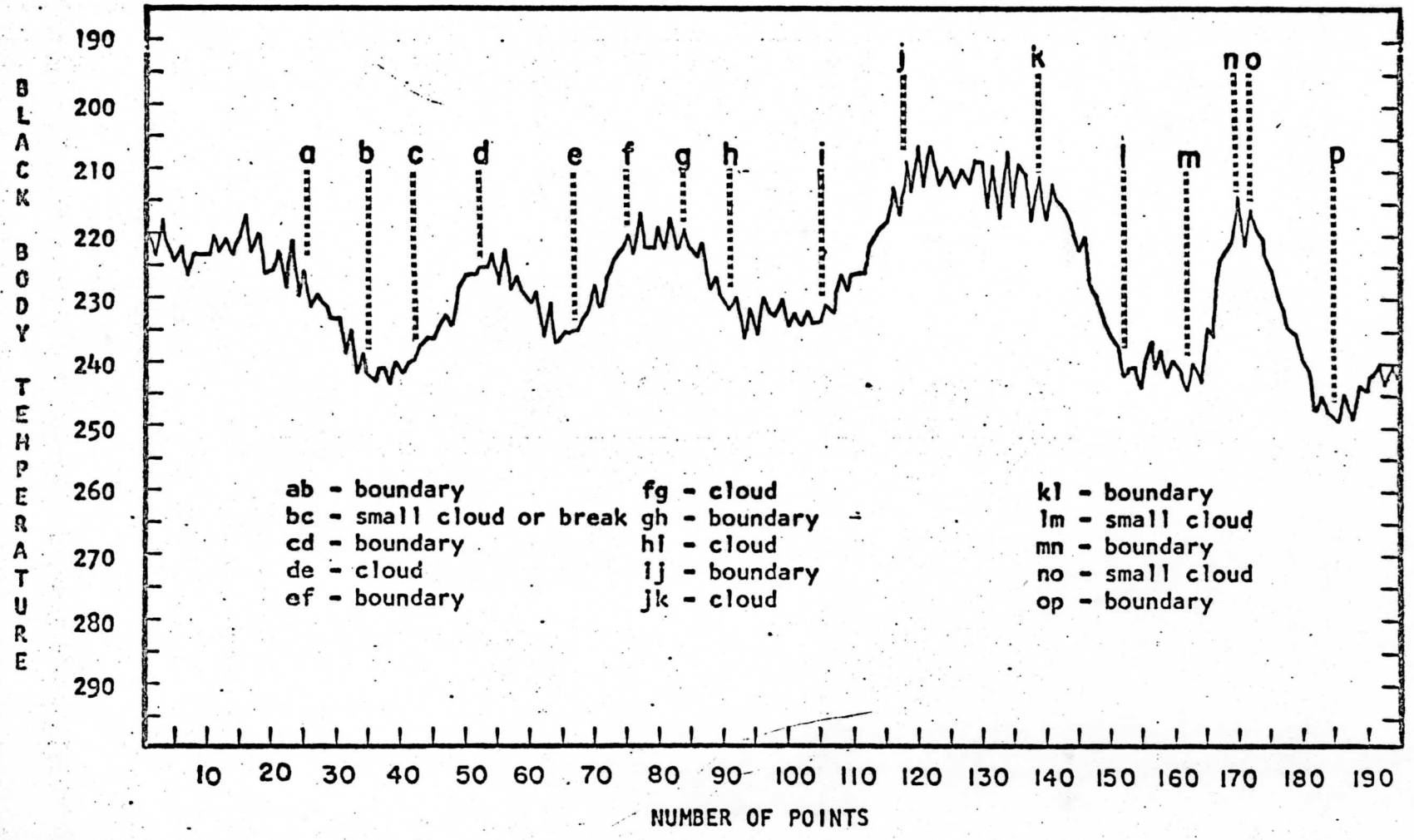
BLACK BODY TEHPERATURE
190
200
210
220
230
240
250
260
270
280
290
a b c d e f g h i j k l m n o p
ab - boundary
bc - small cloud or break
cd - boundary
de - cloud
ef - boundary
fg - cloud
gh - boundary
hi - cloud
ij - boundary
jk - cloud
kl - boundary
lm - small cloud
mn - boundary
no - small cloud
op - boundary
10 20 30 40 50 60 70 80 90 100 110 120 130 140 150 160 170 180 190
NUMBER OF POINTS

Figure 6.

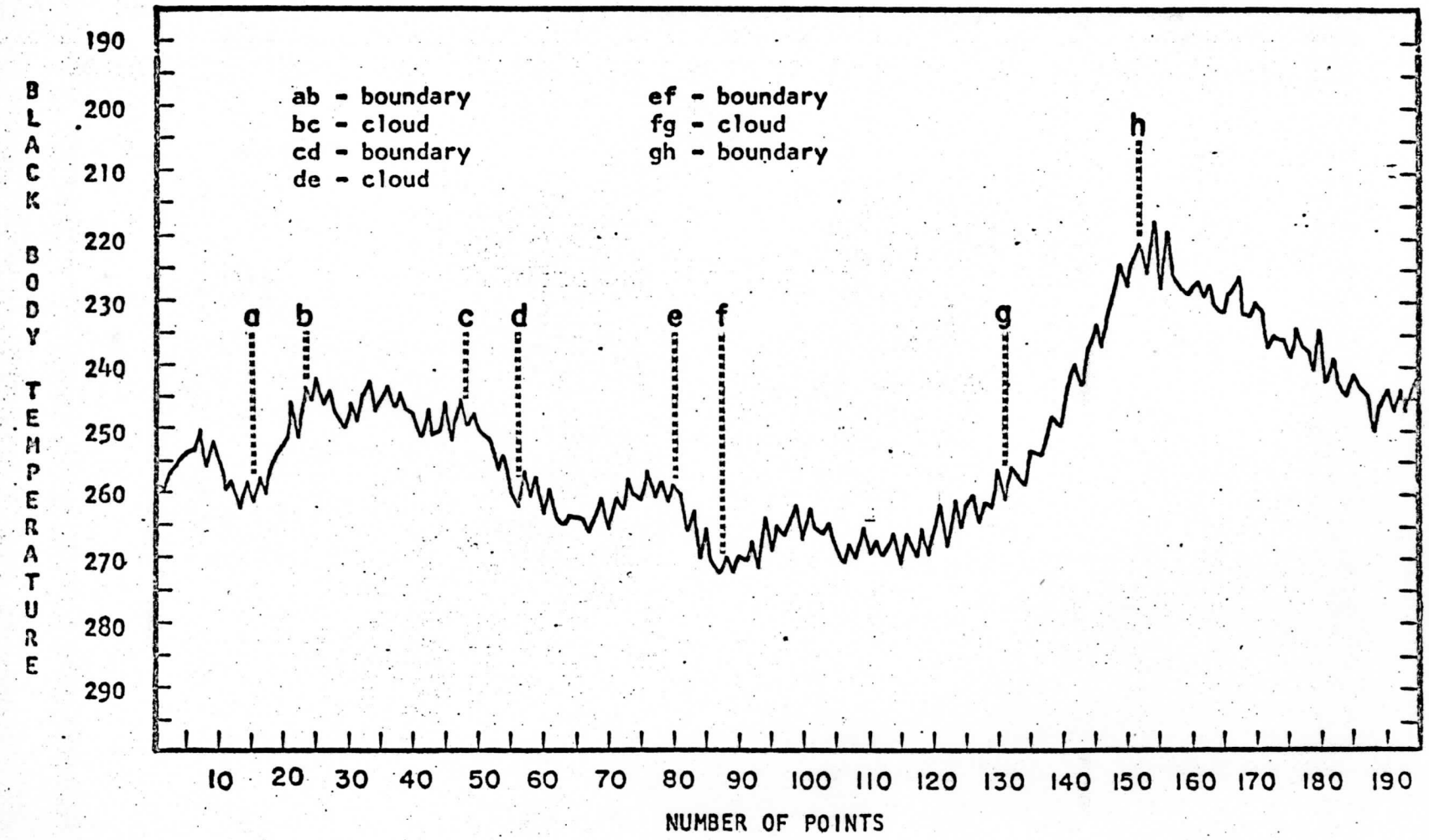
ab - boundary
bc - cloud
cd - boundary
de - cloud
ef - boundary
fg - cloud
gh - boundary
a
b
c
d
e
f
g
h
BLACK BODY TEMPERATURE
190
200
210
220
230
240
250
260
270
280
290
10 20 30 40 50 60 70 80 90 100 110 120 130 140 150 160 170 180 190
NUMBER OF POINTS

Figure 7.

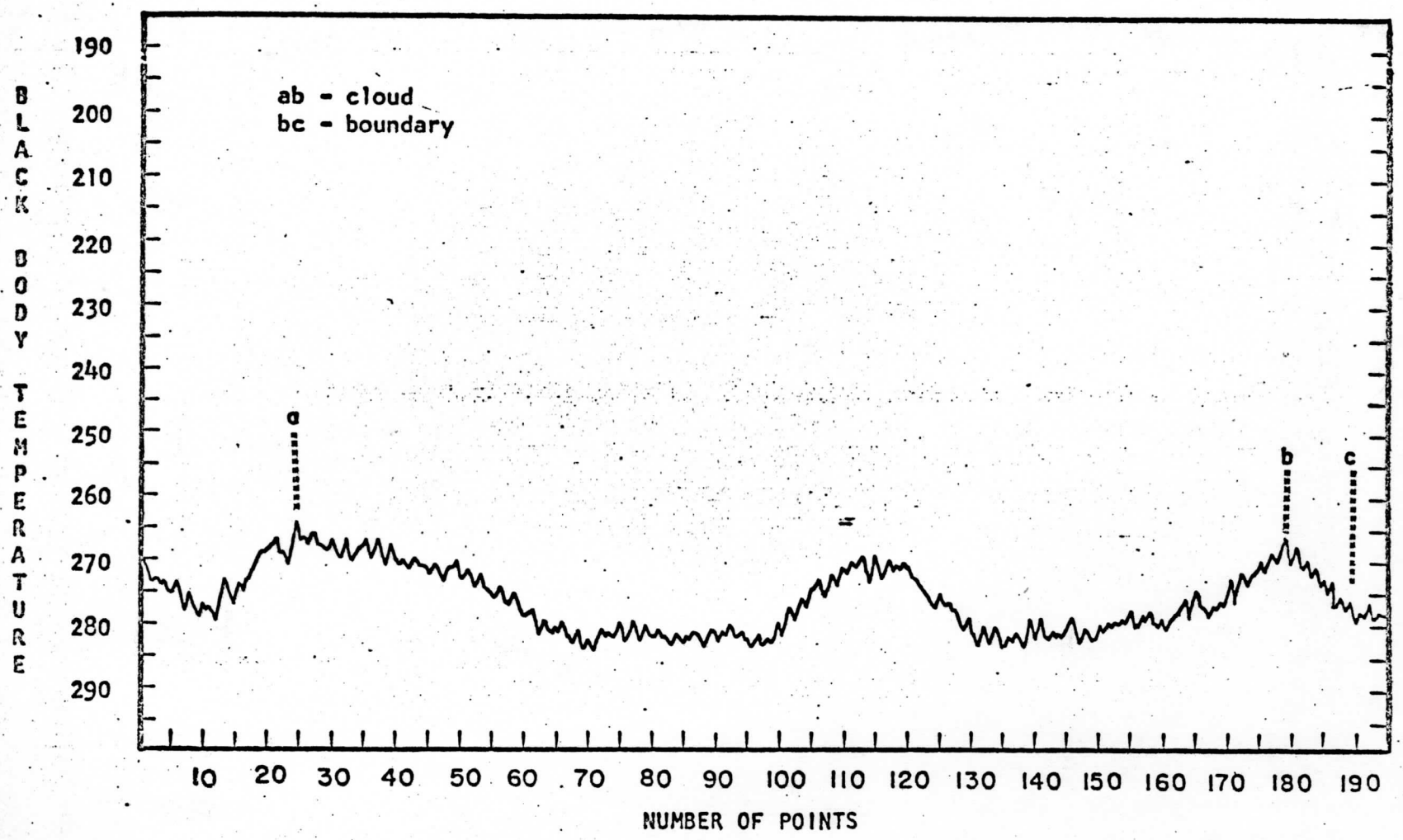
ab - cloud
bc - boundary
a
b
c
BLACK BODY TEMPERATURE
190
200
210
220
230
240
250
260
270
280
290
10 20 30 40 50 60 70 80 90 100 110 120 130 140 150 160 170 180 190
NUMBER OF POINTS

Figure 8.

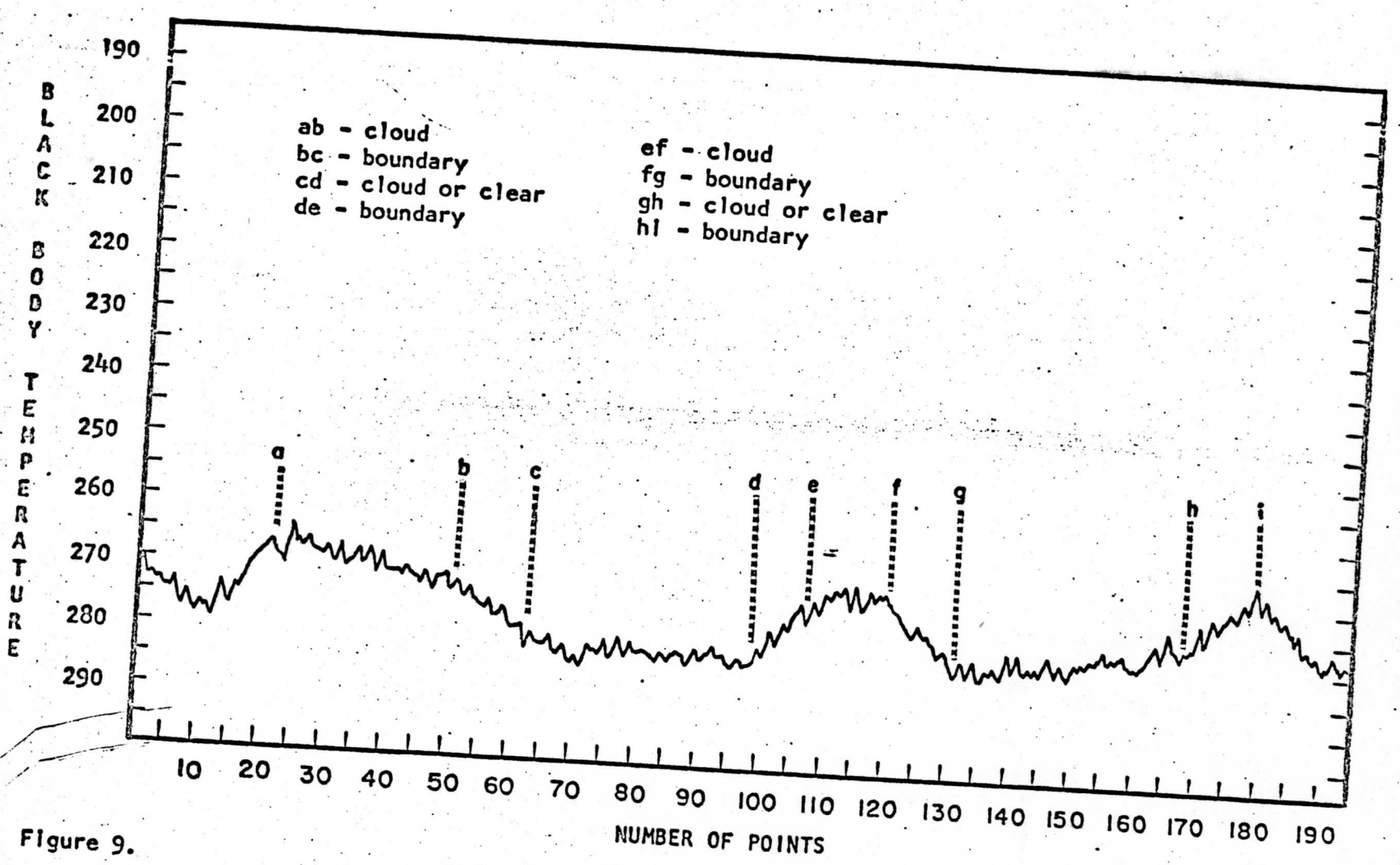
ab - cloud
bc - boundary
cd - cloud or clear
de - boundary
ef - cloud
fg - boundary
gh - cloud or clear
hl - boundary
a
b
c
d
e
f
g
h
BLACK BODY TEMPERATURE
190
200
210
220
230
240
250
260
270
280
290
10 20 30 40 50 60 70 80 90 100 110 120 130 140 150 160 170 180 190
NUMBER OF POINTS

Figure 9.

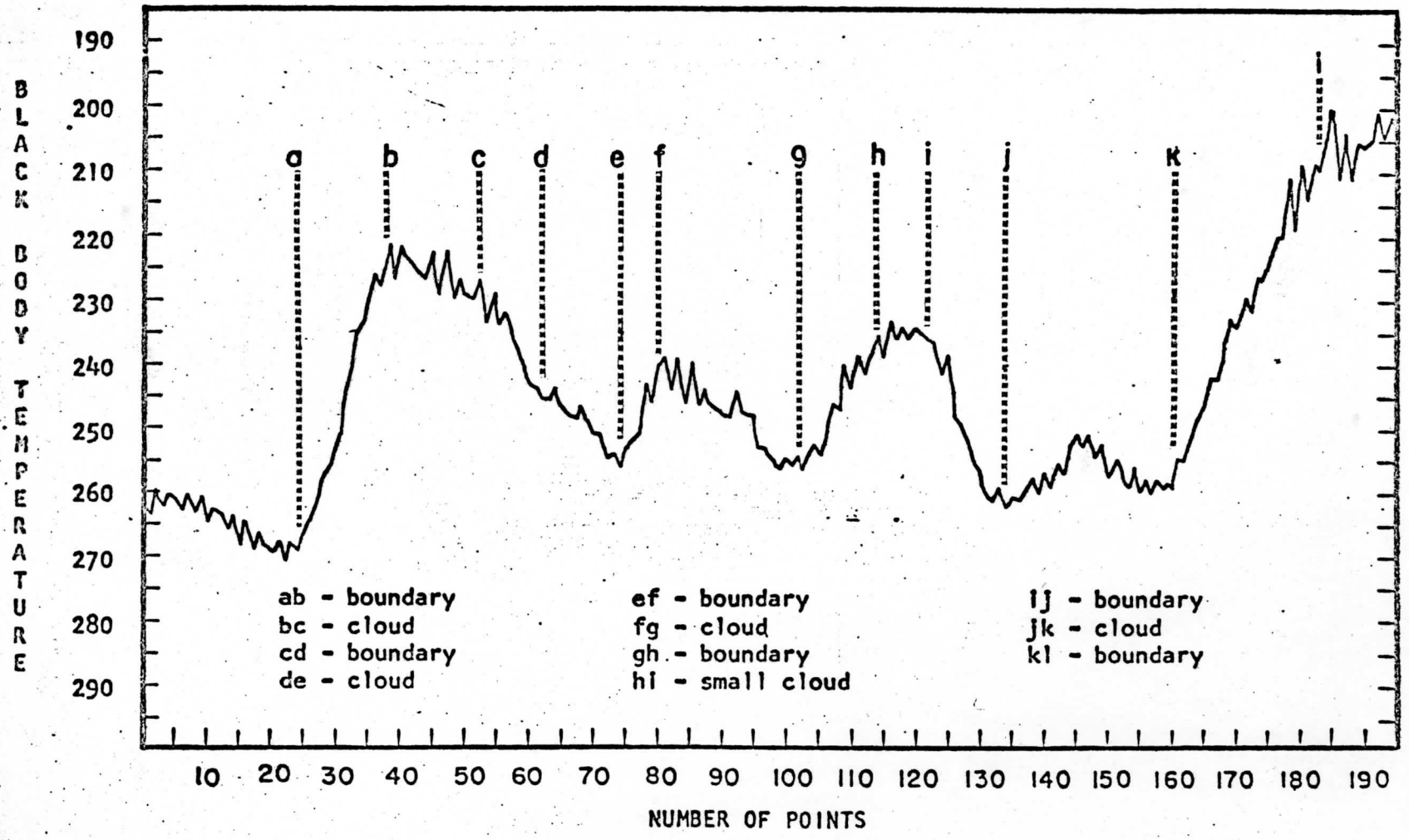
BLACK BODY TEMPERATURE
190
200
210
220
230
240
250
260
270
280
290
a
b
c
d
e
f
g
h
i
j
K
ab - boundary
bc - cloud
cd - boundary
de - cloud
ef - boundary
fg - cloud
gh - boundary
hi - small cloud
ij - boundary
jk - cloud
kl - boundary
10 20 30 40 50 60 70 80 90 100 110 120 130 140 150 160 170 180 190
NUMBER OF POINTS

Figure 10.

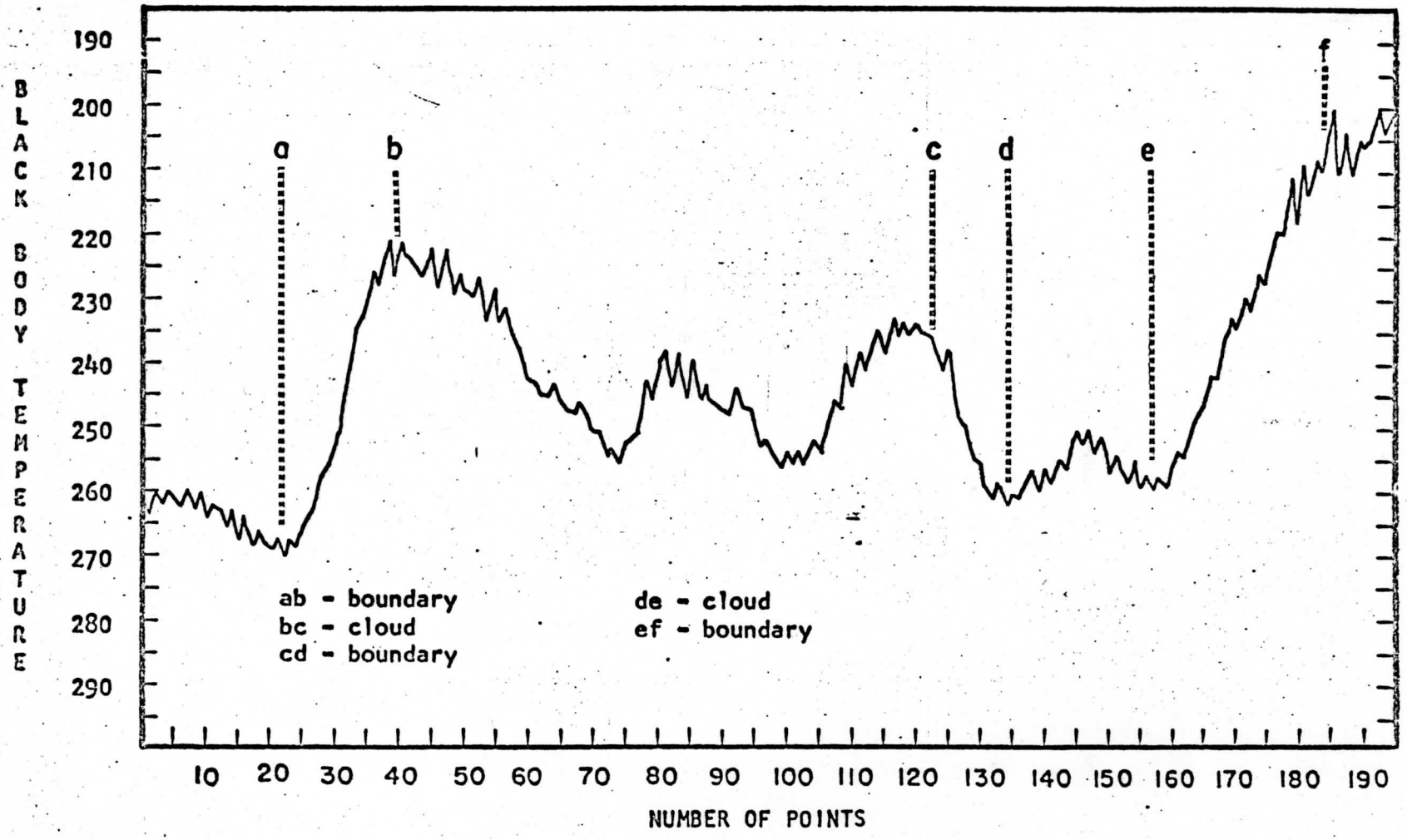
BLACK BODY TEMPERATURE
190
200
210
220
230
240
250
260
270
280
290
a
b
c
d
e
f
ab - boundary
bc - cloud
cd - boundary
de - cloud
ef - boundary
10 20 30 40 50 60 70 80 90 100 110 120 130 140 150 160 170 180 190
NUMBER OF POINTS

Figure 11.

3.3 Applications:

Such a computerized technique as has been discussed is useful for a first look at cloud systems. It is capable of taking the actual satellite signal received, converting it to a single infrared radiation scan, and then differentiating areas of like sloudiness. These areas of similar clouds can then be studied for eights, variability of heights, and other related parameters. A good estimate of the amount of cloud-cover can also be obtained by counting the number of points of cloud-cover and no cloud.

With a single scan the orientation of the cloud systems will not be known. One scan could be representative of a number of different cloud arrangements, as shown in figure 12. Simultaneous ground observations, where possible, or visual satellite pictures over the same area, would greatly enhance the technique as the nephanalysis would be known. If neither is available the generalized cloud arrangement could be obtained, with TIROS or Nimbus, by a display of boundaries of successive parallel infrared radiation scans.

By taking the mean seasonal soundings for the various latitudinal circles involved, the cloud heights can be determined, to within a fair degree of accuracy, from the mean temperatures of the cloud areas between the calculated boundaries (see Fritz and Winston, 1962, and Rasool, 1964). If greater cloud top accuracy is desired, actual soundings can be used when available. Corrections for the absorption

and re-emission of upcoming radiation by water vapor, ozone (Wark et al., 1962), and possibly aerosols can be incorporated. If the amount of cloud cover is known or can be estimated, a technique for determining cloud heights as described by Bohlson (1967) may be employed.

A similar technique may also prove useful with the Applications Technology Satellite (ATS) which has 256 grey scales of brightness in the visual range. A digitized brightness scan could be handled in much the same way as described in section 3.1 .

Future satellites may transmit simultaneous readings in the "atmospheric window" and visual (television) ranges. Such a satellite system would greatly augment this technique.

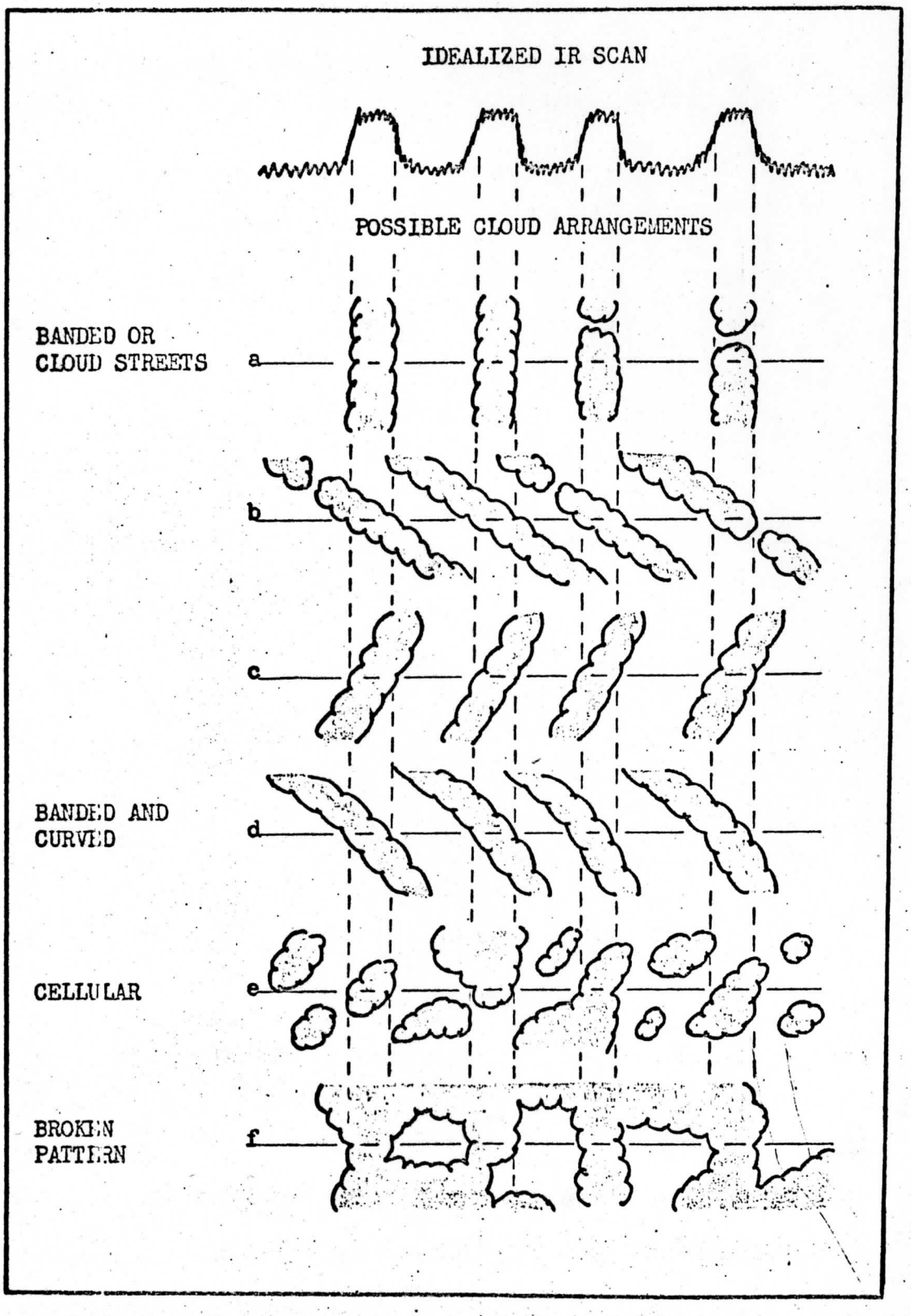
IDEALIZED IR SCAN
POSSIBLE CLOUD ARRANGEMENTS
BANDED OR
CLOUD STREETS
a
b
c
BANDED AND
CURVED
d
CELLULAR
e
BROKEN
PATTERN
f

Figure 12.

IV. SOME CLOUD CHARACTERISTICS

After the boundaries were determined, the cloud areas between the boundaries were examined to ascertain whether certain characteristics of like cloud genera could be determined from the infrared radiation data. The mean black-body temperature and the variance from the mean were calculated for each cloud top. Theoretically, the mean temperature would classify the clouds according to their heights and the variance would distinguish between the extensive horizontal development of stratiform clouds and the vertical development of cumuliform clouds. The heights of the cloud tops can be determined from the mean temperautre, as discussed in section 3.3. The variance within the cloud tops is given by:

$$\sigma^2 = \frac{1}{N}\sum(X - \bar{X})^2$$

where σ^2 = variance

X = temperature variate

$\bar{X}$ = mean temperature of cloud top

N = number of data points used

The variance was computed for scan segments from 10 to 40 data points. Large cloud areas containing more than 40 data points were divided so as to keep the scan length less than 40 points. Figure 13 shows cloud top variance of all large clouds studied versis frequency

of occurrence. All recognizable homogeneous clear areas were excluded from this compilation so as not to give unnecessary weight to the small variance values. In 46 per cent of the cases studied the variance was between 1.0 and 5.0, and in 59 per cent of the cases, between 0.5 and 6.0, which illustrates that for most clouds of large horizontal extent, excluding the boundary conditions, the cloud top temperatures do not vary greatly.

Clouds of small horizontal extension, i.e., 10 to 25 data points, versus frequency of occurrence are shown in figure 14. The variability is greater than that of large clouds, with only 35 per cent of the cases between 0.5 and 6.0 as compared to 59 per cent of the large cloud mass cases. Seventy per cent of the cases occur between variances of 1.0 and 10.0. One would expect the temperature variability values of small cloud tops to be larger than those values of large cloud masses, as the tops of small clouds are not as uniformly developed.

Very little information as to cloud genera could be determined by the variance. However, cumulonimbus clouds, as would be expected, show a much larger variance than other cloud types. Scan segment de of figure 15 is a good example of the variability of cloud top temperatures of cumulonimbus type clouds. Figure 16 shows the occurrence of what appeared to be cumulonimbus clouds versus the variance of cloud top temperatures. Seventy-seven per cent of the cases examined occurred between the large variance values of 6.0 and 17.0. If the cloud top temperatures are extremely low and the variance along the

scan segment large, one can be fairly safe to assume that the clouds are cumulonimbus.

A number of infrared scans taken off the west coast of Africa indicated what appeared to be a large horizontal area of relatively warm stratus clouds with most variance values between 2.5 and 5.0. This area is in the root region of the trade winds where the trade wind inversion limits the vertical development of the clouds, producing very uniform cloud tops and thus a small variance.

Figure 17 depicts a typical scan of a cloudless ocean area For most of these cases studied, the variance over clear ocean areas varied from 0.5 to 1.5 and over clear land areas from 0.7 to 2.5 (see figure 18). The land and ocean areas are homogeneous over a large horizontal expanse, with the oceans varying less than land.

The variance of most of the clouds, other than cumulonimbus and those clouds below the trade wind inversion, ranged from 2.5 to as 15. No distinction could be made whether the clouds were cumuliform of stratiform. The resolution of present scanning infrared radiometers is not great enough to distinguish individual cumulus cells or very small breaks in the clouds. Also, the technique used in this paper determines only significant cloud boundaries and does not calculate minor changes. Therefore, even though the mean temperature of the cloud tops can be calculated with a fair degree of accuracy, the variance is highly influenced by these small breaks, scattered small clouds both resolved and unresolved, and minor boundaries.

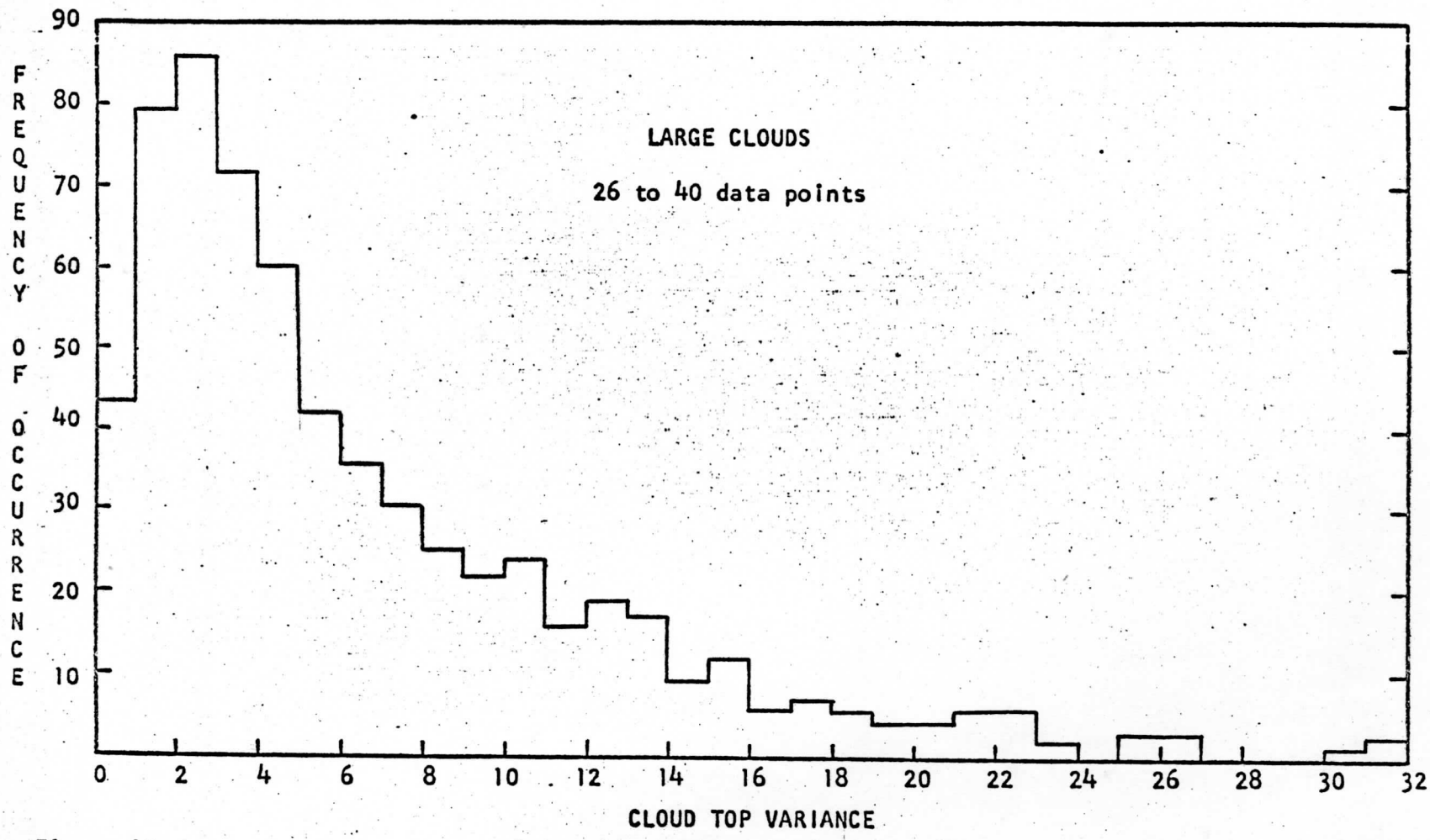
LARGE CLOUDS
26 to 40 data points
FREQUENCY OF OCCURRENCE
90
80
70
60
50
40
30
20
10
0
2
4
6
8
10
12
14
16
18
20
22
24
26
28
30
32
CLOUD TOP VARIANCE

Figure 13.

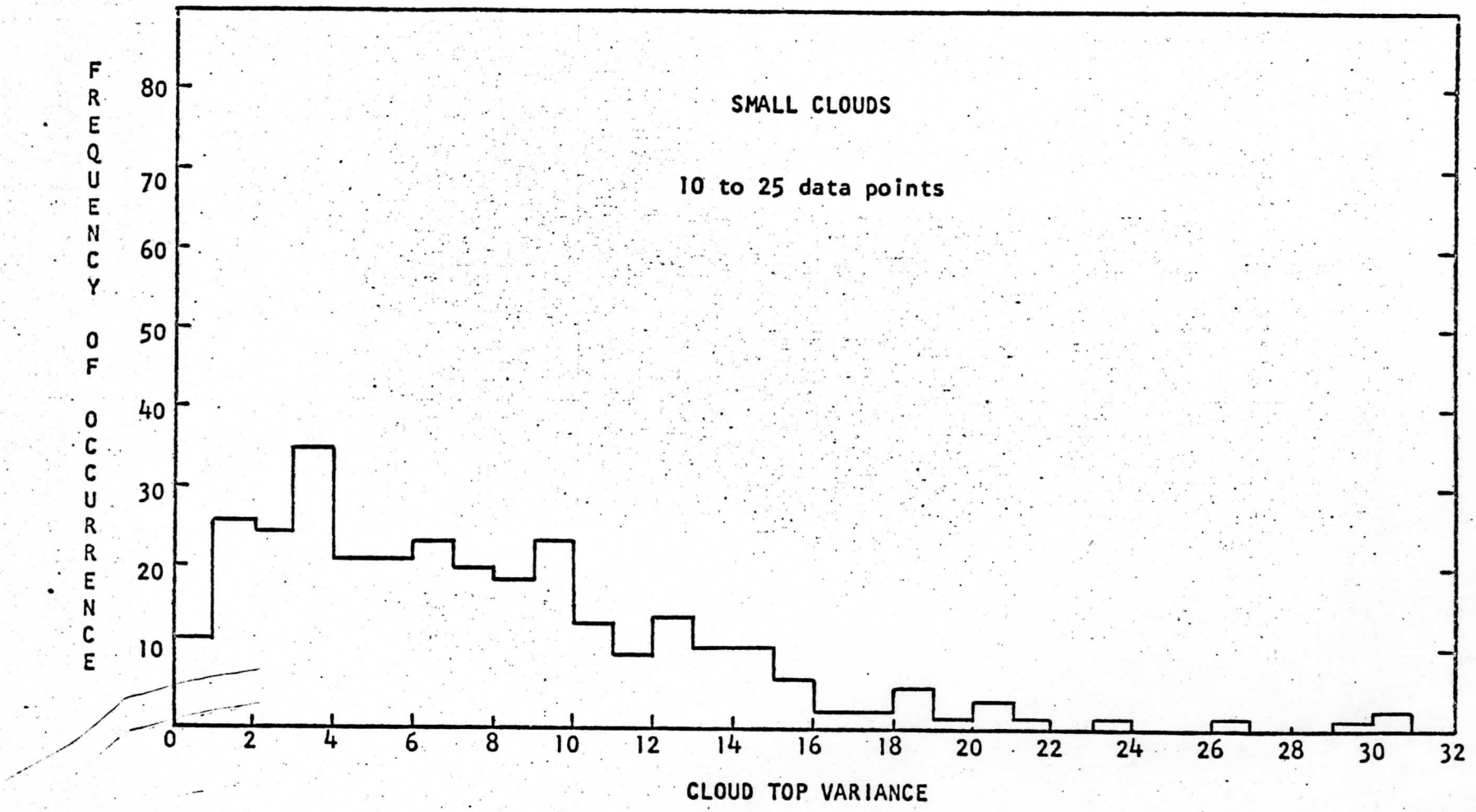
SMALL CLOUDS
10 to 25 data points
FREQUENCY OF OCCURRENCE
80
70
60
50
40
30
20
10
0
2
4
6
8
10
12
14
16
18
20
22
24
26
28
30
32
CLOUD TOP VARIANCE

Figure 14.

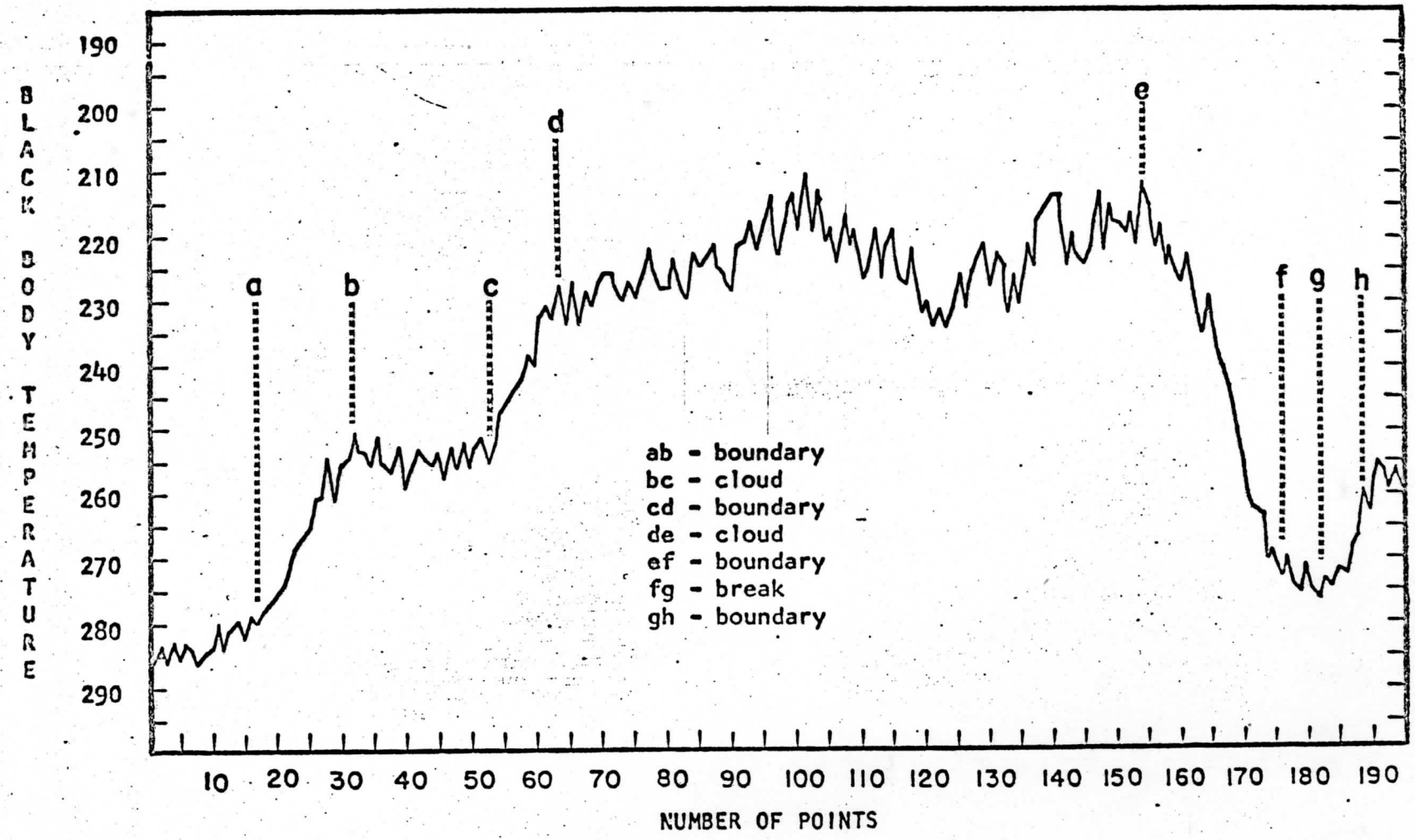
BLACK BODY TEMPERATURE
190
200
210
220
230
240
250
260
270
280
290
a
b
c
d
e
f
g
h
ab - boundary
bc - cloud
cd - boundary
de - cloud
ef - boundary
fg - break
gh - boundary
10 20 30 40 50 60 70 80 90 100 110 120 130 140 150 160 170 180 190
NUMBER OF POINTS

Figure 15.

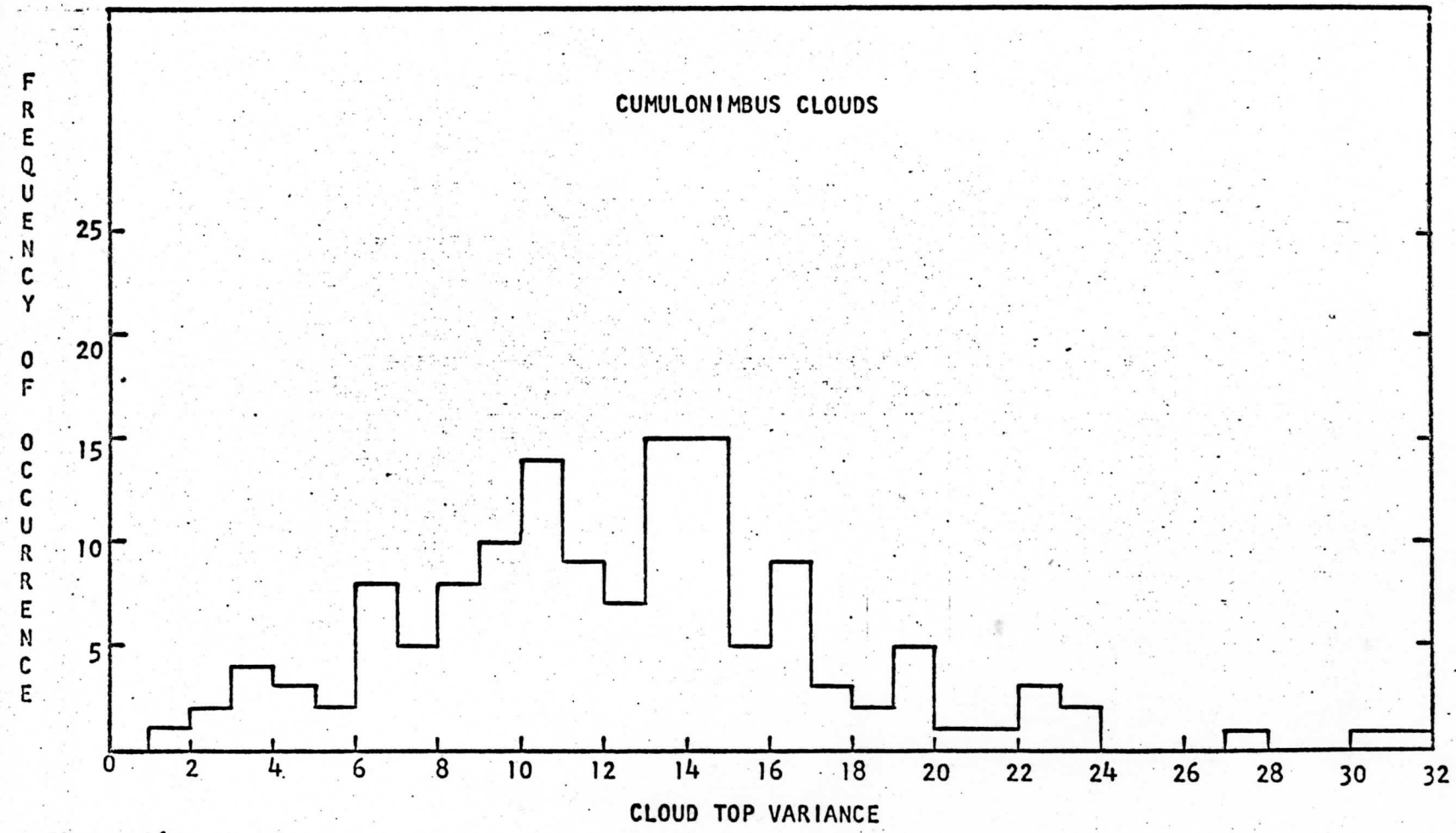
CUMULONIMBUS CLOUDS
FREQUENCY OF OCCURRENCE
25
20
15
10
5
0
2
4
6
8
10
12
14
16
18
20
22
24
26
28
30
32
CLOUD TOP VARIANCE

Figure 16.

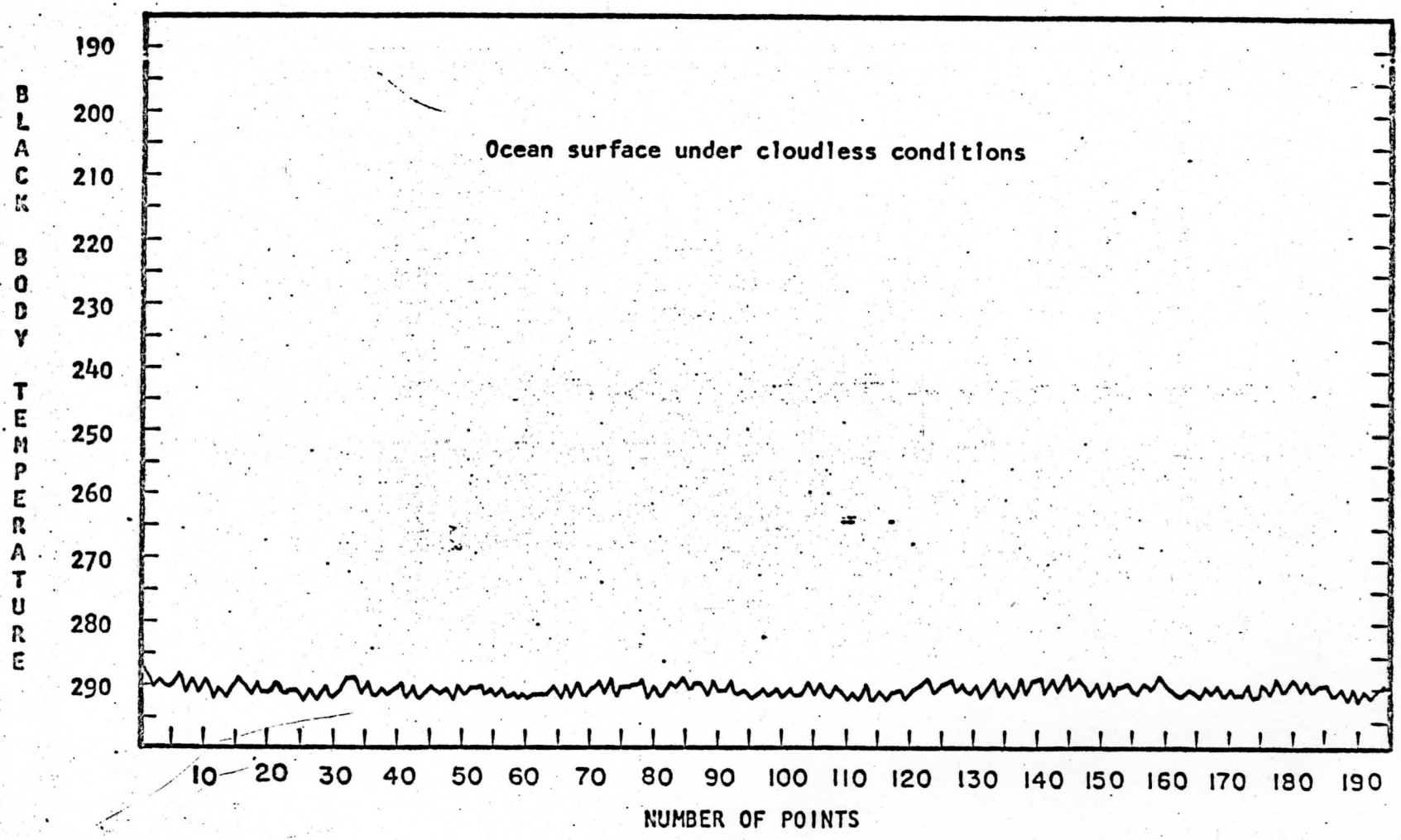
Ocean surface under cloudless conditions
BLACK BODY TEMPERATURE
190
200
210
220
230
240
250
260
270
280
290
10
20
30
40
50
60
70
80
90
100
110
120
130
140
150
160
170
180
190
NUMBER OF POINTS

Figure 17.

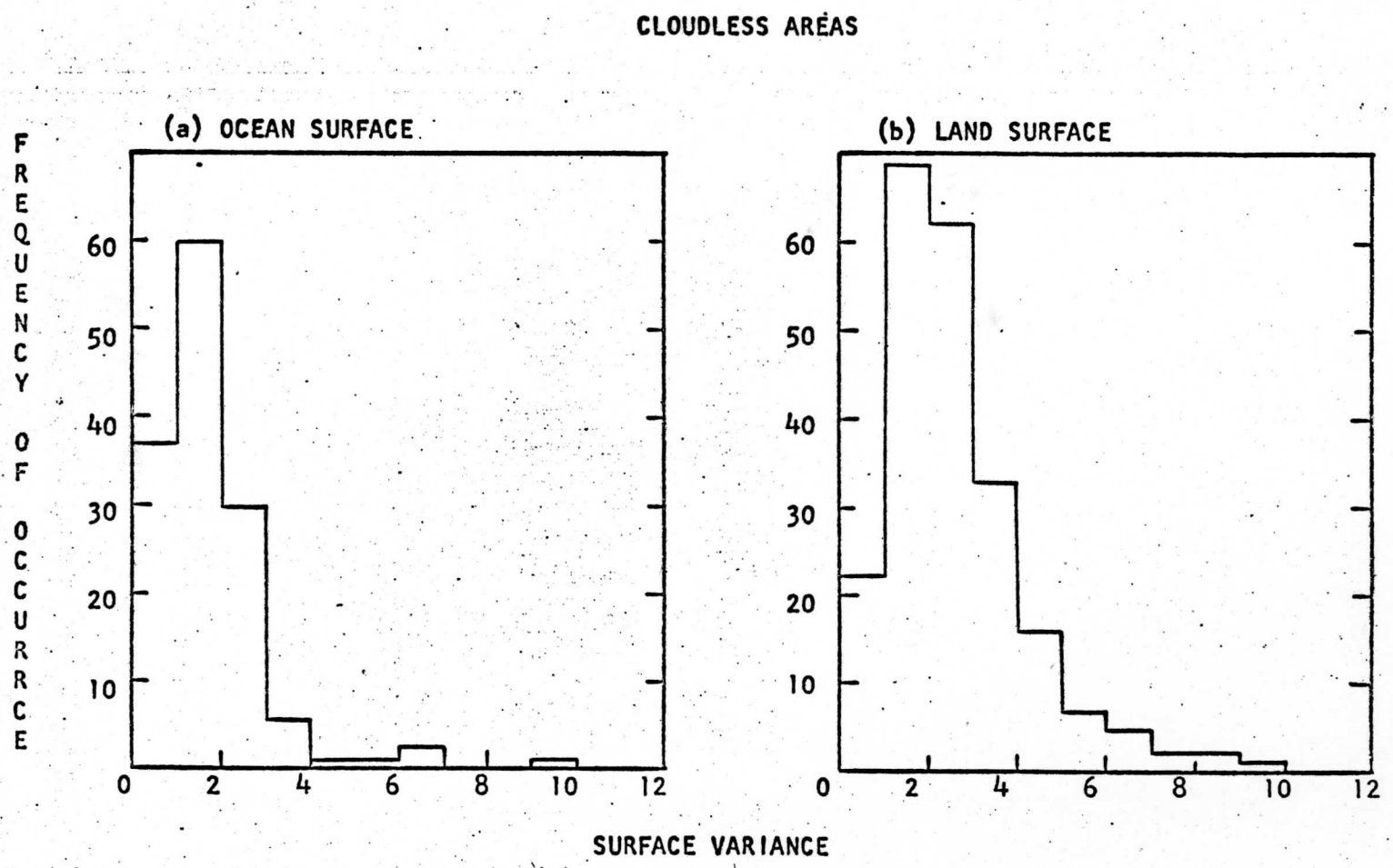
CLOUDLESS AREAS
(a) OCEAN SURFACE
(b) LAND SURFACE
FREQUENCY OF OCCURRCE
60
50
40
30
20
10
0
2
4
6
8
10
12
SURFACE VARIANCE

Figure 18.

V. CONCLUSIONS

This paper has shown a feasible computerized technique for determining cloud boundaries. Criteria were set up so the technique would locate what were considered significant cloud boundaries. These criteria can be adjusted to determine boundaries of less significance or only the most sharply defined boundaries, whatever the needs of the user may be.

Cloud top heights can be determined from the mean black-body temperatures of the cloud areas between the boundaries. The accuracy of these heights may be improved by considering the geographical location, time of satellite pass, vertical atmospheric sounding, and corrections for water vapor and ozone.

Cloud formations can be determined when this technique is used in conjunction with corresponding surface data, visual satellite data, or similar parallel infrared radiation scans.

The variance of the digital temperature data is not a good indicator as to whether the cloud type is cumuliform or stratiform except in the extreme cases of either cumulonimbus clouds or of stratus clouds that are suppressed by a very strong inversion layer. Most cloud areas are layered and are a combination of stratiform and cumuliform types, and the distinctions between the individual classes are too vague to be determined by the variance of cloud top temperatures. Future scanning

infrared radiometers with greater resolution and a technique adjusted to calculate very fine boundary conditions may be able to distinguish a difference between "average" cumuliform and stratiform clouds.

VI. REFERENCES

Bohlson, J. S., 1967: "A technique for determining cloud top heights utilizing satellite data." M. S. thesis at the University of Wisconsin.

Fritz, S., and J. S. Winston, 1962: "Synoptic use of radiation measurements from satellite TIROS II." Mon. Wea. Rev., 90, 1-9.

Glahn, H. R., 1966: "On the usefulness of satellite infrared measurements in the determination of cloud top heights and areal coverage." J. App. Meteor., 5, 189-197.

Nordberg, S., W. R. Bandeen, B. J. Conrath, V. Knude, and I. Persano, 1962: "Preliminary results of radiation measurements from the TIROS III meteorological satellite." J. Atmos. Sci., 19, 20-30.

Rasool, S. I., 1964: "Cloud heights and nighttime cloud cover from TIROS radiation data." J. Atmos. Sci., 21, 152-156.

Wàrk, D. Q., G. Yamamoto, and J. H. Lienesch, 1962: "Methods of estimating infrared flux and surface temperatures from meteorological satellites." J. Atmos. Sci., 19, 369-384.

SOME STATISTICAL REDUCTION TECHNIQUES FOR SATELLITE DIGITAL DATA

by

DAVID LEE NELSON

ABSTRACT

This paper discusses two statistical compression techniques designed to reduce the volume of satellite data while retaining sufficient information content to be immediately applicable to various meteorological problems. The characteristics of both techniques implied by the schemes is a loss in amplitude resolution in the digital signal. The result of this paper is a step-by-step procedure which will allow each investigator to make value judgments on his own data as to the applicability of either technique.

TABLE OF CONTENTS

LIST OF TABLES

LIST OF FIGURES

I. INTRODUCTION

Since the launch of Explorer VII on October 13, 1959, satellite data has been transmitted to the ground at an ever increasing rate, making demands on the users to assimilate and process tremendous volumes of data. To quote from Katz and Doyle (1964):

> So it is that not only have new methods greatly advanced the rates and amounts of data that can be acquired, but at the same time accelerating advances in meteorological research are causing ever increasing demands to be made on the rate at which the accumulated data are converted into usable information.

It is this very statement which has fostered this thesis.

Meteorological research is faced with the very real problem of assimilating and storing data transmitted from satellites. With emphasis being placed on higher and higher resolution, the number of data points per unit area is automatically increased. As a specific example, the N. A. S. A proposed Advanced Technology Satellite will take photographs in one day which will contain more bits of information than the combined Tiros III, IV, and VII output produced in one hundred days each. This proposed ATS output will contain 8192 words per scan, 2000 scan lines, and eight bits of information per word. This yields 131 million bits of information per picture! The effective core storage of a standard two bank CDC 3600 computer with monitor is only two million 400 thousand bits, about two percent of one picture. The only

salvation is that the study of extremely high resolution raw data is usually not done on a large scale. In such a study, individual scans or pieces of scans are analyzed separately. The earth's atmosphere, however, is studied on the large scale, often without the requirement for extremely high resolution. There is a need to devise some techniques for reducing the data into a form that can be readily managed.

Dr. Verner E. Suomi has suggested a technique for reducing infrared or visual data by some degree which will retain all the information content for certain studies and most of the content for others. A second scheme has been suggested by Mrs. Jean Anderson of the Instrumentation Laboratory at the University of Wisconsin, which may have other applications. This thesis will investigate these techniques as to their desirable and undesirable characteristics and for which applications they're appropriate.

The thesis is divided basically into four parts: 1) a presentation of both techniques, 2) the study of the resolution and order losses implied by these techniques, 3) a comparison of the two techniques and suggested applications, and 4) conclusions derived from the study. The final product will be a specific procedure associated with a series of graphs which will allow each investigator to make his own value judgment as to whether a certain scheme will apply in his case and also tell him how much computer storage he will require with an initial amount of raw digital data.

II. DATA

This thesis is designed to propose a technique for the reduction of satellite data; therefore, simulated data could be utilized. In order, however, to have a realistic input which reflects the variability of meteorological data, a representative sample of high resolution infrared radiation scans was employed. An example of a piece of actual data is shown in Table 1. An attempt was made to select individual scans which reflected different geographical areas, different synoptic cloud patterns, and different seasons. In addition, each inevestigator will, of necessity, perform the same tasks done here to arrive at graphs representing the characteristics of his own data. It will be pointed out in succeeding chapters that visual data is also adaptable to these techniques.

ACTUAL EXAMPLE OF RAW DIGITAL DATA

(Voltage Output Form)

672.27	676. 82	678. 54	681. 43	683. 18	683. 76	684. 35
683. 76	686. 70	686. 70	687. 88	687. 88	687. 88	689. 66
687. 29	690. 25	686. 70	689. 06	689. 66	687. 29	691. 44
687. 88	692. 04	689. 66	690. 85	691. 44	687. 88	690. 85
684. 93	688. 47	683. 76	686. 70	687. 88	687. 29	689. 66
687. 88	687. 88	686. 70	686. 11	685. 52	682. 01	683. 76
682. 01	679. 12	679. 12	676. 25	675. 68	675. 11	676. 25
678. 54	680. 27	685. 52	684. 93	690. 85	690. 25	693. 84
693. 84	692. 64	698. 08	694. 44	691. 44	686. 11	689. 66
687. 29	690. 85	691. 44	692. 64	694. 44	693. 84	698. 69
697. 47	697. 47	697. 47	698. 69	699. 91	696. 86	701. 14
696. 26	699. 91	696. 86	694. 44	701. 14	698. 08	698. 69
694. 44	699. 91	696. 26	701. 14	701. 14	699. 30	699. 91
697. 47	704. 23	697. 47	701. 14	699. 30	698. 69	699. 30
699. 91	699. 30	(100 words)				

Table 1

III. MATRIX REDUCTION TECHNIQUE

3.1 Procedure

The Matrix Reduction Technique involves taking the original raw data digital scan and dividing it into a number of equal partitions. The desired number of data points to be included in each partition will be part of the results of this thesis. The next step is to divide the ordinate into a discrete number of classes. The number of classes used will determine the amount of amplitude resolution loss and is discussed in Section V. Each data point is assigned to a class and loses its original value; see Figure 1. The final step is to total the number of events in each class, producing a "Number of Events Versus Class Table," and, in addition, to compute a "Transition Matrix" which depicts the number of transitions between consecutive data points from class 1 to class 1, from class 1 to class 2, etc. The final form of this reduction technique includes only these two items. The computer flow diagram and discussion for this technique is reproduced in the Appendix In addition, Table 2 is a simulated sample of the input and output associated with this procedure.

3.2 Characteristics

There are two characteristics of this technique which limit its

DEFINITIONS

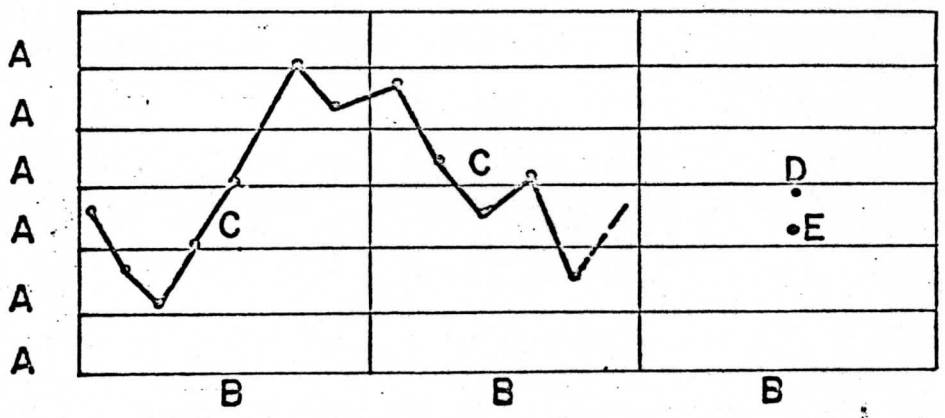

A: CLASS INTERVALS
B: PARTITION INTERVALS
C: DIGITAL RAW SCAN
D: TRUE DATA VALUE
E: ASSIGNED DATA VALUE

Figure 1

TABLE 2

DATA INPUT (ONE PARTITION)

049	044	045	046	044	048	046	048	047	049	049	050	053	056	058
062	064	070	070	072	070	071	069	064	066	062	066	067	067	074
071	076	072	075	073	067	066	061	058	054	055	055	057	063	066
069	072	074	072	074	075	075	072	075	072	075	070	073	072	071

CLASS DEFINITION

Range	Class
040-049	1
050-059	2
060-069	3
070-079	4
080-089	5
090-099	6

DATA OUTPUT

Class Versus Events Table

CLASS	1	2	3	4	5	6
EVENTS	11	9	15	25	0	0

Transition Matrix

From / To	1	2	3	4	5	6
1	10	1	0	0	0	0
2	0	7	2	0	0	0
3	0	1	11	3	0	0
4	0	0	2	22	0	0
5	0	0	0	0	0	0
6	0	0	0	0	0	0

Simulated Example: Matrix Reduction Technique

application. The first is a loss of amplitude resolution in that the data points are assigned to classes. An indication of the amount of resolution loss as a function of the number of classes utilized is discussed in Section V. This characteristic is not prohibitive, however, when one compares this technique to visual data schemes. The assignment of visible emitted radiation to a gray scale is essentially the same process. The second characteristic is a loss of order. As an analogy, one can take an English sentence and add the total occurrences of each letter and the frequency of transition from one letter to another. It will not then be possible to reconstruct the original sentence except under very special circumstances. One scheme was tried to reproduce the original order and is discussed in Section VI. This limitation is not important for certain applications and, in fact, the characteristics of the Transition Matrix are very valuable in certain instances.

3.3 Computer Storage Savings

Given one scan line, the number of computer words required is only a function of the number of partitions and the number of classes selected. The number of partitions selected will determine the number of data points within each partition. The number of computer words required for each partition will equal the number of classes (class versus events table) plus the square of the number of classes (Transition Matrix)*. The total number of storage words required for each partition

*Schemes utilizing one computer word for more than one datum are highly cumbersone at this stage of computer programming techniques.

is then the number of classes times the number of classes plus one. It is now apparent that if one wishes to increase the resolution by increasing the number of classes, the computer storage requirements increase as the square of the number of classes. Figure 2 depicts the percent of computer storage savings assuming a one thousand word input.

Since Figure 2 is based on a one thousand word input, one could transform the abscissa into words per partition in that five partitions implies two hundred words per partition, ten implies one hundred, etc. As could be expected, the percent savings is more sensitive to the number of classes than to the number of partitions since the savings is an inverse function of the number of classes squared and a linear multiple of the number of partitions. It could also be noted that in order to get exceedingly high resolution (large number of classes) it is necessary to have one thousand or more words per partition. If one is only interested in frequency of occurrence and persistence, the number of words per partition could be increased tremendously and resolution could be made as good as we please. For example: if one chose one million words per partition, he could select one hundred classes resulting in a ten thousand one hundred word computer storage requirement and saving roughly ninety-nine percent. Then, the proposed Advanced Technology Satellite input of 131 million bits of information would reduce to about 1.32 million bits and could then be handled by the large core computers. At the other extreme, the use of two classes (cloud

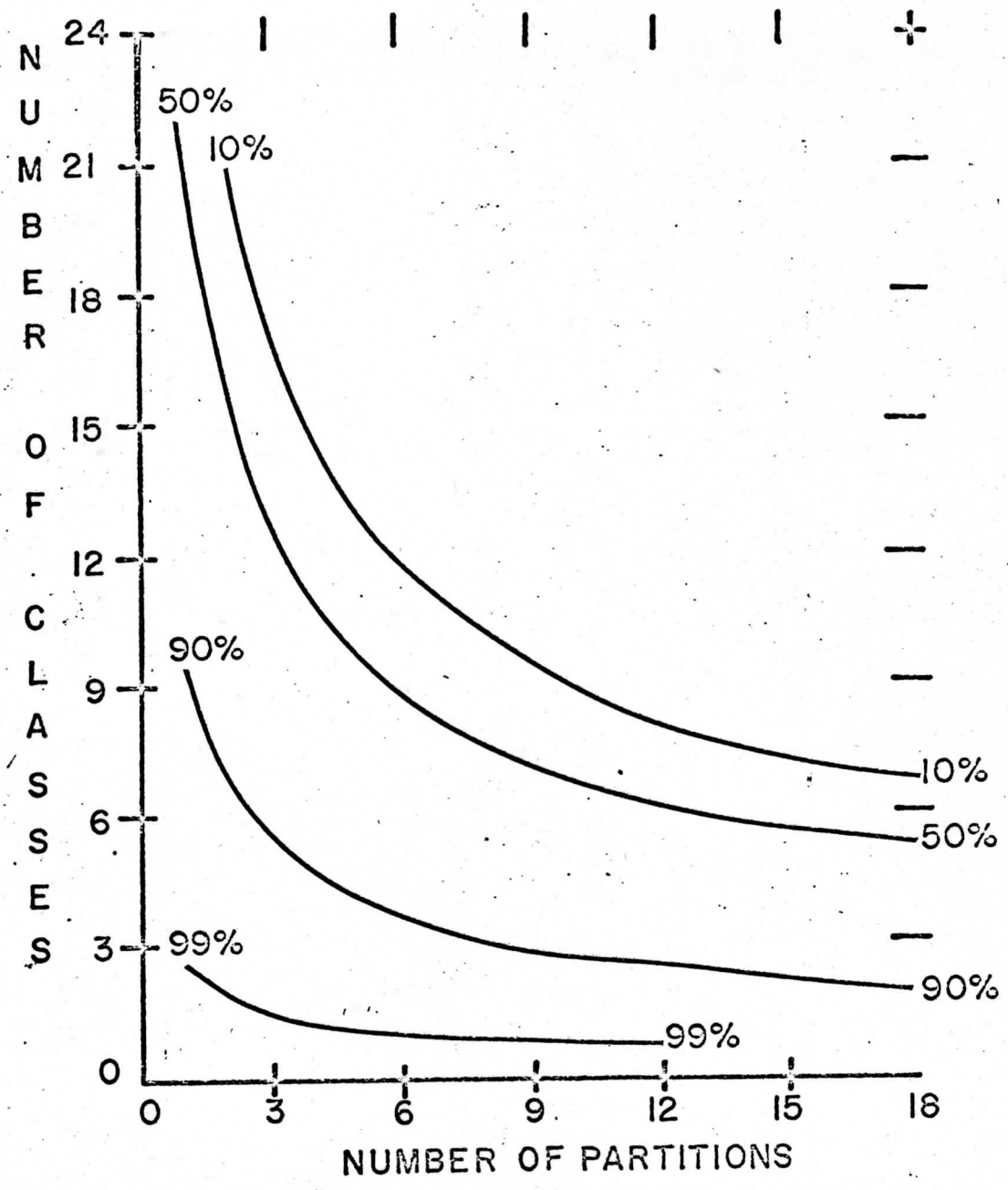

Computer Storage Savings: Matrix Reduction Technique

Figure 2

versus no cloud) and maintaining a ninety-nine percent data reduction, one could select two hundred thousand partitions and relate cloud frequency and cloud persistence between areas having six hundred bits apiece. The equation for the family of curves in Figure 2 is:

$$X = 1 - \frac{P}{N}(C^2 + C)$$

where: X is the decimal equivalent of the computer savings,

P is the number of partitions,

N is the number of input words,

and C is the number of classes.

IV. ORDERED REDUCTION TECHNIQUE

4.1 Procedure

The Ordered Reduction Technique was devised to retain the order that was lost in the Matrix Reduction Technique. One continues to lose amplitude resolution, however. The scheme is quite simple in that one again divides the ordinate into a discrete number of classes, assigning each data point to a class, but partitions are not required. The process is then to start at the left of the scan and count the number of events in the first class until encountering a transition. Then count the number of events in the new class until the next transition, and so on. The result will be paired arrays with the class identification in one and the number of events in the other. The computer flow diagram and discussion is also part of the Appendix. The same simulated input used for Table 2 and the output using this technique is shown in Table 3.

4.2 Characteristics

There is only one characteristic of this technique which limits its application: the loss of resolution. In neither technique were mean values ever used, but in both instances, class intervals were employed. The amount of resolution loss for a given number of classes will not necessarily be the same as the previous technique (see Section V).

DATA INPUT

049	044	045	046	044	048	046	048	047	049	049	050	053	056	058
062	064	070	070	072	070	071	069	064	066	062	066	067	067	074
071	076	072	075	073	067	066	061	058	054	055	055	057	063	066
069	072	074	072	074	075	075	072	075	072	075	070	073	072	071

CLASS DEFINITION

Range	Class
040-049	1
050-059	2
060-069	3
070-079	4
080-089	5
090-099	6

DATA OUTPUT

CLASS	1	2	3	4	3	4	3	2	3	4
EVENTS	11	4	2	5	7	6	3	5	3	14

Simulated Example: Ordered Reduction Technique

Table 3

4.3 Computer Storage Savings

Using this technique, given one scan line, the number of computer words required is a function of the number of classes used and the variability of the data. The only way one can determine the actual number of words required would be to apply the technique to a large volume of data using various numbers of classes. The process then is simply to count the number of class transitions and multiply by two, since the output is a pair of one dimensional arrays. This was accomplished using 248 scans averaging about 900 words per scan yielding 223,008 data points. The results are shown in Figure 3. The percent savings as a function of the number of classes can be directly compared with Figure 2.

The results of this study, as mentioned previously, constitute a direct indication of the variability of the data. Opposite extremes for the data sample are shown in Figure 3. The best and worst scans were defined by the total number of words required for 3, 6, 12, and 24 classes. In the best scan (dashed line), there must be few transitions between classes. The worst example (solid line) shows that with as few as three classes, one saves about one-third of the computer storage required for the original data, and ten classes or more require more storage than the original data.

In the best scan, for 24 classes there were only 120 transitions in 912 data points yielding an average of 7.6 data points between

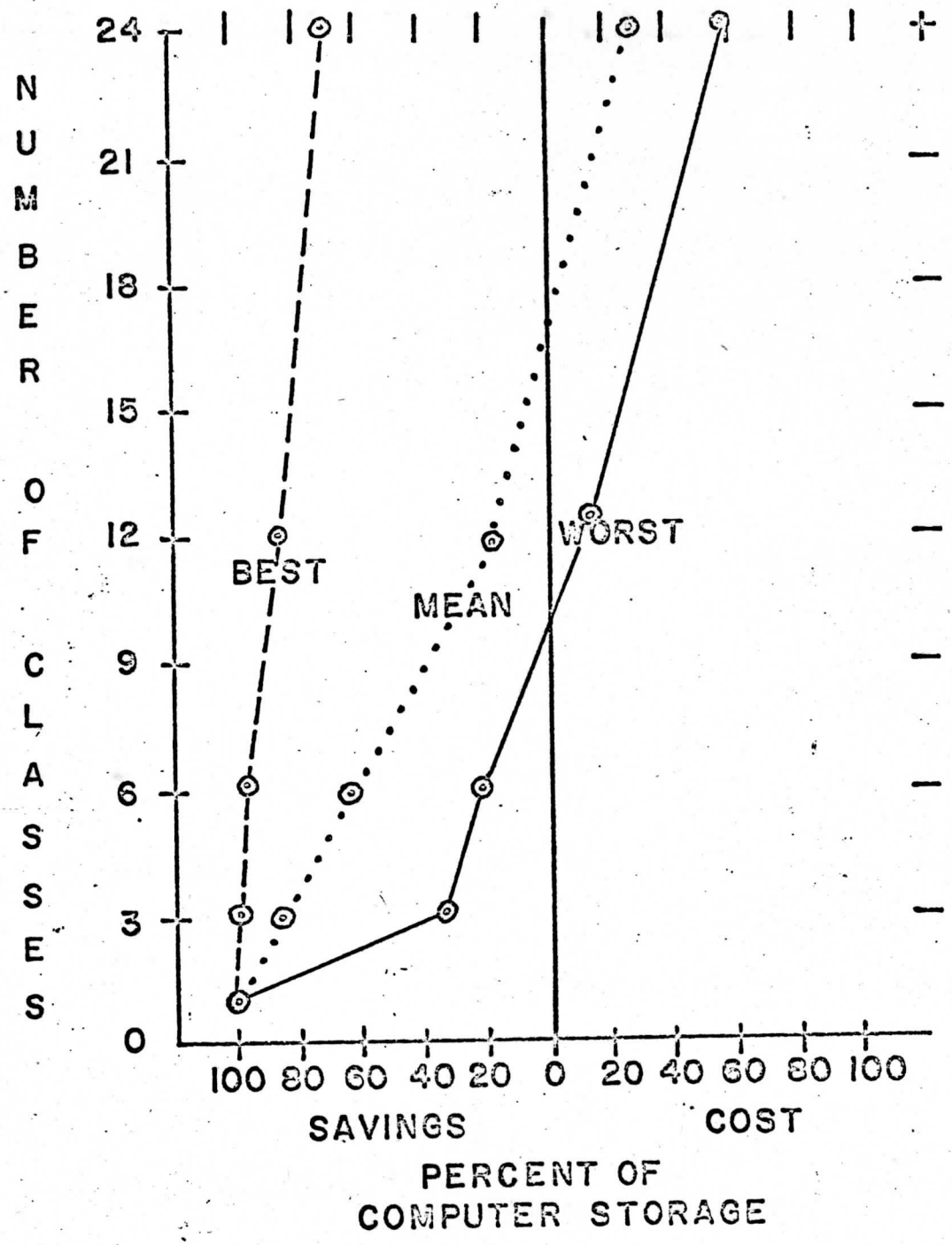

Computer Storage Savings: Ordered Reduction Technique

Figure 3

transitions. Compare this with the worst scan which averages 1.3 data points between transitions for 24 classes. This, then, leads to the topic of information theory. The best scan is a high ordered Markoff chain (especially for fewer classes) which implies low entropy and low information.* On the other hand, the worst example contains the most information since a high degree of freedom exists in the selection of classes.

If one had sufficient data for each latitude belt, each season and time, it would be possible to calculate the probabilities of occurrence of each class following a given class(es) and then compute the entropy of a typical radiation scan under specified conditions. Finally, it would be possible to eliminate sampling or recording data points for which the probability of occurrence approaches unity and again compress the volume of data.

The mean trace (dotted line) is almost linear up to twelve classes with the approximate equation: $X = -7.46C + 107.46$ where X is the percent savings and C is the number of classes. As a best approximation, linear extrapolation of the lower curve indicates that the Ordered Reduction Technique requires more storage than the original data when the number of classes exceeds fourteen.

---

*See Shannon (1949) for a treatment of information theory.

V. THE RESOLUTION LOSS PROBLEM

5.1 General

One of the arguments against the use of the proposed techniques is the loss of amplitude resolution. The amount of resolution loss will be a direct function of the number of classes used, since a large class interval implies a greater error from the true value. We cannot assume that the data points are normally distributed within the range and utilize statistical techniques to analyze the errors. The simplest argument would be to assume a uniform distribution within the range and each class such that all values within the class have equal probabilities. In such a case, the mean deviation of the true value from the assigned value (class mid-point) would be plus or minus the class width divided by four. Then, quite simply, if we double the number of classes (halve the class width) we would reduce the mean deviation by a factor of two.

5.2 Specific

A study was performed on the data by taking a random sample of data groups from the whole and finding the mean deviation. For this purpose, 63,083 data points were analyzed. The entire data range was not used for fear of biasing the results, since the lowest and highest temperatures would be uniform enough to provide a consistent mean

deviation which doesn't exist in most meteorological data. Therefore, the data was arbitrarily stratified to include the middle portion of the data range which is limited to cloud characteristics. The portion studied had five thousand possible data values in the sub-range. In interpreting the results, one divides five thousand by the number of classes to arrive at the possible data values within the class. The results obtained on this data are shown in Figure 4. In this example, one unit of resolution loss is equivalent to one unit voltage change, which is equivalent to approximately a 2°K temperature change within the range used.

As expected, the plot in Figure 4 is asymptotic on both ends. The resolution loss decreases sharply as the number of classes increases from two. At the other extreme, very little resolution loss improvement is realized above twelve classes. The theoretical curve (class width divided by four) is not plotted, since it nearly coincides with the actual plot. The deviation from the theoretical assumption is in the third decimal place for 8, 12, 18, and 24 classes, and in the second decimal place for 4 and 6 classes. When the resolution loss due to the limited number of classes is less than the error range inherent in the instrumentation and digitizing processes, one need utilize no greater number of classes since it won't improve the final product.

Nordberg (1965) has stated that blackbody temperatures derived from Planck's Law using Nimbus I HRIR data are generally within 2°K, which is commensurate with the error inherent in the measurement of

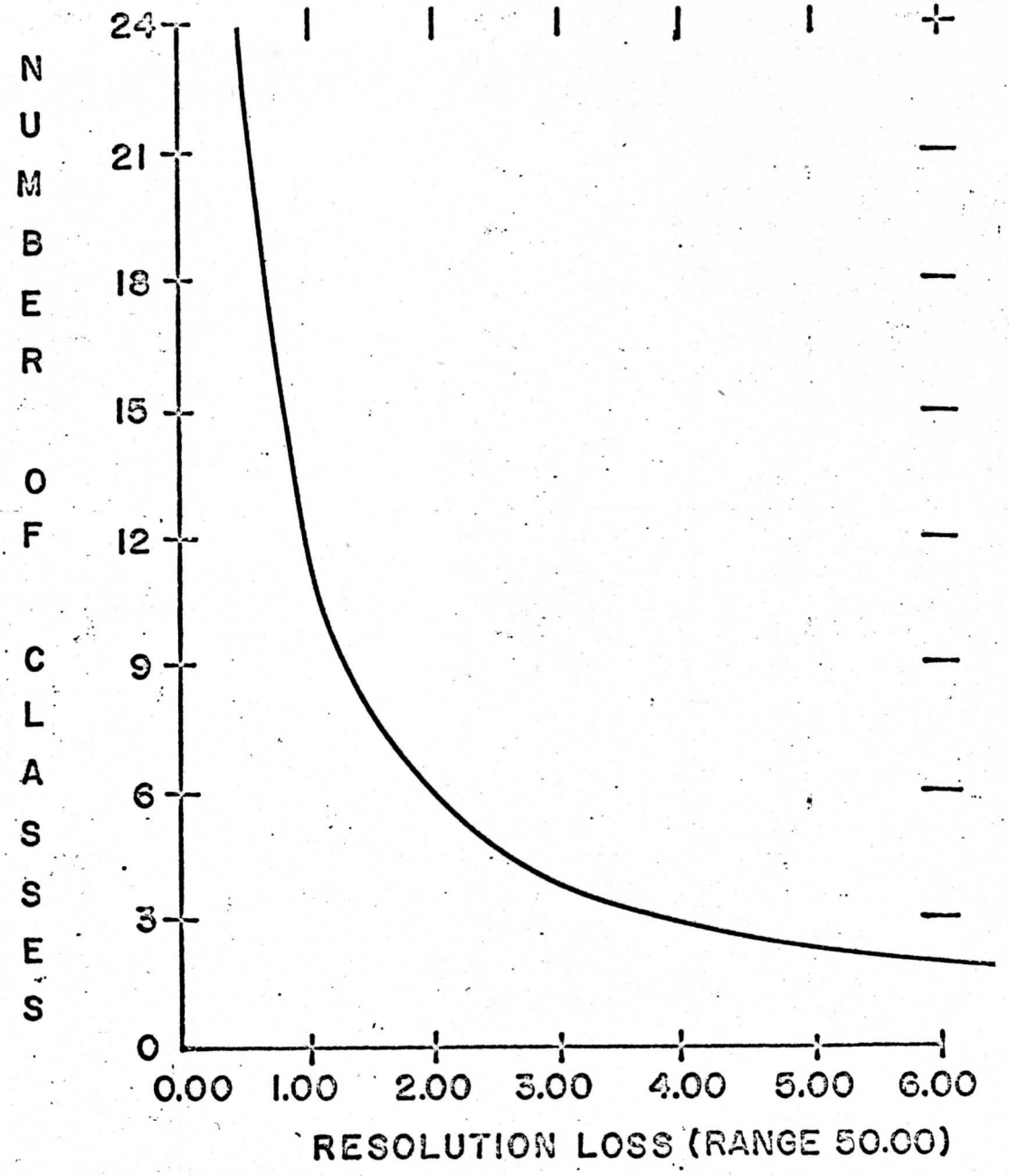

Resolution Loss: Class Mid-point

Figure 4

the intensity of radiation emitted. Analogue to digital conversion error can be neglected, since the time span over which the analogue is integrated can be adjusted to the point that the error is one to two orders of magnitude less than the instrumentation and temperature calculation errors. Comparison with Figure 4, then, indicates that one unit of resolution loss in within the error span mentioned above and occurs at class numbers of twelve or more. Twelve classes can now be considered to be the upper limit in class selection since further improvement is meaningless.

5.3 Improvements

An attempt was made to improve the resolution loss previously treated. The only way one can restore absolute values to the data is to select a number of classes equal to the number of possible data values. This, however, requires more computer storage in both techniques than required for the original data. The proposed improvement scheme will differ slightly for each technique but the idea is the same. It involves replacing the class number with the mean of all data points within the class and computing deviations from this mean instead of from the class mid-point. Table 4 depicts the output for the improved techniques using the same input as Tables 2 and 3.

Definite improvement should be realized in those instances which only have a few data points within the class which all lie in the lower class quarter, for example. The results will differ in the two

MATRIX REDUCTION TECHNIQUE

FROM/TO	46.82	55.11	65.27	72.64	*	*
46.82	10	1	0	0		
55.11	0	7	2	0		
65.27	0	1	11	3		
72.64	0	0	2	22		
*						
*						

ORDERED REDUCTION TECHNIQUE

CLASS	46.82	54.25	63.00	70.60	65.86	73.50	64.67	55.80	66.00	73.00
EVENTS	11	4	2	5	7	6	3	5	3	14

RESOLUTION LOSS

Theoretical mean deviation (class width divided by four)	2.50
Mean deviation from class mid-point	2.23
Mean deviation of improved Matrix Reduction Technique	1.77
Mean deviation of improved Ordered Reduction Technique	1.58

Improved Output and Mean Deviations

Table 4

techniques since in the Matrix Reduction Technique, one computes the mean for all values within a particular class for the entire partition. The Ordered Reduction Technique will utilize mean values for each class between transitions only. For example, in the Matrix Reduction Technique, a mean value will be computed for all data points per partition which fall into class 5, whereas, in the Ordered Reduction Technique, a new mean value will be computed for class 5 each time one encounters the class. One would suspect, then, more improvement in the latter technique. The percent improvement in resolution loss over the mid-point assumption is shown in Figure 5. The Matrix Reduction Technique loss improvement is labeled MRT and Ordered Reduction Technique loss improvement is labeled ORT.

The improvement for the Matrix Reduction Technique decreases from 31% for two classes to 8% for six, then decreases slowly and remains less than 10%. Since the mid-point deviations are so close to the theoretical distribution deviation, the only place one can expect improvement is in the highest and lowest classes of occurrence since the data values will most likely be near the class boundary. The opposite is true for the Ordered Reduction Technique improvement. The percent seems to be independent of the number of classes (remaining in the forties) until one exceeds eight classes. Above eight classes, improvement increases to near 70% at 24 classes. This is due to the fact that the number of elements within a given class between transitions is decreasing and will eventually reach the point at which an individual

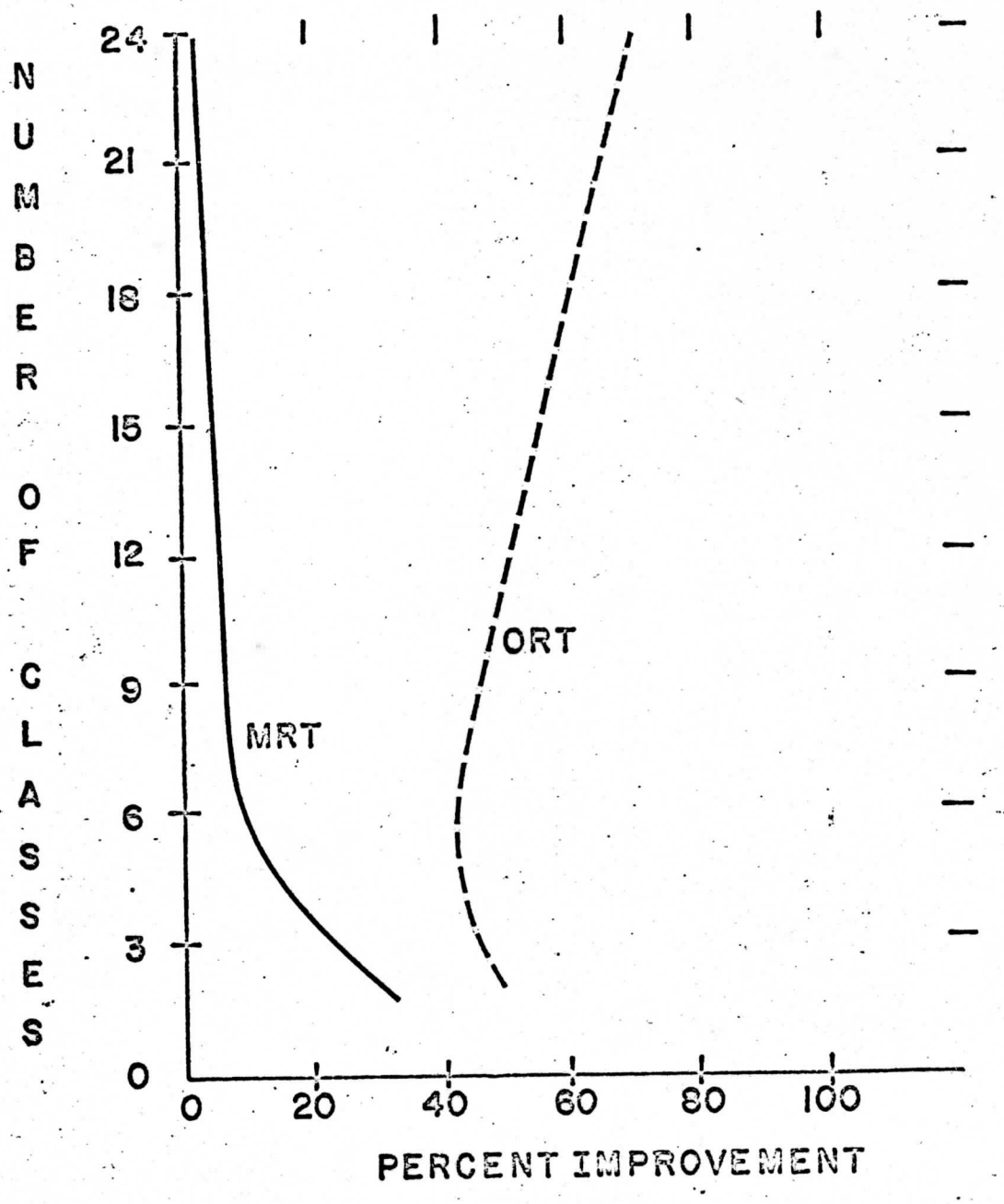

Resolution Loss Improvement

Figure 5

data point will be the only occurrence in the class and the mean deviation will be zero. Therefore, the best resolution for a given number of classes can be obtained by using the improved Ordered Reduction Technique. As pointed out in Section 5.2, one unit of resolution loss (about 2° K) is the optimum since further improvement is meaningless. For the improved Ordered Reduction Technique, this occurs with eight classes as opposed to the twelve required for the mid-point technique. The Ordered Reduction Technique with eight classes saves approximately 48% computer storage. This allows even more reduction in computer storage since fewer classes will suffice.

This improvement in resolution loss, however, requires a trade-off in computer time. It obviously takes more time in the computer to calculate means for each class than to simply count events within a class. The increase in resolution, then, must be paid for by increased time which may limit its application in a real time situation. Each investigator is now faced with a trade-off in storage savings, amplitude resolution loss, order loss, and real time.

VI. THE ORDER LOSS PROBLEM

6.1 General

It was indicated in Section 3.2 that it is very difficult if not impossible to reconstruct exactly the original digital scan from the output of the Matrix Reduction Technique. This particular characteristic limits its use for some applications, but much information content is retained. Some of the more important applications of this technique are noted in Section VII. This section will concern itself with an attempt to reconstruct the original digital scan, keeping in mind that this problem does not exist in the Ordered Reduction Technique.

6.2 Procedure for Reconstruction

Referring to Table 2 as an example, several rules will be used to attempt the reconstruction of the Data Input from the Transition Matrix and the Class Versus Events Table.

The first step is to select the beginning and terminating values by adding the rows and columns of the Transition Matrix and comparing the results with the Class Versus Events Table. From the example, "To" a "1" is lacking, indicating class 1 is the initial value and "From" a "4" is lacking, indicating class 4 is the terminating value.

The second step is to determine the slope of the digital scan by comparing beginning and terminating values. Thus, low transitions

will be reconstructed on the low side and vice-versa, and symmetry will reign when the slope is zero. If symmetry will not solve the zero slope problem, low transitions were arbitrarily chosen to the left.

The third step is to determine the segment lengths within each class. If one subtracts the class X to class X transitions (Persistence) from the total number of events in class X, he will arrive at the discrete number of occurrences of that class. This number divided into the total number of events in that class yields the mean width of each class occurrence. The result, however, must be an integer value; therefore, the closest combination of integers is used, using symmetry again to place odd values and placing low values on the left when symmetry does not solve the problem. In the example in Table 1, the results for class widths would be:

class 1: 11

class 2: 4, 5

class 3: 4, 3, 4, 4

class 4: 8, 9, 8

The reconstruction is now simple. Beginning with class 1, make it 11 units long, then class 2 for 4, class 3 for 4, class 2 for 5, class 3 for 3, class 4 for 8, class 3 for 4, class 4 for 9, class 3 for 4, and class 4 for 8. The reconstructed trace and the original trace are shown in Figure 6.

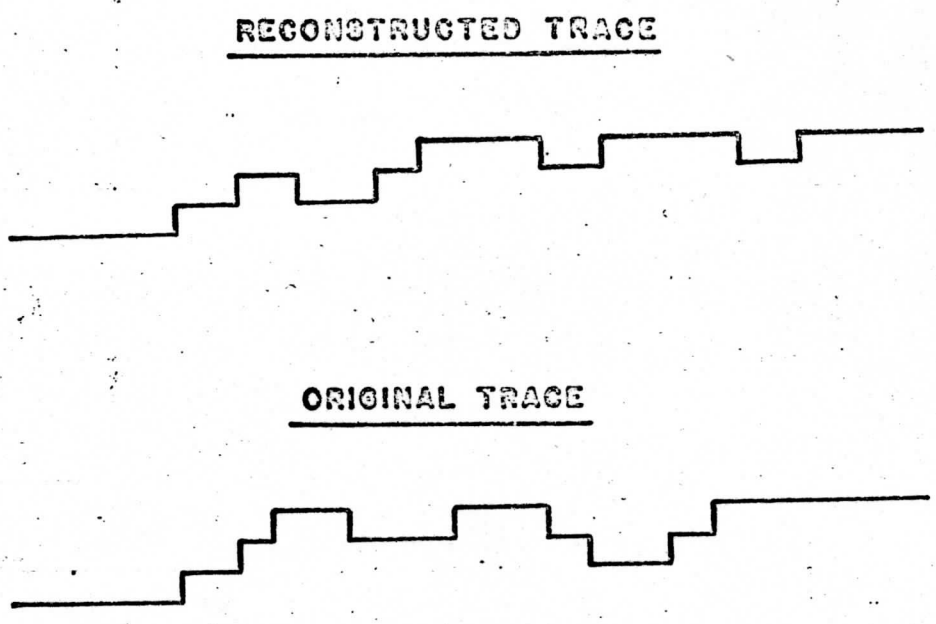

Reconstructed and Original Traces: Matrix Reduction Technique

Figure 6

6.3 Comparison

The correlation coefficient for the two scans in Figure 6 is .738, allowing a 45.5% loss of variance. Other attempts were made, but the correlations were not high and the results are not included.

The significance of the reconstructed trace, however, is not associated with the exactness of the reproduction. The significance lies in the characteristics of the reconstructed trace. A trained analyst should generally be able to describe the cloud conditions from the reconstruction, although orientation will not necessarily exist. It would be my judgment that the trace in Figure 6 depicts multilayered clouds possibly with some build-ups or patches of altocumulus with a clear patch to the left.

VII. COMPARISON AND APPLICATIONS

7.1 Comparison

The output in the Ordered Reduction Technique is basically the original scan in compressed form. The price paid for the compression is a limited loss in amplitude resolution which can be controlled by the selection of classes. More classes, however, save less storage and require more time.

The output in the Matrix Reduction Technique loses orientation in the original scan, but it retains percent cloud cover, percent cloudiness at various levels, average cloud element size, and cloud top heights. Resolution does not improve considerably when one uses the mean values instead of class mid-point; thus twelve classes is the minimum number that keeps the loss within the error range of the data as opposed to eight classes for the improved Ordered Reduction Technique.

The size of data groups to be studied as an entity will determine which technique will save more storage. As a rule, for a given number of classes, large data groups (partitions) should be treated by the Matrix Reduction Technique and small groups by the Ordered Reduction Technique. As the number of classes decreases, the size of data group which should be treated by the Matrix Reduction Technique to save the most storage will also decrease.

Table 5 depicts a typical decision process associated with these

DECISION TREE

Determine

1) Amount of raw data input
2) Percent savings desired
3) Resolution required
4) Size of data groups
5) Time limitation

(A) ASK

ORT——YES——Is Order Required——NO——EITHER

(RE)DETERMINE Resolution limit - Fig 4	(B)		(B)	(RE)DETERMINE Resolution limit - Fig 4
YIELDS Minimum number of classes	(C)		(C)	YIELDS Minimum number of classes
			(D)	DETERMINE Size of data groups
DETERMINE Storage savings Figure 3	(E)		(E)	DETERMINE Storage savings Figures 2 and 3
ASK Does it meet Requirement	(F)	YES	(F)	ASK Does it meet Requirement
NO		STOP		NO
ASK Time limit prohibitive	(G)		(G)	ASK Time limit prohibitive
YES				YES
NO 1st loop only				NO 1st loop only
DETERMINE Improved resolution limit	(H)		(H)	DETERMINE Improved resolution limit

Table 5

techniques. Assume the following example: an investigator desires to run a climatological study by longitude and latitude. He must first determine his input parameters. His restrictions are: 1) raw data is 100 million words, 2) the computer can handle 2 million words, requiring a 98% reduction, 3) the desired resolution loss is established to be four parts per hundred, 4) he wants to study 1° X 1° as a group requiring about 1000 words per partition, and 5) the job is non-operational, thus having no time limit. Referring to Table 5, at step A, it is determined that order is not required, and proceed to step B in the right hand column. It is now determined that four parts per hundred is our limit and Figure 4 limits us to 6 classes for this desired resolution. At step D it is recalled that 1000 words per partition is necessary. At E, Figure 2 yields a 96% savings of storage and Figure 3 yields 62%, which does not meet the requirement at step F. Since time is no restriction, proceed to step H where Figures 4 and 5 will now allow 4.32 parts per hundred for the Matrix Reduction Technique and 5.60 parts per hundred resolution loss for the Ordered Reduction Technique. Returning to step C, the Matrix Reduction Technique still only allows 6 classes, while the Ordered Reduction Technique allows 4. The savings at step E are now 96% and 80%, respectively, which still isn't good enough. In an attempt to find a trade-off, it is determined that a resolution loss limit of six parts per hundred will allow four classes for the Matrix Reduction Technique, and the savings is now exactly 98%.

7.2 Applications

Several general applications for these techniques will be discussed in the succeeding paragraphs. It is not intended that all applications will be discovered or treated, and the order of discussion does not imply any relative importance.

a) Archiving and Editing

One of the important characteristics of the two techniques is that one is able to transform the Ordered Series into the Transition Matrix, but not vice-versa. In addition, the improved Ordered Series has the best resolution loss rate; therefore, archiving should be accomplished using the Ordered Reduction Technique. On the other hand, it is my opinion that it is faster and easier to get a mental image of the cloud distribution from the Transition Matrix, and I recommend it for editing purposes.

b) Climatology

It is not necessary to treat data as individual scans as done here. It would be just as easy to investigate pieces of adjacent scans to study an area. The Matrix Reduction Technique is recommended for climatological studies, since one could select latitudinal, longitudinal, or hemispheric partitions and compile cloud cover as a function of tops (e.g., four classes: surface, low, middle, and high) for various geographical areas.

c) Time Variance Analysis

If one uses either the Transition Matrix or the Ordered Series for a given area on the earth, he could investigate the time variance of either of these outputs to ascertain development, decay, or motions of clouds.

d) Cloud Interpretation

Several investigators including Conover (1962) and the Budd Company (1964) have tried to subjectively solve the problem of interpreting cloud genera from satellite photographs. Others (Katz and Doyle, 1964) have tried objective techniques. It would seem that characteristic cloud types as recognized on the synoptic scale will be associated with discrete and different Transition Matrices. One would need to investigate the most beneficial number of classes to utilize, and the size of partitions (average scale size of homogeneous cloud types), and then determine whether a particular characteristic of the Transition Matrix could be related to a specific cloud type. The Transition Matrix of infrared data contains information as to the average size of cloud elements, the frequency of transition to and from the elements, the percent cloud cover, and the heights of the cloud tops. Some ambiguity may exist, but it would be a step toward completely objective cloud classifications. Visual data could be adapted to this technique; however, brightness would have to be used in lieu of temperature of the tops.

The discussion of a completely objective cloud classification scheme leads to the concept of a completely objective nephanalysis.

In this instance, one is only concerned with the boundaries around homogeneous cloud types and the specific cloud type within the boundary. It is unnecessary to treat equal and arbitrary partitions as done previously. The process involved would be to analyze the first finite number of data points with the Matrix Reduction Technique and then the next adjacent group. Comparison of the results should indicate, with an established set of limits, whether one has changed cloud type. If not, add the first two groups together and proceed in this manner until a different characteristic cloud type is encountered. Then, by identifying the boundary, one has arrived at one partition which includes only one cloud type and its boundary. By the extension of this technique, it would be possible to objectively construct a map depicting homogeneous cloud mass boundaries each of which have been identified.

Other applications are, of course, possible. The intention here was to point out that the schemes were not investigated for the sake of statistics, but that immediate meteorological applications are available.

VIII. CONCLUSIONS

This paper has examined two different statistical reduction techniques as to their procedures, characteristics, and computer storage savings with the following results:

1. Both techniques can provide considerable computer storage savings.

2. Neither technique is always better than the other with respect to computer storage savings.

3. The amplitude resolution loss can be kept within the instrumentation error of the instrument with as few as eight classes.

4. The Ordered Series can be transformed into the Transition Matrix, but not vice-versa.

5. Immediate meteorological applications exist.

6. There exists a need to investigate correlation between cloud types and Transition Matrices for an objective cloud classification scheme and its extension, an objective nephanalysis.

APPENDIX

COMPUTER FLOW DIAGRAM FOR BOTH REDUCTION TECHNIQUES

For the purpose of this flow diagram, certain assumptions will be made:

1) Data is on record in the computer memory.

2) The data will be divided into a specified number of partitions and for each partition, an incidence analysis will be performed over a specified number of classes.

3) The real values of level changes will be provided.

In addition, certain definitions are required:

1) DATA Data record in floating point representation.

2) N Length of DATA in words.

3) NP Number of partitions.

4) M Number of classes.

5) PART An array of partition points within the array DATA, specifying the exact indices to be used in working with the individual partition. This array is dimensioned for NP plus 1 indices in order to contain the initial and terminating indices for the record.

6) RANGE The array of classes to be used in examining incidence of occurrence over frequency levels. For this purpose, RANGE is an M minus 1 dimensioned array subsequently allowing the initial and terminating classes to be open ended. To eliminate the problem of class intervals of different sizes caused by this procedure, the data can be filtered to remove values outside of a maximum-minimum range. Thus, in testing for an element's position on the scale, we will be using two open ended classes, realizing, however, that we have artificially specified upper and lower limits.

7) BIN Frequency table of a given partition.

8) TRAN Transition matrix for a given partition.

9) ORDER Ordered transition table for a given partition dimensioned 2N to allow for the least probable case of every next element changing classes. The arrangement of this array is as follows:

   a) All odd points in the array ORDER contain 1, 2, 3, . . . , M designating which class the present group of elements fall into.
   b) All even points contain the number of consecutive elements within a given class.

With this background, Figure 7 provides the computer flow diagram used for both techniques.

FLOW CHART

Frequency Table, Transition Matrix, Ordered Transition Table
For a Given Partition K

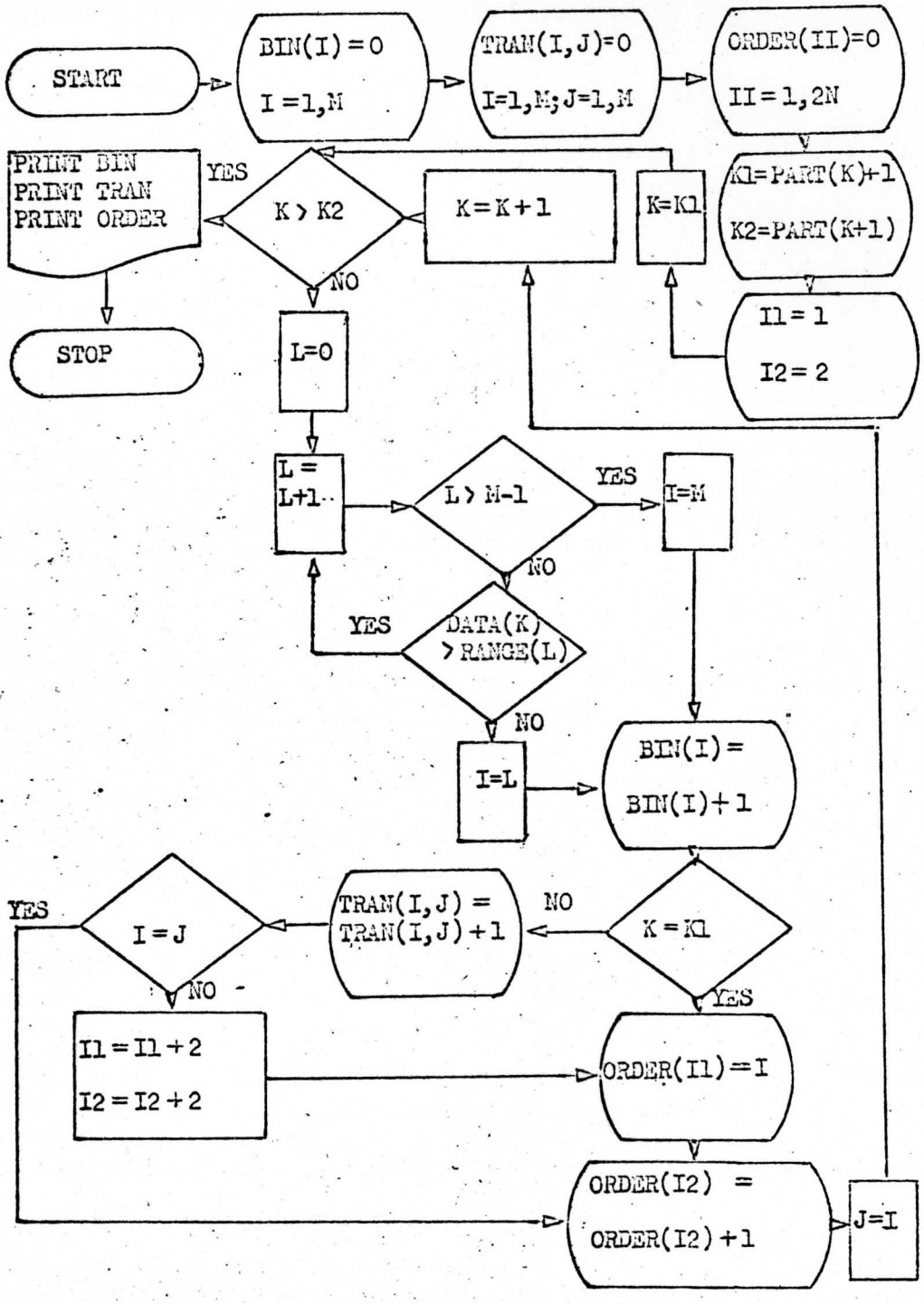

Figure 7

REFERENCES

Anonymous, Final Report for a Study of Cloud Patterns as Seen by Meteorological Satellites, Information Sciences Center, The Budd Company, Oct 30, 1964.

_____, Nimbus I High Resolution Radiation Data Catalogue and User's Manual, Aeronomy and Meteorology Division, Goddard Space Flight Center, Jan 15, 1965.

Conover, J., Cloud Interpretation from Satellite Altitudes, Research Note 81, Air Force Cambridge Research Laboratories, July 1962, and Supplement 1, May 1963.

Glaser, A. H., Meteorological Utilization of Images of the Earth's Surface Transmitted from a Satellite Vehicle, Blue Hill Meteorological Observatory, Oct 1957.

Katz, Y. H., and W. L. Doyle, Automatic Pattern Recognition of Meteorological Satellite Cloud Photography, The Rand Corporation, Dec 1964.

Kern, C. D., Evaluation of Infrared Emission of Clouds and Ground as Measured by Weather Satellites, Environmental Research Paper 155, Air Force Cambridge Research Laboratories, Nov 1965.

Nordberg, W., The Nimbus I Meteorological Satellite-Geophysical Observations from a New Perspective, Goddard Space Flight Center, May 1965.

Shannon, Claude E., and Warren Weaver, The Mathematical Theory of Communication, The University of Illinois Press, Urbana, 1949.

Widger, W. K., Jr., A Generalized Schematic Flow Chart for the Reduction and Processing of Satellite Meteorological Data, Research Note 36, Air Force Cambridge Research Laboratories, June 1960.

AN EVALUATION OF LIMB DARKENING IN THE 8-12 MICRON ATMOSPHERIC WINDOW

by

RICHARD ELLIOTT SMITH

ABSTRACT

A technique for measuring the limb darkening effect is described. Twenty-two data sets were analyzed with this technique to obtain the limb darkening curves for four conditions: tropical land, tropical water, tropical cloud, and mid-latitude land. These curves were then compared with observed limb darkening curves from Tiros data and with theoretically calculated limb darkening curves.

TABLE OF CONTENTS

I. INTRODUCTION

The interpretation of infrared radiation measurements obtained by an earth satellite depends on our knowledge of the constituents of the atmosphere between the satellite and the radiating source and their effects on the upward radiation. In the spectral range of infrared emission the intensity of the upward radiation depends on the vertical temperature and pressure profiles and on the distribution of the absorbing and emitting matter in the atmosphere. Water vapor, ozone, and carbon dioxide have strong absorption bands in this range. Droplets, ice crystals, dust, and aerosols have effects on the infrared radiation also.

In order to determine the effects of the atmosphere on upward radiation, several authors have evaluated the radiance of the earth and the atmosphere within particular wavelength regions. Some of these studies were done specifically to determine the most suitable spectral region for horizon sensors. The spectral regions usually considered are the water vapor band at 6.3 microns, the ozone band at 9.6 microns, the atmospheric window at 11 microns, the carbon dioxide band at 15 microns, and the rotational water vapor band from 21 to 125 microns. These studies have shown that the 15 micron carbon dioxide band and the rotational water vapor band are best suited for horizon sensors (Wark, 1963). The atmospheric window also has a very sharp horizon

in the absence of clouds, but the radiance in this spectral region is subject to large variations due to local meteorological effects, and so its use as a horizon sensor is limited. The spectral radiance of the earth with various model atmospheres has been calculated by Wark, Yamamoto, and Lienesch (1962), Kondratiev and Yakushevskaya (1962), Hanel, Bandeen, and Conrath (1963), and Wark, Alishouse, and Yamamoto (1963). The spectral bands considered by each of these authors vary slightly but include the five spectral bands previously mentioned. The results are usually presented as curves of limb darkening (or brightening). In an atmosphere where temperature decreases with height, the measured intensity of upward radiation decreases as the zenith angle at the radiating source increases. Limb darkening then is defined as the ratio $I(\theta)/I(0)$, the ratio of the intensity of upward radiation at zenith angle θ to the intensity of upward radiation at a zenith angle of zero. Limb darkening is given as a function of θ and is a quantitative measure of the atmospheric effects on upward radiation.

In an attempt to confirm the theoretical calculations of the upward radiance, Tiros data from the Medium Resolution Infrared Radiometer were used by Larsen, Fujita, and Fletcher (1963), Bandeen, Conrath, and Hanel (1963), and by Wark and Lienesch (1964) to obtain the observed limb darkening.

Larsen et al. obtained the limb darkening in the 8 to 12 micron atmospheric window (channel 2, Riros III) using data over the Sahara.

Their results are in substantial disagreement with the calculations of Wark (1962) and the statistical analysis of Wark (1964) (Fig. 1). In the technique used, Larsen et al. made use of the fact that some areas on the earth are scanned twice by the radiometer within a few minutes. These pairs of measurements, one with a large zenith angle and one with a small zenith angle, were combined to form the limb darkening curve. Radiation values at zenith angles less than 30 degrees could not be obtained in pairs, so the assumption was made that no limb darkening exists for zenith angles less than 30 degrees. It was suggested that dust particles may have caused the large deviations from the theoretical values.

After Tiros VII was launched in June 1963, it became possible to compare observations in a different spectral range with theoretical calculations. Channel 1 was sensitive within the 15 micron carbon dioxide band. The preliminary data reduction (Bandeen, Conrath, and Hanel, 1963) showed good agreement between the observations and the theoretical calculations in that a small amount of limb brightening was observed.

Wark (1964) showed that observed limb darkening is greater than the earlier calculations of Wark (1962). This was attributed to partly transparent clouds and geometrical factors in partly cloudy areas. Latitude dependence of limb darkening was found to be small. The results of the analysis was an empirical equation:

$$I(\theta) = I(0)[1 - 6.16 \times 10^{-4}\theta + 9.355 \times 10^{-6}\theta^2 - 4.32 \times 10^{-7}\theta^3] \quad (1)$$

where θ is the zenith angle in degrees (Fig. 1).

It seems desirable to continue comparison of observed with theoretical values of limb darkening. The window region has many practical meteorological uses such as the determination of cloud-top temperatures and sea and land temperatures. An accurate determination of these and other parameters requires that limb darkening corrections be applied to the data. The purpose of this paper is to illustrate a method of observing limb darkening and to compare the observations with the theoretical calculations. This method has eliminated several restrictions imposed by the Tiros data and should yield a more accurate observation of limb darkening in the 8-12 micron spectral region.

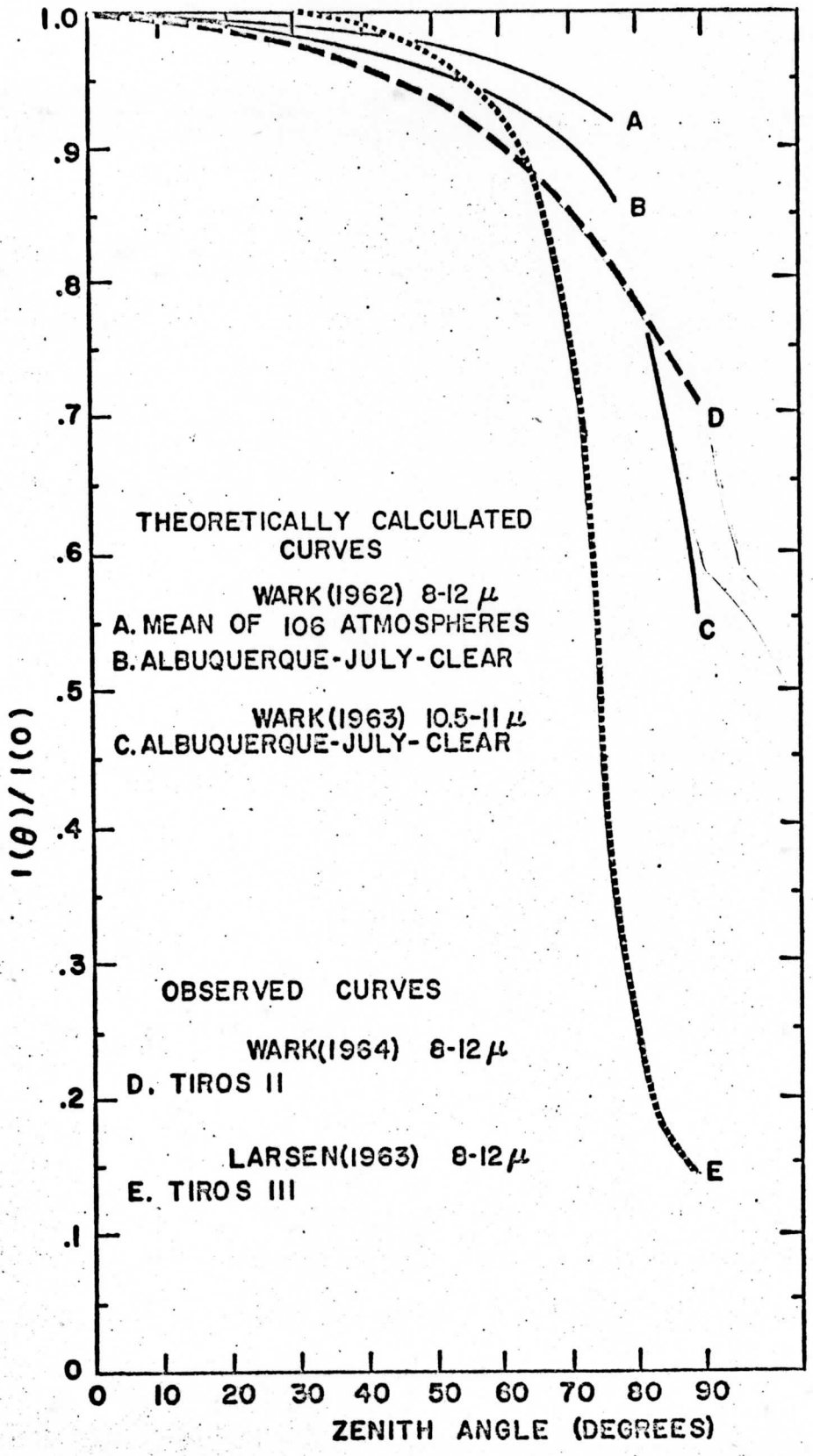
1.0
.9
.8
.7
.6
.5
.4
.3
.2
.1
0
I(θ)/I(0)
0
10
20
30
40
50
60
70
80
90
ZENITH ANGLE (DEGREES)
A
B
C
D
E
THEORETICALLY CALCULATED CURVES
WARK (1962) 8-12 μ
A. MEAN OF 106 ATMOSPHERES
B. ALBUQUERQUE-JULY-CLEAR
WARK (1963) 10.5-11 μ
C. ALBUQUERQUE-JULY-CLEAR
OBSERVED CURVES
WARK (1964) 8-12 μ
D. TIROS II
LARSEN (1963) 8-12 μ
E. TIROS III

Figure 1

II. THE TECHNIQUE OF OBSERVATION

The basis of the technique used here is essentially the same as that used by Larsen et al., that is, to observe the intensity of radiation from a point on the earth at different zenith angles. One difficulty with the Tiros data is that the radiometer can observe the same point only twice due to the scanning geometry (Fig. 2). This, of course, made it impossible for the satellite to view an area all the way from the sub-satellite point to the limb of the earth. The second difficulty was the large field of view of the radiometer, approximately 5 degrees at the half-power points. Corrections for space viewing and the changing size of the scan spot were made on the data.

A radiometer that viewed the same spot on the earth from all zenith angles and at higher resolution than the Tiros instrument should be capable of an accurate determination of limb darkening. Such a system would be available if a sensor were mounted such that the sensor's field of view is perpendicular to the spin axis of a satellite operating in the "wheel mode." Then the radiometer would "look" in the orbital plane of the satellite and would be capable of viewing the same area from all zenith angles.

Horizon sensors are essential elements in the orientation systems and timing mechanisms of most space vehicles and satellite systems. The data for this study were taken from a horizon sensor operating in

the manner just described and illustrated in Figure 3. While this system has definite advantages over the Tiros system, there are several factors to consider. Due to the earth's rotation, even this system does not view exactly the same area from scan to scan. As the satellite moves in its orbit the earth rotates from west to east under the satellite and the scan lines do not overlap but are displaced east to west from each other. The displacement of a scan line from the adjacent scan line is a function of latitude and the time interval between scans. This time interval is equal to the period of revolution, (P), of the satellite about its spin axis. The time interval between data samples, (Δt), is then an integer multiple of P. The displacement between data scans, (Δx), is equal to $v(\phi)$ times Δt where $v(\phi)$ is the tangential velocity of the earth as a function of latitude. A schematic of the data scan geometry is shown in Figure 4. As an example, in Figure 4, during the interval of time required for the satellite to move from its initial position as shown in the figure to position T_5, the Earth will rotate west-to-east and the area of the Earth T_5 will have rotated to and be coincident with the sub-satellite track. The satellite, at position T_5, will then scan the area of the Earth T_5. At the equator, where the displacement is a maximum, the total displacement between the first and fifth scans is approximately 120 nm. At 40 degrees latitude the total displacement is approximately 90 nm. By careful selection of data and areas viewed we can assume that the area between the first and fifth scans is in fact homogeneous and that we are not introducing errors

caused by variations in the radiating surface.

The second factor to consider is the roll and yaw errors in the orientation of the satellite. If there are any significant roll or yaw errors the technique cannot be used, since the satellite will not "look" in the orbital plane and will be unable to view the same area on the earth from successive satellite positions. Roll errors will cause the sensor to "look" to the left or right of the sub-satellite track, and yaw errors will cause the satellite to "look" across-track.

The last factor to consider is the effect of variations in the size of the scan spot on the measured values of radiation. As the scan spot moves from the sub-satellite point to the limb, its size increases considerably and the measured radiation is an integrated value over the scan spot. If the scan spot at the limb contains areas colder than the area observed at zero zenith angle a limb darkening effect is present even without an intervening atmosphere. Similarly, a limb brightening effect is present if the scan spot at the limb contains areas warmer than the area observed at zero zenith angle. Rather than try to correct for such effects, the effect itself is eliminated by selecting homogeneous areas that are large enough to fill the field of view of the sensor even at the limb. Measured values of radiance from the earth near the limb cannot be obtained for zenith angles approaching 90 degrees since the sensor starts to view the atmosphere and space. This effect could not be eliminated but corrections for it were made and will be discussed later.

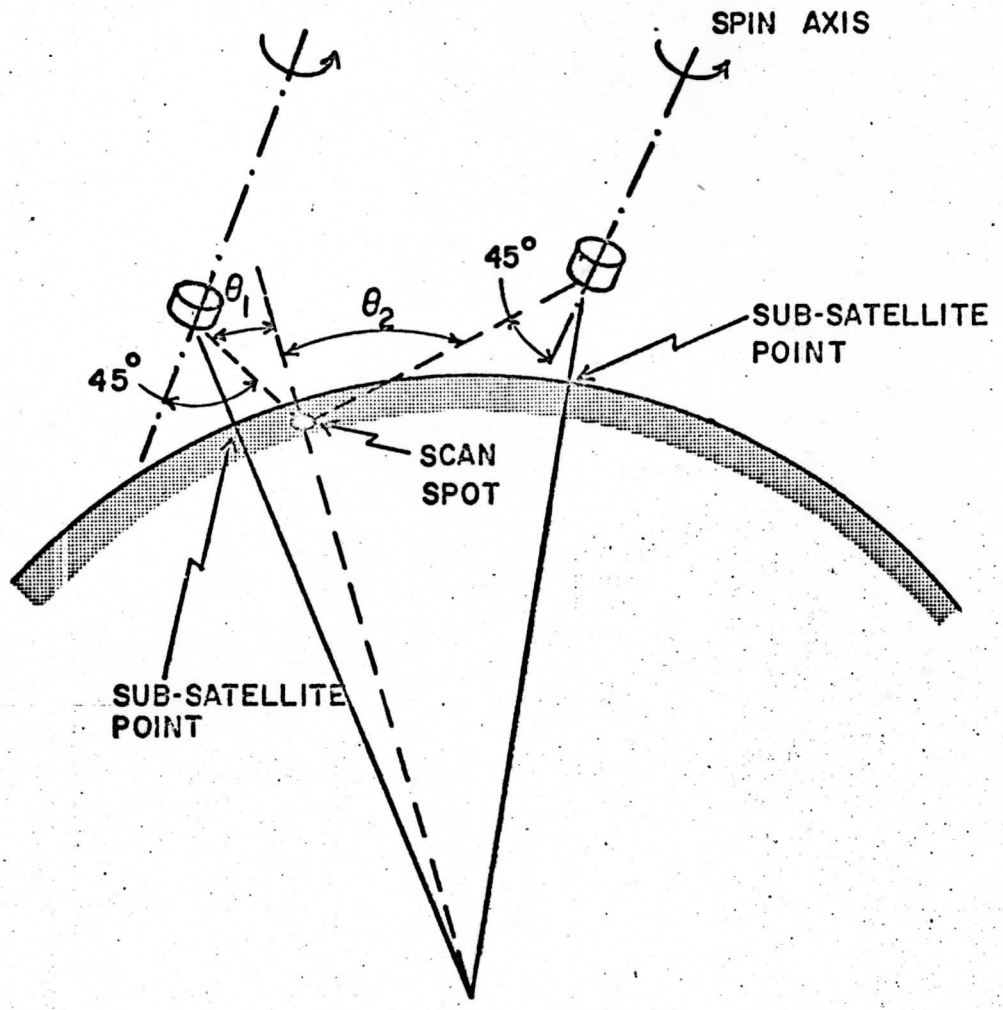

Figure 2. Scan geometry of spin-stabilized Tiros showing the radiometer viewing the same spot on the Earth at two different zenith angles.

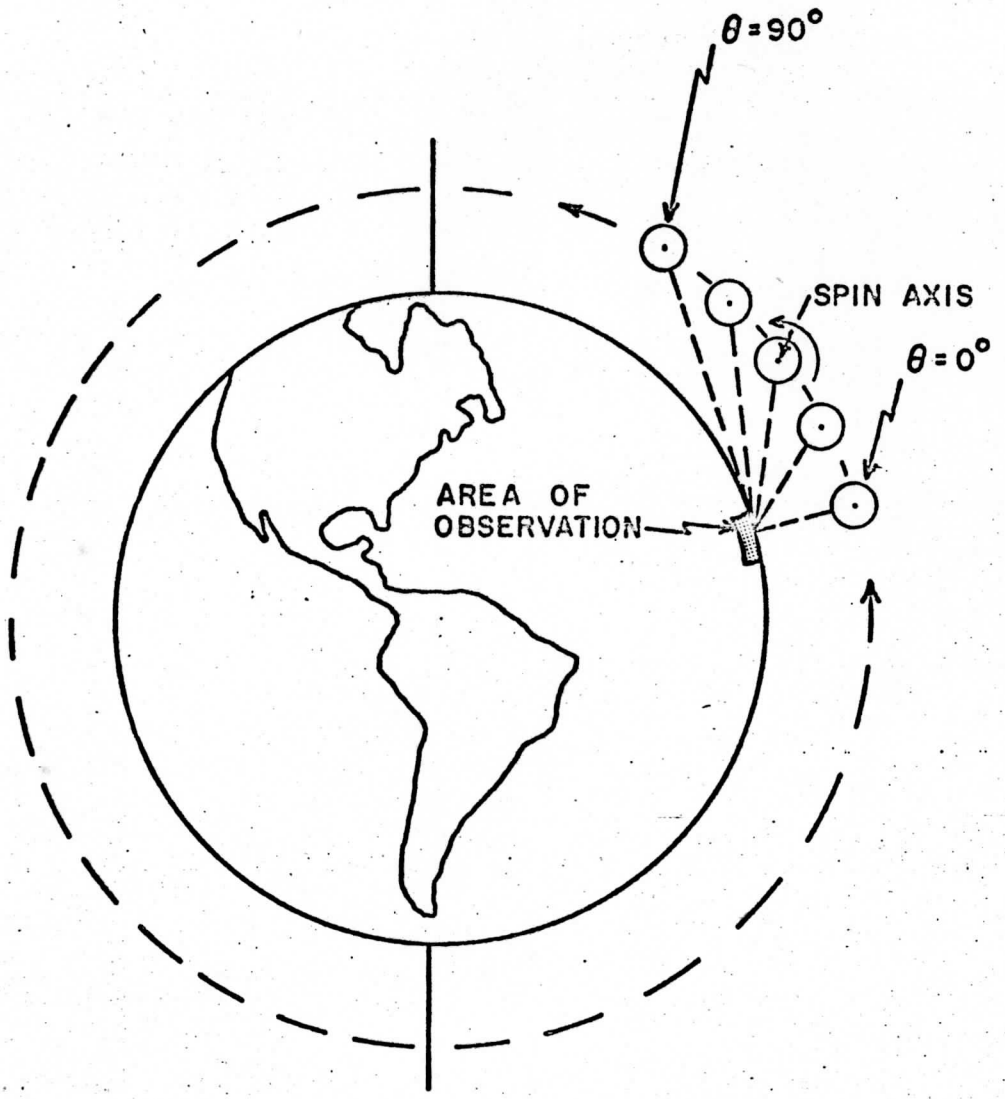

Figure 3. Schematic of a satellite operating in the "wheel-mode". The area of observation may be viewed at all zenith angles from zero degrees to ninety degrees.

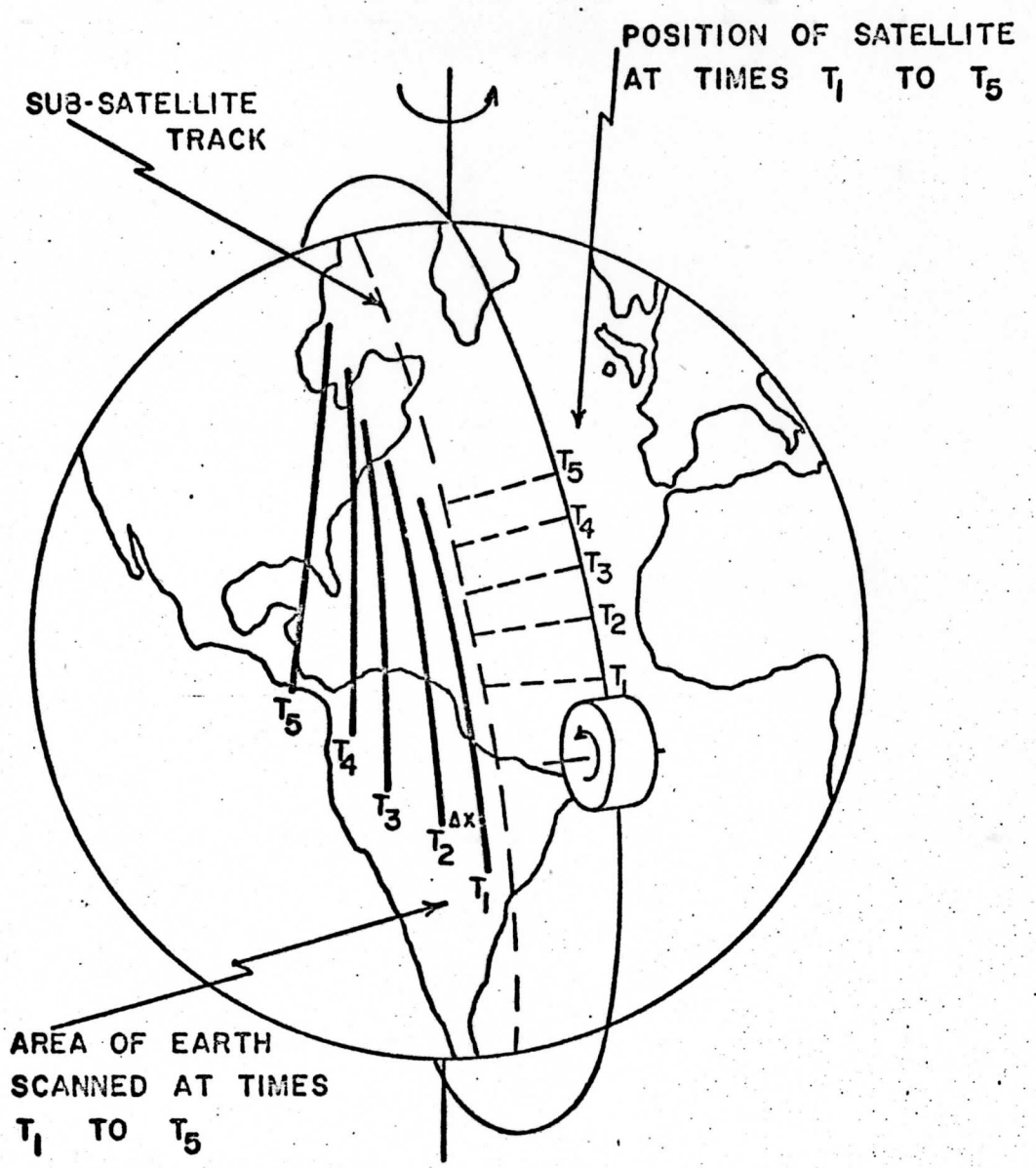

Figure 4. Schematic of the displacement of data scan lines due to the Earth's rotation. The displacements are grossly exaggerated.

III. THE DATA

The data for this study were a series of analog traces of the output of the horizon sensor. The traces are very similar to the data from the Tiros Medium Resolution Infrared Radiometer. Since the scans were all essentially in the orbital plane, it is possible to follow any particular feature from horizon to horizon. The radiation received at the sensor from the scan spot is essentially parallel beam radiation; therefore, the measurement of intensity is implied dimensionally. Thus it is possible to follow the variations in intensity of a feature as it moves from the subsatellite point to the limb. Figure 5 is a schematic of one data set showing the variations in observed intensity as a function of distance from the sub-satellite point. This distance along the trace can be converted to nadir angle of the satellite and zenith angle at the scan spot.

The data were selected to conform to the requirements noted in the previous chapter; that is, the area of concern must be homogeneous and large enough to fill the scan spot even at the limb. Twenty-two data sets were used to obtain limb darkening curves for the following conditions: tropical land, tropical water, tropical cloud, and mid-latitude land. The resulting curves were then compared with the observed curves of Larsen et al. (1963) and Wark (1964) and the theoretically calculated curves of Wark (1963).

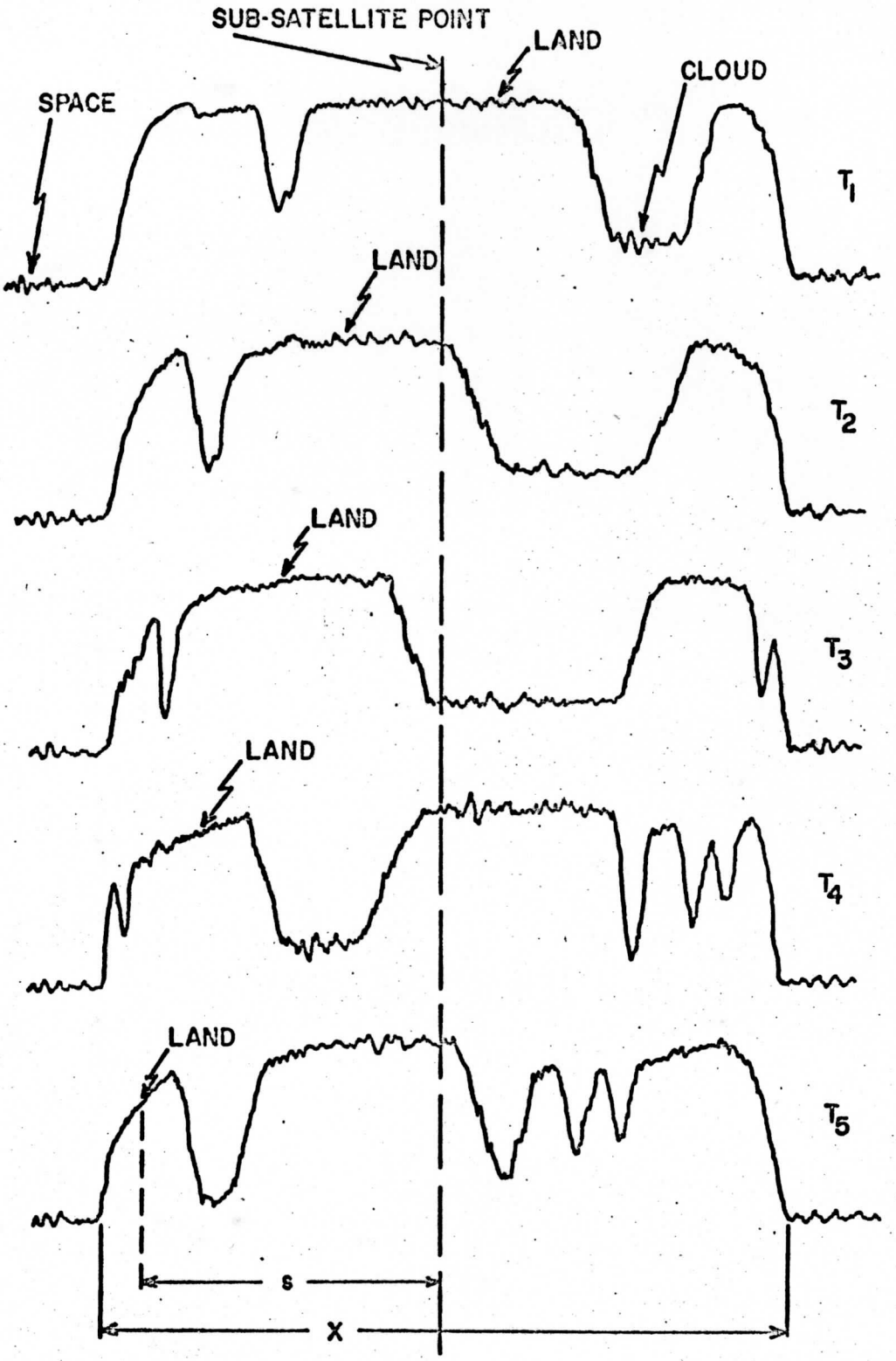

Figure 5. Schematic of one data set showing the variation of intensity of a land feature as a function of distance from the sub-satellite point.

IV. THE CALCULATIONS

The length of the analog trace is a function of the recorder producing the trace, the height of the satellite, the spin rate of the satellite, and the effective aperture angle of the earth within the spectral interval of the sensor. For short periods of time (one orbit), the spin rate of the satellite is considered constant and the trace can be calibrated if the height of the satellite is known and the effective height of the radiating atmosphere is known or assumed. An analysis of the data at the horizon shows that the effective height of the atmosphere can be assumed to be about 40 kilometers (see Appendix). This height agrees with the models of Wark and the empirical results of Walker (1966). The latter's observations, obtained from an Aerobee rocket, showed that the radiance in the 10.2 to 11.8 micron interval of the window reached zero prior to the 50 km level. The calibration of the trace then becomes a matter of geometry (see Fig. 6).

The length of the analog trace from horizon to horizon is denoted by X, and s indicated the distance from the sub-satellite position to a particular feature (Fig. 5). The nadir angle of the satellite corresponding to the feature at s is then

$$\eta = \frac{2\eta_T}{X} s \qquad (2)$$

where η_T is the nadir angle at which the sensor begins receiving

atmospheric radiation and is given by

$$\eta_T = \eta_A + \tfrac{1}{2}\gamma \tag{3}$$

where η_A is the nadir angle at the atmospheric horizon and is equal to

$$\eta_A = \sin^{-1}\frac{D+R}{H+R} \tag{4}$$

and γ is the angular field of view of the sensor. The effective height of the atmosphere is D, R is the earth's radius (taken as 6370 km), and H is the height of the satellite, known from the satellite's ephemeris. The zenith angle of the feature at s is θ and is equal to

$$\theta = \sin^{-1}\left[\sin\eta\,\frac{R+H}{R}\right]. \tag{5}$$

Z_0^1 is the minimum height of the unrefracted ray from the scan spot and is equal to

$$Z_0^1 = [(R+H)\sin\eta] - R. \tag{6}$$

Using equations (2) through (6) the variations of intensity of a feature were calculated as a function of zenith angle and Z_0^1.

Space contamination of the sensor's field of view occurs when the nadir angle of the satellite is equal to

$$\eta = \eta_E - \tfrac{1}{2}\gamma \tag{7}$$

where η_E is the nadir angle at the earth's horizon and is equal to

$$\eta_E = \sin^{-1}\frac{R}{R+H}. \tag{8}$$

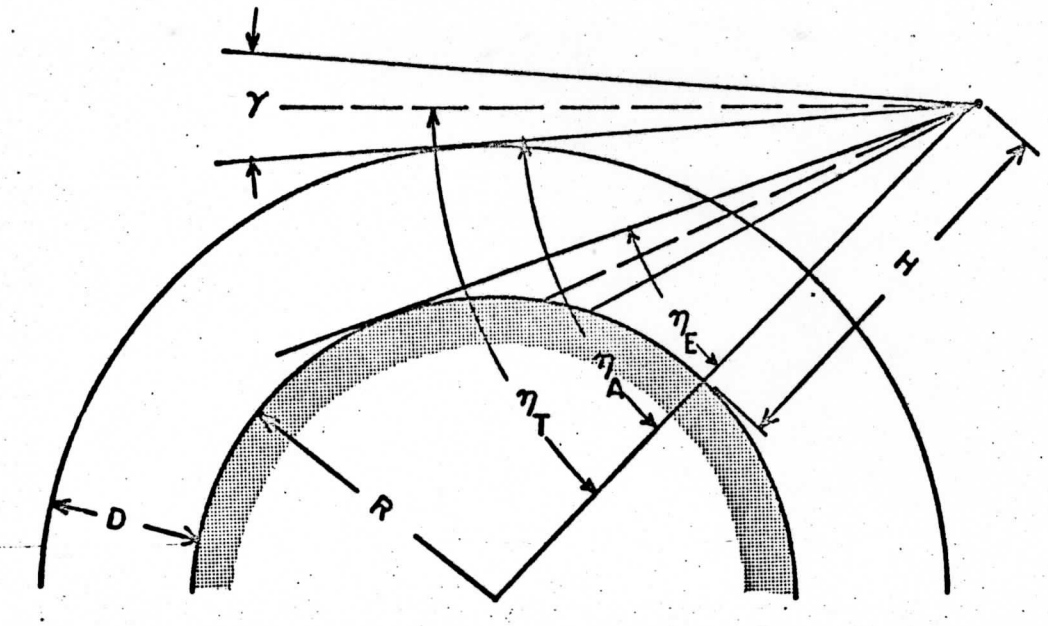

Figure 6a. Geometry of sensor's field of view.

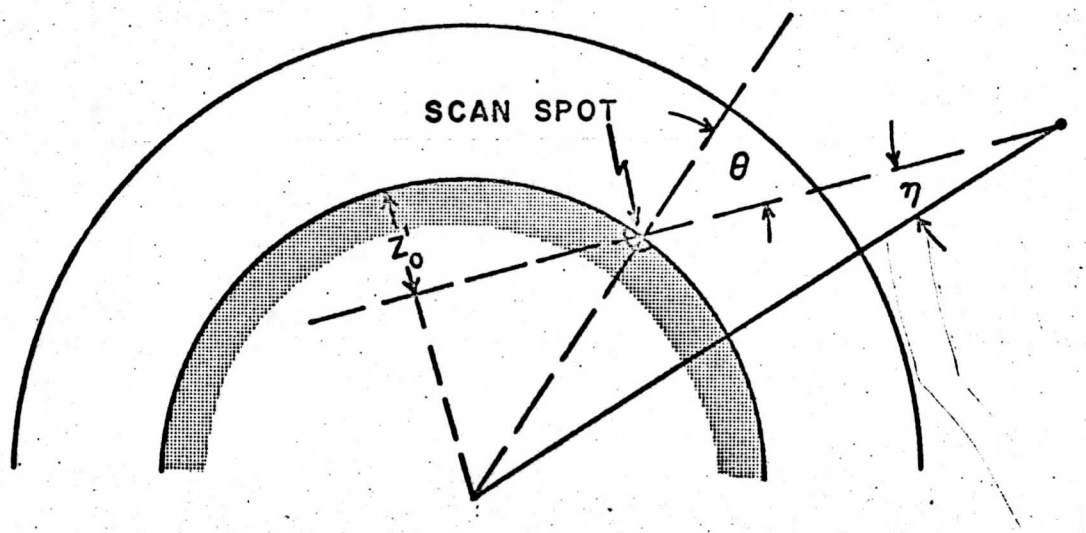

Figure 6b. Geometry of sensor's optical axis.

V. THE RESULTS

Figures 7 through 10 show a comparison of the observed limb darkening with the observed limb darkening of Wark and Larsen. Wark's curve, statistically derived from Tiros observations, shows greater limb darkening than his earlier calculations (see Fig. 1). This was attributed to geometrical factors in viewing partly cloudy areas.

The data for Case 1 were obtained over the Norther Hemispheric continents between latitudes 40 N and 50 N. Case 2 data were obtained over the cloud-free tropical deserts between latitudes 15 N and 25 N. Tropical water data, Case 3, were obtained between 02 S and 25 N, and Case 4 data were obtained over the areas of stratocumulus on the eastern portion of the subtropical high pressure systems between latitudes 05 S and 28 S.

In Case 1, mid-latitude land, the observed data agree more with Wark's calculations than with his empirical curve, since the effects of clouds have been eliminated. The limb darkening of Case 2, tropical land, is greater than Case 1. This is to be expected from the effects of normalizing data with a larger initial value of the radiance. Case 3, tropical water, is very similar to tropical land. Since the temperature difference between Case 2 and 3 is very small, normalizing effects are absent. The tropical water does show slightly more darkening than the tropical land at zenith angles greater than 70-75°. This could be

attributed to a larger atmospheric moisture content over the water and possibly to the geometrical effects of viewing small trade cumulus. Case 4 shows the limb darkening for tropical cloud. Again, the darkening effect is less than Case 2 or 3, due to the effects of normalizing the data. Since the cloud-top temperature was not very low, this case is almost identical with Case 1 because the land temperature at mid-latitude is similar to these cloud-top temperatures in the tropics.

All four cases show one similarity, namely that the curves roughly follow the slope of Wark's empirical curve up to a zenith angle of approximately 75° and then the darkening becomes greater. It will be seen later that this effect is in agreement with Wark's theoretical calculations.

Besides comparing the observations with previous observations (Wark and Larsen), they were also compared with the theoretical calculations. Wark (1963) has calculated for a spectral range from 0 to 2500 cm^{-1}, the spectral radiance of the Earth with eight model atmospheres. Three of these models, all with clear skies, were selected as basis for these comparisons. The H_2O mass is given in centimeters of precipitable water and the O_3 mass is given in centimeter atmospheres. Atmosphere "A" is the ARDC Standard Atmosphere, 1959, with H_2O mass equal to 1.334 and O_3 mass equal to 0.435. Atmosphere "B" was calculated from a sounding for Albuquerque, N. M , July 11, 1958, 0000 GMT, with H_2O mass equal to 1.363 and O_3 mass equal to 0.289.

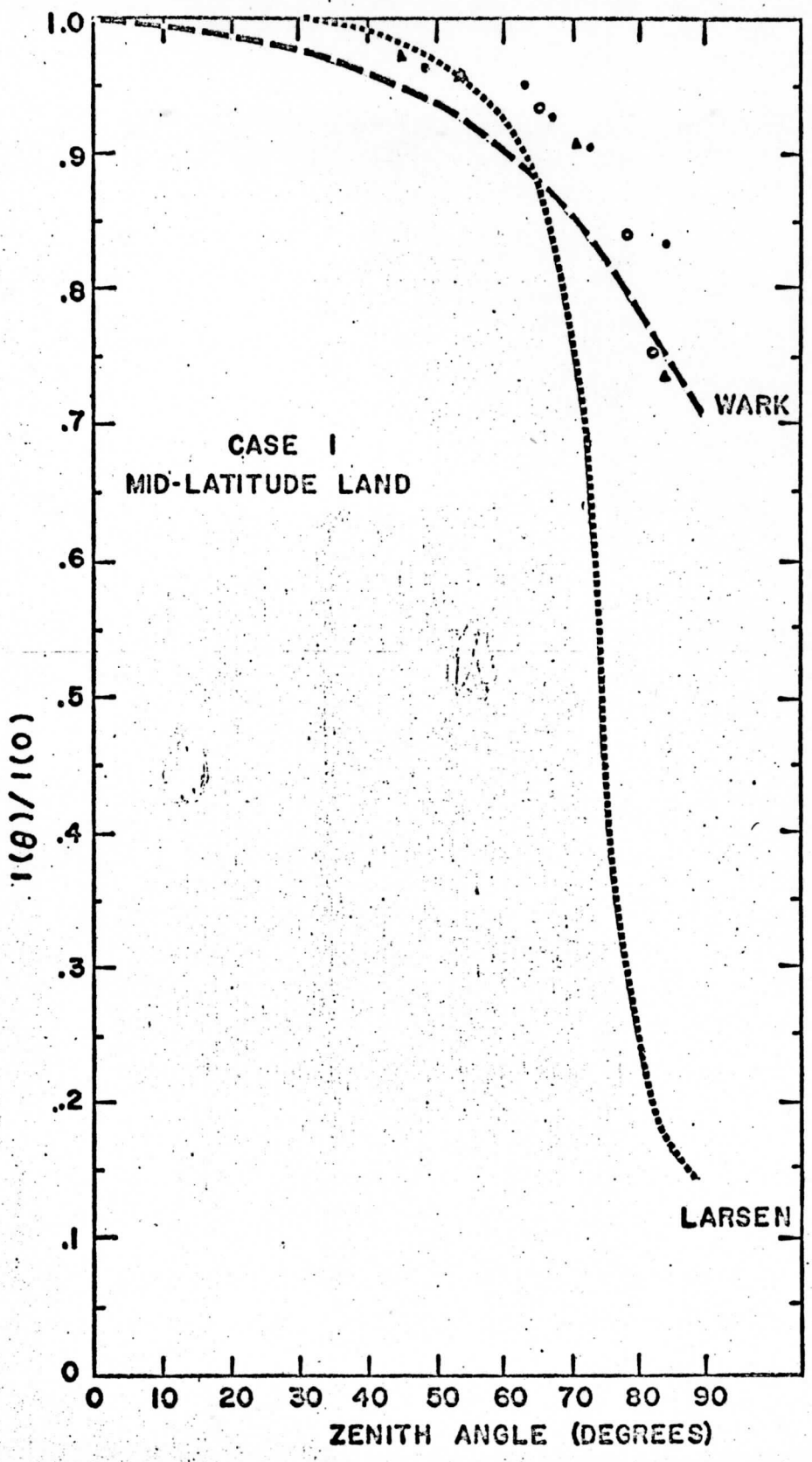
1.0
.9
.8
.7
.6
.5
.4
.3
.2
.1
0
I(θ)/I(0)
CASE I
MID-LATITUDE LAND
WARK
LARSEN
0
10
20
30
40
50
60
70
80
90
ZENITH ANGLE (DEGREES)

Figure 7

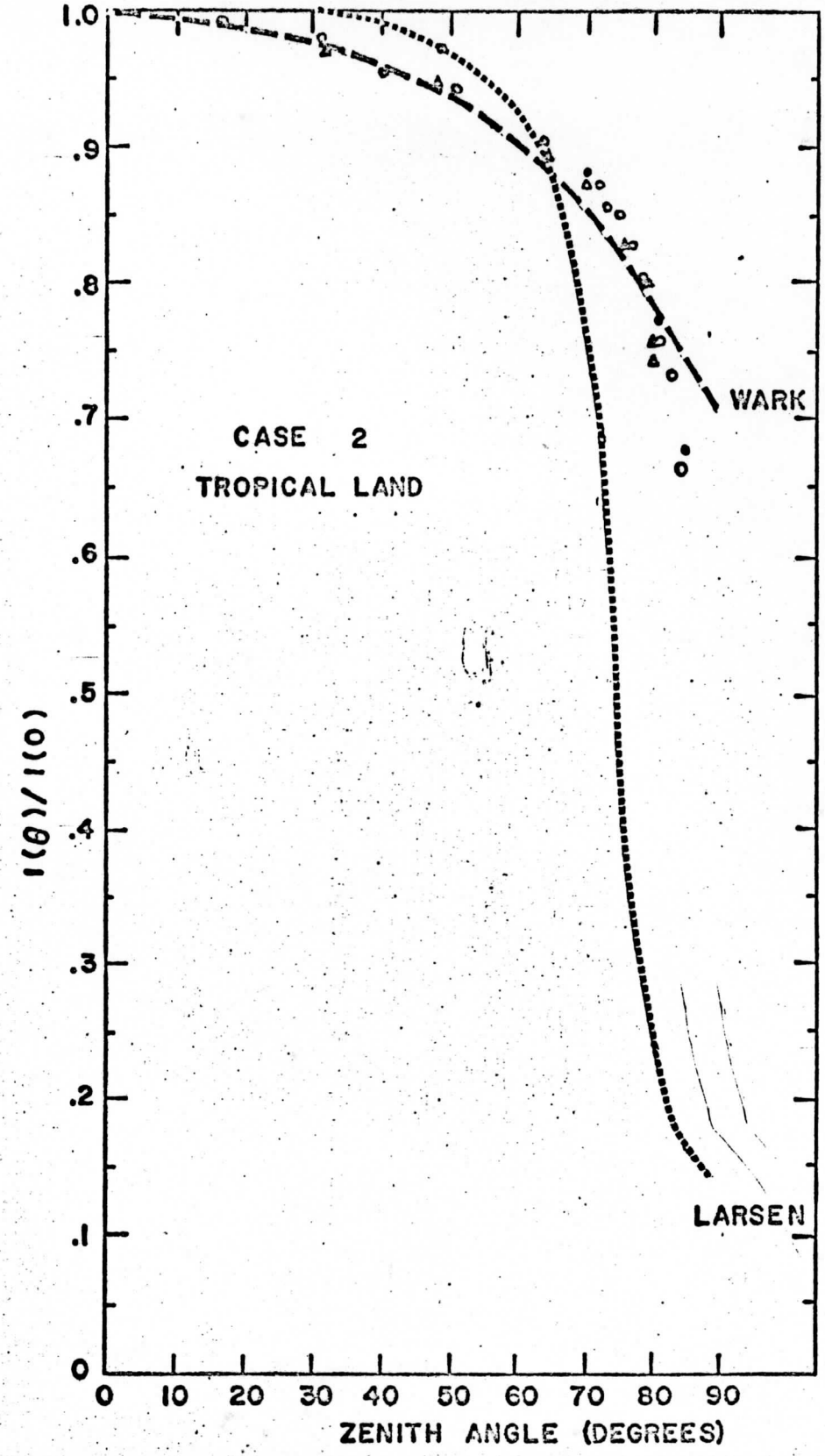
1.0
.9
.8
.7
.6
.5
.4
.3
.2
.1
0
I(θ)/I(0)
CASE 2
TROPICAL LAND
WARK
LARSEN
0
10
20
30
40
50
60
70
80
90
ZENITH ANGLE (DEGREES)

Figure 8

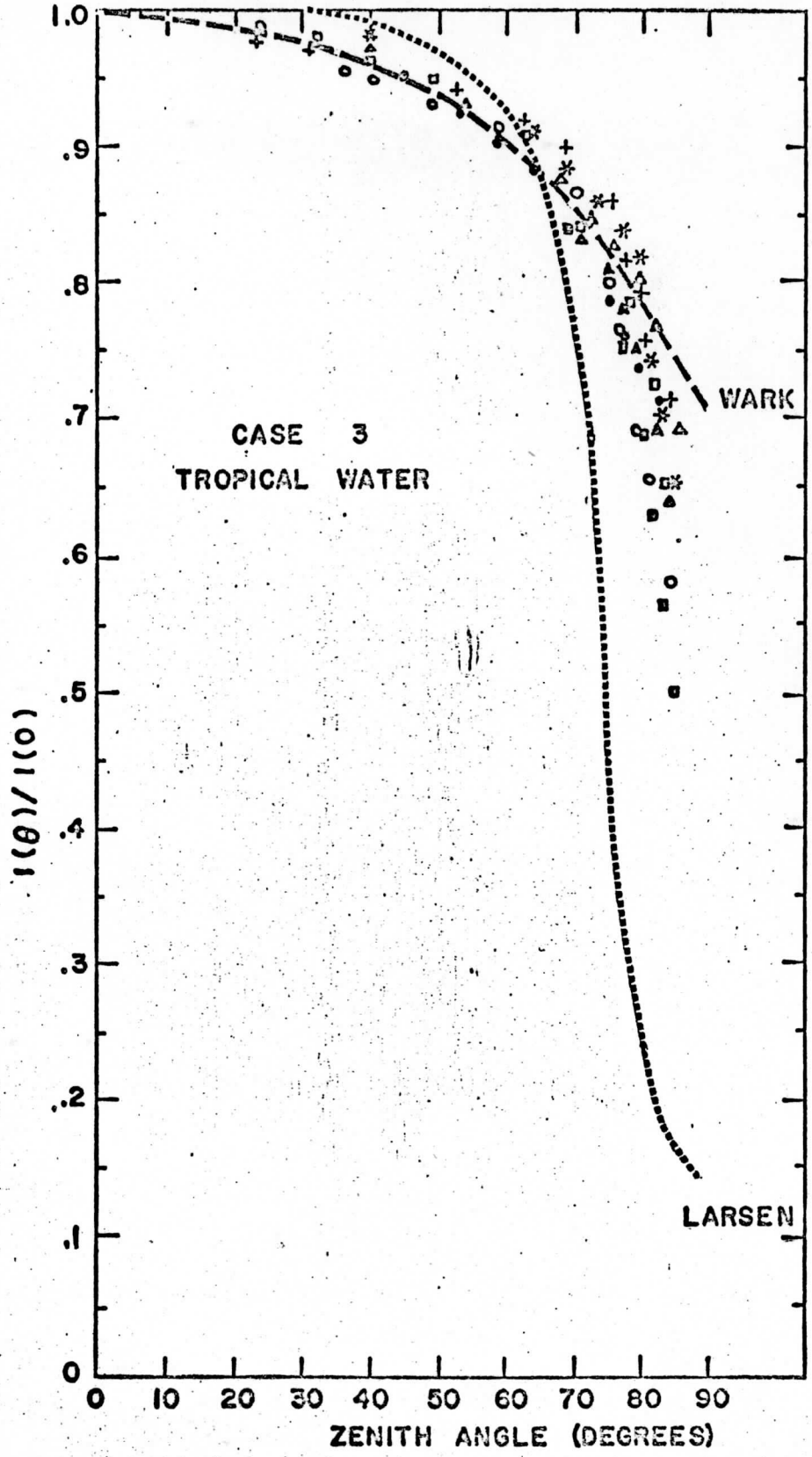
1.0
.9
.8
.7
.6
.5
.4
.3
.2
.1
0
I(θ)/I(0)
CASE 3
TROPICAL WATER
WARK
LARSEN
0
10
20
30
40
50
60
70
80
90
ZENITH ANGLE (DEGREES)

Figure 9

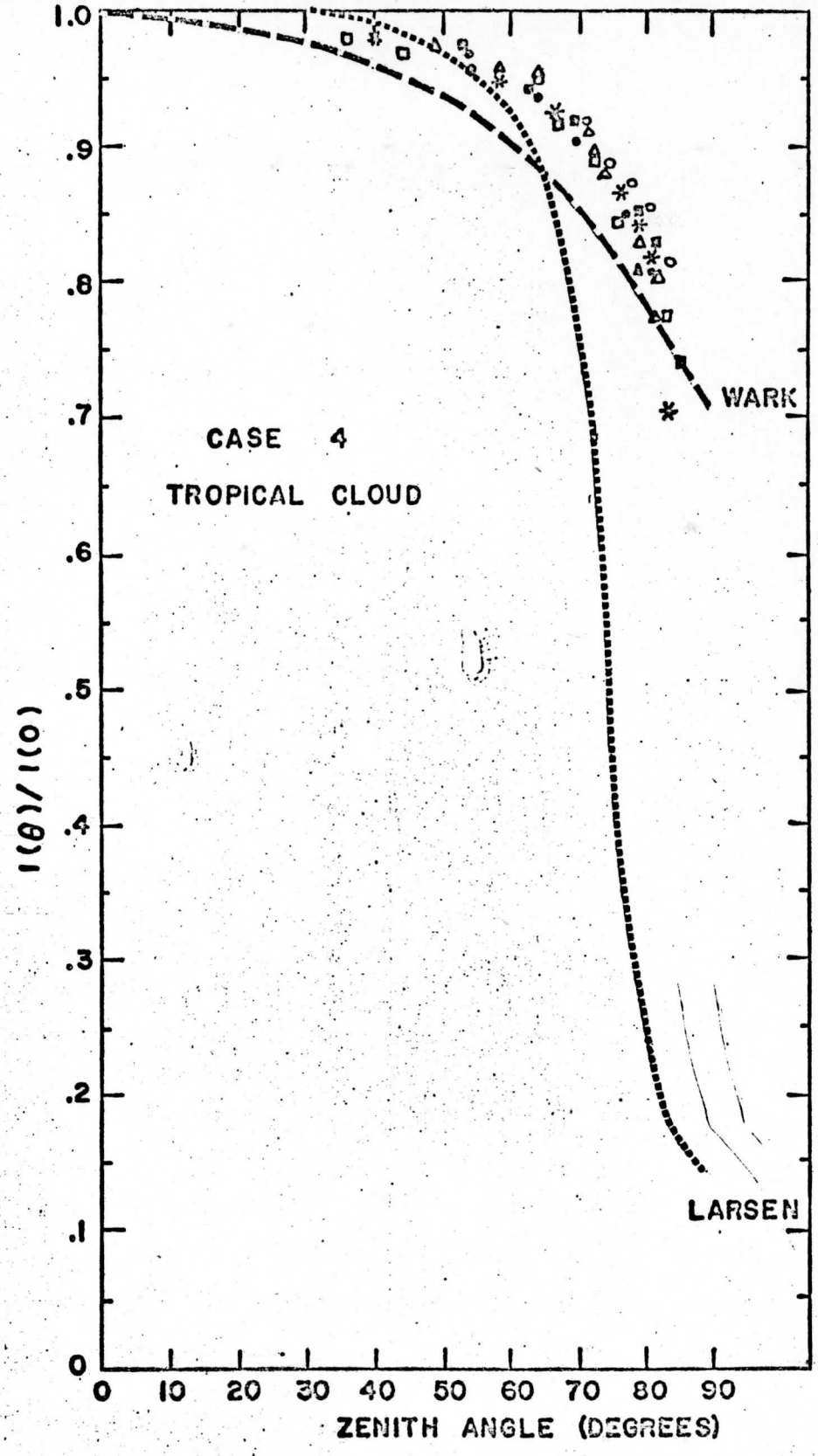
1.0
.9
.8
.7
.6
.5
.4
.3
.2
.1
0
I(θ)/I(0)
CASE 4
TROPICAL CLOUD
WARK
LARSEN
0 10 20 30 40 50 60 70 80 90
ZENITH ANGLE (DEGREES)

Figure 10

Atmosphere "G" was calculated from a sounding for Kindley, Bermuda, August 1, 1958, 1200 GMT, with H_2O mass equal to 5.078 and O_3 mass equal to 0.255. The first step in the evaluation of the theoretical calculations is to "look" at these three model atmospheres with the horizon sensor and determine the limb darkening curves.

For each atmosphere Wark has tabulated the values of the radiance, $I_{\bar{\nu}}$, in each of 77 spectral intervals, for 14 values of Z_0'. The frequency response of the sensor covers 16 of these spectral intervals. The unfiltered radiance, $I(Z_0')$, assuming a transmittance of unity for the sensor, is then

$$I(Z_0') = \sum_{i=1}^{16} [I_{\bar{\nu}}(Z_0')]_i \tag{9}$$

and is represented by curve 1 in Figures 11, 12, and 13. Curves 1 represent the radiance in the 8-12 micron spectral interval. Since the transmittance of the sensor is not unity, curves 1 were filtered with the spectral response of the sensor to obtain curves 2. The filtered radiance, $I_\phi(Z_0')$, is then

$$I_\phi(Z_0') = \sum_{i=1}^{16} [I_{\bar{\nu}}(Z_0')]_i [\phi_{\bar{\nu}}]_i \tag{10}$$

where $\phi_{\bar{\nu}}$ is the average filter response in the spectral interval represented by $\bar{\nu}$. Similarly, the power response of the sensor over its aperture is not unity but is a function of the distance from the optical axis. Curve 2 then must be filtered with the sensor power response to obtain the radiance actually seen by the sensor, $I_s(Z_0')$, where

$$I_s(Z_0') = \sum_{i=1}^{13} [I_\phi(Z_0')]_i [\phi_{\bar{\gamma}}]_i \cdot \qquad (11)$$

Here $\phi_{\bar{\gamma}}$ is the average power response in the aperture angle represented by $\bar{\gamma}$. The power response curve was divided into thirteen intervals to obtain $\phi_{\bar{\gamma}}$, hence the summation of i from 1 to 13. Curve 3 then is the theoretically calculated radiance that this particular sensor should see and which will be used for comparison with the observations. Curve 3 for the three model atmospheres is shown in Figure 14. These curves were normalized and used for comparison with the observations.

The observed limb darkening curves for the four categories, mid-latitude land, tropical land, tropical water, and tropical cloud, are shown in Figures 15 to 18. These figures are merely an extension of the figures 7 through 10. The horizontal variable was changed from zenith angle to Z_0' to facilitate comparisons beyond the geometrical horizon. Zenith angles up to the horizon are indicated on a secondary scale on top of the figure. Although the scatter of the data about the calculated curves appears large, this results from a very small error in the measurement of X on the analog trace. Figure 15 shows the effects of these small errors in measurement on the location of the data for a case of mid-latitude land indicated by (Δ). The errors in the location of the data for errors of 1/4% and 1/2% in the value of X are shown. An over-estimate of the value of X, (+1/4 % and +1/2 %), will lead to an under-estimate of the value of Z_0' and vice versa. Thus the

observations actually agree with the calculations very well. One small deviation is worth noting, however. For values of Z_0' between - 70 and - 20 the observations tend to be slightly lower than the calculations, and for values of Z_0' between + 20 and + 60 the observations tend to be slightly higher than the calculations. This effect can be attributed to dust and aerosols in the atmosphere. Below the geometrical horizon the dust and aerosols would attenuate the radiation from the Earth, while above the horizon the dust and aerosols would become an additional source of radiation. Thus the effects of dust and aerosols are such that the slope of the observed curve is less than the slope of the theoretical curve.

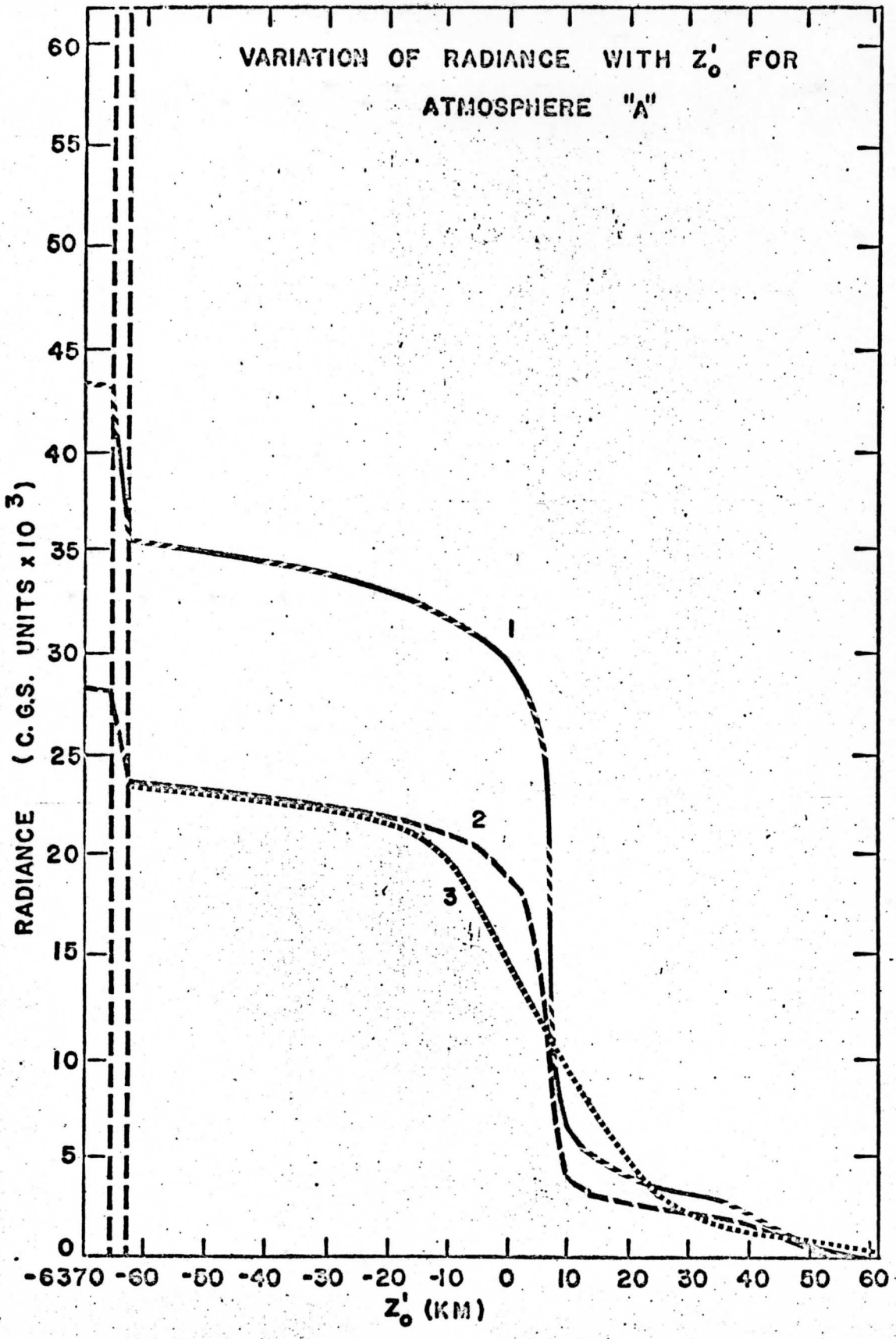
VARIATION OF RADIANCE WITH Z_o' FOR
ATMOSPHERE "A"
RADIANCE (C.G.S. UNITS x 10 3)
Z_o' (KM)
1
2
3
60
55
50
45
40
35
30
25
20
15
10
5
0
-6370 -60 -50 -40 -30 -20 -10 0 10 20 30 40 50 60

Figure 11

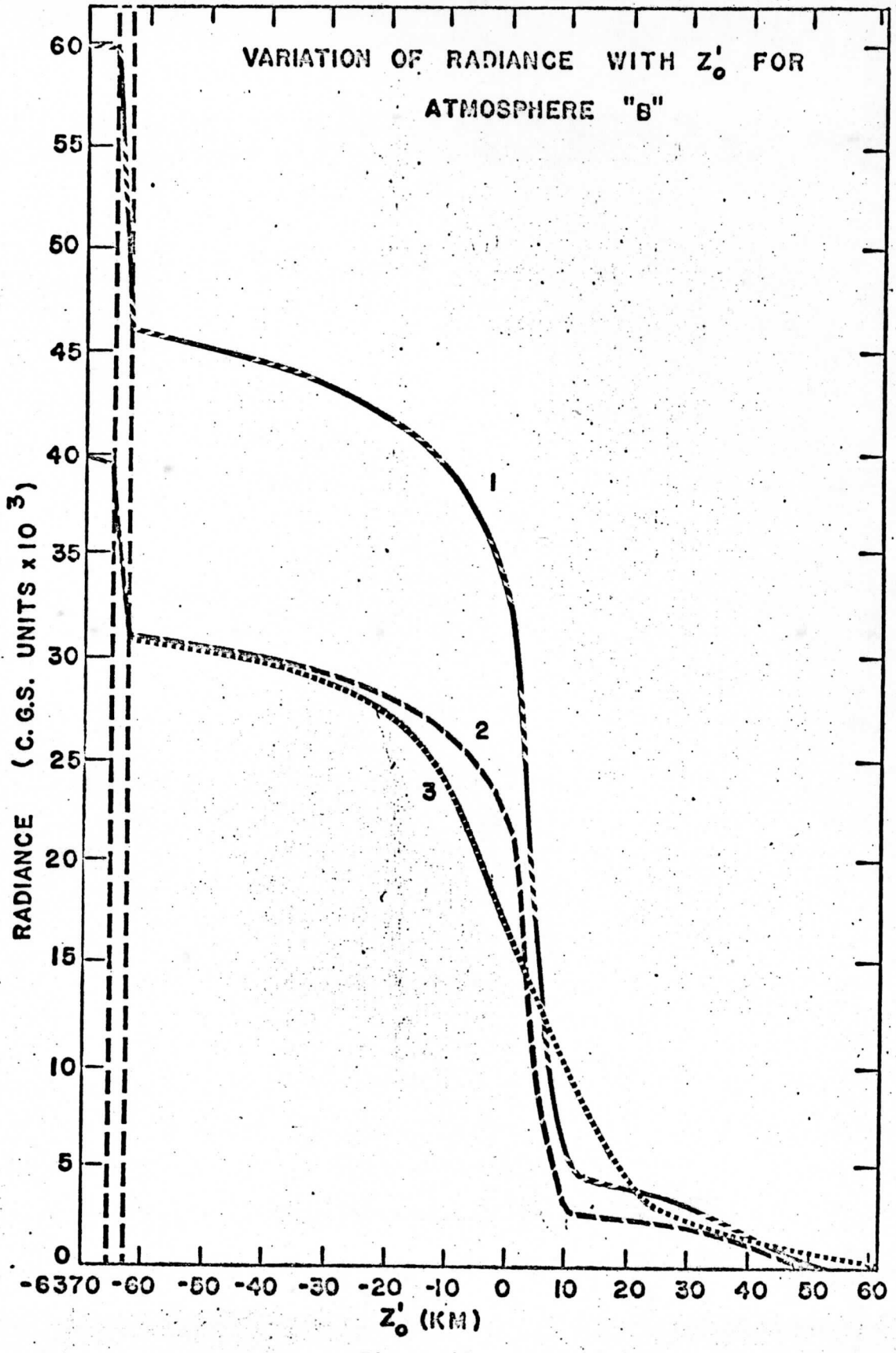
VARIATION OF RADIANCE WITH Z_o' FOR ATMOSPHERE "B"
RADIANCE (C.G.S. UNITS x 10 3)
60
55
50
45
40
35
30
25
20
15
10
5
0
1
2
3
-6370 -60 -50 -40 -30 -20 -10 0 10 20 30 40 50 60
Z_o' (KM)

Figure 12

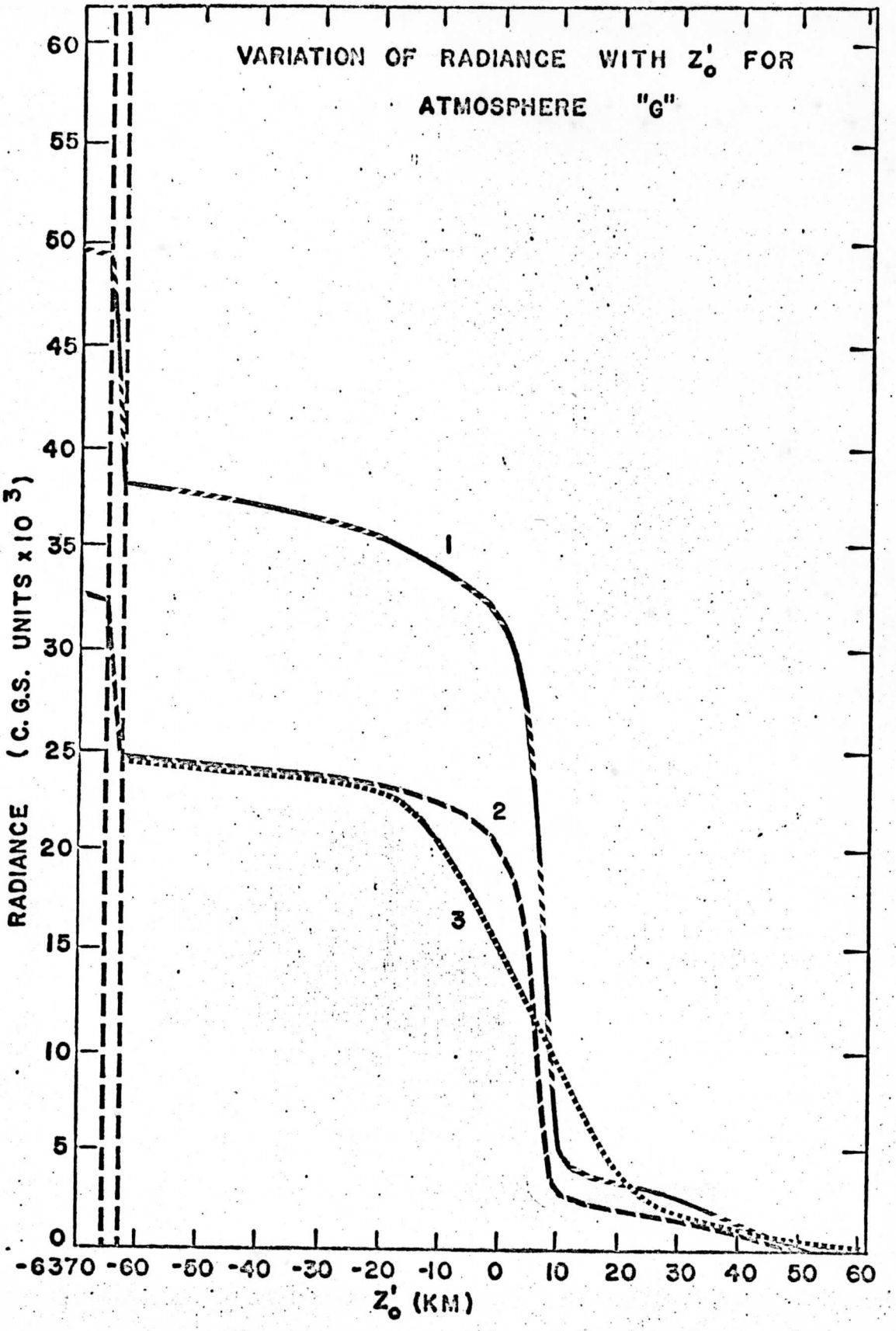
VARIATION OF RADIANCE WITH Z_o' FOR ATMOSPHERE "G"
RADIANCE (C.G.S. UNITS x 10 3)
60
55
50
45
40
35
30
25
20
15
10
5
0
1
2
3
-6370 -60 -50 -40 -30 -20 -10 0 10 20 30 40 50 60
Z_o' (KM)

Figure 13

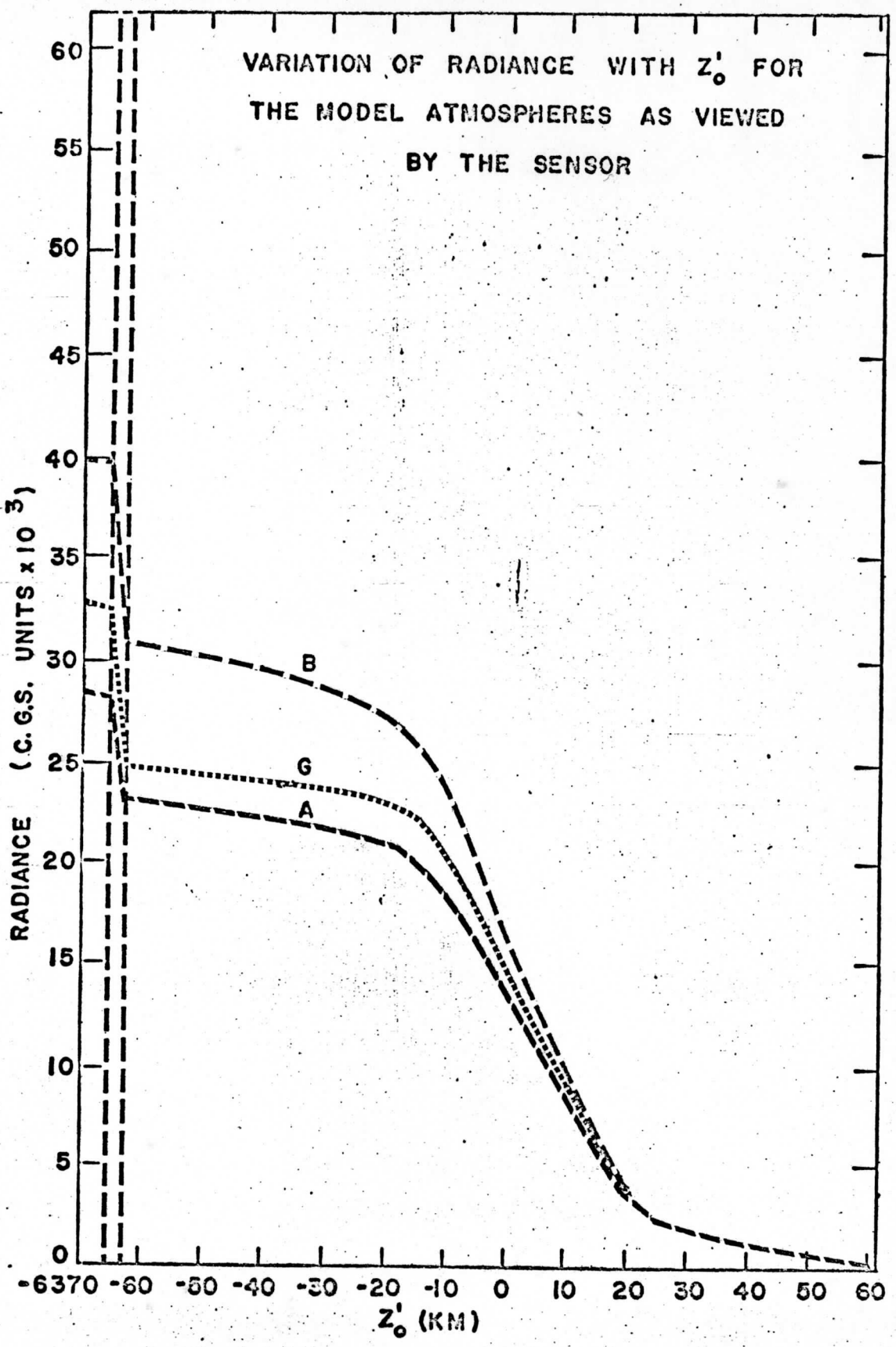
VARIATION OF RADIANCE WITH Z_o' FOR
THE MODEL ATMOSPHERES AS VIEWED
BY THE SENSOR
RADIANCE (C.G.S. UNITS x10^{3})
Z_o' (KM)
B
G
A
60
55
50
45
40
35
30
25
20
15
10
5
0
-6370
-60
-50
-40
-30
-20
-10
0
10
20
30
40
50
60

Figure 14

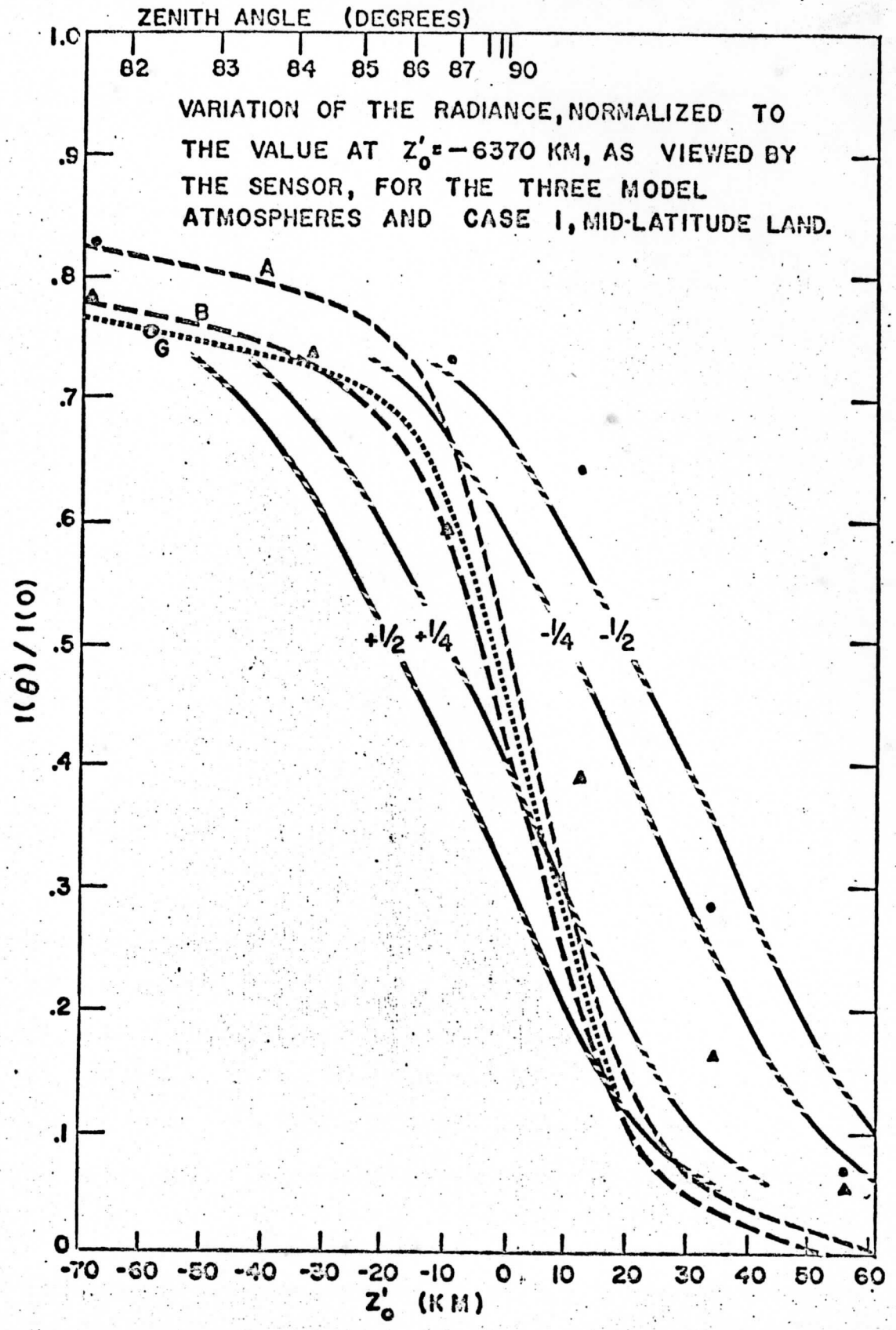
ZENITH ANGLE (DEGREES)
82
83
84
85
86
87
90
VARIATION OF THE RADIANCE, NORMALIZED TO THE VALUE AT $Z'_0 = -6370$ KM, AS VIEWED BY THE SENSOR, FOR THE THREE MODEL ATMOSPHERES AND CASE I, MID-LATITUDE LAND.
A
B
C
+1/2
+1/4
-1/4
-1/2
I(θ)/I(0)
1.0
.9
.8
.7
.6
.5
.4
.3
.2
.1
0
-70
-60
-50
-40
-30
-20
-10
0
10
20
30
40
50
60
Z'_0 (KM)

Figure 15

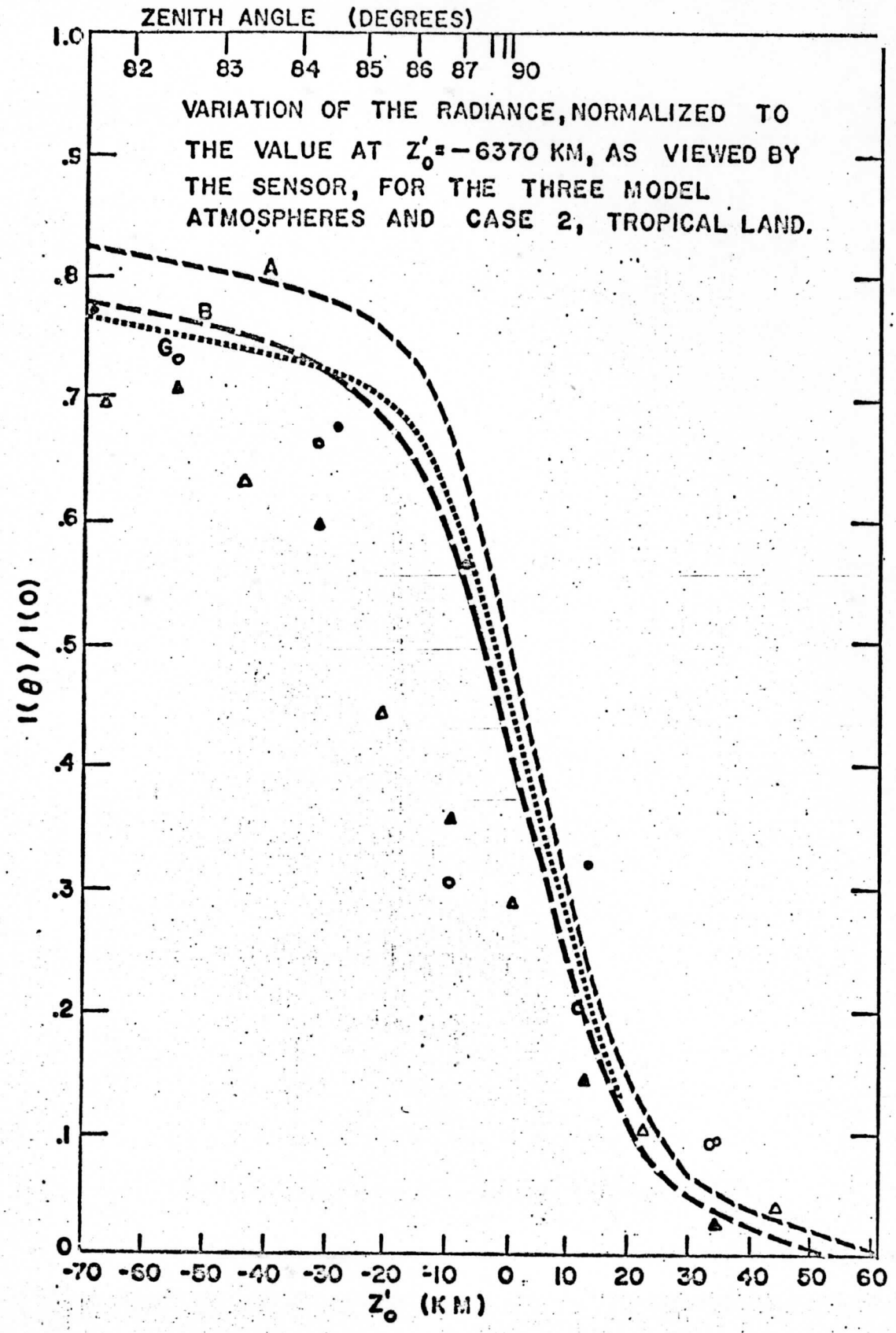
ZENITH ANGLE (DEGREES)
82
83
84
85
86
87
90
VARIATION OF THE RADIANCE, NORMALIZED TO THE VALUE AT $Z'_0 = -6370$ KM, AS VIEWED BY THE SENSOR, FOR THE THREE MODEL ATMOSPHERES AND CASE 2, TROPICAL LAND.
A
B
G_o
$I(\theta)/I(0)$
1.0
.9
.8
.7
.6
.5
.4
.3
.2
.1
0
-70 -60 -50 -40 -30 -20 -10 0 10 20 30 40 50 60
Z'_o (KM)

Figure 16

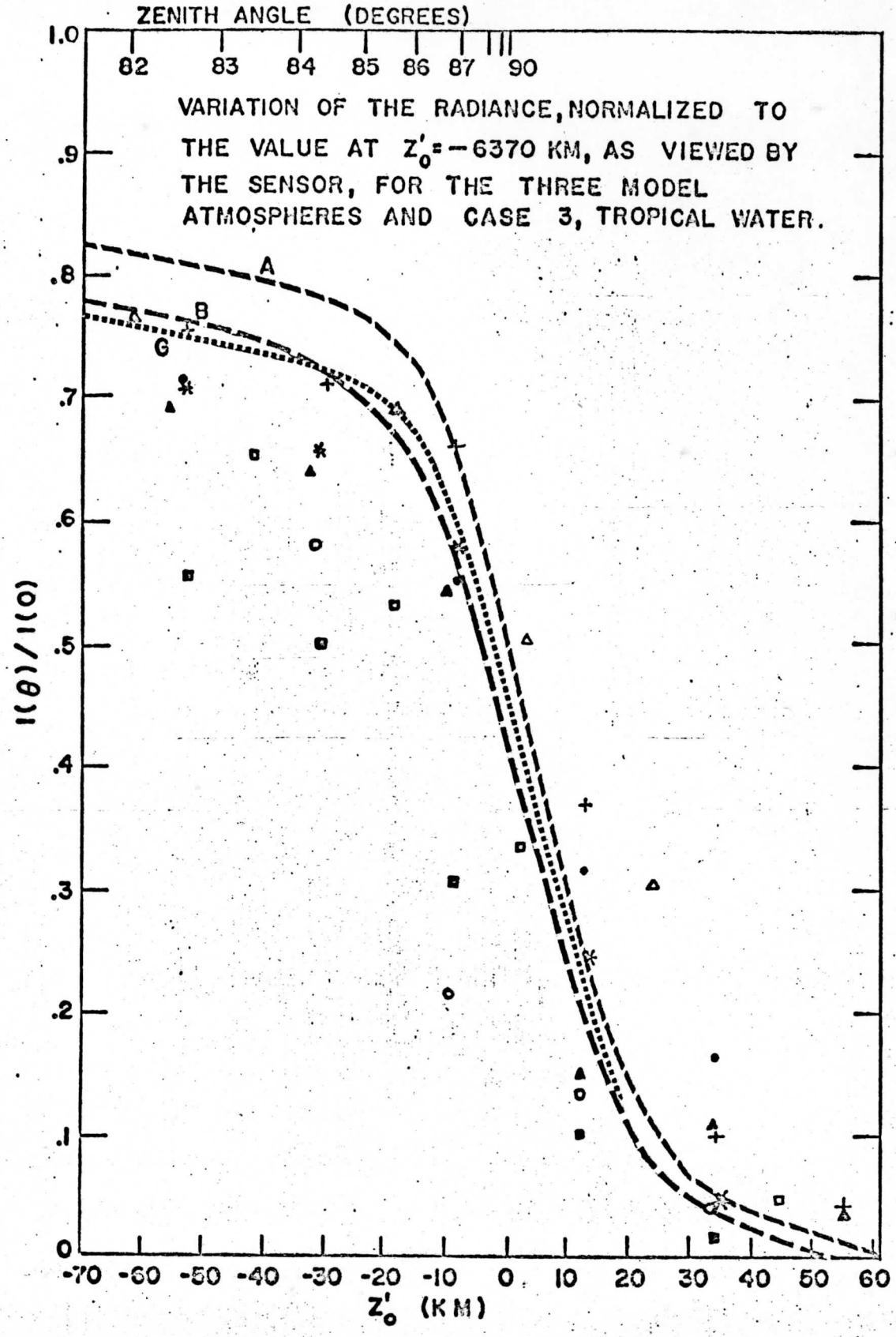
ZENITH ANGLE (DEGREES)
82
83
84
85
86
87
90
VARIATION OF THE RADIANCE, NORMALIZED TO THE VALUE AT $Z'_0 = -6370$ KM, AS VIEWED BY THE SENSOR, FOR THE THREE MODEL ATMOSPHERES AND CASE 3, TROPICAL WATER.
A
B
C
I(θ)/I(0)
1.0
.9
.8
.7
.6
.5
.4
.3
.2
.1
0
-70 -60 -50 -40 -30 -20 -10 0 10 20 30 40 50 60
Z'_0 (KM)

Figure 17

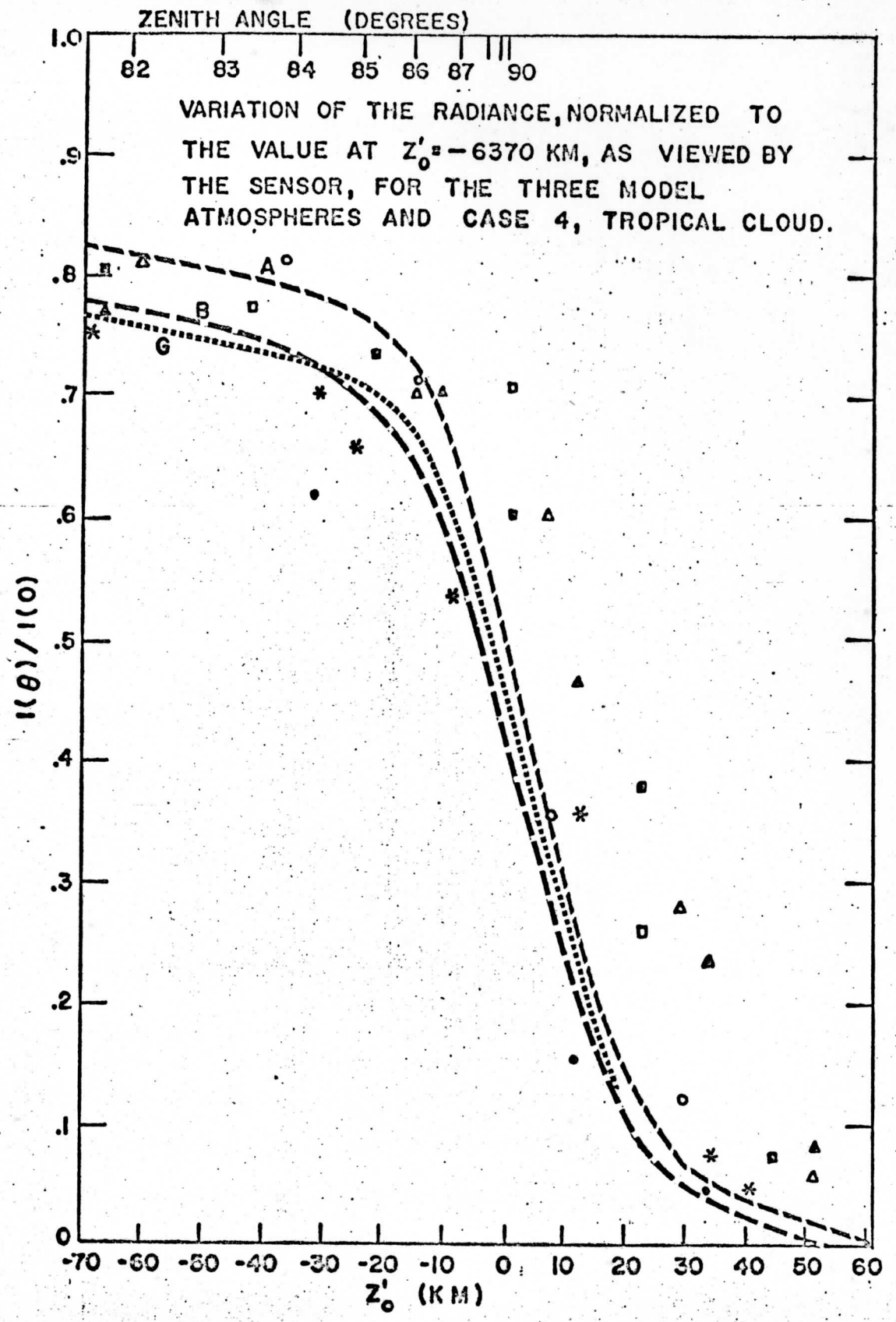
ZENITH ANGLE (DEGREES)
82
83
84
85
86
87
90
VARIATION OF THE RADIANCE, NORMALIZED TO THE VALUE AT $Z'_0 = -6370$ KM, AS VIEWED BY THE SENSOR, FOR THE THREE MODEL ATMOSPHERES AND CASE 4, TROPICAL CLOUD.
A
B
G
I(θ)/I(0)
1.0
.9
.8
.7
.6
.5
.4
.3
.2
.1
0
-70 -60 -50 -40 -30 -20 -10 0 10 20 30 40 50 60
Z'_0 (KM)

Figure 18

VI. SUMMARY

The calculations of Wark et al. (1962) were for zenith angles from 0° to 78.5° while the calculations of Wark et al. (1963) were for zenith angles from 81° through 90° to approximately 60 kilometers above the Earth's surface. A comparison of the observed limb darkening curve for 0 to 78.5° in figures 7 through 10 shows excellent agreement with the theoretical calculations. The observed limb darkening curve for mid-latitude land shows excellent agreement with Wark's calculations for Albuquerque, N. M. The observed curves for tropical land and tropical cloud show greater limb darkening due to the effects of normalizing the data.

A comparison of the observed limb darkening from 81° through 60 km in figures 15 through 18 also show excellent agreement with the theoretical calculations. Again, mid-latitude land shows excellent agreement with the calculations for Albuquerque. In all four cases the slope of the observed curve is less than the slope of the calculated curve, indicating the presence of another source of emission in the atmosphere. Pilipowskyj (1967) has shown that the downward flux of radiation, measured by the Suomi-Kuhn radiometer, from stratospheric aerosols, is from three to ten times greater than the downward flux from ozone. If isotropic radiation is assumed, this additional upward radiance from aerosols may be sufficient to explain the slope of the observed curves.

In conclusion, the observations support the validity of the theoretical calculations of Wark et al. in the 8-12 micron spectral interval. The addition of dust and aerosols in the model atmospheres would eliminate the small deviations of the observed limb darkening from the calculated limb darkening.

Observations at various wavelength intervals may yield information on the spectral emissivity of the aerosol.

APPENDIX

The effective height of the atmosphere can be estimated from an analysis of the data at the horizon. Figure 19 shows the sensor viewing the horizon and a schematic of the sensor's output. When the optical axis of the sensor is at position 1 the sensor views only space, and when the optical axis is at position 3 the sensor views only the earth and the intervening atmosphere. The angle the sensor moves through from position 1 to position 3 is β where

$$\beta = \alpha + \gamma \tag{12}$$

where α is the angle subtended at the sensor by an atmosphere of height D and γ is the aperture angle of the sensor. A good approximation to α is

$$\alpha = \frac{D}{d} \tag{13}$$

where d is the distance from the sensor to a radius vector at the horizon. The time required for the sensor to scan through angle β is t and can be measured on the data trace. The slope of the data trace changes as the sensor view crosses the various boundaries of space/atmosphere and atmosphere/earth and indicates clearly the locations of positions 1 and 3. The earth's horizon is at position 2. The change in slope at position 4 is due to the boundary between the moist troposphere and the dry stratosphere and may be detected if the noise level is low enough.

The angle β is then

$$\beta = \omega t \tag{14}$$

where ω is the spin rate of the satellite. Substituting equations (13) and (14) in (12) and solving for D gives

$$D = (\omega t - \gamma)d \, . \tag{15}$$

An analysis of 40 horizon traces shows that t is fairly consistent and D then is calculated to be 40 km. Three examples of horizon traces showing positions 1, 2, 3, and 4 are given in Figure 20.

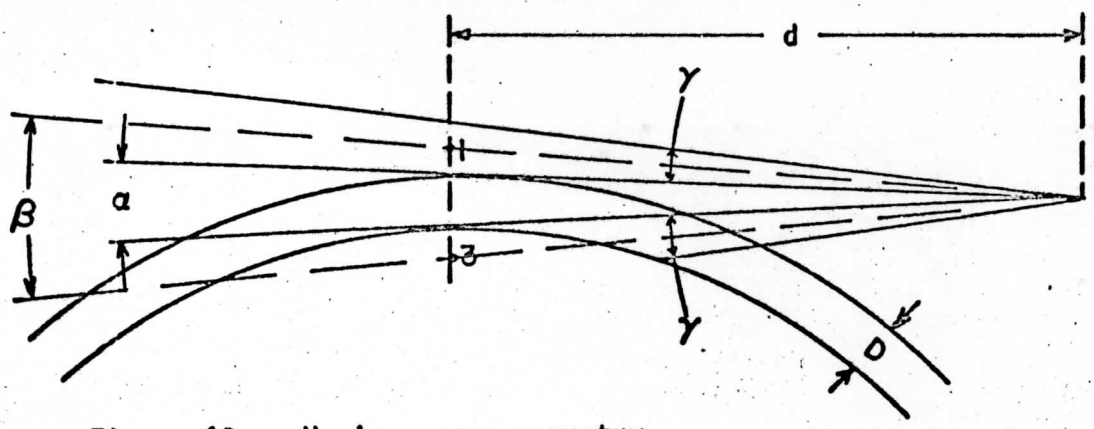

Figure 19a. Horizon scan geometry.

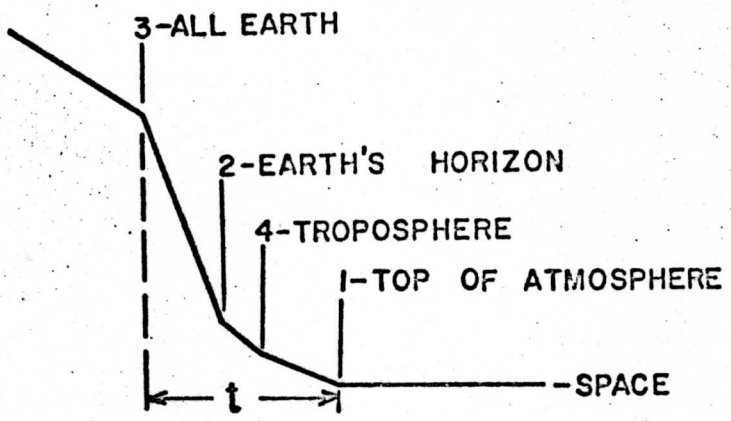

Figure 19b. Idealized sensor output for the horizon scan.

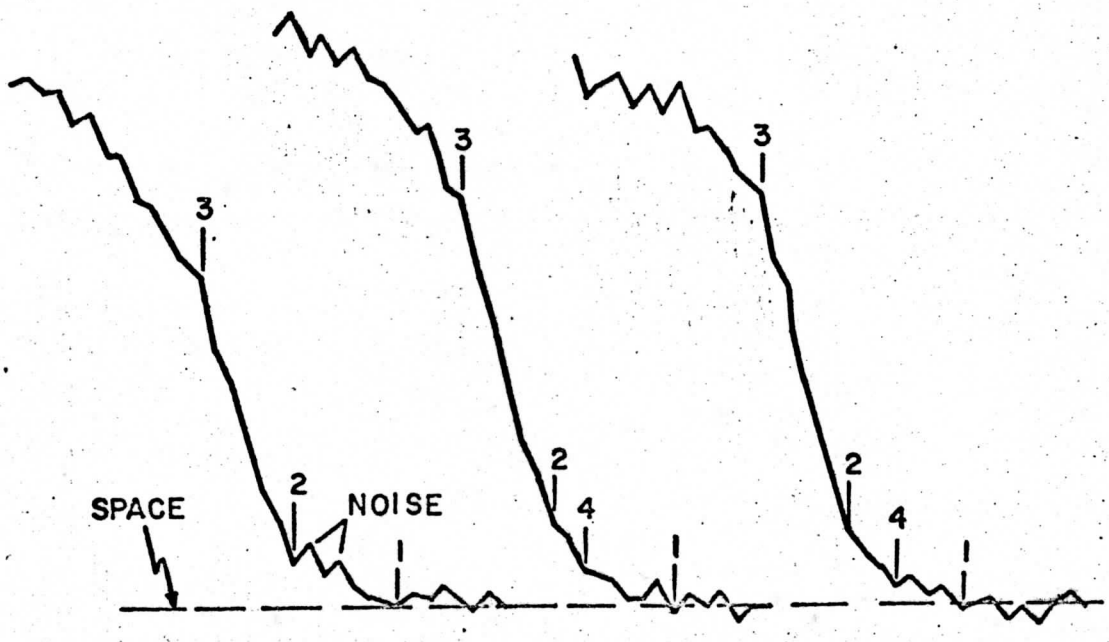

Figure 20. Examples of sensor output for the horizon scan.

REFERENCES

Bandeen, W. R., B. J. Conrath, and R. A. Hanel, 1963, "Experimental Confirmation from Tiros VII Meteorological Satellite of the Theoretically Calculated Radiance of the Earth Within the 15-Micron Band of Carbon Dioxide," J. Atmos. Sci., 20, 609-614.

Hanel, R. A., and D. Q. Wark, 1961, "Tiros II Radiation Experiment and its Physical Significance," J. Opt Soc. Amer., 51, 1394-1399.

Hanel, R. A., W. R. Bandeen, and B. J. Conrath, 1963, "Infrared Horizon of the Planet Earth," J. Atmos. Sci., 20, 73-86.

Kondratiev, K. Y., and K. E. Yakushevskaya, 1962, "The Angular Distribution of the Outgoing Therman Radiation in the Different Regions of the Spectrum," Proceedings of the International Symposium on Rocket and Satellite Meteorology, North Holland Publishing Co., Washington, D. C., April 1962.

Larsen, S. H., T. Fujita, and W. L. Fletcher, 1963, "Evaluation of Limb Darkening from Tiros III Radiation Data," University of Chicago, Mesometeorology Project Research Paper No. 18, Aug. 1963.

Lienesch, J. H., and D. Q. Wark, 1964, "Limb Darkening in the Infrared From Tiros Radiation Measurements," Symposium on Radiation Processes in the Atmosphere, Leningrad, 5-12 Aug. 1964.

Nordberg, W., W. R. Bandeen, B. J. Conrath, V. Kunde, and I. Persano, 1962, "Preliminary Results of Radiation Measurements from Tiros III Meteorological Satellite," J. Atmos. Sci., 19, 20-29.

Pilipowskyj, S., 1967, Personal communications.

Walker, R. G., C. V. Cunniff, and A. P. D'Agati, 1966, "Measurements of the Infrared Horizon of the Earth," Air Force Cambridge Research Laboratories, Environmental Research Papers No. 223, Sept. 1966.

Wark, D. Q., G. Yamamoto, and J. H. Lienesch, 1962, "Methods of Estimating Infrared Flux and Surface Temperature from Meteorological Satellites," J. Atmos. Sci., 19, 369-384.

Wark, D.Q., G. Yamamoto, and J.H. Lienesch, 1962, "Infrared Flux and Surface Temperature Determinations from Tiros Radiometer Measurements," U.S. Weather Bureau, Meteorological Satellite Report No. 10, Aug. 1962, and Supplement to Report No. 10, April, 1963.

Wark, D.Q., J. Alishouse, and G. Yamamoto, 1963, "Calculations of the Earth's Spectral Radiance for Large Zenith Angles," U.S. Weather Bureau, Meteorological Satellite Report No. 21, Oct. 1963.

SECTION B

VARIATIONS OF THE EARTH'S RADIATION BUDGET

by

THOMAS HENRY VONDER HAAR

VARIATIONS OF THE EARTH'S RADIATION BUDGET

Thomas Henry Vonder Haar
Under The Supervision of Professor Verner E. Suomi

More than 40 months of radiometric measurements from the first generation meteorological satellites are used to describe the radiation budget of the earth-atmosphere system. The geographical and temporal variation of the energy exchange between the earth and space is examined with the aid of mean annual and seasonal maps, zonal averages and mean global values.

Maps of the radiation budget components show that the lower latitudes are characterized by radiation patterns which depart considerably from the zonal mean value. These maps mark persistent features of the atmospheric circulation during each season which should be included in numerical models that simulate atmospheric conditions. Radiation budgets of latitudinal zones, including the polar regions, are used to note areas where changing surface and atmospheric conditions modify the large-scale radiation budget, even though the dominant effect is due to seasonal changes in incident solar energy. On a hemispheric scale, the measurements show that, despite the difference in surface features, the northern and southern hemispheres have nearly the same radiation budget over the course of one year. The mean annual planetary albedo was found to be 29% and the equivalent radiation temperature of the earth-atmosphere system is 252^{o}K. Over all time periods for which measurements were available the net radiation budget of the earth showed a small net gain, although the value is close to the limit of error in the measurements. When these new radiation budget data are combined with estimates of the other energy budget terms the net

poleward heat transport required by balance considerations is derived.

The study includes a complete error analysis and the satellite measurements compare well with the few available independent observations. The same sensors used to obtain most of the radiation budget data were used to derive a magnitude of the solar constant equal to 1.99 ± 0.03 cal . cm^{-2} . min^{-1}.

Approved Verner E. Suomi

Date Dec 15, 1967

TABLE OF CONTENTS

INTRODUCTION

Radiant energy exchange across the upper boundary of our earth-atmosphere system is the primary forcing function of large-scale atmospheric and oceanic circulations. For this reason atmospheric scientists have for many years sought more knowledge about the magnitude of this energy exchange and its variations with time and location. The significance of such information has recently been demonstrated by House (1965). Using satellite observations, he has shown that because of a lower planetary albedo in the tropical regions, the required poleward energy transport may be as much as 40 percent greater than was estimated from earlier studies. More observations of this type will give us a better indication of the driving force responsible for large-scale weather variations.

In the past, studies of the earth's radiative budget were based on theoretical calculations of the transfer of radiant energy through the atmosphere whose mean state and constituents were defined by available climatological data. One of the major difficulties that hindered these theoretical studies, the problem of radiative transfer in a cloudy atmosphere, still exists today. A critical synopsis of the earliest work of this kind was summarized by Lettau (1954) and some of the more recent studies are discussed by Budyko and Kondratiev (1964) and House (1965).

An immediate need for information about the earth's radiation budget has arisen because of the rapid development of numerical models of the atmosphere's circulation. These models do not require radiation observations as input parameters, but any model that properly describes the variations of atmospheric conditions must contain a method to account for radiant energy transfer. Thus, such a model can yield computed values of the radiation budget at the top of the atmosphere over various intervals of time and for different locations. Because measurements from satellite provide observed values of this same budget, average values of the observations, particularly of the net radiation, are a good control for the developing numerical models. With this in mind, the Committee on Atmospheric Sciences of the ICSU/IUGG[1] listed as one of five special areas of research to be emphasized in preparation for a Global Atmospheric Research Program (GARP) "...studies of the global distribution of radiation balance (net flux)..." A more recent report[2] reiterated this need by assigning a high priority to the task of obtaining a new radiation climatology.

The purpose of the present study is to use an extended time series of satellite radiation measurements to determine the mean radiative

---

[1] ICSU/IUGG, Second Report of the IUGG Committee on Atmospheric Sciences, 15 September 1966.

[2] ICSU/IUGG, WMO, COSPAR, Global Atmospheric Research Programme (GARP), Report of the Study Conference held at Stockholm, 28 June - 11 July 1967.

budget of the earth-atmosphere system at various locations and for different time periods, and to investigate variation from the mean state.

Late in 1959, the first successful observations of one component of the radiation budget (the infrared radiation from the earth) were obtained from sensors carried on the Explorer VII satellite (Suomi (1958), House (1965)). Several years later, sensors flown on some of the TIROS satellites obtained measurements of both infrared and reflected solar radiation from the earth-atmosphere system. These data were used by House (1965), Bandeen et al. (1965), Rasool and Prabhakara (1967), Winston (1967) and others to investigate the radiation budget over limited periods of time. Even during these time periods the data sampling was often quite limited and in most cases absolute values of the solar radiation budget parameters could not be obtained.

In the present study some of the TIROS data will be combined with additional satellite measurements in order to describe the earth's radiation budget as observed from our first generation of meteorological satellites. Thus, for the first time we will be able to examine more then 40 months of satellite observations in a single study. Because there were occasions when more than one satellite was operating over the same areas at the same time, it is possible to intercompare these data to check on the absolute accuracy of the measurements.

The available data may be separated into two time periods:

a) a period of intermittent observation: Dec. 1959 - June 1963

b) a period of continuous observations: June 1963 - Nov. 1965.

Excluding the Explorer VII values, all of the measurements will be used to derive mean values of net radiation, planetary albedo, and emitted longwave radiation on various spatial scales ranging from global mean values to averages over a 10 x 10 degree latitude-longitude region. The lower limit was necessary since most of the radiation data were obtained from sensors with low areal resolution. Because of the large data sample now available, mean values of the radiation budget parameters will be presented for each of the four seasons and for the annual case. This is possible because every portion of the year was observed in at least two different calendar years. In addition, selected averages that represent the radiation budget during specific years, seasons and months will be discussed and compared with the mean values.

The present study will determine the various spatial and temporal scales of the earth's gain in energy from the sun and its loss of longwave radiation to space. These results are derived from observations from near-earth satellites. As such, they represent only the first stage of a continuous program now underway that should vastly improve our understanding of the energy exchange between our planet and space, and of the response of our earth-atmosphere system to variations in that exchange.

1. THE RADIATION BUDGET: A COMPONENT OF THE ENERGY BUDGET

Energy transfer by radiation is only one component of the total energy budget of the entire earth-atmosphere system. The principle of energy conservation requires that the total energy budget must balance at every location and over all time periods, but the radiative portion of any such budget need not do so. It is precisely this radiative imbalance which can be measured from a satellite that is meteorologically important on various spatial and temporal scales.

Consider a column of unit cross-sectional area extending from the top of the atmosphere to a level beneath the surface (either land or ocean) where all energy exchange is assumed negligible. Starr (1951) and others have developed the detailed expressions for the energy budget of such a system. In a qualitative form these expressions may be represented by the concept of an energy balance equation where:

$$\begin{matrix}\text{ENERGY SOURCES} \\ \text{(or SINKS)}\end{matrix} + \begin{matrix}\text{ENERGY STORAGE} \\ \text{(or RELEASE)}\end{matrix} + \begin{matrix}\text{ENERGY EXPORT} \\ \text{(or IMPORT)}\end{matrix} = 0$$

Such a balance equation validly depicts the energy budget of any portion of the earth-atmosphere system. It does not, of course, represent the total <u>energetics</u> of the column since terms that describe the transformations (conversions) between the various forms of energy are not explicitly included.

The qualitative expression does demonstrate that any imbalance in the source and sink term must be compensated by a change in the total energy content of the column and/or by lateral energy exchange with neighboring columns. One portion of the total source (sink) term is the radiative exchange across the upper boundary or the column. The present study provides new results about this one energy transfer term.

1.1 The Radiation Budget of the Earth-Atmosphere System

A sketch of the radiation budget of the earth-atmosphere system is shown in Figure 1. The balance or imbalance of this budget on any space or time scale is given by the value of the net radiation RN_{EA}. Positive values show a net gain of energy across the top of the atmosphere by radiative processes and the total radiation budget can be written as:

$$RN_{EA} = I_0(1-A) - H_L \qquad (1)$$

where:

I_0 = direct solar irradiance (cal/cm^2 min)

A = the planetary albedo (%)

H_L = infrared radiation from the earth-atmosphere system (cal/cm^2 min)

The first term on the RHS of equation (6) equals the amount of solar energy absorbed in the earth-atmosphere system (i.e., $I_0(1-A) = H_a$). Note also that the product $I_0A = H_r$, the amount of solar energy

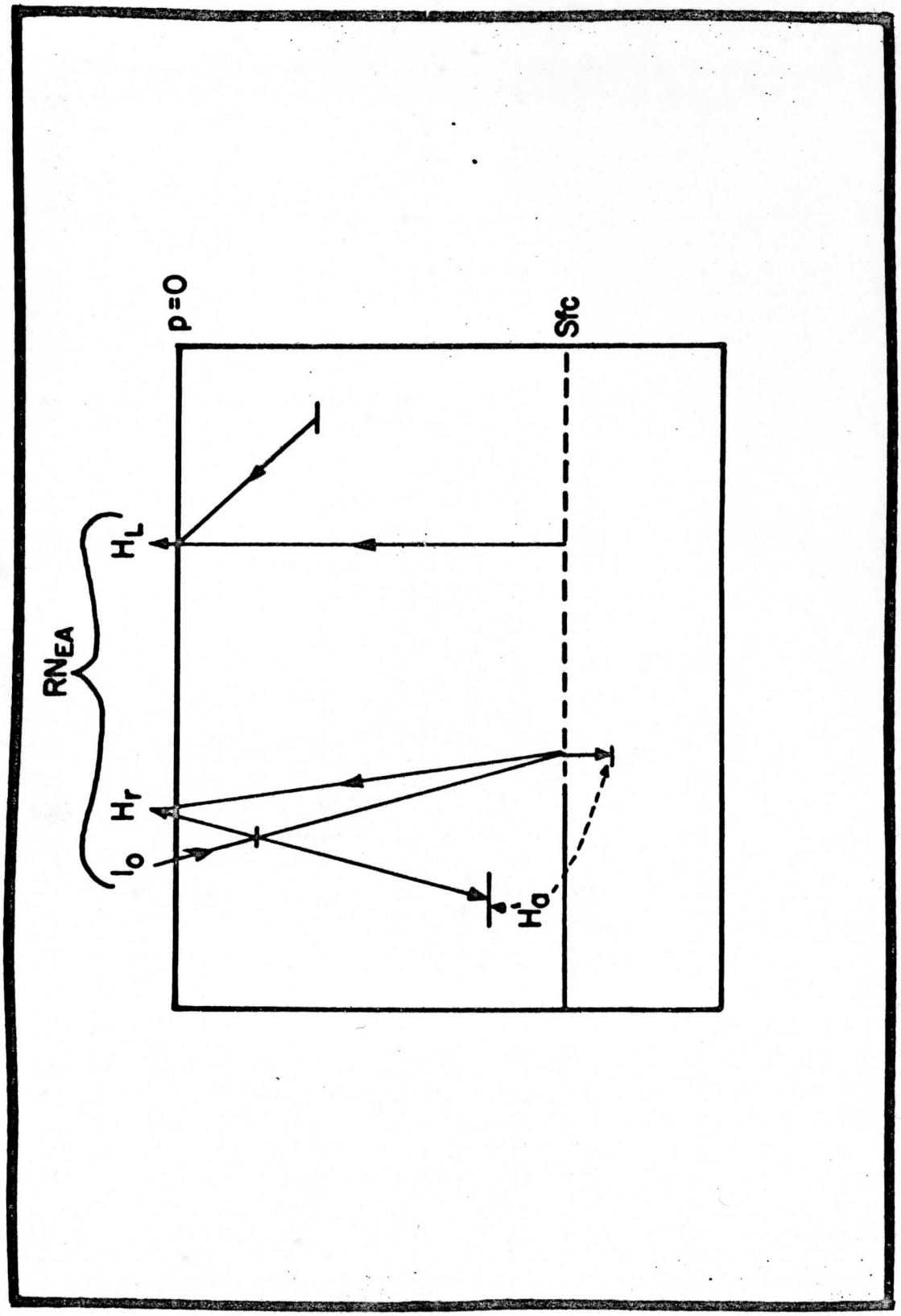

FIGURE 1: The radiation budget of the earth-atmosphere system.

reflected and scattered back to space from the earth's surface and the constituents of the atmosphere.

2. AVAILABLE SATELLITE DATA

Although more than 40 months of satellite observations are used in the present study, they were obtained from three types of sensing systems:

a) low resolution hemispheric sensors

b) low resolution flat sensors

c) medium resolution scanning radiometers

As seen in Figure 2, low resolution sensors provided most of the data (approximately 30 months). They were flown on Explorer VII, Tiros IV and VII and on experimental satellites. In order to investigate a continuous time series of satellite radiation data commencing in June of 1963, this study also includes 12 months of data from NASA's medium resolution, five-channel scanning radiometer carried onboard TIROS VII.

2.1 Radiation Sensing Systems

2.11 Low Resolution Sensors

The principles of the low resolution radiation budget sensors were first formulated by Suomi (1958). On Explorer VII and on the TIROS satellites, black and white hemispheres mounted on aluminized mirrors comprised the sensing system. The design and construction of these sensors has been detailed by B. Sparkman (1964) and House (1965). Through the years the basic principles of this experiment have been

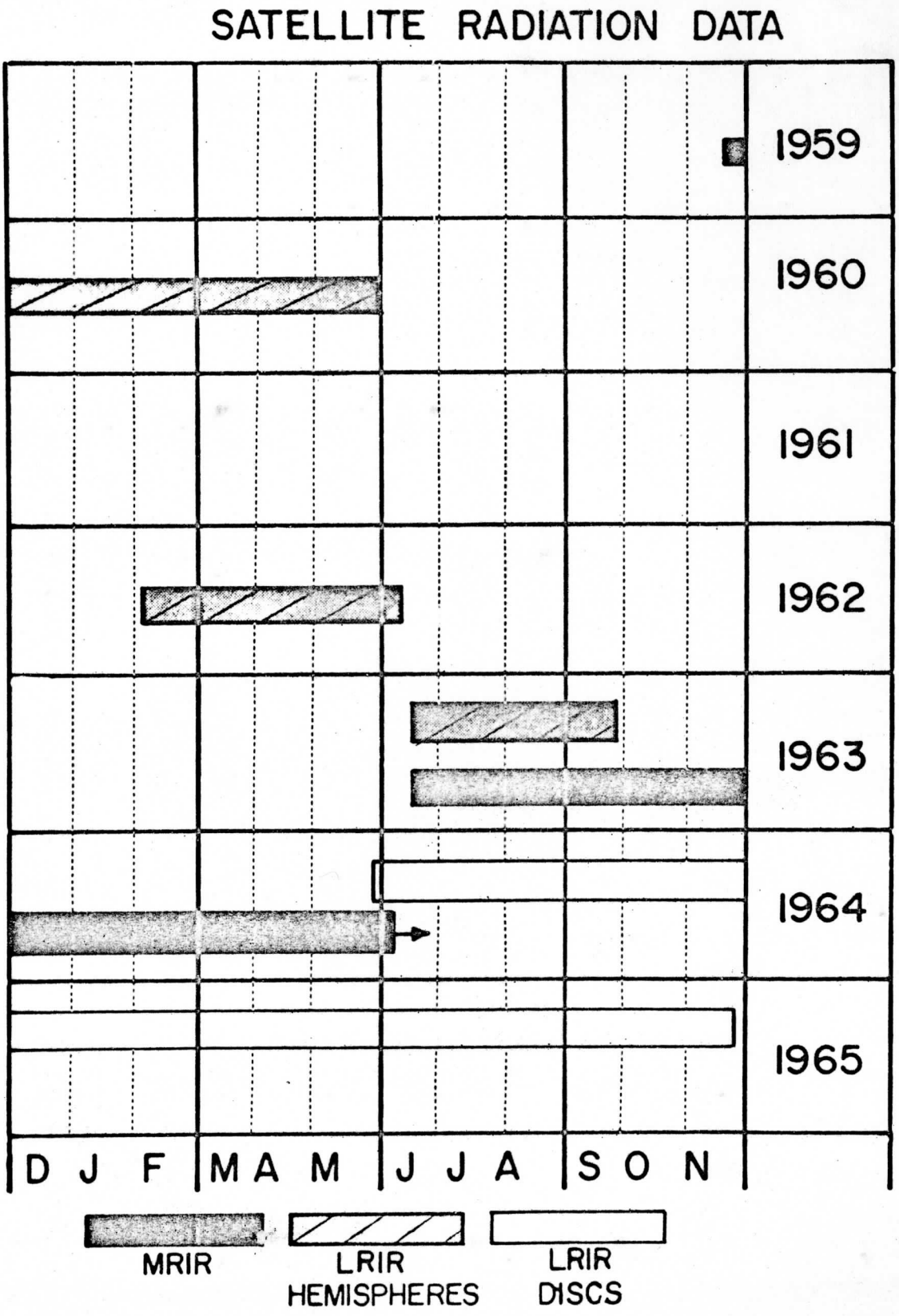

FIGURE 2: Summary of satellite radiation data (other MRIR observations during 1961 and after June, 1964 were not included in this study).

applied to different types of sensors, although the physical construction has been changed to meet the requirements of various spacecraft and to provide more accurate measurements. The experimental satellites carried a heat budget system consisting of black and white flat disc sensors. Improved versions of flat sensors are now being used onboard the ESSA operational satellites.

Radiation budget parameters (longwave radiation, albedo, and net radiation) are derived from the low resolution sensors by measuring the temperatures of the black and white sensors approximately every thirty seconds. These temperatures are used in energy balance equations that equate all gains and losses of energy to the sensors. The gains of energy by the sensors that are caused by direct solar radiation, solar radiation reflected from the earth-atmosphere system, and infrared radiation emitted by the underlying earth and atmosphere are obtained by solution of the energy balance equations. These sensor energy gains are reduced to effective irradiance values at a standard level (30 kilometers) by applying the appropriate geometrical relationships between the sensors and the radiation source (s). The techniques have been developed in detail by House and Suomi et al. (1967). Low resolution sensors can be calibrated against the sun after launch. This is a significant advantage and is done each time the satellite passes in or out of the earth's shadow. It is used both as a check for degradation of the sensors' responses with time and to supplement laboratory calibra-

tion data needed to deduce the irradiance terms. These "inflight calibration" procedures are also explained in the two references mentioned above.

2.12 Medium Resolution Sensors

A complete description of the medium resolution scanning radiometer is given by the NASA Staff Members (1964). This "beam" instrument had been flown on three satellites prior to TIROS VII and, unlike the LRIR, was not designed primarily as a radiation budget sensor since its real resolution was sufficient for even mesoscale investigations and imagery.

Data from this instrument were obtained from NASA in the form of grid-point maps. These map values were smoothed and used to form seasonal averages of diffuse albedo (reflectance) and longwave radiation in a manner similar to that described by Bandeen et al. (1965). The most important exception to their technique was that the MRIR albedo data were not adjusted by a factor needed to obtain global radiative equilibrium on an annual basis. (See section 2.22).

2.2 Special Characteristics of the Satellite Data

Although the data set used in the present study is the most extensive available at the present time, it differs substantially from an optimum system for measuring the earth's radiation budget as discussed by Godson (1958) and others. Ideally, measurements of the earth's

radiation budget should be made by continuously recording, accurate solar and thermal radiation sensors positioned over all locations at the "top of the atmosphere." In practice, the data used in this study were obtained from several sensors flown on different types of satellites, each having different viewing geometries (Figure 3) and orbital characteristics (Table 1).

Table 1

Satellite	Exp. VII	TIROS IV	TIROS VII	Disc LRIR
Latitudinal coverage	± 50°	± 50°	± 60°	± 85°
Longitudinal coverage	sporadic	360° with gaps	360° with gaps	360°
Local time coverage	24 hr*	24 hr*	24 hr*	0900-2100 LT

*Approximate orbital synodic cycles for Explorer VII, TIROS IV, and TIROS VII were 65, 60, and 75 days respectively.

The results of this study and their intercomparison with future studies are related to the special characteristics of the types of data that were used. For this reason, the following sections contain a discussion of the coverage in space and time of the satellite observations and the adjustments applied to some of the data.

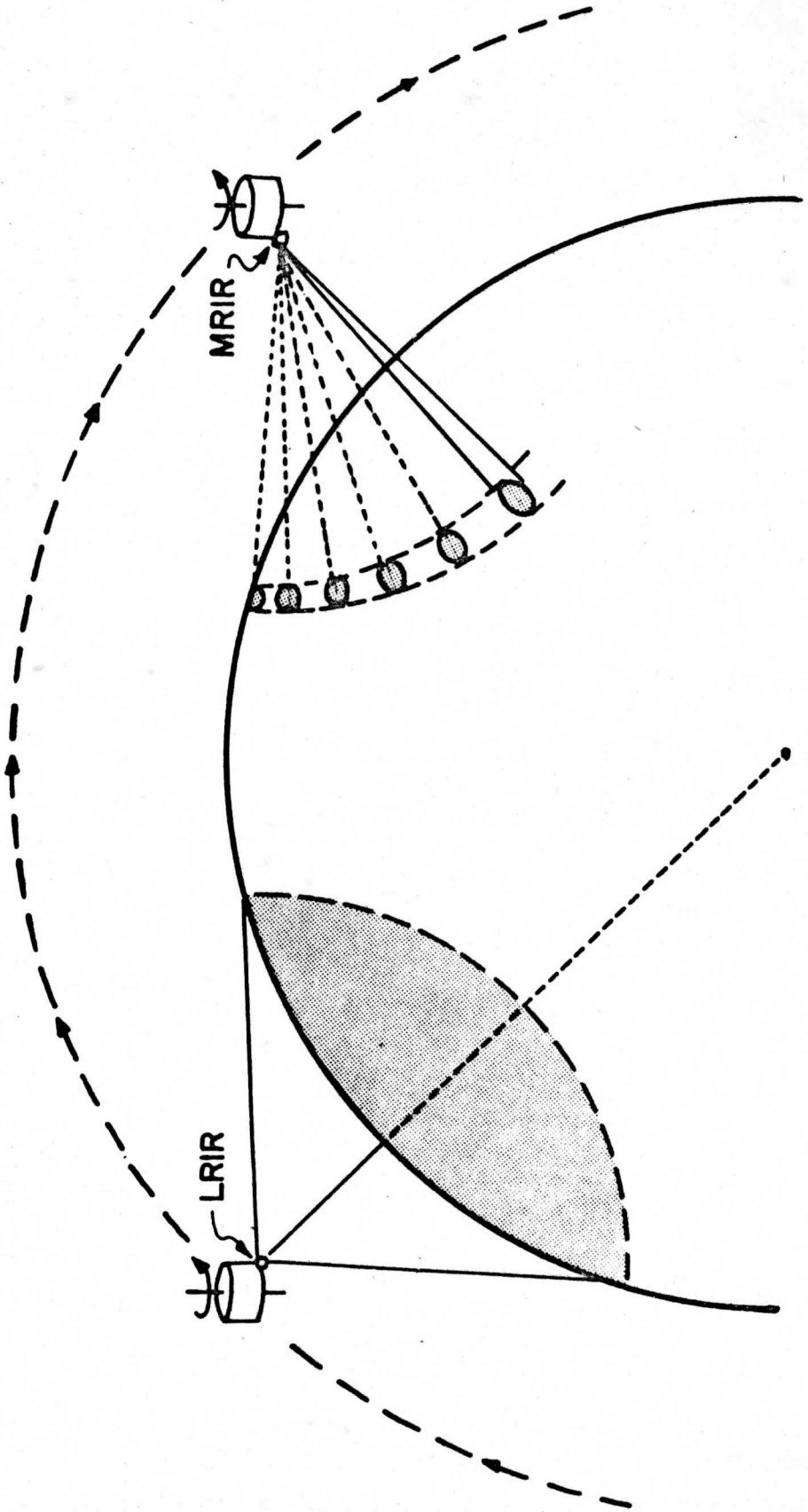

FIGURE 3: Simplified viewing geometries of the low and medium resolution TIROS radiation sensors.

2.21 Coverage in Time and Space

Data sampling distribution in space and time varied for each of the satellites. Some knowledge of this sampling pattern is necessary in order to interpret our results. Rados (1967) and Widger (1967) have recently discussed these problems in detail for the TIROS satellites. Within the operational lifetime of any radiation sensing system, spatial coverage is restricted:

a) in latitudinal extent by the inclination of the satellite's orbit to the equator

b) over some regions by a combination of onboard data storage capacity and ground station readout frequency

c) over other areas because data recording was not possible during the time of ground station readout.

Local-time sampling over a given location will vary if a satellite's orbit had a nodal precession that departs from -1.0 degrees per day (i.e., departs from the rate and direction of the earth's course around the sun). This departure was a common characteristic of the earlier satellites' orbits and as a result measurements at a location were obtained at all local times only during the course of one orbital synodic period.

The sampling constraints mentioned thus far apply specifically to measurements of the infrared irradiance which are obtained during both day and night. Albedo measurements, and the net radiation values derived in part from them, were obtained only when the satellites were

over the solar-illuminated portion of the earth. Thus, an additional constraint was placed on the albedo calculations in order to insure adequate illumination of the area viewed; no calculations were made if the local solar zenith angle was greater than 70 degrees.

All of the spatial sampling problems noted above are evident on the maps of the radiation parameters obtained from this study. Restrictions on the gross temporal coverage can be noted by comparing the albedo (daytime data) and infrared (day and night) maps. The sampling problems discussed above can be summarized with reference to Table 1 as follows:

a) spatial sampling was limited primarily in the north-south direction by the inclination of each satellite's orbit. However, in all cases measurements were made between $\pm$ 50° latitude and 18 months of pole-to-pole data are used.

b) The available satellite data represent the two extremes of sampling in time. On one hand, the satellites in moderately inclined orbits sampled over all local times, but only during the course of a finite time period never less than 60 days. At the other extreme, some data obtained from a near polar orbit was confined, over most of the earth, to only two local times.

In section 3 the effect of imperfect sampling on the accuracy of the results is considered.

2.22 Data Adjustments

The MRIR albedo data from TIROS VII were the only values used in this study to which special adjustments were applied after normal data reduction had been completed. This was necessary because these data have a history of uncertainty arising from post-launch sensor deterioration (NASA Staff Member (1964)) and because the "albedo" sensor measured only that portion of reflected solar radiation from 0.55 - 0.75 microns. Two adjustments were made:

a) one so that the data were more representative of the total (0.3-3 micron) albedo

b) a second adjustment so that the absolute magnitudes of the MRIR albedo values agreed with the albedo values obtained from the LRIR data when the sensors were viewing the same areas at the same time.

In this study the MRIR albedo data were obtained from NASA. The correction for degradation suggested by the NASA Staff Members (1964) was applied to all the albedo (reflectance) values. However, the factor 1.60 used by Bandeen et al. (1965) to adjust the albedo data so that global net radiation equaled zero was not used in the present study. Instead, adjustment (a), based on the work of Bartman (1967) was applied to the "red" MRIR (0.55 - 0.75 micron) albedo values to account for that portion of the reflected and scattered radiation (mostly in the

blue region) not viewed by the sensor. The adjustment was limited to the lower range of albedo values (i.e., to relatively cloud-free regions); and the largest adjustment increased the MRIR albedo values by a factor of 1.30.

These adjusted MRIR measurements were compared with LRIR albedo values obtained over the same regions during the same time periods. It was found that to force the LRIR and MRIR values to agree, each MRIR value had to be multiplied by the factor 1.18. Both Bartman (1967) and Solomonson (1966) have suggested that a factor of this size may account for the error in the MRIR albedo data due to the isotropic assumption implicit in the data reduction technique.

3. ACCURACY OF THE RADIATION DATA

Before we can discuss the radiation budget results, the accuracy of the albedo, longwave radiation and net radiation values must be established. The "first generation" satellite sensors that provide the measurements summarized in this paper were relatively simple instruments. The satellites did not carry active onboard calibration equipment and none of the sensors were recovered for recalibration in a laboratory. However, most of the data used in this study were obtained from low resolution sensors (LRIR) which were designed so that an in-flight calibration against the sun was possible twice each orbit. By using these special measurements as well as pre-launch laboratory tests and comparisons with independent measurements made over the same areas at the same times it was possible to obtain accuracy estimates for the albedo and infrared radiation measurements. Thus, the complete error analysis proceeded as follows:

1. Accuracy estimates were derived for the disc LRIR measurements.
2. The MRIR data were examined by comparing them with disc LRIR data obtained over the same regions at the same time.
3. Error estimates obtained by House (1965) were used for the hemispheric LRIR values.

3.1 Albedo and Longwave Radiation Accuracy Estimates

3.11 Random Error

The effect of random error is negligible because the results presented in this study are values averaged over space and time. The smallest sample used to obtain an average (i.e., the mean albedo of a 10 x 10 degree region during one specific season) was about 400 measurements. The largest amount of data (5×10^8 observations) were combined to obtain the mean annual net radiation budget of the entire earth. Because only such large samples were used, any random error arising from quantization of the satellite signal, noisy data, etc., has been removed from the results.

3.12 Bias Error

A special kind of bias error may occur in satellite radiation data. It is caused by deterioration of some part of the experiment due to exposure to the environment of space. In the case of the disc LRIR such an error can be caused by a drift in the electronics, by a change in the spectral characteristics of the sensors, or by physical damage to the experiment. Fortunately, these sensors' long-term stability can be checked each time the satellite passes in and out of the earth's shadow by observing their response to the (constant) step function of direct solar radiation. The disc LRIR data used in the present study were

periodically checked in this manner and no apparent degradation of the black sensors was observed. The white sensors did change response with time but the data reduction technique described by Suomi et al. (1967) was used to remove the effect of this degradation from the measurements used in this study. Thus, no bias error due to sensor degradation should be present in the disc LRIR data.

Additional bias errors that affect the albedo and longwage radiation measurements may be categorized as:

a) determinate bias error (i.e., an error whose magnitude and direction can be evaluated with good confidence, and

b) indeterminate systematic error (i.e, an error whose magnitude and direction can only be inferred indirectly by referring to some independent standard, if one exists).

Two kinds of determinate bias errors may occur in the disc LRIR albedo and infrared radiation values; they are:

a) error in the original temperature calibration of the instruments

b) error due to inaccurate determination of sensor calibration constants.

Each of these errors can act in a positive or a negative direction. A quantitative estimate of the bias error introduced into the radiation budget parameters by these errors was made by using a technique analogous to that of House (1965). This straightforward scheme uses reasonable estimates of the inaccuracies of the sensor temperature

measurements and calibration constants to evaluate differentiated forms of the albedo and longwave radiation equations. Results showed that the most probable bias errors in the albedo and longwave radiation data were $\pm$ 1% and $\pm$ 0.01 cal $\cdot$ cm^{-2} $\cdot$ min^{-1}.

The most probable error is derived quantitatively by assigning a reasonable magnitude and direction to various possible errors. In this way compensating effects (i.e., arising from differences in two quantities, each having a bias error with the same magnitude and direction) are allowed in the error analysis. (This method may be contrasted with a maximum absolute error estimate which would not include compensating effects.) For example, we assume that all sensor temperature measurements may be either too high or too low since there is no reason to expect a sign change after launch. Indeed, if the thermistors had a drift of calibration due to the effects of high energy radiation in space, each would drift in the same direction since each thermistor is fabricated from the same material. Similarly, if the materials from which the sensors were fabricated deteriorated due to the space environment one would expect that these changes would also have the same sign. For these reasons, the most realistic view is to assume that any additional bias error arising from sensor characteristics may add to the magnitude of the errors already evaluated but should not change their directions.

The albedo and longwave radiation measurements may contain additional, indeterminate, systematic error. Examples are:

a) errors due to the sampling in time and space

b) errors due to the isotropic assumption

Point (a) arises from the sampling constraints discussed in a previous section, and (b) results from the data reduction requirements. We can obtain an estimate of the magnitude and direction of these possible bias errors by considering several other studies.

Spatial sampling by these LRIR sensors was quite good. All areas were viewed and when zonal and global averages were formed, each region or zone was weighted equally in forming the mean. The temporal sampling problem is worse because, over most of the earth, disc LRIR data were obtained at local times near 0900 and 2100 hours. A first approximation to information about the diurnal variation of globally averaged albedo and longwave radiation data has been presented by Astling and Horn (1964) and by Vonder Haar and Hanson (1967). These studies show general agreement and results from the latter are shown in Figure 4. Both of the studies contain spatial sampling problems of their own and are representative of limited time periods (26 and 90 days, respectively). When Figure 4 is considered, it is apparent that albedo and infrared measurements made only near 0900 and 2100 may contain bias errors of $+0.015$ ly $\cdot$ min^{-1} and -2% since the values that represent

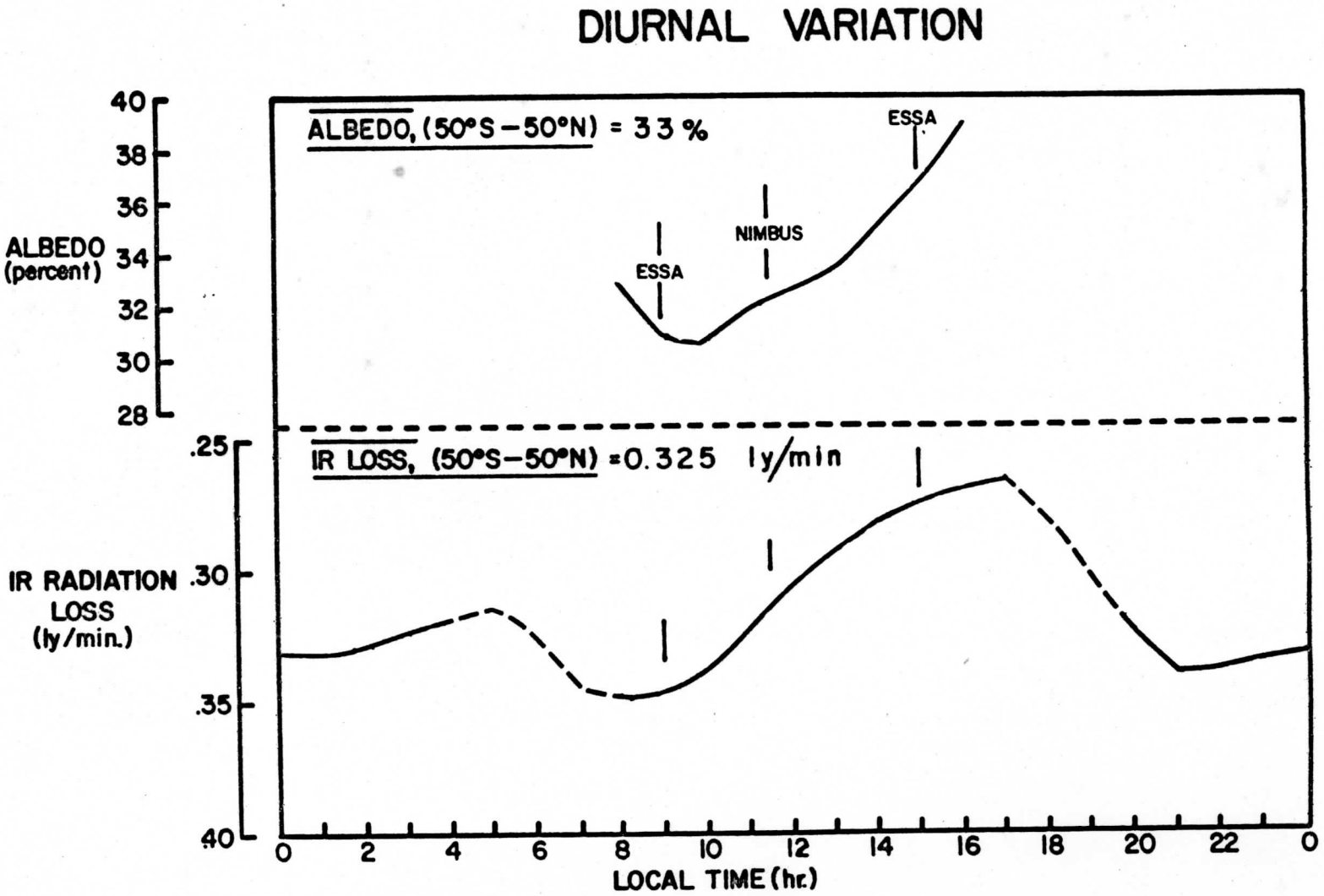

FIGURE 4: Diurnal variation of planetary albedo and outgoing longwave radiation based on TIROS IV measurements.

these times in the figure differ by these amounts from the daily average.

The anisotropic nature of the radiation measured by the satellites, especially the reflected and scattered solar radiation, causes difficulties in the use of the MRIR satellite radiation data for many purposes. (See (Bartman (1967).) Estimates of the error involved by neglecting the anisotropic effect on these data for radiation budget studies have been made by Ruff et al. (1967). They conclude that average values of absorbed solar energy (H_a) derived from MRIR albedo values would not be in error by more than 5%. Bignell (1962) has discussed the same problem for the hemispheric sensors. Based on his results, House (1965) states that albedo and longwave radiation averages obtained from these sensors may be in error by 1 or 2%, even if persistent anisotropic conditions (i.e., limb brightening and darkening) occur. Since the flat disc sensors give less weight to limb radiation than hemispheres, bias error arising from such effects should be even less.

The above discussion of possible indeterminate bias error in our results shows that we have no firm basis for raising (or lowering) the bias error estimates derived from an evaluation of determinate bias error. It is important to note that a correction for bias error would require that all absolute values of a given quantity would be raised or lowered the same amount and in the same direction.

An additional fact concerning any LRIR error analysis has been discussed by House (1965) and Suomi et al. (1967). They have shown that

albedo and longwave radiation values from LRIR experiments are interdependent in a manner that causes any bias error in either of them to have an opposite effect on the other (i.e., if the albedo is too high the longwave values are too low). In section 3.22 it is shown that this effect is important in minimizing the error in net radiation values derived from LRIR measurements.

3.13 Accuracy Tests

In order to check the accuracy limits determined above, two tests were performed. They consist of comparisons between disc LRIR measurements and independent observations. The tests were essentially limited by the scarcity of reliable independent data.

During the southern hemisphere winters of 1964 and 1965, disc LRIR measurements of outgoing radiation were made over the dark polar regions. At the same time, balloon-borne radiometers launched from several locations in the Antarctic measured the total upward longwave radiation from the earth-atmosphere system. The following winter, 1966, the first radiation budget measurements from the second generation satellites were obtained from a MRIR sensor on NIMBUS II. In the table following they are compared with the LRIR data.

AVERAGE LONGWAVE RADIATION FROM THE REGION 70-90 S. DURING JUNE-JULY-AUGUST

Data	Source	Date	H_L (cal·cm^{-2}·min^{-1})
Disc LRIR	present study	1964 and 1965	0.175 ± 0.01
Radiometersonde	Kuhn and Cox (1967)	1964 and 1965	0.18
Nimbus MRIR	Raschke et al. (1967)	1966 (June and July)	0.18

The comparisons agree remarkably well and serve as a good test for our LRIR accuracy estimates. They do not, however, give information about daytime LRIR measurements nor about the diurnal sampling problem. To test the LRIR values over all time periods and over many locations, they were compared with MRIR measurements made over the same regions during the same time periods. In Figure 5 a scatter diagram of zonal averages of LRIR longwave radiation values vs. concurrent MRIR values is displayed. These values depart from a one-to-one relationship by less than ± 0.02 cal · cm^{-2} · min^{-1}. Although the MRIR data are not of high accuracy, this agreement between two completely independent data sets is very encouraging. A similar test of albedo data was not possible because the original MRIR values were erroneous. (See 2.22.)

In summary, tests of the disc LRIR measurements against independent observations show that these data have absolute accuracies within

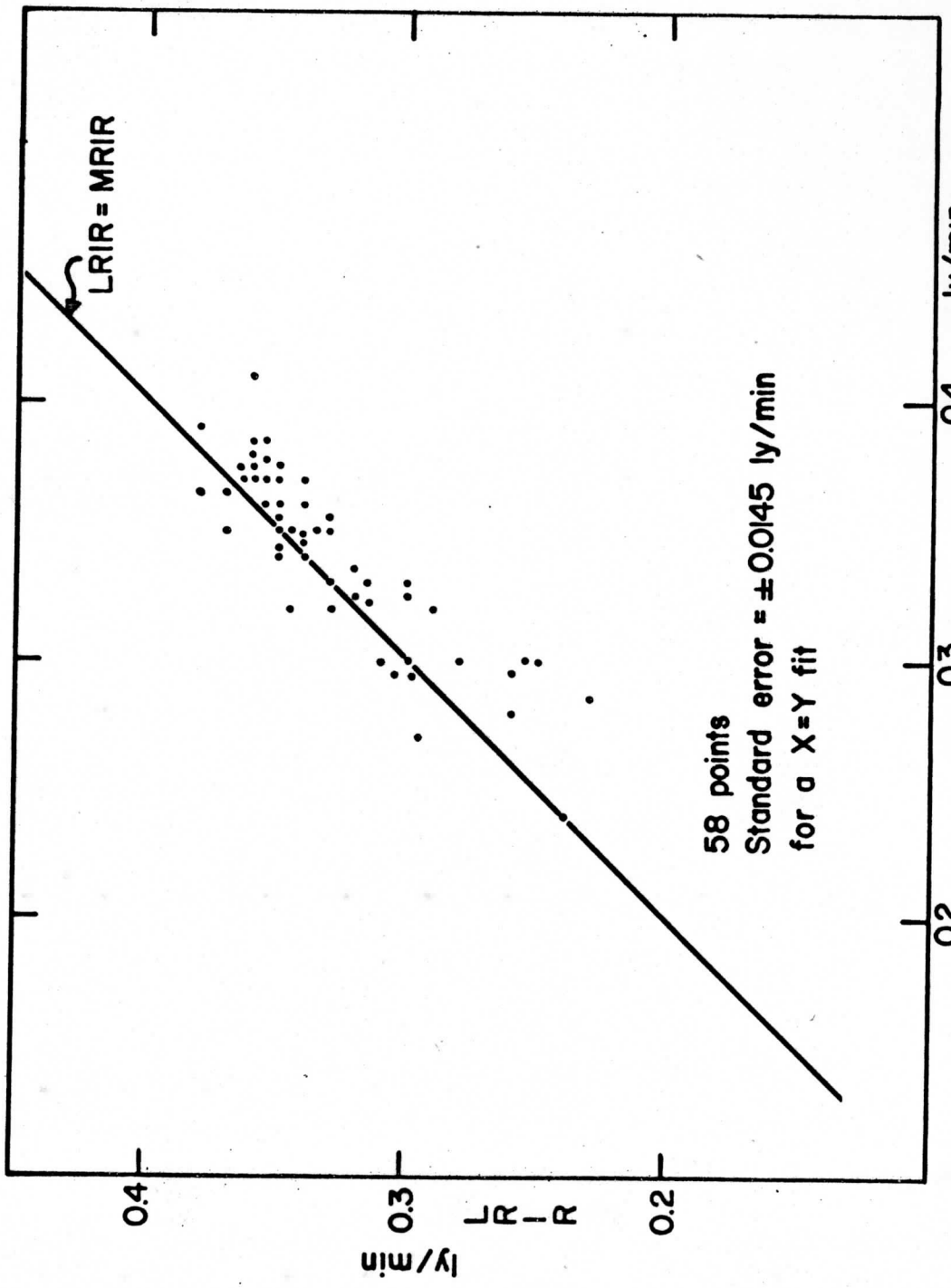

FIGURE 5: Comparison of zonally averaged longwave radiation measurements obtained from LRIR and MRIR sensors during the same time periods.

the error limits assigned to them. Apparently the local time sampling problem does not introduce significant indeterminate bias error at least on the area scale of a latitudinal zone. Because of the interdependence of the LRIR albedo and infrared values already mentioned, the tests performed on the infrared data also imply that the LRIR albedo values do not contain large bias errors. A third, though somewhat indirect, accuracy check is provided in Appendix A where the disc LRIR sensors were used to derive a very reasonable value of the solar constant.

3.2 Net Radiation Error Analysis

Values of net radiation used in the present study were derived from equation (1) by using albedo and infrared radiation measurements together with incident solar radiation values computed by assuming a magnitude of the solar constant.

3.21 Effect of Albedo and Longwave Radiation Accuracy

Before deriving the most probable error in the net radiation data, it will be helpful to illustrate the effect of various albedo and infrared radiation bias errors on the accuracy of a typical net radiation value. By differentiating equation (1), we obtain:

$$dRN_{EA} = dI_0 - I_0 dA - A dI_0 - dH_L \qquad (2)$$

We assume the solar constant is known perfectly ($dI_0 = 0$) and equals 2.00 cal · cm^{-2} · min^{-1}. Using representative values of $I_0 = 0.5$ cal · cm^{-2} · min^{-1}, A = 30% and $H_L = 0.33$ cal · cm^{-2} · min^{-1}, we have determined dRN_{EA} for different magnitudes and directions of the possible errors dA and dH_L. The results are shown in Figure 6 as a nomogram. In the first and third quadrants of this figure the net radiation bias errors are minimized. This results when albedo and longwave radiation errors are in opposing directions. When the inverse is true, the resulting difference between two large numbers can cause errors that are twice as large.

Figure 6 is useful in considering the effect of our A and H_L error estimates on net radiation values derived from them. This nomogram shows that errors $dA = \pm 0.01$ and $dH_L = \pm 0.01$ would result in net radiation errors of ± 0.005 or ± 0.015 cal · cm^{-2} · min^{-1} (dashed circles), depending on the direction of these albedo and longwave radiation errors. As mentioned in 3.12, the LRIR observations which comprise 80% of the data used in this study do in fact have inversely related albedo and infrared bias errors that would make the smaller value ($\sim \pm 4$ watts/m^2) the reasonable choice, if the solar constant were known perfectly.

3.22 Effect of Uncertainty in the Solar Constant

Recently, Drummond et al. (1967) have reported some preliminary results from an experiment designed to measure the solar constant from

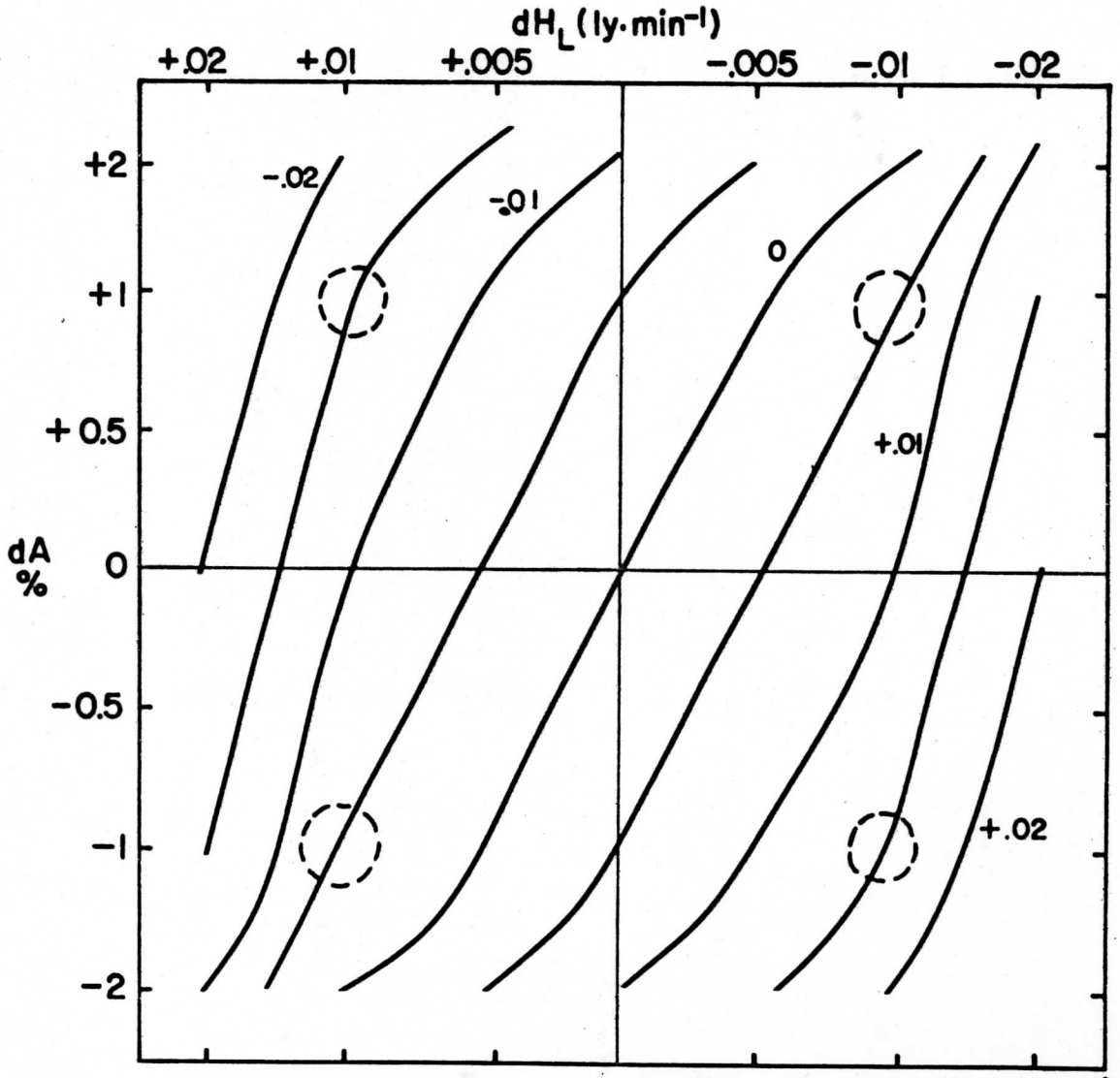

FIGURE 6: Nomogram showing absolute error in net radiation (cal . cm^{-2}. min^{-1}) resulting from albedo and longwave radiation measurement errors.

a high altitude aircraft. They obtained a value of 1.95 ly · min^{-1} which may have an uncertainty of less than 2%. Until these data became available most recent studies have used the values of 2.00 ± .04 (Johnson (1954)) or 1.98 ± 0.1 (Nicolet (1951)) derived from measurements made at the earth's surface. Because the absolute magnitude and the possible error of the solar constant is important to the present radiation budget study, satellite observations from the disc LRIR sensors were also used to derive a value of this parameter. The results of this first measurement of the solar constant from a satellite yielded a magnitude of 1.99 ly · min^{-1} ± 0.03 (± 1.5%). After considering each of the measurements mentioned above, a value of 2.00 ± 0.03 was chosen for use in the present study.

Because of the uncertainty in I_0, our net radiation error estimate cannot be obtained from Figure 6. Rather, it is necessary to reevaluate equation (2) with typical radiation budget values and their associated absolute errors.

The following data were used:

Parameter	Value	Percent Error	Absolute Error
Insolation (I_0)	0.5 ly/min	1.5%	± 0.0075 ly/min
Longwave radiation (H_L)	0.33 ly/min	3%	± 0.01 ly/min
albedo (A)	30 (percent)	3.5%	± 1.0 (percent)

From this evaluation we obtain a most probable bias error for net radiation (dRN_{EA}) of $\pm$ .01 cal $\cdot$ cm^{-2} $\cdot$ min^{-1} ($\sim \pm 7$ watts/m^2). This error results in equal measure from uncertainties in the solar constant and from the inacccuracy of the albedo and longwave radiation measurements, when the latter errors are inversely related.

3.3 Error Analysis Summary

The error analysis presented in this chapter has been directed primarily toward the disc LRIR data even though 40% of the measurements used in this study were obtained from two other sensing systems. However, the MRIR longwave radiation values are shown in 3.13 to have an accuracy comparable to the disc LRIR data and in 2.22 the medium resolution sensor's albedo measurements were adjusted to agree with the LRIR data, this forcing their accuracies to be the same. In addition, House (1965) has provided an error analysis for zonal averages of hemispheric LRIR data and his estimates fall within the error limits derived in this section.

For these reasons, all the data used in this study were assigned the following most probable bias errors:

Longwave radiation (H_L)	$\pm$ 0.01 cal $\cdot$ cm^{-2} $\cdot$ min^{-1}
albedo (A)	$\pm$ 1.0 percent
net radiation (RN_{EA})	$\pm$ 0.01 cal $\cdot$ cm^{-2} $\cdot$ min^{-1}

Because of large data samples, no random error should influence these results. These error limits are valid only if no large indeterminate bias error influenced the measurements, but tests using independent observations did not suggest the presence of such errors. Over a typical range of averaged observations these absolute errors yield percentage errors of 3 - 5% and 2 - 8% for longwave radiation and albedo data respectively. Of course when two regions have the same albedo, the error in reflected shortwave radiation (H_r) is less where the incoming solar radiation is greater.

These error estimates affect the various questions treated in this study to different degrees. Because all random error has presumably been removed by averaging over space and time, and because all apparent sensor degradation bias has been resolved, relative values of the radiation parameters can be considered without concern. Of course, the relative error in the net radiation results will be less over regions where the earth-atmosphere system has a large radiation imbalance. Thus, the tropical latitudes and the winter polar regions can be observed more accurately. Indeed, these regions are most important from an energy budget viewpoint. One problem that requires great accuracy cannot be considered in the present study; it is the longterm (climatological) warming or cooling of the earth-atmosphere system. We can, within the absolute accuracy of our measurements, examine the balance

or imbalance of the radiation budget over different areas at various time periods, locate the primary radiation source and sink regions, compute required energy transports and investigate other similar radiation budget problems with an extended time series of observational data.

4. RADIATION BUDGET RESULTS

The exceedingly large amount of albedo and longwave radiation measurements (5×10^8) obtained from the satellite experiments were used to form averages over different spatial and temporal scales. We begin our discussion of these results by considering maps of albedo, longwave radiation and net radiation which show the geographical variations of the radiation budget. After that, the scale of spatial averaging is increased to form the budgets of individual latitudinal zones, hemispheres and the entire earth.

The observations used to form averages for any time period (i.e., a season) are shown in Figure 2 although none of the Explorer VII data were included in the results presented in this section. Mean albedo values were obtained by averaging reflected solar radiation and insolation values separately and deriving a mean albedo from their ratio. The average insolation for different locations and time periods was computed based on a solar constant of 2.00 $cal \cdot cm^{-2} \cdot min^{-1}$.

4.1 Geographical Variations

The satellite observations used in this study include measurements during each of the four seasons obtained in at least two calendar years. Thus, for the first time, we can derive mean seasonal and annual maps

of the radiation budget parameters.[1] Such mean maps are useful for examining regions within latitudinal zones where the radiation budget differs significantly from the zonal mean value. For this reason, "high" and "low" regions noted on the maps were chosen relative to the average for that time period and zone rather than to some absolute magnitude. A 10x10 degree latitude-longitude grid was used to construct the maps since the low resolution sensor data requires this limit on the spatial resolution. Thus, the maps show sufficient detail for a study of the radiation budget of large areas, but cannot be used to examine the budget at a specific location.

Spatial and temporal sampling problems were discussed in section 2.21 and some of the constraints mentioned there are evident on the maps. All the maps contain both solid and dashed isolines and the dashed lines cover regions where the number of satellite observations at a grid point was approximately 25% less than the number of grid points analyzed with solid lines. Isolines of albedo, longwave radiation and net radiations were drawn at intervals greater than the error limits of the data discussed in section 3.3. The map values for regions where a strong diurnal variation of cloudiness may be expected must be interpreted with care since more than one-half of our observations were obtained near 0900 and 2100 local times. This problem is discussed in sections 2.21, 3.12 and 6.0.

A complete set of maps (about 200) describing the radiation budget

[1] Others (Rasool (1964), Winston and Taylor (1967)) have used TIROS radiation data to obtain maps for selected months and seasons and recently Raschke and Pasternak (1967) have done the same with several months of NIMBUS data.

for all the time periods (months, seasons and years) observed by the first generation satellites will be presented in a separate atlas of the earth's radiation budget.

4.11 Mean Seasonal Budgets

(a) Longwave Radiation. Mean seasonal maps of the longwave radiation (H_L) from the earth-atmosphere system are shown in Figures 7 and 8. Such maps are a good indication of atmospheric conditions because clouds play a dominant role in determining the magnitude of the outgoing infrared energy. In the absence of clouds, the temperature and moisture content of the atmosphere and the local surface temperature strongly influence values of H_L.

The most significant feature common to all four seasons is the contrast between the zonal pattern of isolines in the higher latitudes of both hemispheres and the presence of many local regions of high and low outgoing radiation in the tropics and subtropics. In these seasonal maps the zonal patterns result from many observations obtained over both clear and cloudy regions in the latitudes where migratory storm systems dominate the circulation pattern. The highs and lows found at lower latitudes show persistent features of the earth-atmosphere system during the respective seasons. In each hemisphere the boundary between these two types of radiation patterns moves north and south in phase with the seasonal path of the sun and from winter to summer both boundaries range from twenty to forty-five degrees

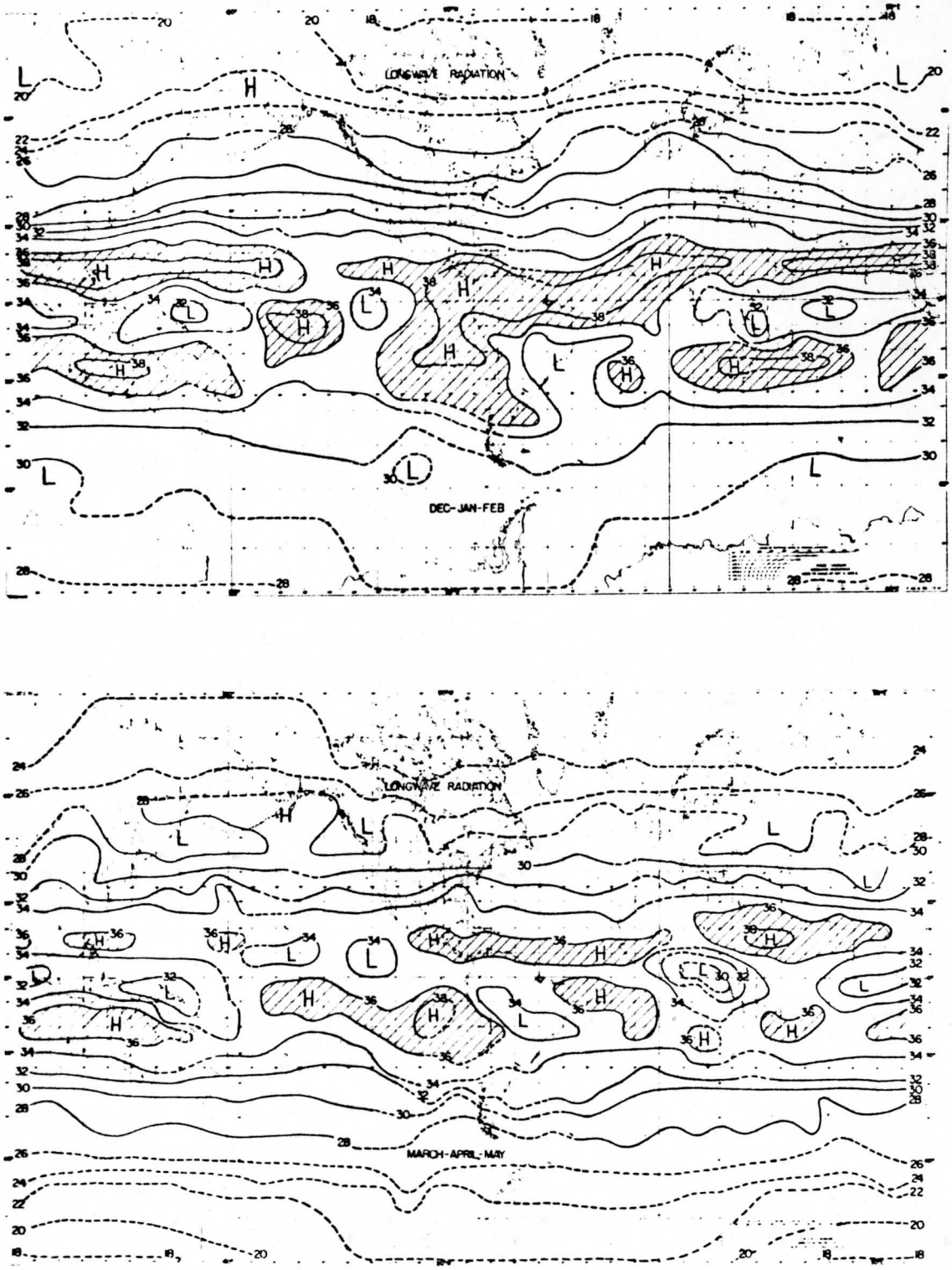

FIGURE 7: Mean values of outgoing longwave radiation from the earth-atmosphere system (H_L) during Dec.-Jan.-Feb. and Mar.-Apr.-May. Units are 10^{-2} cal . cm^{-2} . min^{-1} and regions of $H_L > 0.36$ cal . cm^{-2} . min^{-1} are shaded.

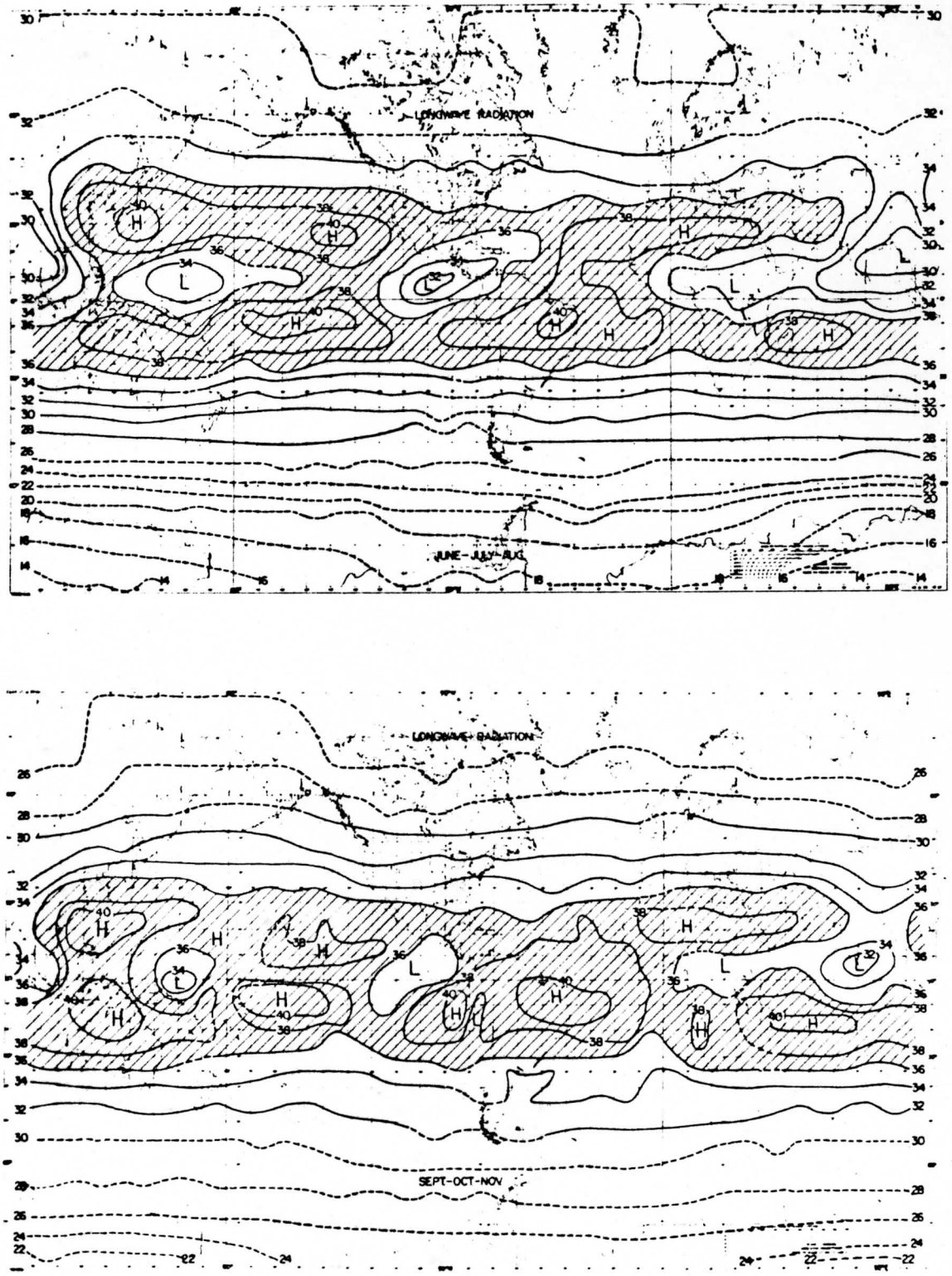

FIGURE 8: Same as Figure 7 for June-July-Aug. and Sept.-Oct.-Nov.

respectively, thus marking the equatorward intrusion of storm tracks each season. The east-west continuity of the boundaries is quite strong but some breaks do occur. These breaks show as weakened north-south gradients of outgoing longwave radiation (i.e., the south-central Pacific, south Atlantic and the region near 20°N, 140°W during DJF; the region of the summer monsoon and near the Caribbean during JJA). Winston (1967) has already demonstrated that variations in this gradient are related to the mid-latitude circulation pattern in the northern hemisphere, thus pointing out a good application of these maps for regions where the circulation pattern is not well known.

Within the regions where the outgoing longwave radiation decreases toward the poles at all longitudes the effect of the distribution of land and ocean is noticeable, especially in the northern hemisphere. Thus, in DJF the isolines of H_L drop southward over the continents which are colder than oceans at the same latitude. In the southern hemisphere lower values of outgoing radiation are observed over the Antarctic continent than over nearby ocean regions. Seasonal variations in the mean temperature of the earth and atmosphere at mid-latitudes are also evident in the poleward gradients of longwave radiation. These gradients are strongest during the winter seasons and weakest during summers. With the exception of the zone near 50°N during MAM, seasonal averages of longwave radiation from the earth-

atmosphere system poleward of 40° latitude can be well represented by zonal mean values when the continentality effect is considered.

On the other hand, these maps show that zonal averages of outgoing radiation over one-half the earth (30°N - 30°S) would give only a rough approximation to the true value at most longitudes. This is due to the pronounced nonzonal, sometimes even meridional, orientation of the regions of high and low outgoing radiation. An elementary climatological view of these regions would mention a northern and southern subtropical zone (warm, dry and cloudless) broken by a tropical convergence region (warm, wet and cloudy). We will discuss the major departures from this simple picture as seen in the seasonal H_L maps.

High values of emitted infrared energy that mark the northern subtropical zone show definite seasonal variations at most longitudes. Near 140°W for example, lower values of H_L indicate cloudy conditions during the winter and spring but a strong high covers the same region for the other six months. The entire band is strongest during the summer and least well defined in MAM. The regions of maximum outgoing radiation have values greater than 0.40 cal $\cdot$ cm^{-2} $\cdot$ min^{-1} and the only maxima that is observed near the same longitude during all four seasons occurs at 120°E.

In recent years continuous photographic and radiometric observation of the tropical regions has shown that earlier ideas regarding the position and intensity of cloudiness associated with the convergence zone require modification (i.e., Kornfield, et al. (1967)). Lower values of outgoing radiation from this region identify it on the mean seasonal H_L maps. Within the spatial resolution of the radiation sensors, the maps show that this cloudy belt is definitely discontinuous and marked by persistent regions of low outgoing radiation at preferred locations each season. Low regions with a meridional orientation (120°W during DJF and MAM, 90°E in MAM) may correspond to the double-ITC areas noted by Kornfield et al. In several seasons the radiation maps show the presence of cloudy regions extending from the convergence zone across the subtropics and into the mid-latitudes. As a whole, the convergence zone is strongest during MAM and most discontinuous in SON. Four primary H_L minima (20°, 90° and 160°E; 110°W) remain near the same longitudes each season and the cloudy belt is not well defined in the Atlantic sector except during MAM. The lowest values of outgoing radiation in this zone (0.30 $cal \cdot cm^{-2} \cdot min^{-1}$) are found over the summer monsoon.

In the southern hemisphere the subtropical region of high outgoing radiation is best defined during Spring. Primary maxima, exceeding 0.40 $cal \cdot cm^{-2} \cdot min^{-1}$, persist near 40° and 130°E, 90° and 150°W.

Lower values of H_L denote major breaks in the zone over the west central Pacific and east of South America, particularly during the summer and fall. Along with its northern counterpart and the tropical convergence zone, this subtropical belt has a seasonal latitudinal displacement in phase with the solar declination.

(b) Albedo. Mean seasonal albedo maps (Figures 9 and 10) were also obtained from the satellite measurements. These maps are less representative of atmospheric conditions than the infrared data since the effects of snow, ice and deserts emphasize land versus ocean differences better than thermal effects. In fact, the mean albedo data provide more information about the type of surface in view (and in the case of clouds, the persistence of cloudiness) than about the shortwave energy budget. However, since incident solar radiation varies only as a function of latitude across these mean maps, values of reflected and absorbed solar energy can be inferred from them.

In general, the albedo and longwave radiation maps show the expected inverse relation between the two quantities. Within the tropics and subtropics most regions of high outgoing longwave radiation have mean albedo values less than twenty percent. In the south-central Pacific and near the east coast of Brazil the measured albedos were less than 15% during all seasons except DJF. Low values of H_L near the equator correspond with albedo values of more than 30%. In the

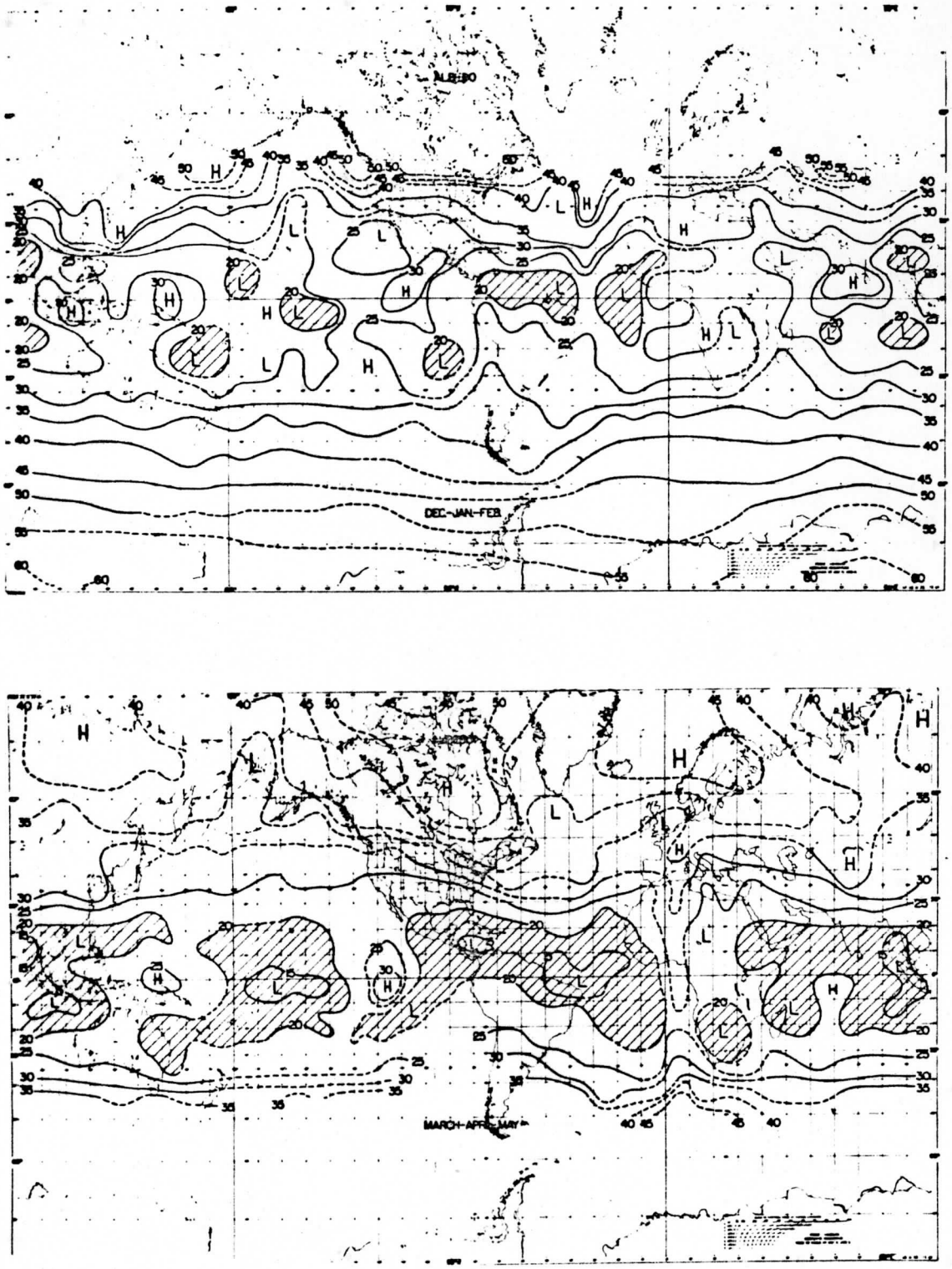

FIGURE 9: Mean values of planetary albedo (A) during Dec.-Jan.-Feb. and Mar.-Apr.-May. Regions of A < 20% are shaded.

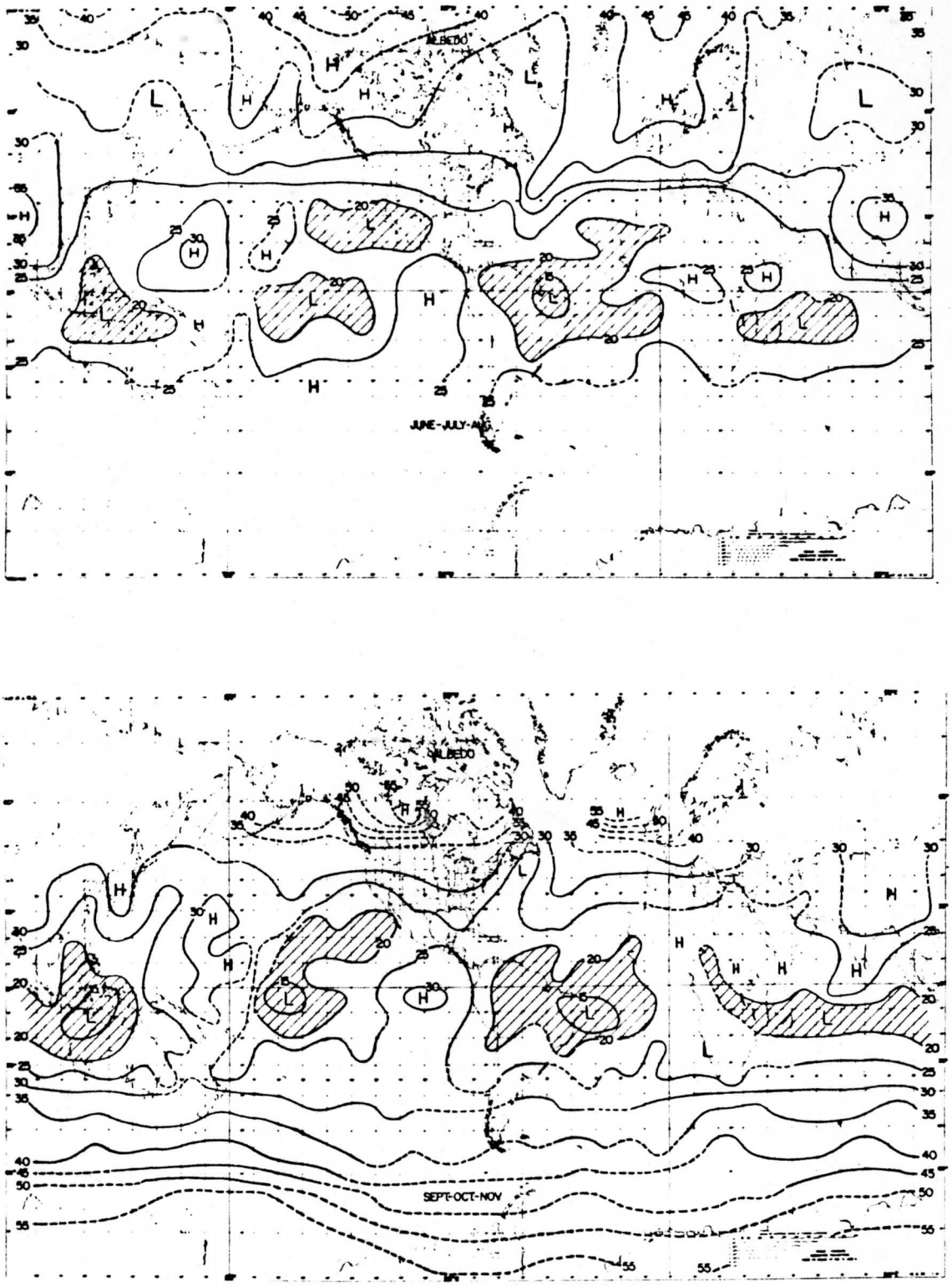

FIGURE 10: Same as figure 9 for June-July-Aug. and Sept.-Oct.-Nov.

subtropical regions an exception to this inverse relation is found over the deserts of Australia and Africa which have both high albedos and high values of infrared energy.

The departures from mean zonal values examined with the aid of the longwave radiation maps apply also to the albedo data within 30°N - 30°S if the desert effects are considered. In higher latitudes, however, the effect of ocean-land contrasts is much more striking when albedo maps are examined. For example, during the northern hemisphere Spring and Summer the oceanic regions near 40° - 60°N have a zonal pattern but the continents contain bright and dark areas primarily because of the influence of snow and vegetation. Near Hudson Bay and eastern Canada the albedo difference of 15% from MAM to JJA is probably due as much to changes at the surface as to changing atmospheric conditions. The absence of land in the same latitudes of the southern hemisphere causes more zonal albedo patterns in the corresponding seasons since these mean values are obtained from many observations of clear and cloudy regions in the migratory storm belt.

The highest mean seasonal albedo values observed over a large area in the northern hemisphere were 55% over central Canada during Spring and Fall. Undoubtedly there are higher values over small areas, but the low resolution sensors cannot define them especially if they are surrounded by darker regions. In the southern hemisphere the

albedo isolines show a gradual increase toward the pole, and the border of the Antarctic continent seen on these maps has a mean albedo greater than 55%.

(c) Net Radiation. The geographical distribution of mean seasonal albedo and longwave radiation data were combined with incident solar energy values to derive the net radiation maps shown in Figures 11 and 12. These maps are most valuable for an energy budget study because they show the geographical variation of the net energy gain or loss between portions of the earth-atmosphere system and space.

Two features of these maps are of special interest. One is the north-south movement of the zero isolines which mark the latitudes where the earth-atmosphere system is in radiative equilibrium at its upper boundary. Except during MAM these isolines have a zonal orientation in both hemispheres and they move in phase with seasonal variations of solar declination. The range in latitudinal location is more than sixty degrees in the northern hemisphere but less (about 50°) in the southern hemisphere. This occurs because, unlike the northern polar regions, the Antarctic is a net energy sink during all seasons.

These maps also show that within the broad zonal belts of net energy gain and loss there are definite highs and lows that mark departures from the zonal mean. The location of these regions changes with season in response primarily to differences in atmospheric condi-

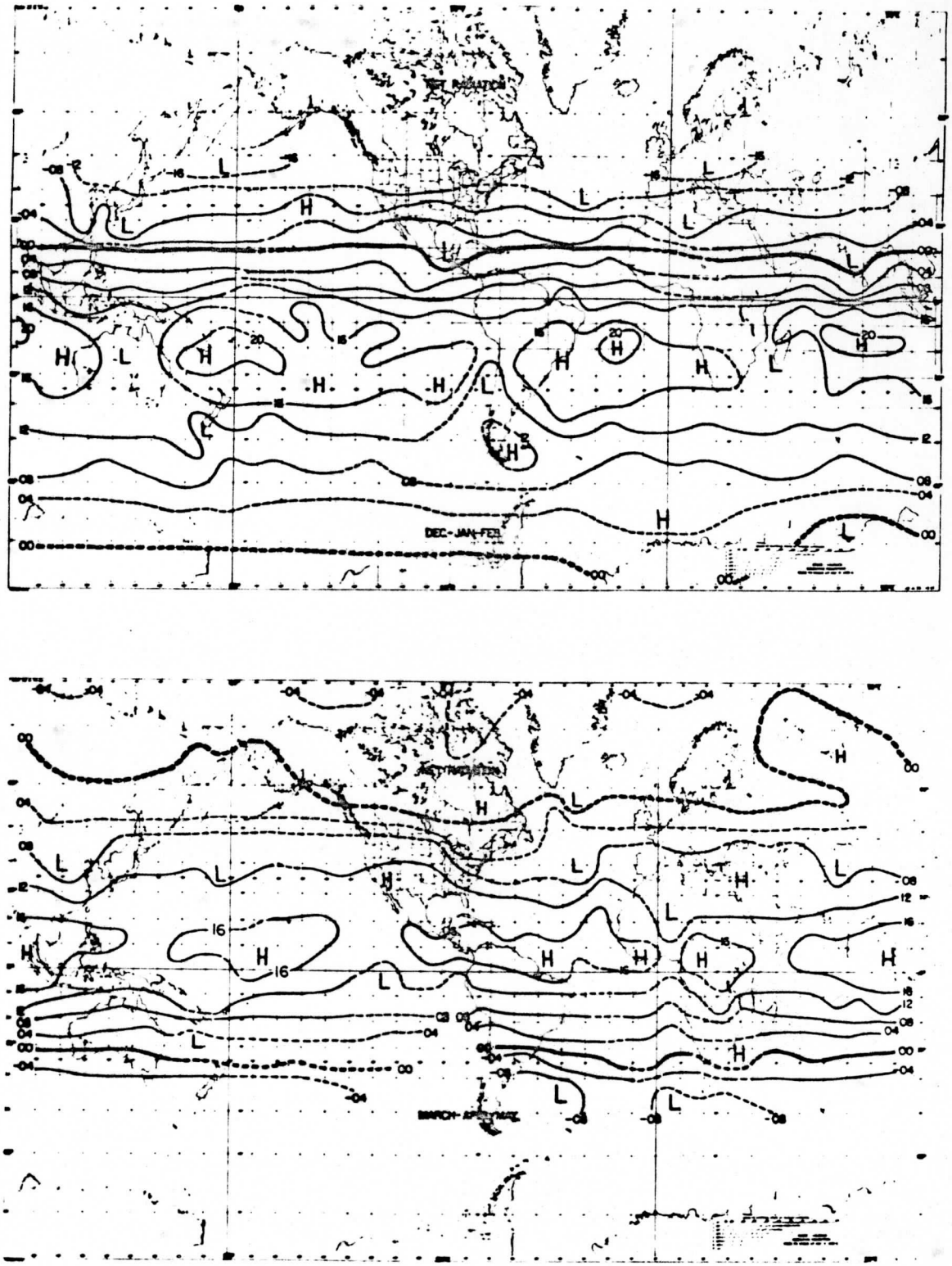

FIGURE 11: Mean values of the net radiation budget of the earth-atmosphere system (RN_{EA}) during Dec.-Jan.-Feb. and Mar.-Apr.-May. Units are cal . cm^{-2} . min^{-1} and isolines of RN_{EA} =0.0 are double-width.

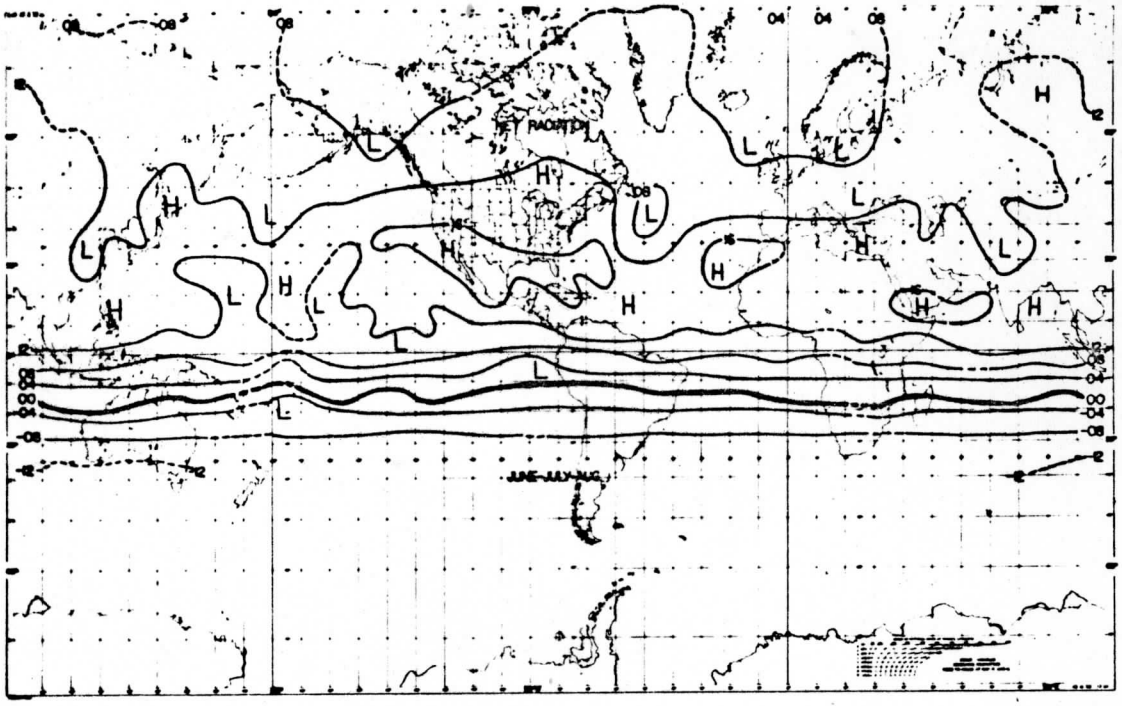

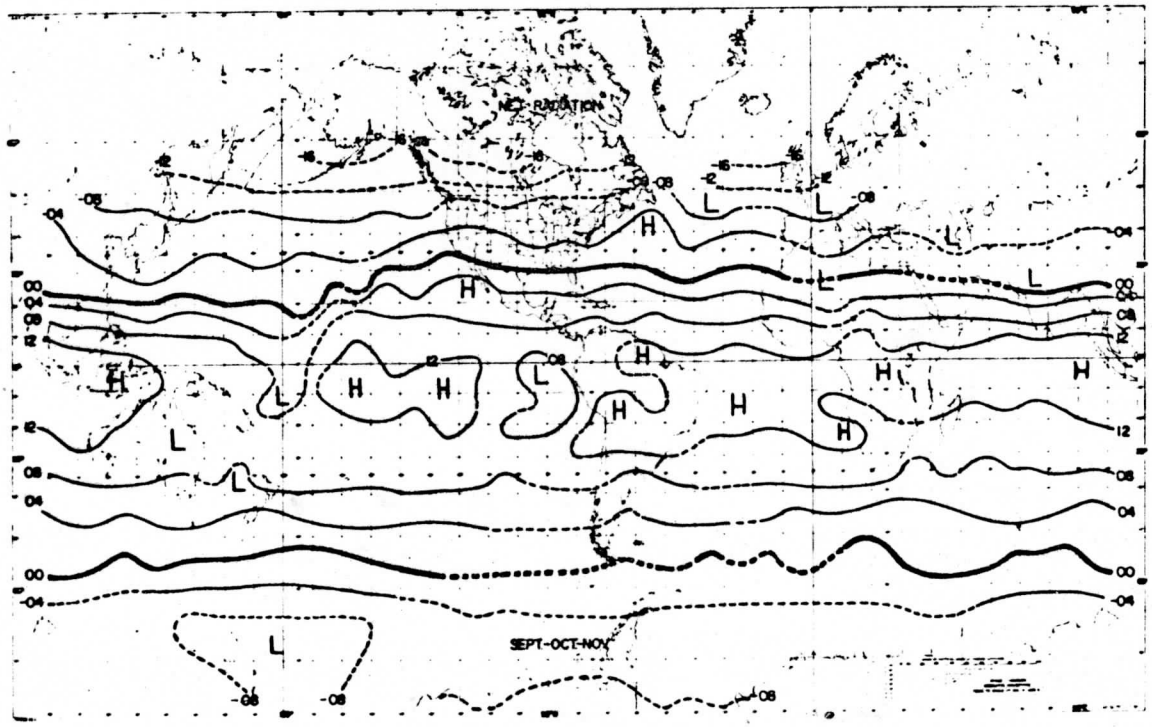

FIGURE 12: Same as Figure 11 for June-July-Aug. and Sept.-Oct.-Nov.

tions. For example, within the region of net energy gain (25°N - 25°S), the principal areas of energy input to our system are located east of Australia, in the Atlantic and over the Indian Ocean during DJF. At these locations the net radiation values exceed +0.20 cal·cm^{-2}·min^{-1}. In other seasons the highs shift to different longitudes and their intensities drop to +0.16 or +0.12 cal·cm^{-2}·min^{-1}. Note that in JJA the Indian monsoon region gains more than +0.12 cal·cm^{-2}·min^{-1}; here the large amount of reflected solar energy is more than compensated by the decreased outgoing longwave radiation. Within the tropics and subtropics there are also areas of relatively low net radiation over the deserts of Africa and Australia in the spring and summer and over the stratus-covered oceanic desert west of South America. Such areas have high albedos and high values of outgoing longwave energy.

During the warmer months of the northern hemisphere the important nonzonal features in upper latitudes include highs over central Asia and regions of lower than average net radiation in the north Atlantic, near Alaska and in northern China.

(d) Winter-Summer Differences. As an example of the seasonal variation of the radiation budget at different locations, maps showing these changes from winter to summer are shown in Figures 13 and 14. The differences were obtained as JJA minus DJF and they ranged from zero to $\pm$ 0.10 cal·cm^{-2}·min^{-1} and $\pm$ 20 percent for longwave radiation and albedo respectively.

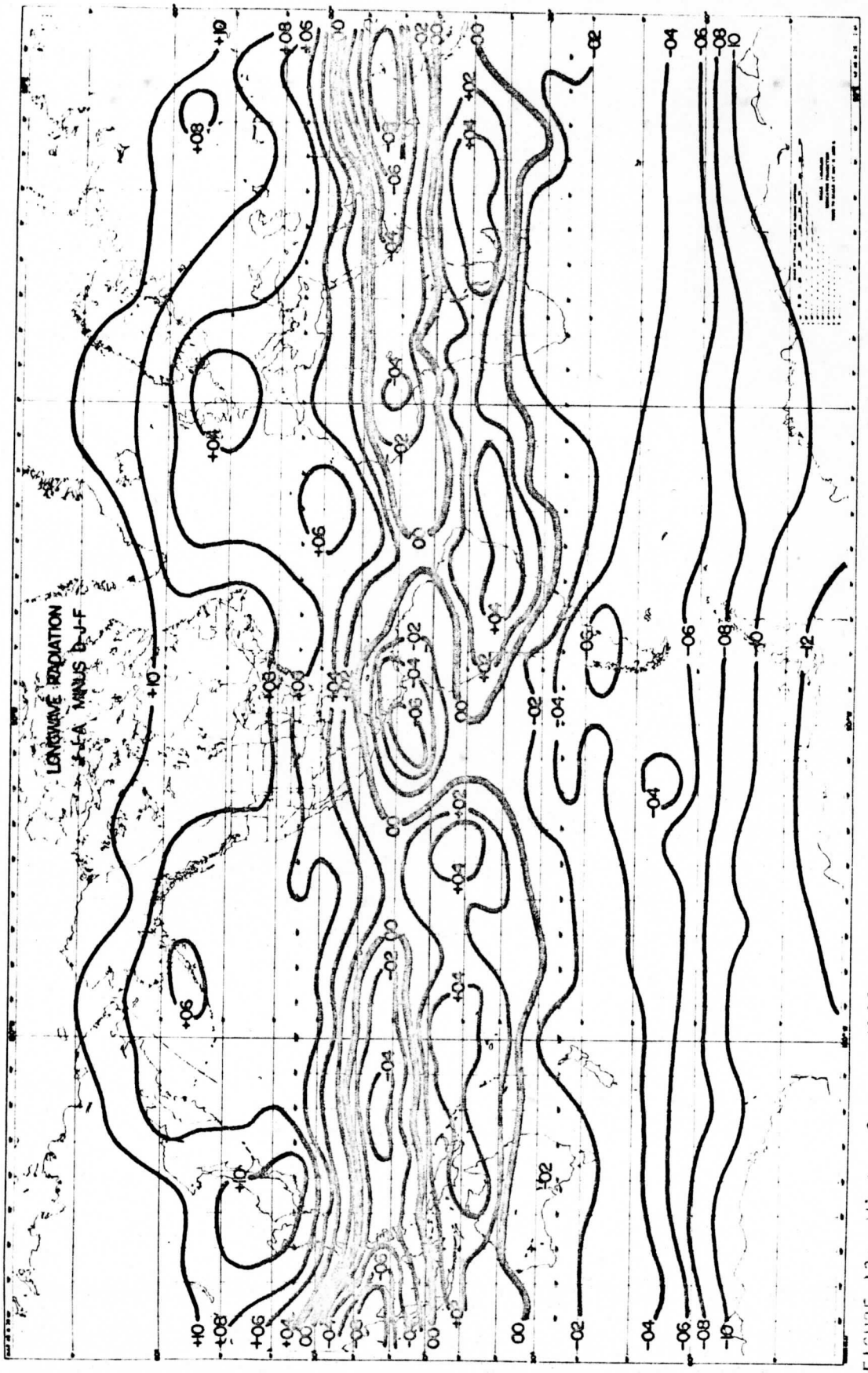

FIGURE 13: Winter-Summer differences in outgoing longwave radiation expressed as JJA minus DJF. Units are cal . cm^{-2} . min^{-1}.

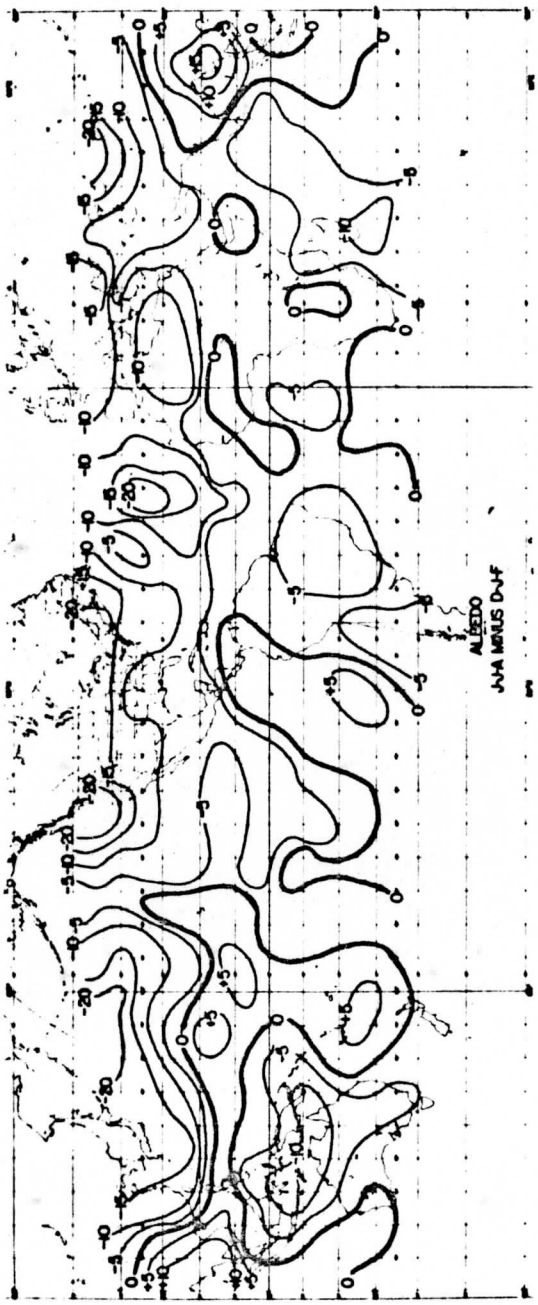

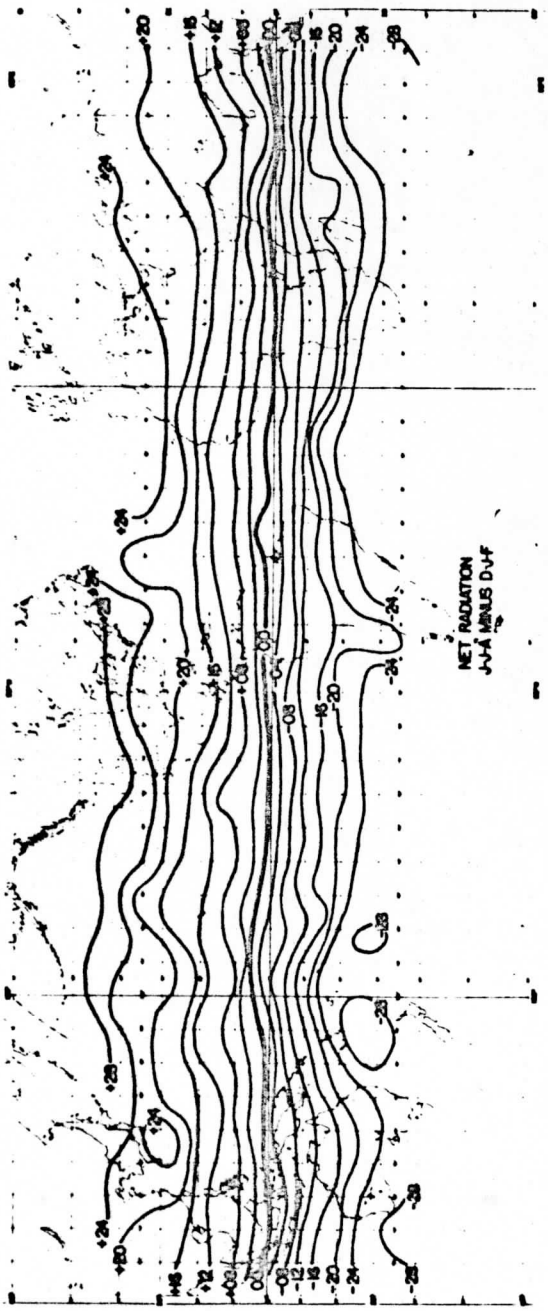

FIGURE 14. Same as figure 13 for net radiation and planetary albedo.

The albedo and longwave maps show large changes that are caused by the summer monsoon and the seasonal movement of the Bermuda high pressure region. Over the Sahara the increased winter albedo must result from cloudiness associated with storms moving into this region from the north and west. An interesting feature west of central America has a longwave radiation difference similar to the summer monsoon but the albedo change is much less. This implies that the amount of clouds did not vary greatly from winter to summer, but that many more middle and high clouds occur during the summer. Smaller changes in the albedo and infrared maps can be associated with the seasonal movement of the tropical cloudy and subtropical clear regions discussed previously.

Winter-Summer differences of net radiation depend on changes in atmospheric conditions as well as the seasonal variation of incident solar radiation. The extreme zonal orientation of the isolines of net radiation difference shows that despite large changes in the albedo and infrared fields the seasonal range of net radiation at a latitude is highly dominated by changes in incident solar energy. This results when differences in albedo and longwave radiation have compensating effects on the local radiation budget. In the winter-summer example only a few regions do not follow this normal pattern and they cause deviations from the zonal field. For example, the area south of Japan

has higher than average net radiation during the summer and a low value during winter, thus amplifying the seasonal range. On the other hand, subtropical regions in the North Atlantic and near the coast of Chile have normal (low) winter values but also low values in summer which combine to reduce the winter-summer range of net radiation.

In this section the primary purpose has been to describe the observed radiation patterns on the mean seasonal maps. When combined with a suitable amount of cloud cover data and available meteorological information (real or simulated), a thorough investigation of the meteorological cause and feedback effect will be possible. Obviously ocean-continent differences are not the only cause of zonal anomalies and while some of the local patterns (i.e., the monsoon effect) were expected, others (in the east Pacific and over the Atlantic) cannot be simply explained. Continuous cloud observations from the ATS and ESSA satellites will be a great aid to further research in this area.

4.12 Mean Annual Budgets

The geographical variations of mean annual values of albedo, long-wave radiation and net radiation are shown in Figures 15 - 17. In order to obtain a true representation of the annual case, the maps were derived from mean seasonal data. Mean albedos were obtained by weighting each seasonal value by the incident solar radiation for that

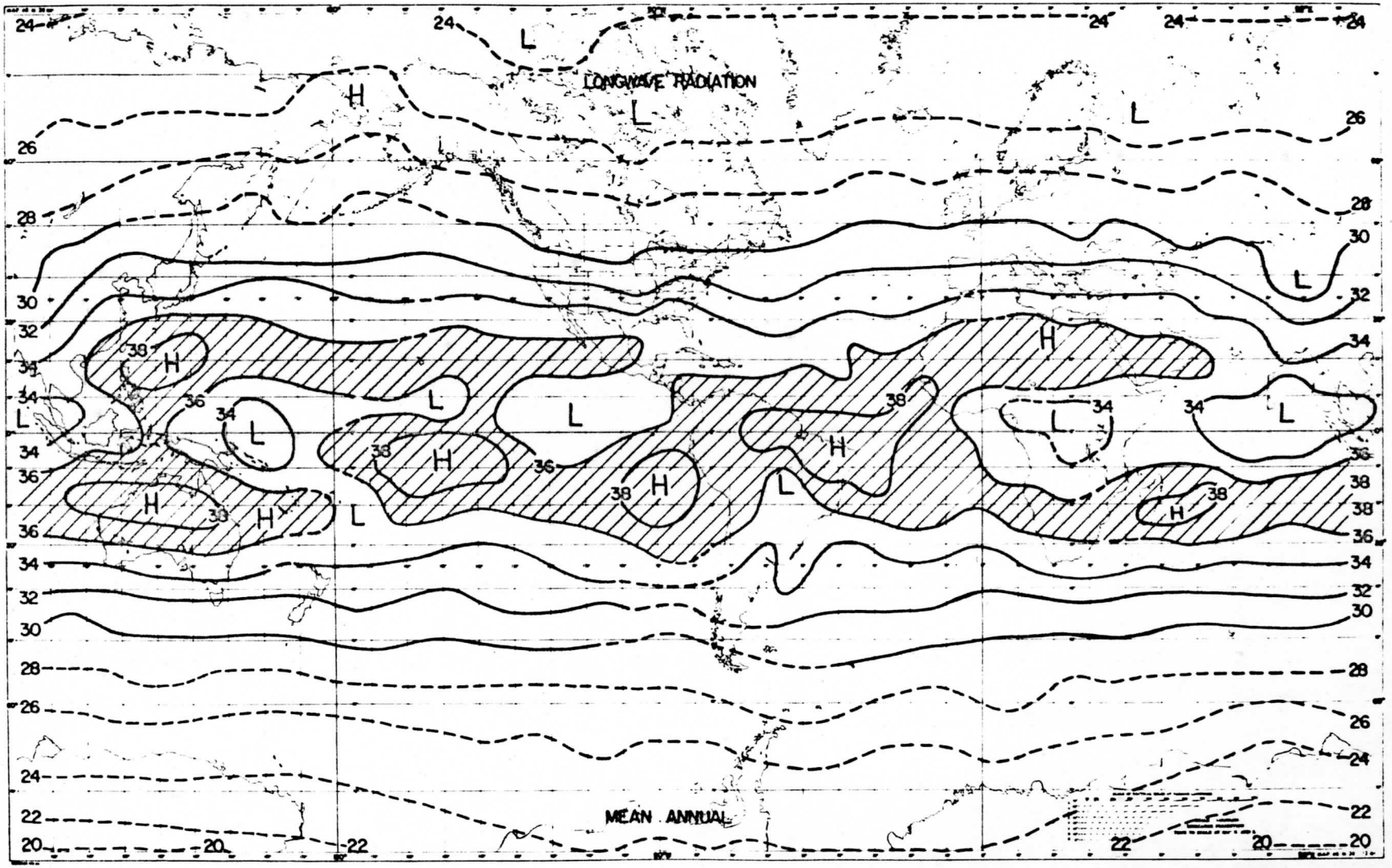

FIGURE 15: Mean annual values of longwave radiation from the earth-atmosphere system (H_L). Units are 10^{-2} cal . cm^{-2} . min^{-1} and regions of $H_L > 0.36$ are shaded.

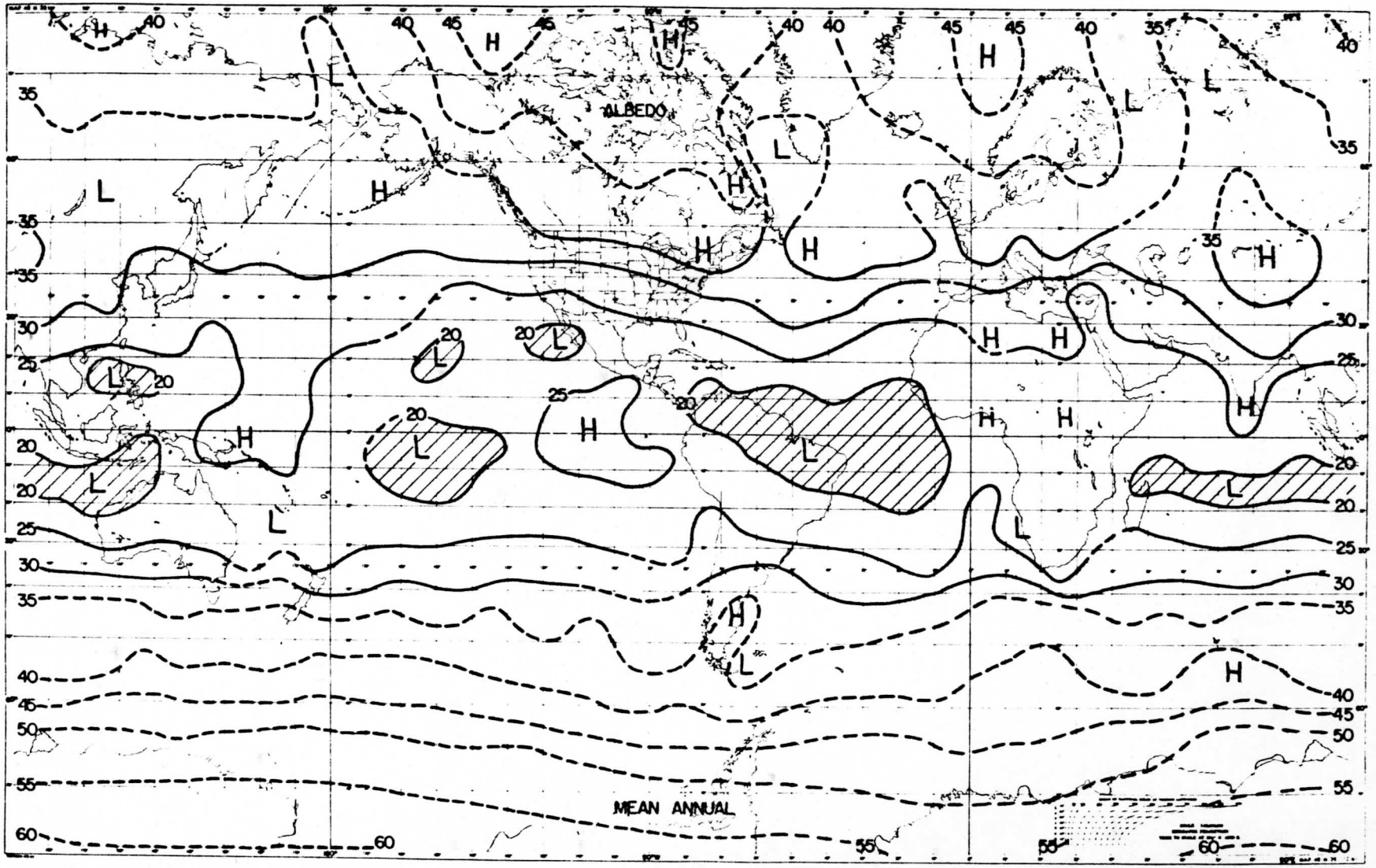

FIGURE 16: Mean annual values of planetary albedo (A) in percent. Shaded areas have A < 20%.

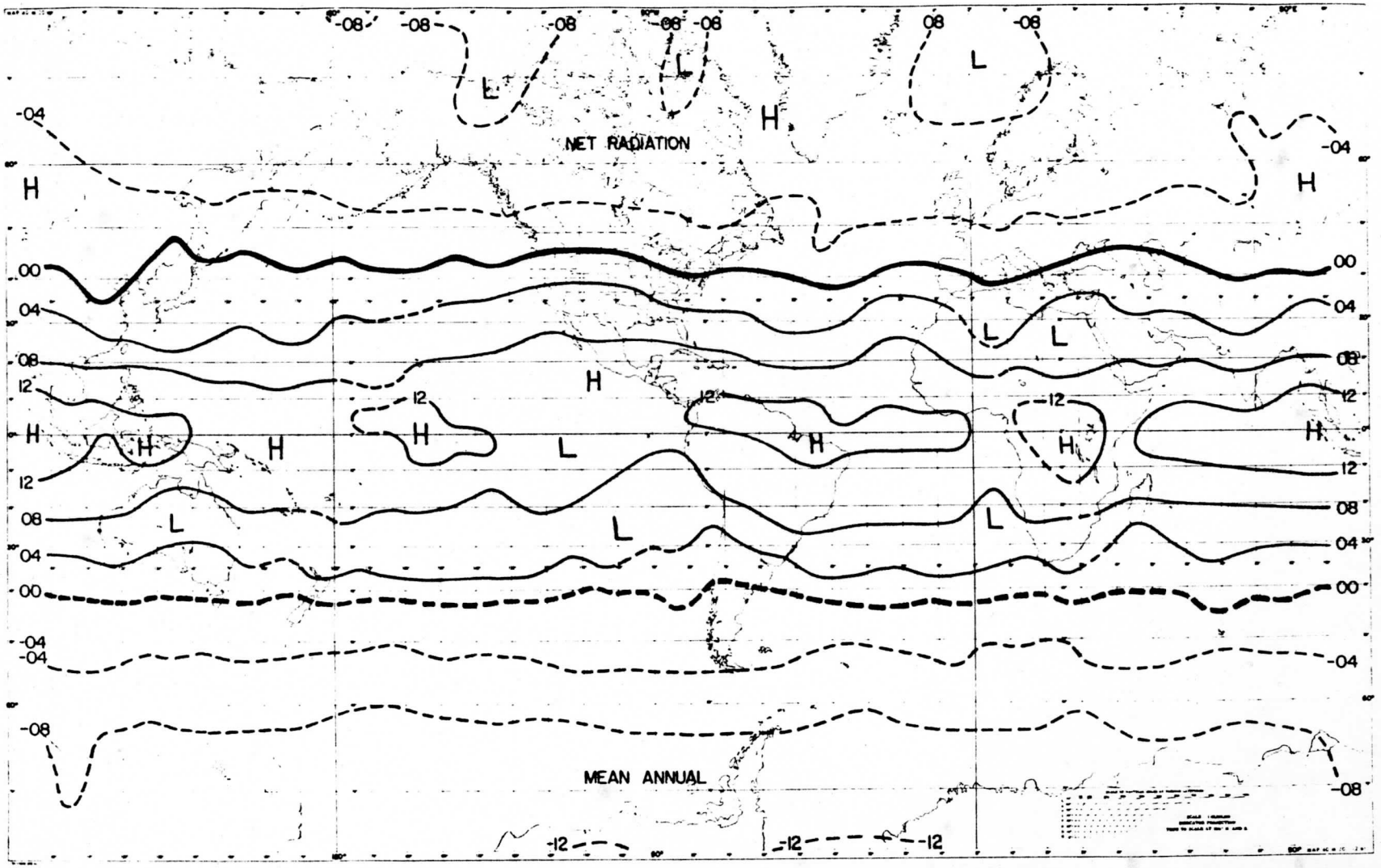

FIGURE 17: Mean annual values of the net radiation budget of the earth-atmosphere system (RN_{EA}). Units are 10^{-2} cal . cm^{-2} . min^{-1}.

time period and thus at higher latitudes the summer situation has the greatest influence on the mean annual albedo.

As in the mean seasonal maps, isolines of longwave radiation have a zonal orientation over the poleward half of each hemisphere. At these latitudes lower values of H_L are observed over the continents, especially central Asia and Antarctica. The region 10° - 30°N contains a zone of generally high outgoing longwave radiation with maxima centered over the western Pacific and the Sahara.

A band of lower H_L values results from cloudiness and the high water vapor concentrations near the intertropical convergence zone. At most longitudes this feature is centered near 5°N on the mean annual map although it cannot be seen over the Atlantic. Principal minima ($H_L < 0.34$ cal$\cdot$cm$^{-2}\cdot$min^{-1}) are found south of India, over equatorial Africa and east of New Guinea. Near 110°W in the Northern hemisphere and near New Guinea in the south lower values of H_L extending into the mid-latitudes may mark the regions of persistent interaction between the lower and higher latitude circulation patterns.

In the southern hemisphere the subtropical regions of high outgoing infrared energy contains two maxima (east of South America and in the central Pacific) that have a mean annual location very near the equator. Other maxima in this zone, over northwest Australia, west of South America and near Madagascar, are found at 20°S. When all of these

areas are considered, the southern hemisphere region of high outgoing radiation has a greater mean annual intensity than its northern hemisphere counterpart.

Many areas on the mean annual albedo map have high and low values that are inversely related to the patterns of longwave radiation. This occurs at locations where bright cold clouds or warm dark regions persist during most of the year. Examples are over the central Pacific and east of New Guinea. Some albedo values that do not follow this pattern are highly influenced by surface characteristics (i.e., the land masses at higher latitudes in the northern hemisphere and the Sahara region). Other departures from an inverse pattern could be caused by warm (low) clouds (i.e., west of Peru) or the presence of much cirrus cloudiness.

The most extensive region of low albedo (less than 20%) is found over northern South America and the Central Atlantic. Near 70°S a combination of clouds with ice and snow yields mean annual albedos near 60%. Similar latitudes in the northern hemisphere have maximum values greater than 45%.

The geographical distribution of net radiation has a very zonal nature on the mean annual map which emphasizes the dominant role of incident solar energy in the radiation budget at any location. In the higher latitudes of the northern hemisphere the regions of maximum net

energy loss by the earth-atmosphere system correspond to locations with the highest albedo. However, near the Antarctic continent where the albedo is uniformly high, net radiation values of -0.12 cal$\cdot$cm$^{-2}\cdot$min^{-1} are found over the relatively warmer regions where the outgoing longwave radiation exceeds the zonal mean. In both hemispheres the earth-atmosphere system is in radiative equilibrium with space near forty degrees of latitude.

Near the equator, the zonal pattern of net radiation gain is disrupted by maxima that occur because the longwave radiation is low (near Sumatra and over tropical Africa) or because the absorbed solar radiation is very high (east of South America). Relative minima are found over warm bright regions such as the land and oceanic deserts and over cold bright regions where the reflected solar energy plays a major role (i.e., 110°W at the equator).

These mean annual maps were derived from measurements obtained from the first generation of meteorological satellites. As such, they represent the first stages of a global radiation climatology that can be extended when other observations become available. Like the mean cloudiness maps being compiled from photographic data these radiometric averages provide new information about the global pattern of atmospheric conditions. However, the quantitative nature of the radiation budget data extends their usefulness much further. They can be used as a control for numerical models and provide information about

the variation of the earth's brightness in the shortwave and longwave portions of the spectrum. Perhaps the most important use of these data will be in studies that not only consider the cause of the measured values but also the effect the observed energy exchange has on future atmospheric conditions at a given location.

4.2 Budgets of Latitudinal Zones

4.21 Mean Meridional Profiles

One of the most common depictions of the earth's radiation budget has always been plots of the budget components as a function of latitude only. Figure 18 presents the data of this study in such a form. Although the maps of the previous section show that these zonal averages do not properly represent the true budget at many longitudes, especially equatorward of 30°, mean meridional profiles are useful to examine gross seasonal changes forced by the variation of incident solar energy.

The solar energy absorbed in the earth atmosphere system, H_a, at any latitude is closely related to the available energy except near the summer poles and the equator. In these regions the higher albedo, especially over Antarctica, reduces the H_a values despite the large amount of incident solar radiation. The largest amount of solar radiation ($0.54\ cal \cdot cm^{-2} \cdot min^{-1}$) retained by the earth-atmosphere system

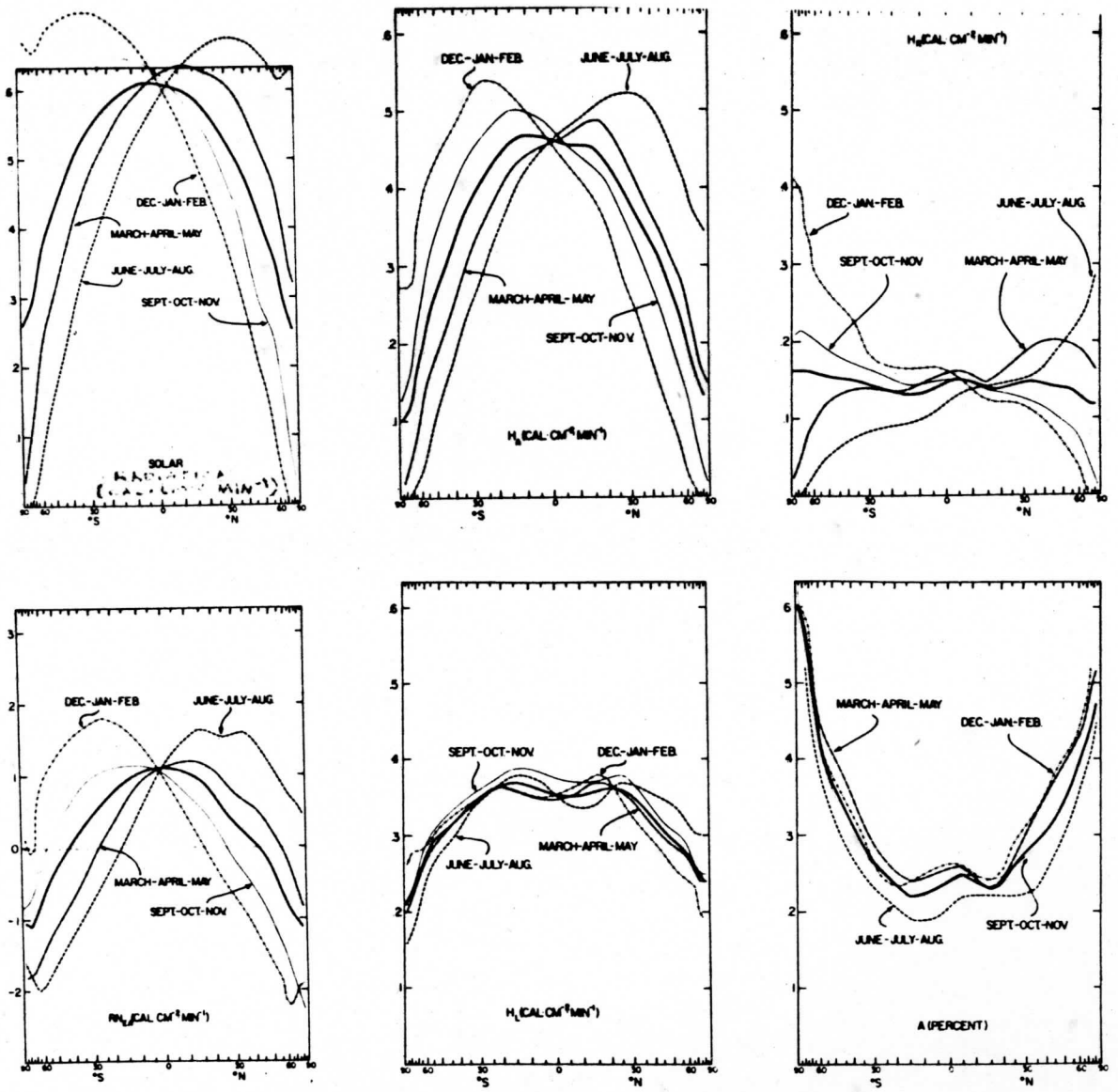

FIGURE 1 : Pe[illegible] meridional profiles of the components of the radiation budget of the earth-atmosphere system for each season and the [illegible] case (solid line).

is at 25°S during Summer. On an annual basis the subtropical regions of the southern hemisphere absorb more energy than the same area in the north.

Zonal averages of reflected shortwave radiation, H_r, show similar departures from a pattern forced by the sun. In each seasonal profile the effects of the clear, dry subtropics and the cloudy, wet tropical regions are apparent. Poleward of 40° in both hemispheres the summer averages show that reflected solar radiation increases toward the pole and this also occurs during Spring in the southern hemisphere. The reflected energy exceeds 0.40 cal·cm^{-2}·min^{-1} poleward of 70°S during DJF. Changing incident solar energy and the general increase of the planetary albedo toward the poles cause the mean annual values of H_r to be nearly the same at all latitudes. The largest annual value (0.16 cal·cm^{-2}·min^{-1}) occurs at the south pole and other maxima are found at 5°N and 35°N.

A different view of the shortwave radiation budget is seen in the mean profiles of albedo. These data represent the latitudinal variations of the "reflecting capability" of the earth-atmosphere system. A puzzling feature on this plot is the significantly lower albedo of the tropics and subtropics during JJA. This effect influences the H_a values so that the absorbed solar energy over the entire earth is nearly the same during JJA and DJF despite the changing distance from the earth to the sun.

Because of this result, the effect could be interpreted as an extreme example of Simpson's hypothesis (see Rossby (1959)) of the response of a planetary system to changes in the amount of incident solar radiation by adjusting its albedo.

Zonal averages of albedo measurements also show that the darkest region overall is in the subtropics of the southern hemisphere and that the mean albedo of the Antarctic region always exceeds 60%. In the northern polar regions the albedo ranges from 45 to 55% although values for the poorly illuminated seasons are based on marginal measurements.

The other, infrared, portion of the radiation budget is notable because of the very small changes in absolute magnitude at most latitudes. Largest seasonal differences ($\pm$ 0.10 cal $\cdot$ cm^{-2} $\cdot$ min^{-1}) occur at the poles and, as expected, the Antarctic region has the lowest overall radiation temperature. The smallest seasonal variations are found over the oceans of the southern hemisphere and the corresponding latitudes in the north show the continental effect. When all seasons are considered, the outgoing longwave radiation is highest at most latitudes during SON. This does not correspond to the season of lowest albedo JJA, which may be explained by the presence of more bright clouds during the Spring/Fall season and/or more worldwide cirrus clouds during JJA. On a mean annual basis the highest region of outgoing infrared energy occurs over the subtropics of the southern hemisphere.

The total radiation budget of the earth and atmosphere at various latitudes and times is displayed by the RN_{EA} curves. Near the equator the budget changes very little with season, always being about +0.10 $cal \cdot cm^{-2} \cdot min^{-1}$. At the poles, however, the winter to summer change is very large: $\pm$ 0.20 in the south and $\pm$ 0.25 in the north. The range in the Arctic is larger because of changes in the surface albedo which actually result in a definite gain of energy during the northern summer. During both summer seasons the regions from the equator to fifty degrees latitude show net energy gains greater than 0.10 $cal \cdot cm^{-2} \cdot min^{-1}$ with maxima located near 25°S and 15° and 35°N.

Note that the net radiation deficit is greater at 60° than at the pole in the respective winters. This was also noted by Raschke et al. (1967) in NIMBUS measurements over the southern hemisphere and is caused by the higher values of longwave radiation at lower latitudes when the infrared component dominates the total budget. A similar reversal is found over the southern polar regions during summer and here magnitudes of albedo and incident solar energy yield a constant value of absorbed energy from 60° - 90°S and thus the infrared component decides the budget.

At all latitudes away from the equator, the net radiation budget is greatest in Summer, Spring, Fall, and Winter in that order. Thus, the total radiative forcing function is in phase with seasonal changes of incident solar radiation. Surface and atmosphere effects are most

obvious in the polar regions (discussed above) and during JJA where the net energy gain at 25°N is weakened by high values of outgoing longwave radiation at this latitude.

In general, the poleward gradients of net radiation are greatest during the colder seasons of both hemispheres, although contrast between middle and high latitudes in the south during DJF is also very large. For the mean annual case the average gradient is -0.03 cal·$cm^{-2}\cdot min^{-1}$ per degree latitude poleward of 20 degrees. When all other energy budget effects are negligible these net radiation profiles represent the total forcing function that drives the atmosphere and hydosphere. The role of these radiation budget values on the required energy transports of the total energy budget will be discussed in section 5.

4.22 Time-Latitude Sections

In order to better examine the seasonal changes of the various components of the radiation budget, time-latitude sections are displayed in Figure 19, although the data are the same as in the previous section.

It is apparent that one component of the radiation budget, the absorbed solar radiation, has a mean seasonal variation at all latitudes very similar to the changes in incident solar energy at the top of the atmosphere. Note that the region of maximum absorption (> 0.40

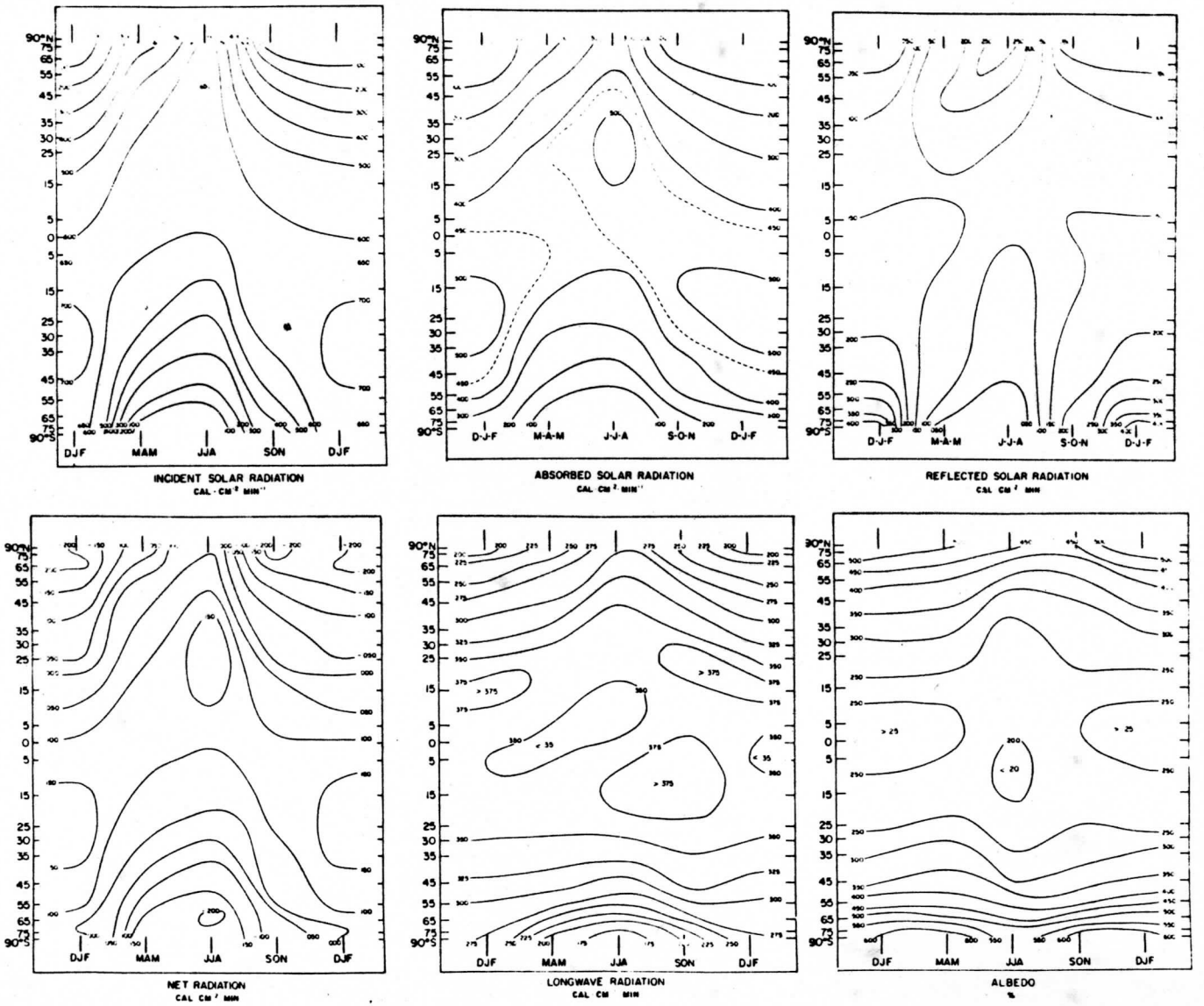

FIGURE 19: Time-latitude sections showing the seasonal variations of the radiation budget components.

cal·cm^{-2}·min^{-1}) lies along the seasonal path of the sun. Because the earth-atmosphere system absorbs energy in proportion to the amount available, the net radiation chart also shows a pattern that follows the sun. For example, the greatest seasonal change in net radiation at most middle and high latitudes occurs between Summer and Fall. At this time these regions change from a net energy gain to a net loss as the insolation falls off rapidly.

The time-latitude section of reflected solar radiation also shows a dependence on the available energy, particularly near the equator. This relationship is modified by atmospheric conditions when higher albedo values (> 25%) coincide with periods of maximum insolation equatorward of 15°. Surface features can also influence the reflected energy pattern. For example, the region 40 - 60°N reflects more solar radiation in the Spring than during Summer probably because of snow on the continents at these latitudes.

On both the albedo and longwave radiation sections the seasonal movement of the two subtropical clear regions and the intervening convergence zone can be observed. The patterns are not identical because of the features noted on the mean seasonal maps. Albedo values less than 20% mark the most northern extent of the southern subtropical belt at 5°S. This low zonal value results primarily from a region of low albedo over South America and the Atlantic. At this same time a major

reason for the lower albedo values near 35°N is an extensive clear region south of California. The infrared energy from the tropical regions is lowest from March until July and the seasonal maps show that these zonal means are strongly influenced by low values near India and New Guinea.

A zone of nearly constant longwave radiation is found near 35°S and the albedo of the Antarctic, as expected, shows the smallest seasonal variation. The change in longwave radiation from one season to the next is greatest before and after winter in the south polar region.

Two minima of net radiation over the Arctic are seen on the time-latitude section. The one during SON results from relatively high longwave radiation values that counteract the weak solar absorption at this time, while the winter minima is due to low infrared emission from the cold region. This observation, together with the reversal of net radiation near the poles in some seasons, emphasizes the importance of longwave radiation on the radiation budget of the higher latitudes.

Over all other areas it is apparent that, on a large spatial and temporal scale, changing surface and atmospheric conditions cannot override the influence of incident solar energy on the resulting radiation budget. However, with the aid of the longwave radiation and albedo sections we can examine the gross feedback effects. Over all regions except the tropical convergence zone the longwave radiation generally opposes seasonal changes of net radiation forced by the sun. Albedo

values either remain the same or decrease as the incident energy increases. Thus the longwave radiation works as a negative feedback mechanism and the albedo changes act to amplify seasonal variations of net radiation. However, in the cloudy convergence zone (which moves over a range of latitudes) the higher albedo and lower infrared values act as negative and positive feedback effects respectively.

Time-latitude sections of longwave radiation, albedo and net radiation derived from 30 consecutive months of satellite measurements are shown in Figure 20. On these charts the values poleward of 65° before June 1964 were obtained by extrapolation and reference to subsequent polar measurements. During this two and one-half year period the seasonal changes of net radiation during each year show definite similarities. Some differences do occur, however, and they must result from changes in albedo and/or the amount of outgoing longwave radiation.

The period June - November 1963 and the same interval during 1965 have a net radiation pattern that is nearly the same at all latitudes. Positive values of net radiation extend from 15°S to the north pole in JJA with maxima greater than +0.15 cal$\cdot$cm$^{-2}\cdot$min^{-1} during both years. The albedo sections for these times show low values over the tropics and subtropics of both latitudes and the generally high outgoing radiation decreased by the cloudy convergence zone near 15°N. During these months of 1964 the net radiation pattern is similar to the other

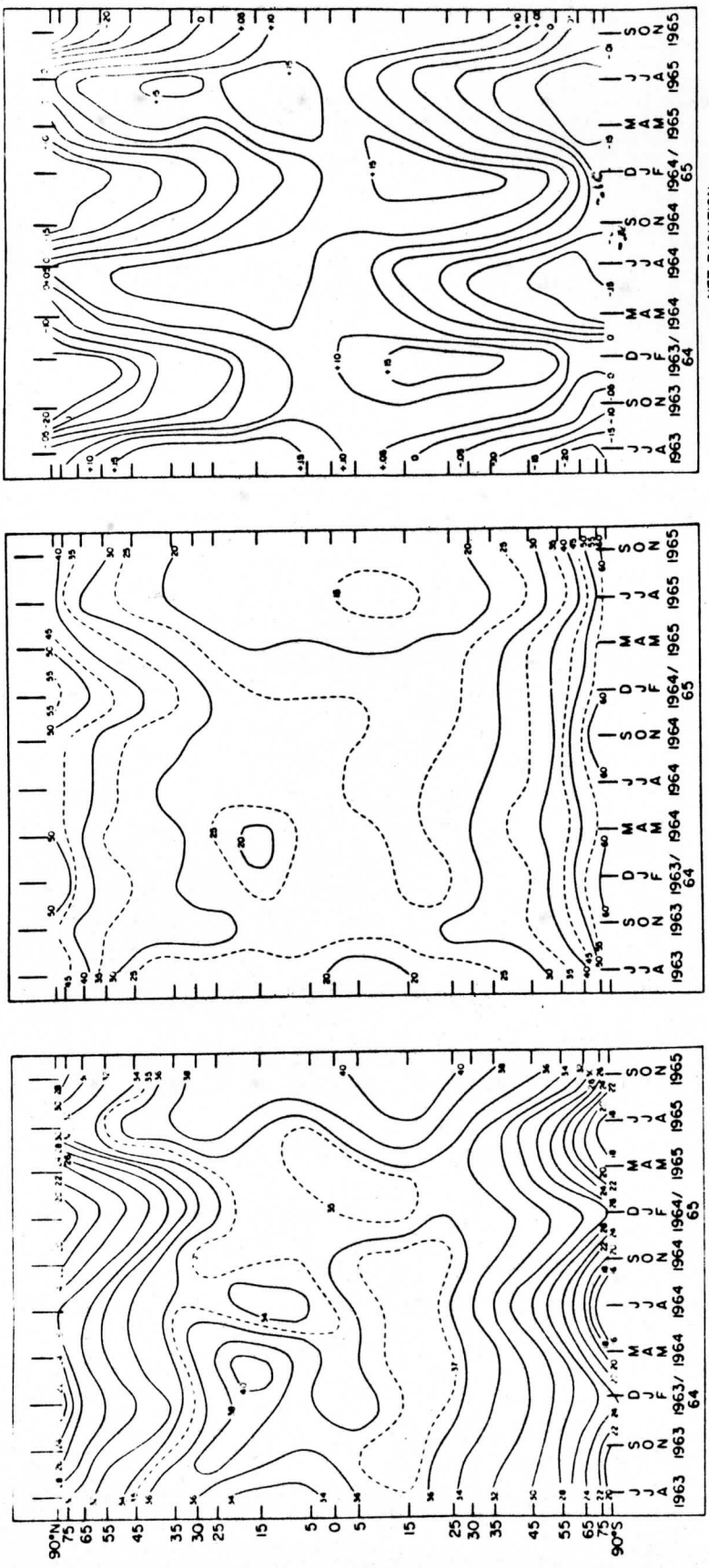

FIGURE 20: Time-latitude sections of planetary albedo, outgoing longwave radiation and the net radiation budget for the period JJA, 1963 to 50N, 1965.

two years in the southern hemisphere. However, the net gain of energy over the northern hemisphere is less in JJA of 1964 and results in a more moderate change of net radiation from summer to fall at 20° - 50°N. The immediate cause of this difference was a region of low outgoing radiation and higher albedo located near 15°N, the normal position of the convergence zone at this time. Along with this cloudier tropical region the entire hemisphere had lower than average values of outgoing radiation.

The two time periods between those mentioned above cover the first five months of 1964 and 1965. Although the net radiation section does show some differences in the radiation budgets at these times (i.e., in the southern polar regions), the overall patterns were rather similar. The other sections show that in the early months of 1964 both subtropical regions had high values of outgoing radiation. At the same time in 1965 the winter subtropics were apparently cloudier and the convergence zone had a larger latitudinal extent.

These charts demonstrate that noticeable differences exist between the radiation budgets of the same months in different years. With the aid of albedo and longwave radiation data some inferences into the cause of these differences can be made. Future work should include the location of the primary features that cause a zonal anomaly and an analysis of the atmospheric conditions before and after such an occurrence.

4.23 Budgets of Selected Zones

Figure 21 shows how all the radiation budget components within some latitudinal zones change from July 1964 through November 1965.

The two polar regions have some significant differences. For example, in the south the shortwave radiation parameters are exactly in phase with seasonal changes of insolation and the reflected solar energy always exceeds the amount absorbed. In the Arctic, however, the measured albedo was greater than 50% only in March. The reduced albedo during the summer, most probably due to the melting of ice and surface puddling, shifts the maximum of the absorbed solar energy curve to July. The time of maximum energy gain thus has a one-month lag from the time of maximum insolation. In both polar regions, the outgoing infrared energy increases rapidly during the Spring and decreases at a slower rate in the Fall. The albedo over Antarctica stays near 60% over the entire year but at the other pole the annual range is 20%. Average net radiation values over 70° - 90°N show that the region has a net gain of energy across its upper boundary from May through August. In contrast, the southern area has only a small net gain during mid-summer.

Mid-latitudes of the northern hemisphere reflect more solar energy during Spring partly because of snow on the continents. Although this albedo change shifts the H_a curve out of phase with the insolation as at 70° - 90°N, the increased longwave radiation during the summer

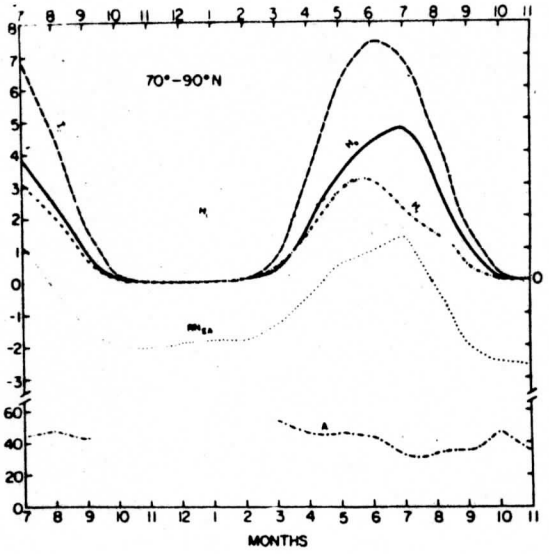

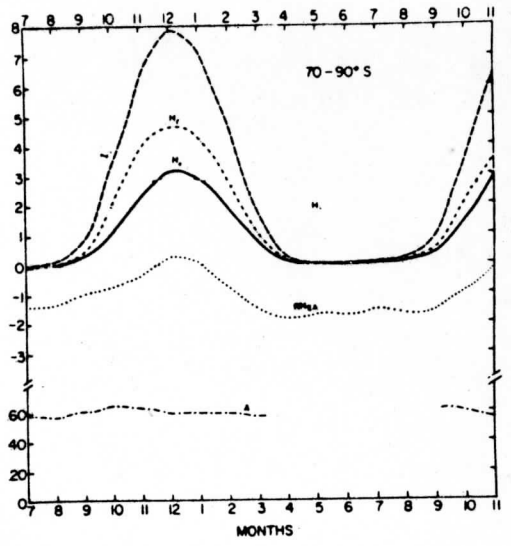

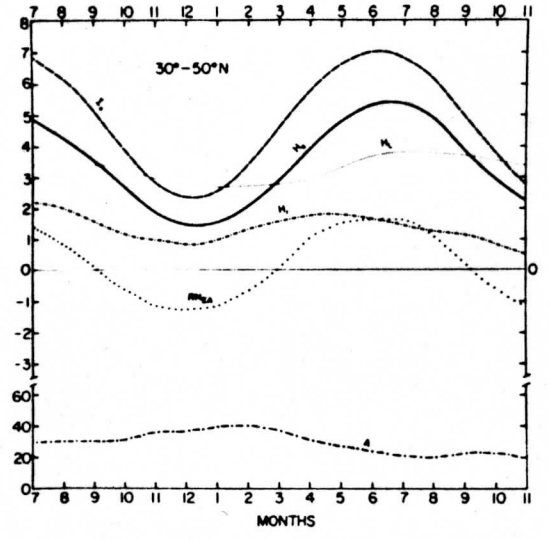

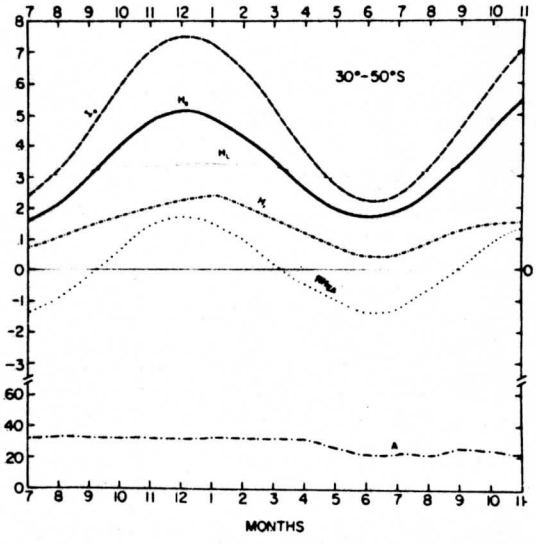

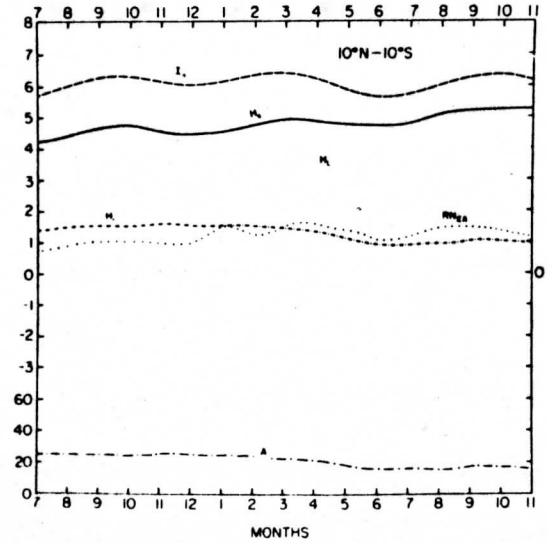

FIGURE 21: The radiation budgets of selected latitudinal zones from July, 1964 through November, 1965.

counteracts this effect in the total radiation budget. The same latitudes in the other hemisphere are characterized mainly by an unchanging amount of outgoing longwave radiation.

From 10°N - 10°S the radiation budget component change very little with time. Note, however, that the net radiation values respond to very small changes of longwave radiation and even to the slight variations of incident solar energy.

As a whole, the plots in Figure 21 show that even on a monthly time scale the budgets of large zonal areas do not show many sudden fluctuations. These first measurements of the polar radiation budgets over a long time period illustrate some important differences between the two regions.

4.3 Global and Hemispheric Budgets

4.31 Temporal Variations

In Figure 22, the measured radiation budgets of the northern and southern hemispheres and of the entire earth are shown as a function of time. Data from ten consecutive seasons are displayed beginning with JJA (season III) of 1963. The mean annual values of the radiation budget parameters are represented by horizontal dashed lines.

The radiation budgets of both hemispheres show the expected twelve month cycle forced by the sun. Because they are six months

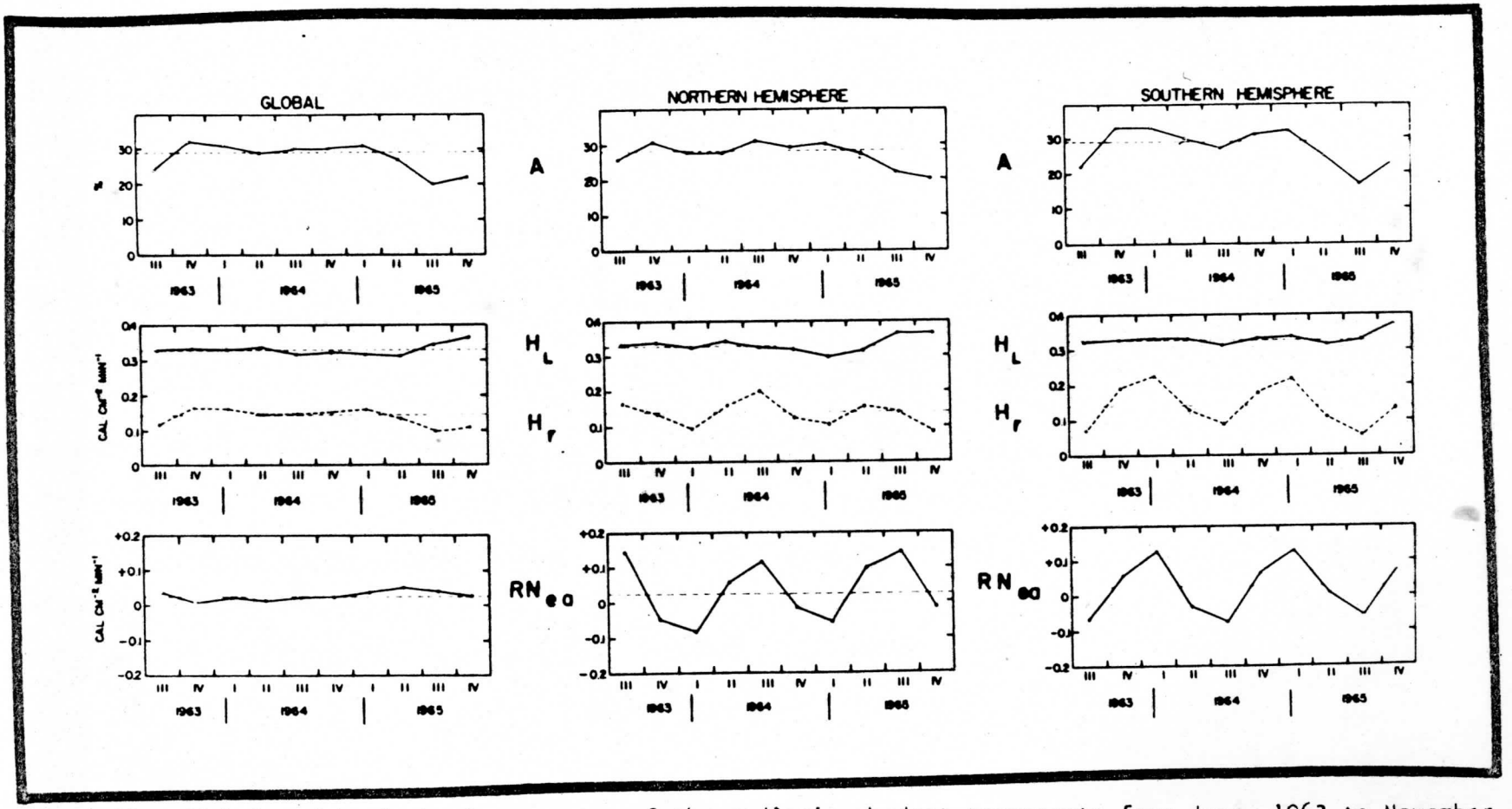

FIGURE 22: Global and hemispheric averages of the radiation budget components from June, 1963 to November, 1965. Dashed lines show the mean annual values.

out of phase the net radiation over the entire earth has only small temporal variations. The largest net gain of energy is found from March-August of 1965. At this time the total albedo of both hemispheres was quite low and apparently not completely compensated by increased outgoing radiation.

One naturally suspects that some instrumental problem has influenced the observations at this time but extensive data checks gave no reason to discard these measurements. In addition, some other facts preclude hasty rejection. Note that the albedo increases during the southern hemisphere Spring of 1965 and that measurements during JJA of 1963 (from a different set of sensors) also show relatively low albedos for both hemispheres. An indirect indication that the sensors were returning proper values during mid-1965 was obtained when a reasonable value for the solar constant was derived partly from measurements made at this time. Another check on the satellite data was made by comparing longwave radiation values with seasonal averages of the upward infrared radiation near the top of the atmosphere derived from balloon-borne radiometers. Kuhn and Cox (1967) have summarized such measurements over Guam and Canton Islands and at Green Bay, Wisconsin. The average deviation of the balloon and satellite measurements during March-August 1965 at these locations was less than 0.01 $cal \cdot cm^{-2} \cdot min^{-1}$, and the balloon data were slightly higher.

Of course, from only two and one-half years of data, we cannot determine if the changes in the radiation budget represents true anomalies or just some periodic phenomenon. These first measurements, thus, emphasize the need for a continuous program to observe the earth's radiation budget in order to extend this time series.

4.32 Mean Annual and Seasonal Values

Figure 23 and Table 2 present the mean annual and seasonal values of all the radiation budget measurements. In the figure the seasons are listed by number (1 = DJF) and the horizontal line shows the mean annual value.

The mean seasonal data emphasize that over these large areas all components of the shortwave radiation budget are in phase with the sun during an "average" year. In contrast, the outgoing longwave radiation has a small annual range (i.e., 0.03 $cal \cdot cm^{-2} \cdot min^{-1}$ for the northern hemisphere, even less for the southern hemisphere). The net result on the total radiation budget of each hemisphere is a seasonal variation that closely follows the sun. For example, the satellite observations indicate that the most positive net radiation value for the northern hemisphere occurs in summer and that during the winter the same region has a net radiation deficit.

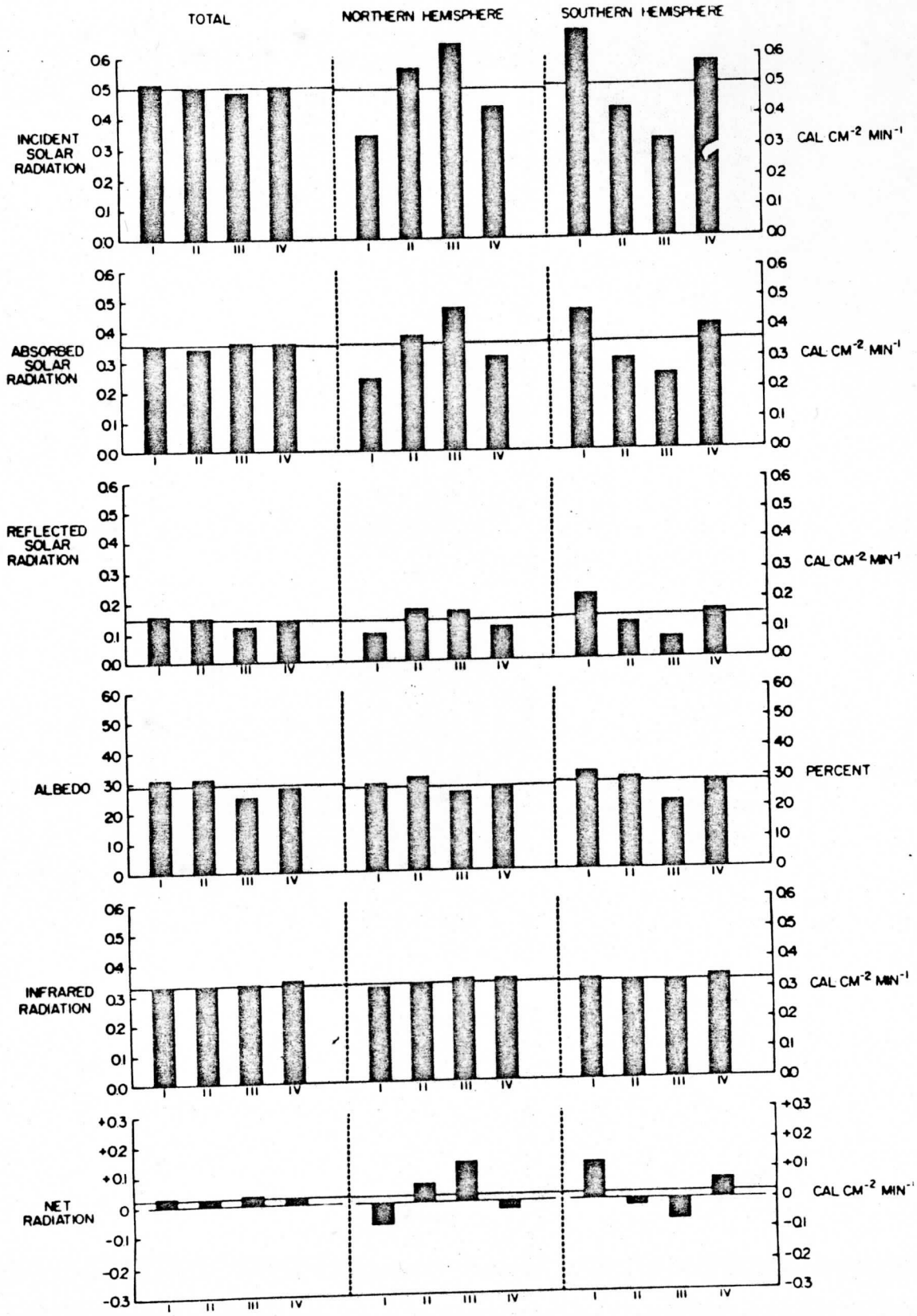

FIGURE 23: The mean seasonal variation of the radiation budgets of the entire earth and each hemisphere.

TABLE 2

MEAN ANNUAL AND SEASONAL RADIATION BUDGET OF THE EARTH-ATMOSPHERE SYSTEM OBSERVED FROM THE FIRST GENERATION METEOROLOGICAL SATELLITES

	GLOBAL AVERAGE					NORTHERN HEMISPHERE					SOUTHERN HEMISPHERE				
	DJF	MAM	JJA	SON	ANNUAL	DJF	MAM	JJA	SON	ANNUAL	DJF	MAM	JJA	SON	ANNUAL
I_0	.51	.50	.49	.50	.50	.34	.56	.65	.42	.50	.69	.43	.32	.58	.50
H_a	.35	.35	.37	.36	.35	.24	.39	.48	.31	.36	.46	.30	.25	.41	.35
H_r	.16	.15	.12	.14	.15	.10	.18	.17	.12	.14	.22	.13	.07	.17	.15
A	.31	.31	.25	.28	.29	.29	.31	.26	.27	.28	.32	.30	.22	.29	.29
H_L	.32	.33	.33	.34	.33	.32	.33	.34	.34	.33	.33	.32	.32	.34	.33
*RN_{EA}	.03	.02	.03	.02	.02	-.07	.06	.03	-.03	.02	.13	-.02	-.07	.06	.02

I_0 = incident solar radiation ($cal \cdot cm^{-2} \cdot min^{-1}$)

H_a = absorbed solar radiation ($cal \cdot cm^{-2} \cdot min^{-1}$)

H_r = reflected solar radiation ($cal \cdot cm^{-2} \cdot min^{-1}$)

A = planetary albedo (percent)

H_L = emitted infrared radiation ($cal \cdot cm^{-2} \cdot min^{-1}$)

RN_{EA} = net radiation budget of the earth-atmosphere system ($cal \cdot cm^{-2} \cdot min^{-1}$)

*Probable absolute error of $\pm$ 0.01 $cal \cdot cm^{-2} \cdot min^{-1}$.

Some small, second-order, features of each hemisphere's budget can result from mean seasonal changes in the physical state of the earth-atmosphere system (i.e., changes in the type or amount of cloudiness or changes in the albedo of the earth's surface). On the gross time and space scale considered in this section, such departures from the overriding solar effect are difficult to observe with accuracy. However, a closer view of Figure 23 does show that in both hemispheres the albedo is larger during December-May than during June-November. An inverse relation between the longwave radiation values for these time periods is barely discernible for the northern hemisphere and there is some indication that the longwave radiation may even increase as the albedo increases in the southern hemisphere. Because we are dealing with such relatively small changes it is not realistic to enter into a discussion concerning changes in cloud cover or the heights of clouds that could account for the small variations observed. It does appear, however, that a small secondary effect on the radiation budgets of each hemisphere is caused primarily by seasonal variations of the mean reflectivity of the earth-atmosphere system. This effect acts to amplify the seasonal variations of the net radiation budget of the northern hemisphere and it reduces the variation of the same parameter in the southern hemisphere. One possible cause may be the difference in the surface albedo of the polar regions during their respective summer seasons.

When the entire earth is considered, the relative mean seasonal changes in the radiation budget are quite small. There is a slight maximum of absorbed solar energy during June-July-August, a consequence primarily of the lowered albedo of the northern hemisphere during this time. Average values of outgoing longwave radiation are particularly unchanging with season, although they increase a small amount during the last six months of each year. The entire earth is very close to radiative equilibrium during the spring-fall transition seasons, a fact noted also by House (1965).

The mean annual values of all the radiation parameters were nearly the same for each hemisphere. This emphasizes the effect of clouds, rather than surface features, on the hemispheric-scale radiation budgets. For both regions (and therefore the entire earth) the mean annual outgoing infrared radiation was 0.33 $cal \cdot cm^{-2} \cdot min^{-1}$ (corresponding to an equivalent black-body temperature of 252°K). Calculations of London (1957) and work discussed by Lettau (1954) agree with this value to within 2 or 3 percent. The shortwave portion of the budgets show each hemisphere to have a planetary albedo of approximately 29 percent, with an indication that the southern hemisphere may be slightly "brighter." On a global scale, this observed albedo value together with insolation averaging 0.5 $cal \cdot cm^{-2} \cdot min^{-1}$ requires that, in the mean, each square centimeter column of the earth-atmosphere system absorb 0.35 and reflect 0.15 calories per minute of the incident solar energy.

The planetary albedo value of 29 percent is slightly lower than any earlier estimate. Bartman (1967) has recently summarized the latest theoretical estimates and few available observations; he notes that the recent trend is toward lower values (near 30 percent). For example:

Reference	Planetary Albedo
Dines (1917)	50%
Aldrich (1919)	43
Simpson (1928)	43
Baur and Phillips (1934)	41.5
Fritz (1948)	34.7
Möller (1950)	35
Houghton (1954)	34
Lettau (1954)	34
London (1957)	35
Angström (1962)	33-38
House (1965)	35
Bandeen et al. (1965)	32
Vonder Haar (1968)	29 (± 1)

The earliest estimates (45 - 50%) gave way to lower values (near 35%) primarily because of new information about the albedo of clouds. The slightly lowered values obtained from global satellite observations apparently result from a better assessment of the amount of clouds.

Only the last three values were derived from satellite observations and in each of these studies the sampling in space and time was different. Raschke and Pasternak (1967) recently obtained 30% from three months of NIMBUS data.

When the albedo and longwave radiation observations are used to derive the total (net) radiation budget, we find again that each hemisphere, and the earth as a whole, has a net radiation imbalance of plus 0.02 $cal \cdot cm^{-2} \cdot min^{-1}$ for the mean annual case. This value of approximately $\pm$ 14 $watts \cdot m^{-2}$ is close to the absolute accuracy of the satellite sensors for measuring net radiation ($\pm$ 10 $watts \cdot m^{-2}$). For this reason, we can state that, within the accuracy of our measurements, the entire earth-atmosphere system was nearly in radiative equilibrium during the time of these observations. Although a small positive imbalance (i.e., warming of the earth-atmosphere system) is indicated, it must be emphasized that this applies only to the relatively short (in a climatological sense) time period for which we have data.

Note that the average solar input to our system is 349 $watts \cdot m^{-2}$ and thus the measurements used in this study allow us to examine the global radiation balance with an accuracy of $\pm$ 3%. If a solar constant of 1.95 (see 3.22) rather than 2.00 $cal \cdot cm^{-2} \cdot min^{-1}$ had been used the net radiation budget would still have a small positive imbalance.

In summary, the mean annual global and hemispheric satellite observations show that:

a) During the time period of observations (approximately 1963-65) the entire earth-atmosphere system was in near radiative equilibrium.

b) Despite the physical differences between the hemisphere (i.e., the larger land areas in the northern hemisphere) each had similar albedos and the same mean value of outgoing longwave radiation ($0.33\ cal \cdot m^{-2} \cdot min^{-1}$).

c) On the average over space and time, each square meter of atmosphere and underlying surface retained 71% of the solar energy incident on it (i.e., the mean value of available solar energy was $248\ watts \cdot m^{-2}$).

Point (b) validates the assumptions made by earlier investigators when they computed the radiation budget of the northern hemisphere and used it to represent the long-period global budget.

5. ENERGY BUDGET RESULTS AND REQUIRED TRANSPORTS

Satellite measurements of the radiation budget can be combined with estimates of the other energy terms to derive the total energy budget of the earth-atmosphere system. The results show the principal regions of net energy gain or loss on various time and space scales. When the entire earth is considered, energy budgets can also be used to compute the required poleward energy transport by the atmosphere and oceans.

In order to note the major components of the energy budget and to point out the role of the radiation term, the following section presents a simple depiction of the energy budget of the earth-atmosphere system.

5.1 The Energy Budget of the Earth-Atmosphere System

The total energy budget of an earth-atmosphere column (Figure 24) can be expressed as the sum of two separate budgets, one for the surface and one for the atmosphere alone. For the earth's surface (either land or ocean) the energy balance equation can be written in schematic form[1] as:

$$RN_E - LE - H = G_E + \Delta F \qquad (3)$$

RN_E = net radiation balance of the surface

---

[1]The approach and notation used here closely follows that of Sellers (1966).

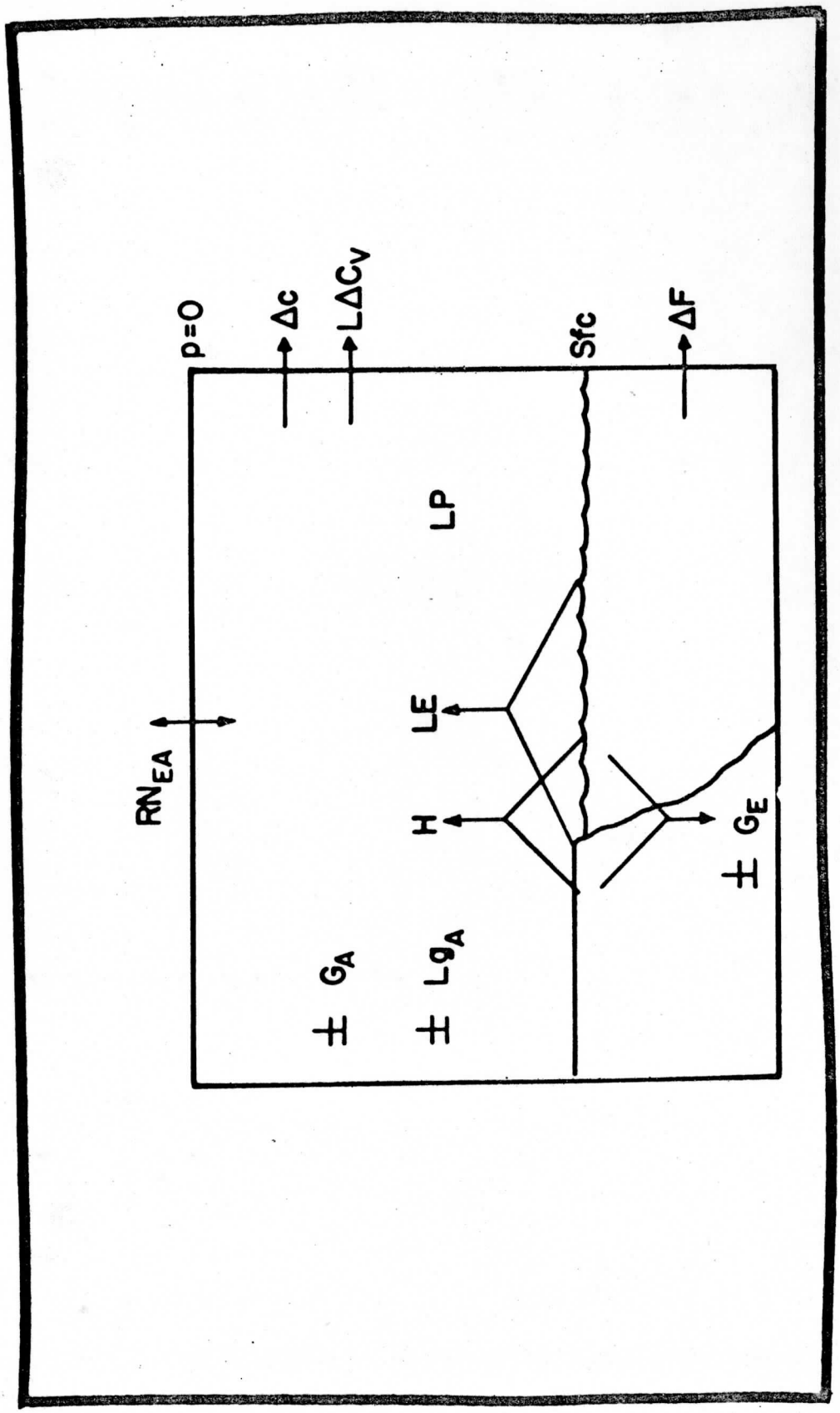

FIGURE 24: Major components of the energy budget of the earth-atmosphere system.

LE = net energy removed from or added to the surface by phase transformation of water; (E = amount of water that leaves the surface and is added to the atmosphere, L = Latent heat of phase transformation (600 cal/gm))

GE = subsurface storage (or release) of energy

ΔF = subsurface horizontal energy divergence (transport); (the term represents the action of ocean currents and is zero for a land surface)

Similar to (3), an energy balance equation for the atmosphere only is:

$$RN_A + LP + H = G_A + \Delta C \qquad (4)$$

where:

RN_A = the net radiation budget of the atmosphere (a positive value represents a net gain of energy by the atmosphere due to radiation processes)

L_P = net heat added to or removed from the atmosphere by phase transformation of water (L = latent heat of phase transformation, P = precipitation that leaves the atmosphere and arrives at the surface)

H = net energy added to or removed from the atmosphere by exchange processes at the atmosphere-surface interface

G_A = storage (or release) of energy within the atmosphere

ΔC = horizontal energy divergence (transport) in the atmosphere

Because the transport and storage as well as the transformation of latent energy in the form of water vapor are vital to the atmosphere's energy budget, equation (4) must be expanded by considering the water budget of an atmospheric column. It is:

$$L(E - P) = L_{g_A} - L\Delta C_v \tag{5}$$

where:

g_A = storage (or release) of water vapor in the atmosphere

ΔC_v = transport (divergence) of water vapor

The equation states that any difference between the water vapor added to or removed from an atmospheric column must be balanced by an appropriate storage (or release) of water vapor and/or transport of vapor in or out of the column.

Substituting (5) into (4) yields the atmosphere's balance equation when latent heat transport and storage are included. By adding the result to (3) we obtain the total schematic energy balance equation for the earth-atmosphere system:

$$RN_{EA} - G_A - G_E - L_{gA} = \Delta C + \Delta F + L\Delta C_v \tag{6}$$

This shows that the <u>total</u> divergence of energy (including the latent form) from a system must be balanced by the release (negative storage) of sensible and latent heat within the system and the net radiation balance of the system.

With the aid of (5) we can obtain an alternate equation:

$$RN_{EA} + L(P-E) - G_A - G_E = \Delta C + \Delta F \qquad (7)$$

Here the transport and storage terms do not include latent heat, and the precipitation-evaporation difference within the system is considered as a source or sink of energy. Both (6) and (7) have been derived because they have been used in previous radiation and energy budget work and will be referenced later in the present study.

Each of these equations may be applied to a volume of the earth-atmosphere system on any space or time scale. Some of their terms may reasonably be neglected when very long time periods and/or very large areas are treated. For example, when the entire (global) earth-atmosphere budget is considered, all transport terms are zero. If the budget of any size volume is considered over long time periods, all storage terms are negligible provided no climatic change occurs. Of course, there are a few minor effects (i.e., the melting of snow and ice) that occasionally take on local importance and which have not been included in the general equation.

5.2 Mean Seasonal Energy Budgets

The information needed to evaluate the energy budget terms, other than the radiative term, on a mean seasonal basis is very limited. In particular, the geographical variation of precipitation and ocean storage is not well known. However, Rasool and Prabhakara (1966) have recently compiled mean monthly values of the energy budget terms for

latitudinal zones between 60°N and 60°S. Their values of ocean storage, evaporation and precipitation were used with the mean seasonal RN_{EA} data from this study to evaluate equation (7). The solution gives $(\Delta C + \Delta F)$, the net non-latent energy available for transport by the atmosphere (sensible heat + potential energy) and oceans, as a function of latitude and season.

These values, weighted by the area of each zone, were used to derive the required poleward transports during each season (Figure 25). It was assumed that (a) excess energy gained by the entire earth over a season was distributed equally by area, and (b) during the polar night the net energy loss poleward of sixty degrees is completely represented by the net radiative loss. Because of these necessary assumptions and the large uncertainty in the climatological data, the accuracy of these energy budget results is difficult to estimate.

During the Spring and Summer in both hemispheres, Figure 25 shows that the required transports poleward of thirty degrees are very small. Thus, in every season, one-fourth of the earth's surface area is decoupled from the remainder, in the sense that only a small net energy exchange between the two regions is required. The atmosphere and oceans move energy southward from as far north as 30°N during March-August. Maximum cross-equatorial exchange (23×10^{19} cal/day) occurs in JJA and is nearly matched by northward transport in DJF.

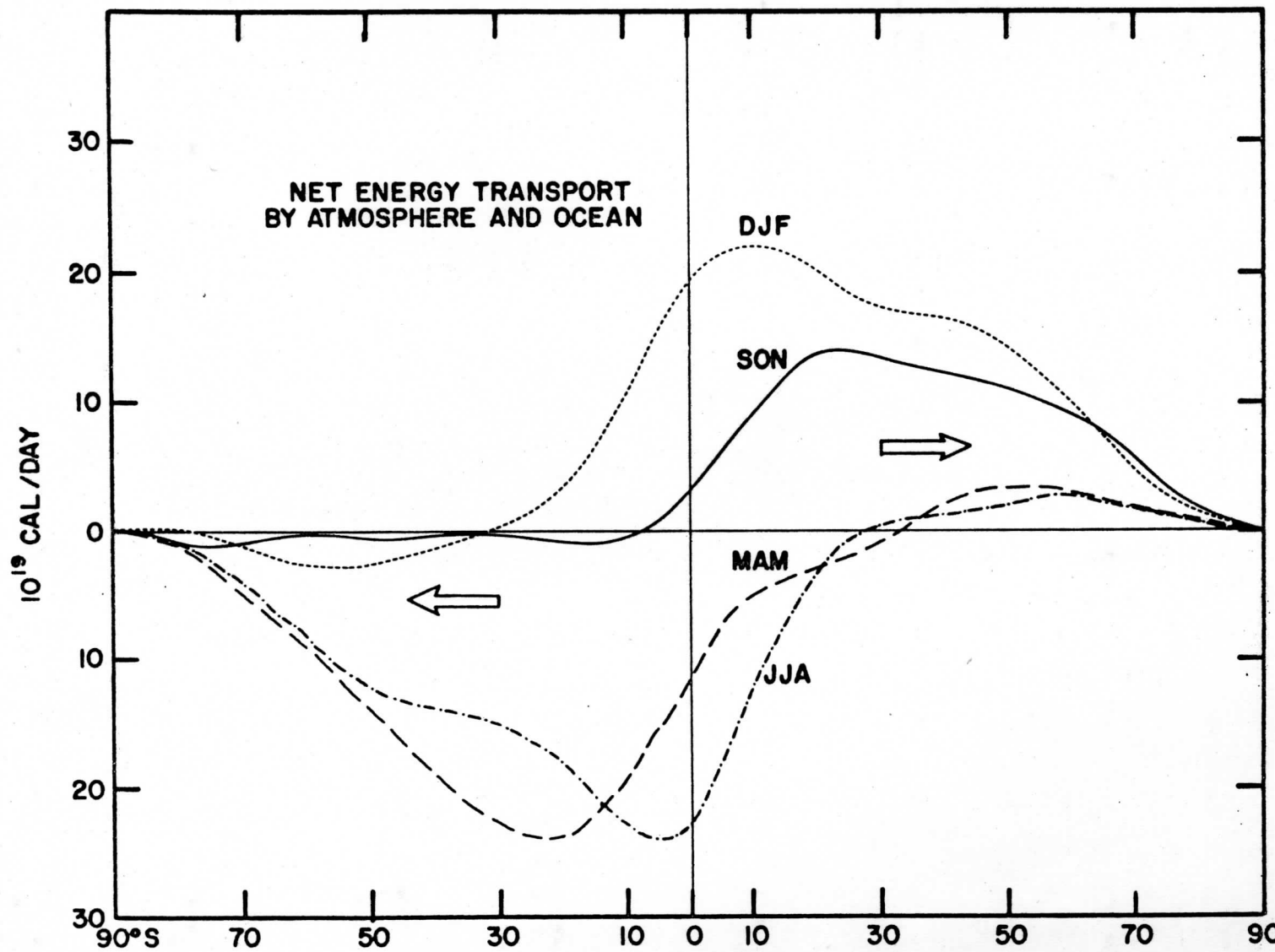

FIGURE 25: Seasonal values of the required poleward energy transports by the atmosphere (sensible heat + potential energy) and the oceans. Points above the zero line represent northward transport.

Despite the opposing effect of energy storage and release from the oceans, the transport from or into a hemisphere shows the similar pattern of solar dominance each season. The oceanic effect, however, is evident in the Fall curves. At this time the large ocean area in the Southern hemisphere continues to store energy and evaporation exceeds precipitation at the mid-latitudes. Both of these processes have a smaller magnitude in the northern Fall and thus less energy must be brought poleward to compensate for the decrease in available solar energy.

During each winter season the reduced transport near thirty degrees results from a combination of annual maxima of evaporation at fifteen degrees and annual maxima of energy release by the oceans at thirty-five degrees. The polar regions require energy input during all seasons and the net radiation gain in the north during the summer apparently cannot supply all the energy needed at this time.

A time-latitude section in Figure 26 illustrates the mean seasonal variation of the required transport of non-latent energy. Note the abrupt change from northward to southward transport over the equatorial half of the earth during the first four months of each year. The radiation budget maps showed that zonal features in the subtropics were least well defined at this time and that the tropical convergence zone was strong. Together these results imply that increased atmospheric activity during this transition season may be forced by the energy requirements of the southern hemisphere oceans.

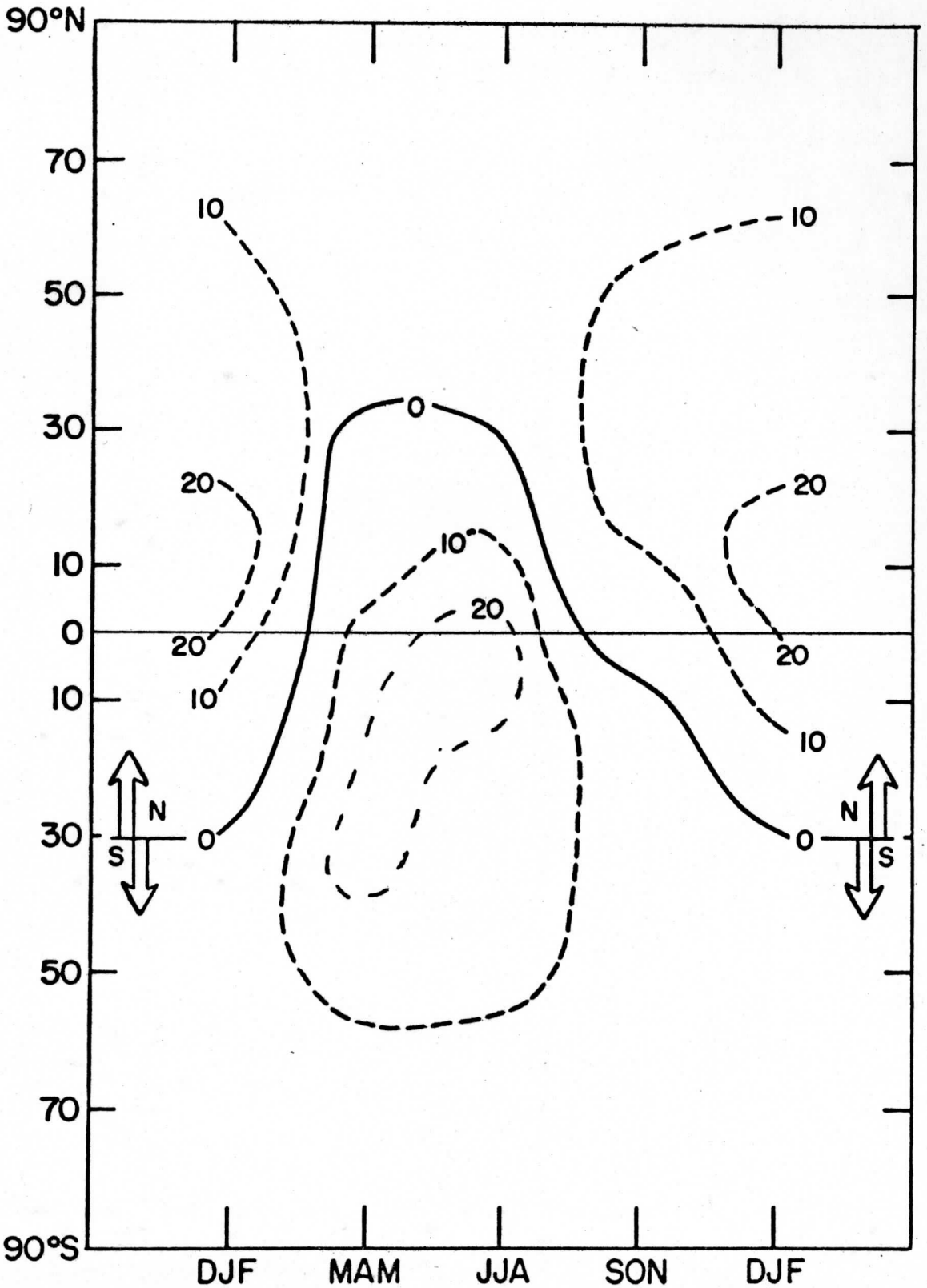

FIGURE 26: Time-latitude section of the required transport of non-latent energy by the atmosphere and oceans. Units are 10^{19} cal . day^{-1}.

Since the transports in this study include the contribution by the ocean as well as the total (sensible heat + potential energy) transport by the atmosphere, comparisons with other studies are difficult. Holopainen (1965) presented winter and summer transport values and he considered the contribution of both mean meridional circulations and eddies in the atmosphere. The shape of his curves agrees very well with those in Figure 25, but the magnitudes of his transport values averaged only 50 - 60% of those derived in this study. Some of this difference (perhaps as much as 40% according to Budyko and Kondratiev (1964)) can be attributed to oceanic transport and the remainder to computational uncertainties in both studies. He has shown that the double maxima in winter is due to peak transport values by the meridional cell near the equator and by eddies at mid-latitudes. This explains the mechanisms of transport for the available energy which is influenced by oceanic considerations noted previously.

Poleward transports of sensible heat by atmospheric eddies north of 20°N have been computed by Haines and Winston (1963). Similar seasonal transports were derived by Krueger et al. (1965) in order to infer the conversion between zonal and eddy available potential energy. Both of these studies show seasonal variations over the northern hemisphere in agreement with Figures 25 and 26.

The results most comparable with those of the present study are from Rasool and Prabhakara (1966), since we used their climatological

data. We find, however, large differences ($>10^{20}$ cal/day) in the required transport, especially during SON and DJF. Their SON values are much closer to the transports computed for the preceding six months, whereas in Figure 25 the SON and DJF curves are more similar. Such large differences result primarily from the different radiation budget data of the two studies and emphasize the importance of these data on the derived transports. An additional comparison is made in the next section.

5.3 The Mean Annual Case

A larger amount of climatological data that can be used to estimate energy budget terms is available for the mean annual case. In particular, Budyko (1963) has determined the mean annual geographical variation of evaporation, heat equivalent of precipitation, and oceanic energy divergence. Using these maps and the net radiation data of Figure 17, we derived the required net energy divergence by the atmosphere (ΔC) from equation 7. For this mean annual case, all storage terms are neglected. Figure 27 shows the results; the geographical distribution of regions of net sensible heat and potential energy export (D) and import (C).

The major features of this map agree well with the computations of Budyko who used empirical expressions to compute the net radiation budget of the earth-atmosphere system. In general, the absolute values of energy divergence are higher, by 10 to 20 kcal $\cdot$ cm^{-2} $\cdot$ yr^{-1} than Budyko's, especially at lower latitudes.

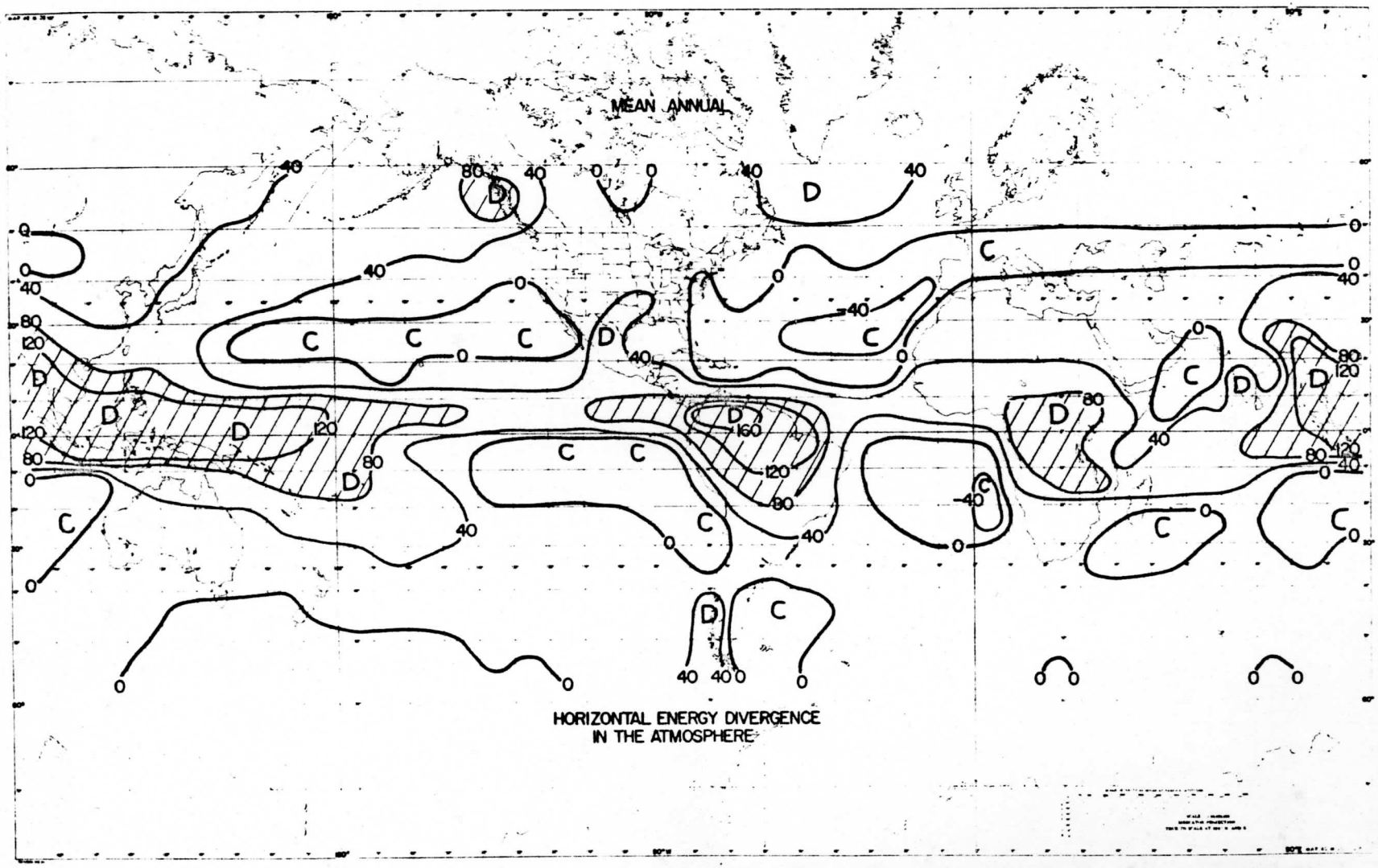

FIGURE 27: Geographical distribution of required divergence of non-latent energy by the atmosphere for the mean annual case. Units are kcal . cm^{-2} . yr^{-1} and the major energy exporting regions are shaded.

The regions of greatest energy export by the atmosphere are over Columbia (160 kcal $\cdot$ cm^{-2} $\cdot$ yr^{-1}), Southeast Asia and northeast of New Guinea (> 120) and equatorial Africa (> 80). Inspection of the radiation budget maps shows that each of these regions have high values of net radiation (> 60 kcal $\cdot$ cm^{-2} $\cdot$ yr^{-1}). Over Columbia this results primarily from a low albedo and the other regions have moderate albedos together with low values of outgoing longwave radiation. Each of the areas also receive more than 100 kcal $\cdot$ cm^{-2} $\cdot$ yr^{-1} from the release of latent heat. The maximum near Indonesia and Southeast Asia is decreased by 10 or 15% because of ocean energy transport from that region. Divergence minima near the equator are found over the Arabian Sea and the subtropical oceans of both hemispheres. Even though these regions have a net gain of energy across their upper boundaries, the excess of evaporation over precipitation during a year requires that the atmosphere imports energy. A notable exception is in the southwest Pacific where the cloudy band noted on the radiation maps releases enough latent heat to become a net energy source region.

At higher latitudes the continental regions of the United States, Central Asia, North Africa and Australia are very close to net energy balance in that the required mean annual atmospheric energy transports are small. Under such conditions, small changes in either the radiation or water budgets could influence the required atmospheric energy divergence.

The effects of precipitation maxima near the coasts of British Columbia and Chile are evident in the divergence centers found at these locations. Indeed the entire map of atmospheric energy export and import closely resembles the geographical distribution of precipitation (Budyko's). These results thus reaffirm the current opinion that latent heat processes must be incorporated into any model designed to simulate atmospheric conditions.

The required net energy transport by the atmosphere (sensible heat plus potential energy) and the oceans across latitudinal zones was also derived for the mean annual case. In Figure 28, three curves of $(\Delta C + \Delta F)$ are shown. The solid line and the unconnected points show the required transport that results when the radiation data of the present study are combined with estimates of the other terms in equation 7 derived from the data of Sellers (1966) and Rasool and Prabhakara (1965), respectively. For this annual case, the differences between the two curves result primarily from differences in the evaporation and precipitation estimates by the two studies. The relatively good agreement between the two curves occurs partly because each study used data presented by Budyko. The third (dashed) curve in Figure 28 shows the transports computed by Rasool and Prabhakara (1966) using some TIROS VII radiation data and the same climatological values used in our unconnected curve. Comparison of these two curves shows that the results of the present study require higher transport by the atmo-

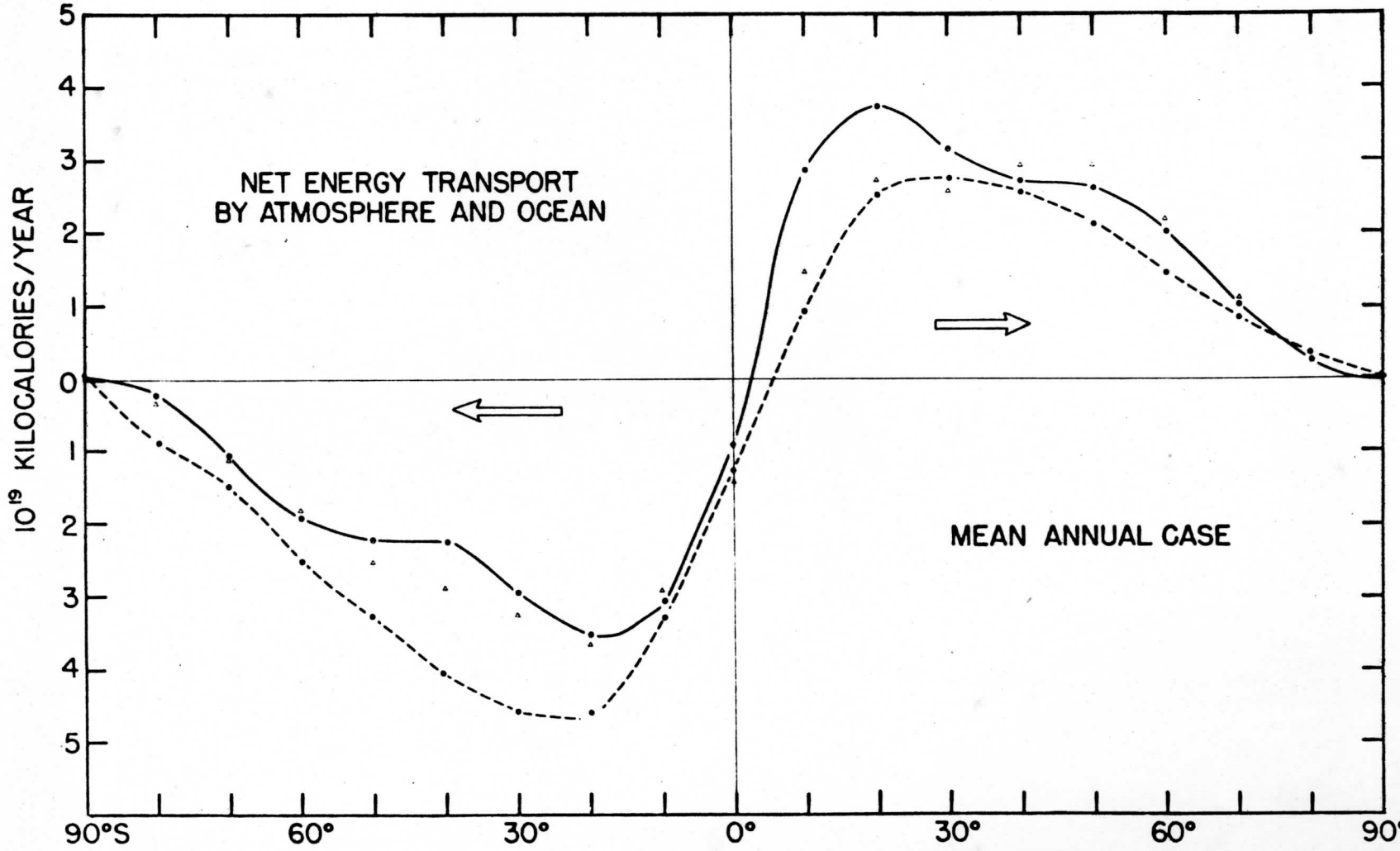

FIGURE 28: Poleward transport of non-latent energy derived from the radiation data of the present study and the energy budget values of Sellers (solid line) and Rasool and Prabhakara (unconnected points). Dashed line is from Rasool and Prabhakara.

sphere and oceans in the northern hemisphere and lower values in the south than were derived by Rasool and Prabhakara. Some of this departure is due to differences in the radiation budget data and the remainder can be attributed to the lack of TIROS VII data poleward of sixty degrees.

These curves illustrate the best estimates at this time of the required energy transport derived from the energy budget method. All of them show that a southward transport of non-latent energy (about 10^{19} kcal $\cdot$ yr^{-1}) across the equator is required. Both curves derived from the radiation data of this study show that the net transport is nearly the same in each hemisphere and has a mean annual value of about 2.2×10^{19} kcal $\cdot$ yr^{-1} ($\sim$ 23 watts $\cdot$ m^{-2}). A region of zero net flux near 5°N marks the mean position of the tropical convergence zone.

The partitioning of this transport between ocean and atmosphere and the latent heat contribution is shown in Figure 29. In this illustration, each of the terms in equation 6 are displayed except that all storage terms are assumed to be zero for this mean annual case. The required transport (RT) derived only from the net radiation data (RN_{EA}) is also shown. It represents the sum of the other transport terms which sometimes have opposite signs (i.e., southward transport of latent heat at 10°N versus northward transport by the other terms). House (1965) has summarized earlier estimates of RT, generally made for the northern hemisphere. The results of this study agree best with his data and those of Lettau (1954) in that the northern hemisphere region of

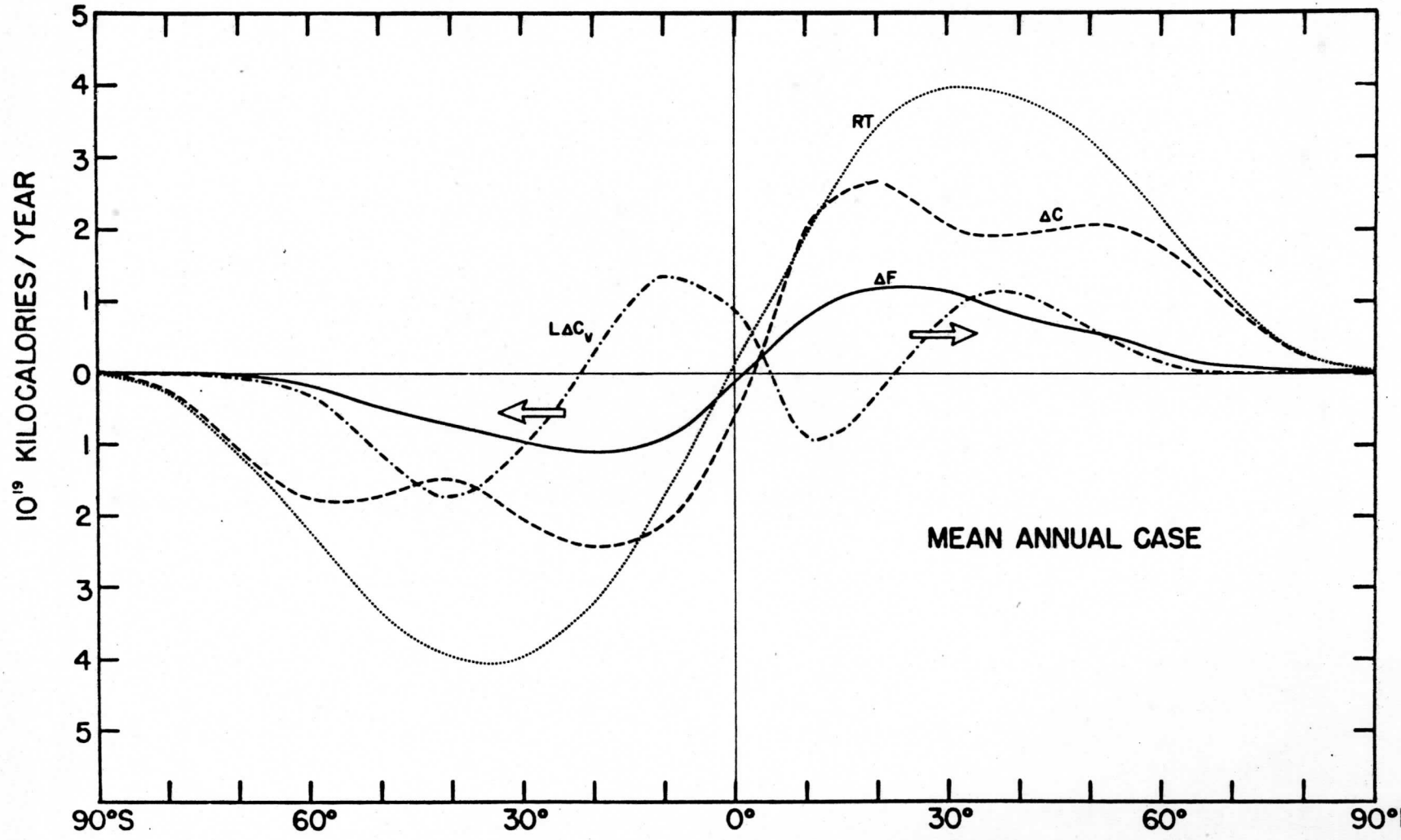

FIGURE 28: The total poleward energy transport required by the radiation budget (RT) and the contributions by the oceans (ΔF), the atmosphere's transport of latent heat ($L\Delta C_v$) and sensible heat + potential energy (ΔC).

maximum transport is $\sim 4 + 10^{19}$ kcal $\cdot$ yr^{-1} at 30°N. In the other hemisphere the radiation data show a flat maximum between 30 and 40 degrees of about the same magnitude. Because each hemisphere has the same radiation budget, the total net energy transport across the equator is zero.

The components of RT ($L\Delta C_v$, ΔF and ΔC) were obtained by using Sellers' (1966) values for the latent heat and oceanic transports and obtaining the atmosphere's contribution as a residual. Sellers' describes the various sources of his data and provides a good summary of previous work. The ocean values account for 20 - 25% of the total transport in both hemispheres. Latent heat is transported both equatorward and poleward from the evaporation maxima centered near 25°N and 25°S. This moisture converges between 5 and 10 degrees north, the mean location of the ITC. More water vapor is moved from the southern hemisphere and the net northward flux across the equator ($\sim 4.5 \times 10^{16}$ gm $\cdot$ day^{-1} or $\sim 10^{19}$ kcal/$\cdot$ yr^{-1}) compensates the southward energy transport by the atmosphere (ΔC) and oceans (ΔF).

Although obtained as a residual, the mean annual meridional values of ΔC show the double maxima and other features also noted by Holopainen (1965) for the northern hemisphere. In general the values of this study are about 15% larger than his results, but in view of all the assumptions involved there is good agreement. Our southern hemisphere results show a pattern of non-latent atmospheric energy

transport quite similar to that in the north.

Holopainen has also separated his data into contributions by various eddies and by the mean meridional cells. If we follow his suggestion and assign one-half of the total atmospheric energy transport to the eddies, a hemispheric average of this quantity over a year is 0.85 x 10^{19} kcal $\cdot$ yr^{-1} (4.4 watts $\cdot$ m^{-2}). A recent evaluation of the mean annual atmospheric energy cycle by Dutton and Johnson (1967) gave 5.6 watts/m^2 as the amount of energy continually being generated and dissipated within the atmosphere. Since the transport of sensible heat by the eddies is the primary conversion mechanism between zonal and eddy available potential energy the results of this study provide an indirect check on the magnitude they derived for this portion of the energy cycle (5.35 watts/m^2). The agreement with their computations, based in part on the energy dissipation rates of Kung (1966), is relatively good.

As a whole the energy budget data of this section compare well with various independent studies. They also point out the need for much more information on the other energy processes, now that radiation data are available on a global scale.

6. SUMMARY

The purpose of the present study has been to describe the radiation budget of the earth-atmosphere system as measured by the first generation meteorological satellites. Throughout the text some of the more noteworthy features of the observed budgets on various spatial and temporal scales have been discussed along with their meteorological implications. In the course of these discussions, the usefulness of these data for more detailed research, some of it non-meteorological, has been apparent.

Special attention should be given to the radiation budgets of the polar regions since the first extended series of measurements over them indicate that changing surface and atmospheric conditions may definitely override the normally dominant effect of incident solar radiation on the net budget. The mean seasonal and annual maps of albedo, longwave radiation and net radiation should be examined together with maps derived from specific seasons and months (to be published in atlas form).

Despite the large effect of seasonal changes in incident solar energy, time-latitude sections and budgets of selected zones have shown that the same seasons have different radiation budgets in different years. Atmospheric features that cause such changes and the response of the circulation pattern to them can be studied by using conventional meteorological data, computations of the energetics of the

atmosphere and numerical models. Indeed, one attribute of the radiation data is that they give us a vantage point midway between that which has happened and the future response of our system. From the radiation data, research efforts can proceed in either direction.

On a mean annual basis the measurements during 1963-65 show a small net gain of energy by the earth-atmosphere system of at least 0.01 cal $\cdot$ cm^{-2} $\cdot$ min^{-1}. Although this is a small percentage of the annual incident solar energy and may result from some undetected measuring problem, it may also represent part of a regular fluctuation in the energy exchange between our system and space. The addition of this energy to the mass of the atmosphere would raise the mean temperature 15°C/yr; to a 100 meter layer of the oceans, nearly 1°C/yr; and, as suggested by Rossby (1959), a 1000 meter layer of deep ocean water would be warmed at a rate of less than 0.1°C/yr.

Some of the results of this study may aid the development of numerical models that are designed to simulate atmospheric conditions. In particular, the relative distribution and absolute magnitudes of the radiation budget parameters can serve as a control for the models techniques of computing radiant energy transfer and their mean distributions of atmospheric variables that determine the radiation budget. The required poleward energy transports computed by the energy budget method in this study can be compared with those derived from the plentiful supply of data within the models. Because the mean annual

location of maximum regions of required atmospheric energy divergence corresponds very well with the distribution of latent heat release, the need to include this process in the models is re-emphasized. These same areas also have a net energy gain by radiation at the upper boundary that is generally half as large as the latent heat term. Thus, the longitudinal variation of the radiation budget between 30 degrees north and south must also be considered in numerical models.

New energy budget results derived from the radiation values and climatological data compare favorably with independent studies. However, the need for more extensive and accurate information about the other energy budget parameters is very evident now that satellite measurements of the radiation budget are available on a global scale. Some information about the energy transport from the tropical regions can be obtained from geosynchronous satellite observations. Thus, the major energy exporting areas noted in this study can be examined in detail with the high spatial resolution and time sampling provided by these new satellite observations.

Even though the radiation measurements of this study agree with independent observations from balloons and some early results from the NIMBUS satellites, a considerable effort was devoted to an error analysis. The value of at least a passive means of inflight calibration of the radiation sensors cannot be overemphasized. The low resolution sensors that provided the bulk of the data for this study had this

capability, but other problems remain. Some of these can be remedied by improved technology, while others require some scientific study. All radiation budget experiments require precise knowledge of the magnitude of the solar constant and another problem is lack of information about the diurnal variation of albedo and longwave radiation. As in this study, some measurements of the solar constant can be obtained from the radiation sensors and special equipment flown on satellites may provide better data also. The diurnal problem will not be resolved if our operational satellites are always placed into similar sun-synchronous orbits, and other sensors on geosynchronous satellites may be required. Since the solar radiation terms often dominate the total budget, the current emphasis on studies of the anisotropic nature of reflected radiation should be continued.

Estimates of the accuracy of any radiation budget measurements are essential in order to compare the observations with those obtained from different sensors. Like good wine, the value of these data should improve with age and when they have been joined by the results from the second generation satellites, we shall have just begun to properly examine the energy exchange between earth and space.

REFERENCES

Astling, E. G., and L. H. Horn, 1964: An Analysis of Diurnal Variations in TIROS II Radiation Data. Annual Report, Grant WBG-10, Department of Meteorology, The University of Wisconsin.

Bandeen, W. R., M. Halev, and I. Strange, 1965: A radiation climatology in the visible and infrared from the TIROS meteorological satellites, NASA TN D-2534.

Bartman, F. L., 1967: The reflectance and scattering of solar radiation by the earth, Technical Report 05863-11-T, College of Engineering, University of Michigan.

Bignell, K. J., 1961: Heat balance measurements from an earth satellite — An analysis of some possibilities, Quart. J. Roy. Meteor. Soc., Vol. 87, 231-244.

Budyko, M. I. (ed.), 1963: Atlas of the heat balance of the globe (in Russian), Moscow.

Budyko, M. I. and K. Y. Kondratiev, 1964: The heat balance of the earth, Research in Geophysics, Vol. 2: Solid Earth and Interface Phenomena, M.I.T. Press,529-554.

Drummond, A. J., J. R. Hickey and W. J. Scholes, 1967: Multichannel radiometer measurement of solar irradiance, J. Spacecraft and Rockets, Vol. 4, No. 9, 1200-1206.

Dutton, J. A. and D. R. Johnson, 1967: The theory of available potential energy and a variational approach to atmospheric energetics, Advances in Geophysics, Vol. 12, Academic Press, New York, 333-436.

Godson, W. L., 1958: Meteorological applications of earth satellites, Roy. Astron. Soc. of Canada, Vol. 52, No. 2, 49-56.

Haines, D. A. and J. S. Winston, 1963: Monthly mean values and spatial distribution of meridional transport of sensible heat, Mon. Wea. Rev., Vol. 91, No. 7, 319-328.

Holopainen, E. O., 1965: On the role of mean meridional circulations in the energy balance of the atmosphere, TELLUS, XVII, 3, 285-294.

House, F. B., 1965: The radiation balance of the earth from a satellite, Ph.D. thesis, Department of Meteorology, University of Wisconsin.

Johnson, F. S., 1954: The solar constant, J. Meteor., Vol. 11, No. 1, 431-439.

Kornfield, J., A. F. Hasler, K. J. Hanson and V. E. Suomi, 1967: Photographic cloud climatology from ESSA III and V computer produced mosaics, Bull. Amer. Met. Soc., Vol. 48, No. 12.

Krueger, A. F., J. S. Winston and D. A. Haines, 1965: Computations of atmospheric energy and its transformation for the northern hemisphere for a recent five-year period, Mon. Wea. Rev., Vol. 93, No. 4, 227-238.

Kuhn, P. M. and S. K. Cox, 1967: personal communication.

Kung, E. C., 1966: Large-scale balance of kinetic energy in the atmosphere, Mon. Wea. Rev., Vol. 94, No. 11,627-640.

Lettau, H.H., 1954: A study of the mass, momentum, and energy budget of the atmosphere. Archiv fur Meteorologie, Geophysik, und Bioklimatologie, Series A, Band 7, 133-157.

London, J., 1957: A study of the atmospheric heat balance, Final Report, Contract AF 19(122)-165, Research Division, College of Engineering, New York University.

NASA Staff Members, 1964: TIROS VII Radiation Data Catalog and Users' Manual, National Aeronautics and Space Administration, Washington.

Nicolet, M., 1951: Sur la de'termination du flux e'nerge'tique du rayonnement extraterrestre du soleil, Archiv fur Meteorologie, Geophysik, und Bioklimatologie, Series A, Band 3, 209-216.

Pasternak, Musa, 1967: An atlas of total outgoing long-wave radiation and of short-wave reflectances from NIMBUS II observations, Document X-622-67-500, NASA Goddard Space Flight Center.

Rados, R. M., 1967: The evolution of the TIROS meteorological satellite operational system, Bull. Amer. Met. Soc., Vol. 48, No. 5, 326-337.

Raschke, E. F., Möller and W. R. Bandeen, 1967: The radiation balance of the earth-atmosphere system over both polar regions obtained from radiation measurements of the NIMBUS II meteorological satellite, Document X-622-67-460, NASA Goddard Space Flight Center.

Raschke, E. and Musa Pasternak, 1967: The global radiation balance of the earth-atmosphere system obtained from radiation data of the meteorological satellite NIMBUS II, Document X-622-67-383, NASA Goddard Space Flight Center.

Rasool, S. I., 1964: Global distribution of the net energy balance of the atmosphere from TIROS radiation data, Science, Vol. 143, No. 3606, 567-569.

Rasool, S. I., and C. Prabhakara, 1966: Heat budget of the southern hemisphere, Problems in Atmospheric Circulations, Spartan Books, Washington, D.C., 76-92.

Rossby, C.-G., in The Atmosphere and the Sea in Motion (Bolin, ed.), 1959: Rockefeller Institute Press, New York, 9-50.

Ruff, I., R. Koffler, S. Fritz, J.S. Winston, and P. K. Rao, 1967: Angular distribution of solar radiation reflected from clouds as determined from TIROS IV radiometer measurements, ESSA Technical Report NESC-38, Washington, D.C.

Sellers, W.D., 1965: Physical Climatology, The University of Chicago Press, Chicago and London.

Solomonson, V. 1966: Anisotrophy of reflected solar radiation from various surfaces as measured with an aircraft-mounted radiometer, Research Report, Contract NASr-147, Colorado State University.

Sparkman, Barbara B., 1964: Experimental analysis of the TIROS hemispheric sensor, M.S. thesis, Department of Meteorology, The University ofWisconsin.

Starr, V. P., 1951: Applications of energy principles to the general circulation, Compendium of Meteorology, American Meteorological Society, Boston, 568-574.

Suomi, V. E., 1958: The radiation balance of the earth from a satellite, Annals of the IGY, Vol. I, 331-340.

Suomi, V. E., K. J. Hanson and T. H. Vonder Haar, 1967: The theoretical basis for low-resolution radiometer measurements from a satellite, Annual Report, Grant WBG-27, Department of Meteorology, University of Wisconsin, 79-100.

Vonder Haar, T. H. and K. J. Hanson, 1968: A note on the diurnal variation of planetary albedo and outgoing longwave radiation, unpublished.

Widger, W. K., 1967: Tabulations of some of the most frequently required information on individual TIROS satellites, Bull. Amer. Met. Soc., Vol. 48, No. 5, 339-346.

Winston, J. S., 1967: Planetary-scale characteristics of monthly mean long-wave radiation and albedo and some year-to-year variations, Mon. Wea. Rev., Vol. 95, No. 5, 235-256.

Winston, J. S. and V. R. Taylor, 1967: Atlas of world maps of long-wave radiation and albedo for seasons and months based on measurements from TIROS IV and TIROS VII, ESSA Technical Report NESC 43, Washington, D. C.

APPENDIX: SATELLITE OBSERVATIONS OF THE SOLAR CONSTANT

1. Purpose

Recent high-altitude aircraft observations by Drummond et al. (1967) have provided another estimate of the magnitude of the solar constant. Their value of 1.95 ly/min may have an accuracy of $\pm$ 2% ($\pm$ 0.04 ly/min) the same error limit quoted by Johnson (1954) for his value of 2.00 ly/min.

For many studies this uncertainty may be trivial, but when highly accurate albedo and longwave radiation observations are used together with an estimate of the solar constant in a study of the earth's radiation budget, the chosen value significantly effects net radiation magnitudes and the estimated absolute error of these data. (See 3.22.) In order to aid the choice of a proper value and to estimate its accuracy a third measurement of the solar constant was derived from the observations of heat budget sensors carried on a satellite.

2. Method

Black and white flat sensors were used and the reduction of their measurements into irradiance and albedo values has been completely described by Suomi et al. (1967). Twice during each orbit these sensors pass across the terminator. Because of the satellite's altitude the sensors are exposed to direct solar radiation while still located

above a dark earth. On these occasions only longwave radiation from the earth and direct solar radiation from the sun are incident on these sensors. In this study we will examine a long-time series of such measurements, remove the contribution due to IR radiation and thus obtain the solar constant as seen by the sensors (the direct solar radiation). This measurement can be used to obtain the magnitude of the solar constant if the effects of sun-sensor geometry, sensor absorptivity and earth-sun distance are removed.

3. Measured Values

Suomi et al. (1967) define two quantities that are measured each time the sensors pass from night to day. For flat spinning sensors they are:

$$D^* = (E_B - E_W)_t = 2I_0 r' \cos\gamma\,(\alpha'_B - \alpha'_W)$$

$$W^* = (E_{W_t} - E_{W_N}) = 2I_0\, r' \cos\gamma\, \alpha'_W$$

where the E values are proportional to energy loads on the black or white sensors at location t, the day side of the terminator, or N, the night side of the terminator. I_0 is the solar constant, r' the factor to account for variations in earth-sun distance, γ the angle between the solar radiation and a normal to the sensors and α' the ratio of a sensor's absorptivities for shortwave radiation over longwave radiation. With the aid of the illustration in Figure A1, it is seen that the solar

constant as seen by the sensor set is given by $(D^* + W^*) = E_{B_T} - E_{W_N}$ (i.e., the total longwave and shortwave radiation less the longwave component). In practice, both D^* and W^* were computed at point t about 2000 times and the variation of their sum with time is also shown in Figure A1.

Now

$$(D^* + W^*) = 2I_0 r' \cos\gamma \, \alpha'_B$$

and thus the white sensor's absorptivity ratio is eliminated from consideration. The quantity $(D^* + W^*)$ varies with time primarily because γ changes. Fortunately the effects of γ and r' are known exactly and can be removed. Thus the variation of $I_0\alpha'_B = (D^* + W^*)/2\, r'\cos\gamma$ is also shown in Figure A1. The best fit of all the data points is a line with $Y = I_0\alpha'_B = 2.17$ ly/min. The standard error is 0.04 ly/min (1.5%) and since D^* and W^* are measured values, the $I_0\alpha'_B$ data also have a possible bias error of $\pm .02$ ly/min.

The invariance of $I_0\alpha'_B$ over a long time period is encouraging, it implies that:

a) the absorptivities of the black sensor did not change with time (this agrees with data from similar sensors flown on other satellites)

b) the absorptivities did not change significantly as the angle of incident solar radiation varied

c) the solar constant is indeed constant

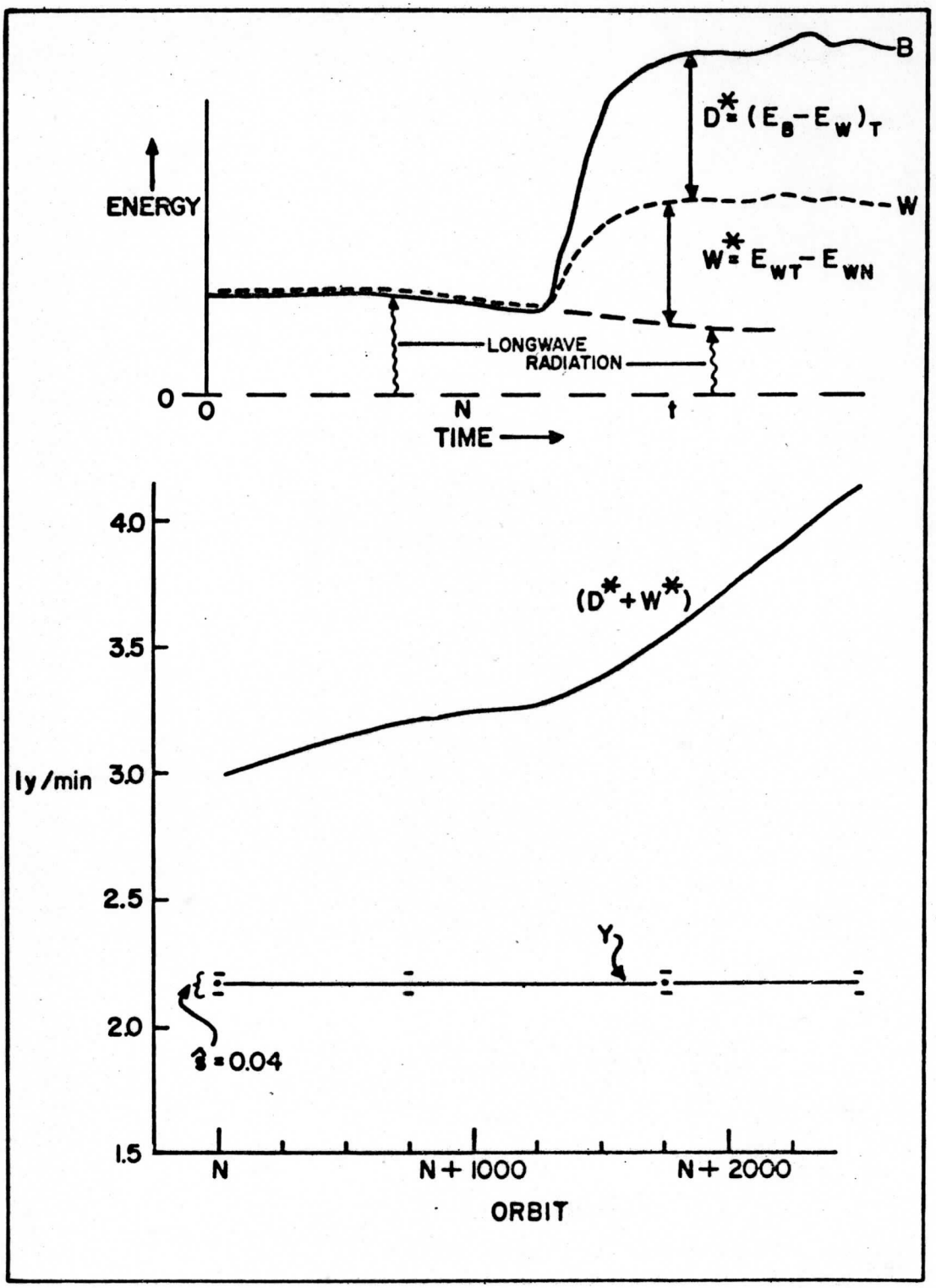

FIGURE A1: Example of parameters computed at each terminator crossing (upper portion) and the variation with time of $(D^* + W^*)$ and $Y = (D^* + W^*)/2\ r'\ \cos\gamma$.

There is, of course, the possibility that any two or all of these three statements are false and that changes did occur in compensating directions, but this is improbable.

4. Necessary Laboratory Data

In order to derive an estimate of the solar constant (I_0), we must use the best value of α'_B determined before launch. Since the value apparently did not change in orbit, this laboratory estimate would be valid, baring a sudden undetected change just after launch. As mentioned

$$\alpha'_B = ((\alpha_{SW}/\alpha_{LW}))_B$$

and the two components were obtained separately for experimental reasons. The mean shortwave absorptivity was obtained by weighting precision spectrometer measurements made at Lion Research Corp. by the shape of the extraterrestrial solar irradiance curve given by Johnson (1954); refer to House (1967).[1] The value for $\alpha_{B_{SW}}$ was 0.97 ± 0.01. Absorptivity of the black sensor to infrared radiation typical of that emitted by the earth and atmosphere from the regions where the measurements were made was determined by Hanson (1966).[1] He used hohlaraum data for the black paint provided by Shoffer

---

[1] unpublished report

(1962)[1] and obtained $\alpha_{B_{LW}} = 0.90$. His calculations agree to within $\pm .02$ with independent estimates by Sparkman (1964) and the author using a second set of hohlaraum data for the same paint. Thus the best estimates of $\alpha'_B = 1.075$ and a reasonable bias error is $\pm .02$.

5. Results and Error Analysis

Solving for $I_0 = (I_0 \alpha'_B)/\alpha'_B$ we obtain a solar constant magnitude of 2.01 ly/min from our satellite observations. A simple estimate of the possible bias error can be made if we let

$$(I_0 \alpha'_B) = Y = 2.17 \text{ ly/min}$$

$$dY = \pm 0.02 \text{ ly/min}$$

$$\alpha'_B = X = 1.075$$

$$dX = \pm 0.02$$

and

$$dI_0 = \frac{y\,dx - x\,dy}{y^2} = \pm 0.05 \text{ ly/min}$$

for the worst absolute error and $dI_0 = \pm .017$ ly/min for the best case (a range in percent error from 2.5% to less than 1%). A small part of the possible bias error in the measurement results from slight changes of adsorbtivity at different incidence angles. The best estimate of both the magnitude and direction of this error yields a solar constant of 1.99 ± 0.03 cal $\cdot$ cm^{-2} $\cdot$ min^{-1}.

The goal of any solar constant measurement should be at least 1% accuracy since the best estimates of the variation of this parameter

are within that range. With the data of the present study, checks on the absolute magnitude of α'_B and its variation with angle will be made in order to remove some small uncertainties. Sensors now being carried on the ESSA satellites can be used to obtain more accurate measurements of $Y = \alpha'_B I_0$ since they are better isolated from the spacecraft itself. Although this improved design may pose some problems regarding the geometry of the sensing surfaces, ESSA data together with careful pre-launch study of α'_B should provide more accurate measurements of the solar constant. The addition of a relative calibration mechanism on the satellite would eliminate any uncertainty arising from degradation occurring between pre-launch tests and the start of normal operations at altitude.